

AD-A045 021

JOHNS HOPKINS UNIV LAUREL MD APPLIED PHYSICS LAB

F/G 3/2

INTER-RELATIONSHIPS OF SOLAR AND INTERPLANETARY PLASMA, MAGNETI--ETC(U)

JUL 77 E C ROELOF, R E GOLD

N00017-72-C-4401

UNCLASSIFIED

SCIENTIFIC-2

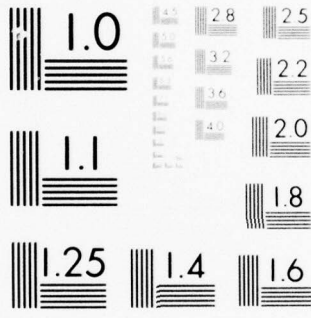
AFGL-TR-77-0166

NL

1 OF 2

AD
A045021





MICROCOPY RESOLUTION TEST CHART
NATIONAL BUREAU OF STANDARDS-1963-A

AD A 045021

AFGL-TR-77-0166

INTER-RELATIONSHIPS OF SOLAR AND INTERPLANETARY
PLASMA, MAGNETIC FIELDS AND ENERGETIC
PARTICLES RELEVANT TO THE PREDICTION OF
SOLAR-TERRESTRIAL DISTURBANCES

E.C. Roelof
R.E. Gold

The Johns Hopkins University
Applied Physics Laboratory
Laurel, Maryland 20810

29 July 1977

Scientific Report No. 2

Approved for public release; distribution unlimited

AIR FORCE GEOPHYSICS LABORATORY
AIR FORCE SYSTEMS COMMAND
UNITED STATES AIR FORCE
HANSCOM AFB, MASSACHUSETTS 01731

Qualified requestors may obtain additional copies from the Defense Documentation Center. All others should apply to the National Technical Information Service.

Unclassified

SECURITY CLASSIFICATION OF THIS PAGE (When Data Entered)

REPORT DOCUMENTATION PAGE		READ INSTRUCTIONS BEFORE COMPLETING FORM
1. REPORT NUMBER AFGL-TR-77-0166	2. GOVT ACCESSION NO.	3. RECIPIENT'S CATALOG NUMBER
4. TITLE (and Subtitle) Inter-relationships of Solar and Interplanetary Plasma, Magnetic Fields and Energetic Particles Relevant to the Prediction of Solar-Terrestrial Disturbances	5. TYPE OF REPORT & PERIOD COVERED Scientific Interim	
	6. PERFORMING ORG. REPORT NUMBER Scientific Report No. 2	
7. AUTHOR(s) E. C. Roelof and R. E. Gold	8. CONTRACT OR GRANT NUMBER(s) MIPR No. FY 71217700005 to Contract N00017-72-C-4401, Department of the Navy	
9. PERFORMING ORGANIZATION NAME AND ADDRESS The Johns Hopkins University Applied Physics Laboratory Laurel, Maryland 20810	10. PROGRAM ELEMENT, PROJECT, TASK AREA & WORK UNIT NUMBERS 61102F 2311G101	
11. CONTROLLING OFFICE NAME AND ADDRESS Air Force Geophysics Laboratory Hanscom AFB, Massachusetts 01731 Monitor/M. A. Shea / PHG	12. REPORT DATE 29 July 1977	
	13. NUMBER OF PAGES 155	
14. MONITORING AGENCY NAME & ADDRESS (if different from Controlling Office)	15. SECURITY CLASS. (of this report) Unclassified	
	15a. DECLASSIFICATION/DOWNGRADING SCHEDULE	
16. DISTRIBUTION STATEMENT (of this Report) Approved for public release; distribution unlimited		
17. DISTRIBUTION STATEMENT (of the abstract entered in Block 20, if different from Report)		
18. SUPPLEMENTARY NOTES Work performed as Task ZF10 of Contract N00017-72-C-4401, Department of the Navy. Continues work previously performed under MIPR No. FY71217600002		
19. KEY WORDS (Continue on reverse side if necessary and identify by block number) Solar-Terrestrial disturbance prediction Solar energetic particles Solar coronal magnetic fields Solar wind stream origins Interplanetary radio scintillations		
20. ABSTRACT (Continue on reverse side if necessary and identify by block number) A summary is presented of research results from the past year's efforts supported under this contract. The research covered inter-related topics in solar-terrestrial relationships. It is recommended that the present dual approach of investigations of solar-terrestrial events both of the past solar cycle as well as contemporary observations be continued. Comparison of phenomena among different phases of the solar cycle have identified several inter-relationships useful in the development of prediction techniques for geomagnetic disturbances and solar energetic particle events.		

DD FORM 1473
1 JAN 73

EDITION OF 1 NOV 65 IS OBSOLETE

Unclassified

SECURITY CLASSIFICATION OF THIS PAGE (When Data Entered)

<p>1. TITLE AND SUBTITLE</p>	<p>1. TITLE AND SUBTITLE</p>
<p>2. AUTHOR(s)</p>	<p>2. AUTHOR(s)</p>
<p>3. PERFORMING ORGANIZATION NAME(s)</p>	<p>3. PERFORMING ORGANIZATION NAME(s)</p>
<p>4. PERFORMING ORGANIZATION NUMBER</p>	<p>4. PERFORMING ORGANIZATION NUMBER</p>
<p>5. REPORT NUMBER</p>	<p>5. REPORT NUMBER</p>
<p>6. AUTHORING ORGANIZATION NAME(S)</p>	<p>6. AUTHORING ORGANIZATION NAME(S)</p>
<p>7. AUTHORING ORGANIZATION NUMBER</p>	<p>7. AUTHORING ORGANIZATION NUMBER</p>
<p>8. PERFORMING ORGANIZATION REPORT NUMBER</p>	<p>8. PERFORMING ORGANIZATION REPORT NUMBER</p>
<p>9. PERFORMING ORGANIZATION REPORT NUMBER</p>	<p>9. PERFORMING ORGANIZATION REPORT NUMBER</p>
<p>10. PERFORMING ORGANIZATION REPORT NUMBER</p>	<p>10. PERFORMING ORGANIZATION REPORT NUMBER</p>
<p>11. PERFORMING ORGANIZATION REPORT NUMBER</p>	<p>11. PERFORMING ORGANIZATION REPORT NUMBER</p>
<p>12. PERFORMING ORGANIZATION REPORT NUMBER</p>	<p>12. PERFORMING ORGANIZATION REPORT NUMBER</p>
<p>13. PERFORMING ORGANIZATION REPORT NUMBER</p>	<p>13. PERFORMING ORGANIZATION REPORT NUMBER</p>
<p>14. PERFORMING ORGANIZATION REPORT NUMBER</p>	<p>14. PERFORMING ORGANIZATION REPORT NUMBER</p>
<p>15. PERFORMING ORGANIZATION REPORT NUMBER</p>	<p>15. PERFORMING ORGANIZATION REPORT NUMBER</p>
<p>16. PERFORMING ORGANIZATION REPORT NUMBER</p>	<p>16. PERFORMING ORGANIZATION REPORT NUMBER</p>

1. INTRODUCTION

In Scientific Report No. 1 (Roelof and Gold, 1976), we emphasized the dominant influence of coronal and interplanetary magnetic field structure on solar energetic particle time histories. We demonstrated that the key to "decoding" the spatial profile of coronal energetic particle injection lay in the solar wind velocity variations. Thus, prediction of the solar wind stream structure not only allows forecasting of geomagnetic disturbances, but also lies at the heart of predicting time histories of solar particle events. As stated in Scientific Report No. 1:

"We therefore recommend the dual course of incorporating the latest results of the interpretation of interplanetary scintillations into prediction techniques while also proceeding with a comprehensive study of plasma, magnetic field and energetic particle data from the last solar cycle and on into the current cycle."

We indeed followed this dual course during this past year by pursuing scientific investigation related to prediction techniques on the following inter-related subjects:

- Coronal magnetic fields
- Origin of solar wind streams
- Coronal propagation of energetic particles
- Observation and theory of interplanetary radio scintillation
- Sources of heavy ion enhancements in solar particle events
- Synthesis of solar and interplanetary plasma, magnetic field and energetic particle observations
- Interplanetary propagation of relativistic Jovian electrons

Interaction of solar energetic particles with the Earth's
bow shock

Substorm association of energetic particle bursts in the
magnetotail and upstream of the bow shock

These efforts involved our colleagues at JHU/APL (not funded
under this contract), B. L. Gotwols, S. M. Krimigis, D. G. Mitchell and
R. D. Zwickl, as well as collaborations with the following scientists
at other institutions:

Air Force Geophysics Laboratory

M. A. Shea, D. F. Smart

American Science and Engineering

A. S. Krieger, J. T. Nolte, G. Vaiana

Center for Astrophysics (Harvard)

R. H. Levine

European Space Research and Technology Centre

R. Reinhard

McMath-Hulbert Observatory

E. R. Hedeman, H. W. Dodson Prince

Massachusetts Institute of Technology

A. J. Lazarus, J. D. Sullivan

National Aeronautics and Space Administration

A. F. Timothy, R. P. Lepping

National Atmospheric and Oceanic Administration

P. S. McIntosh, D. J. Williams

University of California at San Diego

R. W. Fillius

University of Iowa

W. M. Cronyn, F. T. Erskine, S. D. Shawhan

University of Malaya

C.-K. Ng

University of Tokyo

T. Iijima

The next section summarizes this work which has been published in 5 journal articles (reprints attached in the Appendix) and 5 conference articles in press (JHU/APL preprints also attached in the Appendix). In addition, 2 other articles are in press (J. Geophys. Res.), as well as a special UAG Report, and 5 manuscripts are in preparation.

Eleven contributed papers were presented at the Fall and Spring National Meetings of the American Geophysical Union, and three invited papers were given:

International Symposium on Solar-Terrestrial Physics

(E. C. Roelof), Boulder, Colorado, June 7-18, 1976

American Geophysical Union Spring National Meeting

(R. E. Gold and E. C. Roelof), Washington, D. C., May 30-June 3, 1977

L. D. DeFeiter Memorial Symposium on Study of Travelling

Interplanetary Phenomena (E. C. Roelof and S. M. Krimigis), Tel Aviv, Israel, June 7-10, 1977.

2. SUMMARY OF SCIENTIFIC RESULTS

Solar wind stream structure is causally related to geomagnetic disturbances and controls the interplanetary magnetic field, thereby linking the Earth to the corona. We have therefore studied the basic question of location of solar wind sources. The Skylab period offered an excellent opportunity to compare solar wind velocities from the MIT experiment on IMP 7 and 8 with the American Science and Engineering soft x-ray images of the corona. Nolte et al. (1976) verified that equatorial coronal holes were sources of solar wind. From a detailed study of the same data, Nolte et al. (1977) deduced the three-dimension structure of the Alfvén critical surface above hole and non-hole associated solar wind stream sources. Levine and Roelof (in preparation) are comparing potential field calculations based on the Kitt Peak, magnetograms during the same period with the JHU/APL 3 MeV proton observations.

Although the structure of coronal magnetic fields during Skylab is characteristic only of the decline of Solar Cycle 20, there appears to be causal relationships between coronal fields, solar wind and energetic particles which can be generalized to other portions of the solar cycle. Roelof (1976) summarized the general approach of synthesizing solar and interplanetary data, and Roelof and Krimigis (1977) have emphasized the necessity for recognizing and compensating for the interplanetary and magnetospheric processes that distort the information on coronal emission contained in near-Earth energetic particle observations. For example, Ng and Roelof have used simultaneous anisotropy measurements from the JHU/APL experiments on IMP 7 and 8 to show that the Earth's bow shock

acts like an efficient reflector of 0.3 MeV solar protons and electrons when the interplanetary field line extended from the spacecraft intersects the nominal shock surface. Thus it is likely that previous near-Earth measurements under-estimated the anisotropies in low energy solar flare proton and electron events. Another magnetospheric "contaminant" of solar particle anisotropies is the upstream escape of ≤ 1 MeV magnetospheric protons and electrons. These particles are commonly observed during substorm intensification plasma sheet, and Roelof et al. (1977) have shown their acceleration is closely associated with the westward intrusion of the westward auroral electrojet. Gold, Roelof, Lepping and Williams have found "slabs" of interplanetary field lines populated with > 50 keV protons upstream of the bow shock following the SSC within the solar proton event of October 29, 1972. However, the temporal, spectral and anisotropy signatures of upstream magnetospheric particle bursts are now easily recognized, so that one can proceed with the analysis of solar energetic particles even in the presence of magnetospheric particles.

Using the solar-wind mapping techniques which our group has developed, Gold et al. (1977a) demonstrated that $\sim 70\%$ of ~ 1 MeV/nucleon particle event histories during 1972-1976 were dominated by "spatial" injection longitude profiles at the corona. Nolte and Roelof (1977) found a complementary result during the first year (1965) of the previous solar cycle. They compared the Mariner 4 solar wind and energetic particle histories with the global chromospheric polarity structure constructed from H_{α} filtergrams. Statistically, solar wind streams and energetic particles were emitted from different magnetic

structures. Nolte and Roelof are now preparing a detailed analysis of the Mariner 4 energetic particle events.

An extremely interesting flare event (April 10, 1969) near solar maximum has been re-analyzed using solar wind mapping techniques by Gold et al. (1977b). Observations from 5 spacecraft distributed over 180° in longitude of ~ 10 MeV proton data and solar wind data have been combined to produce the first true coronal injection history and large-scale distribution in helio-longitude for a solar flare proton event. Once again, it is found that the protons are preferentially injected into the interplanetary medium well away ($\sim 90^\circ$) from the flare site, even though solar wind heating is centered above the flare.

Coronal and interplanetary signatures also cast light on the origin of a newly discovered class of small solar particle events rich in H_e^3 and elements as heavy as Fe. Zwickl et al. (1977) have established the following characteristics for 10 events (September 1972 - December 1975): i) no association with solar flares (importance > 1); ii) large and prolonged (> 1 day) outward flowing anisotropies; and iii) a loose association with low speed solar wind.

Another recent discovery is the ubiquity of relativistic Jovian electrons throughout the solar system. Gold et al. (1977c) have argued that these electrons are quasi-trapped within the "pin wheel" shaped cavities bounded by the junctions of co-rotating interplanetary magnetic "interaction regions" beyond 5 AU. Thus these electrons are responding to solar wind stream structure on the scale of tens of AU.

Solar wind structure beyond 1 AU can be probed directly by ground-based measurements of interplanetary radio scintillations along

the line-of-sight to celestial radio sources at large solar elongation angles ($\epsilon > 60^\circ$). Erskine et al. 1977 have analyzed scintillation indices from 33 sources observed May - December 1974 at 34.3 MHz with the COCOA-Cross Array at the Clark Lake Radio Observatory in California. Comparison with IMP 7 and 8 solar wind data revealed that the largest scintillation responses at large ϵ were to enhanced density structures in the solar wind, rather than to high velocities. This result has been confirmed recently by Gotwols, Mitchell, Roelof, Cronyn and Erickson using COCOA-Cross data from May to August, 1976. They have found that the scintillation spectrum broadens (as the index increases) in response to solar wind density enhancements. Both the 1974 and 1976 results are in good agreement with the weak-scattering extended-medium calculations of Mitchell and Roelof (1976) and Mitchell (1977).

In the broadest sense, all of the phenomena which we have studied are organized by coronal magnetic fields. We recognized some five years ago that a global description of these fields was a pre-requisite for solar-interplanetary studies. P. S. McIntosh of NOAA/ERL had developed a technique for deducing the boundaries of large scale magnetic polarity regions in the low corona from absorption features seen in H_α filtergrams. Consequently, in 1972 we undertook the compilation of an atlas of H_α synoptic charts for Solar Cycle 20. A staff of solar cartographers (under the supervision of McIntosh and supported by this contract and its predecessor), has completed 130 synoptic charts (Carrington Rotations 1487-1616). The atlas begins at solar minimum (November 1964) and ends in the decline of Solar Cycle 20 (August 1974) when monthly H_α charts

began to be published in Solar Geophysical Data. Final graphics for the atlas are being completed at JHU/APL and McIntosh is doing final editing and annotation of the H_{α} charts at NOAA/ERL. The atlas will be published this Fall (1977) by NOAA/EDS as a UAG Special Report.

3. CONCLUSIONS AND RECOMMENDATIONS

We believe the results of this year's research have validated the recommendations made in Scientific Report No. 1 (Roelof and Gold, 1976). We have been able to extract significant new information bearing directly on the prediction of geomagnetic disturbances and solar energetic particle events from our work on solar-terrestrial relationships in Solar Cycle 20, on the IMP 7 and 8 period (1972 - present), and on interplanetary radio scintillations.

We have considerably expanded our computerized Solar Cycle 20 archive of solar and interplanetary magnetic field, plasma and energetic particle data with the assistance of the National Space Science Data Center and M. A. Shea and D. F. Smart of AFGL. Its utility has been greatly enhanced by the development of graphical data representation from multiple spacecraft in a solar rotation format. These programs equally well handle the IMP 7 and 8 data. Thus cross-comparisons of solar-terrestrial phenomena are readily obtainable between the present and past solar cycle. One gains considerably from such comparisons because the greater sensitivity and range of species measured by contemporary instruments allows a deeper understanding of the phenomena which can then be applied to the interpretation of earlier observations with crude instrumentation.

We therefore recommend a continuation of the present scientific program with incorporation of the results as improvements in the prediction technique developed under our previous contract with the Air Force Geophysics Laboratory.

REFERENCES

*Publications supported in part under this contract and appended below

- Erskine, F. T., W. M. Cronyn, S. D. Shawhan, E. C. Roelof and B. L. Gotwols
Interplanetary scintillation at large elongation angles: Response
to solar wind density structure, J. Geophys. Res. 82, in press,
1977.
- *Gold, R. E., S. M. Krimigis and E. C. Roelof, Spatially dominated solar
particle events 1972-1976, Proc. 15th Int. Cosmic Ray Conf.
(Plovdiv, Bulgaria), in press 1977a.
- *Gold, R. E., E. P. Keath, E. C. Roelof and R. Reinhard, Coronal structure
of the April 10, 1969 solar flare particle event, Proc. 15th Int.
Cosmic Ray Conf. (Plovdiv, Bulgaria), 1977b.
- *Gold, R. E., S. M. Krimigis, E. C. Roelof and R. W. Fillius, The
relationship between Jovian electrons and solar wind stream
structure, Proc. 15th Int. Cosmic Ray Conf. (Plovdiv, Bulgaria),
in press, 1977c.
- Mitchell, D. G., Analysis of interplanetary scintillation spectra at
large elongation angles, J. Geophys. Res. 82, submitted, 1977.
- *Mitchell, D. G. and E. C. Roelof, A mathematical analysis of the theory
of interplanetary scintillation in the weak-scattering
approximation, J. Geophys. Res., 81, 5071, 1976.
- *Nolte, J. T. and E. C. Roelof, Solar wind energetic particles, and coronal
magnetic structure: The first year of solar cycle 20, J. Geophys.
Res. 82, 2175, 1977.

REFERENCES (Continued)

*Publications supported in part under this contract and appended below

*Nolte, J. T., A. S. Krieger, A. F. Timothy, R. E. Gold, E. C. Roelof, G. Vaiana, A. J. Lazarus, J. D. Sullivan and P. S. McIntosh, Coronal holes as sources of solar wind, Solar Phys., 46, 303, 1976.

*Nolte, J. T., A. S. Krieger, E. C. Roelof and R. E. Gold, High coronal structure of high velocity solar wind streams, Solar Phys., 51, 459, 1977.

*Roelof, E. C., Solar particle emission, in Physics of Solar Planetary Environments, Proceedings of the International Symposium on Solar-Terrestrial Physics (Boulder), Colorado, D. J. Williams, American Geophysical Union (Washington, D.C.), 1, 214, 1976.

Roelof, E. C. and R. E. Gold, Prediction of solar energetic particle event histories using real-time particle and solar wind measurements, Air Force Geophysics Laboratory Technical Report AFGL-TR-76-0136, 1976.

*Roelof, E. C. and S. M. Krimigis, Solar energetic particles below 10 MeV, Proceedings of the L. D. DeFeiter Memorial Symposium on Study of Travelling Interplanetary Phenomena, ed. M. A. Shea and C. S. Wu, D. Reidel (Dordrecht), in press, 1977.

*Roelof, E. C., E. P. Keath and T. Iijima, Fluxes of 750 keV protons and > 30 keV electrons at ~ 35 Re. 4. Association of intense bursts of energetic particles in the magnetotail with the expansion phase of geomagnetic substorms, J. Geophys. Res. 82, in press, 1977.

REFERENCES (Continued)

*Publications supported in part under this contract and appended below

- *Zwickl, R. D., S. M. Krimigis, R. E. Gold, E. C. Roelof and T. P. Armstrong,
Observations of enhanced abundances of He through Fe nuclei during
solar flare events, 1972 to 1976, Proc. 15th Int. Cosmic Ray
Conf. (Plovdiv, Bulgaria), in press, 1977.

SPATIALLY DOMINATED SOLAR PARTICLE EVENTS 1972-1976

R. E. Gold, S. M. Krimigis and E. C. Roelof

Applied Physics Laboratory/The Johns Hopkins University
Laurel, Maryland 20810 USA

We have examined low energy solar particle data from the APL/JHU experiments on IMP-7 and 8 during 50 solar rotations between September 1972 and May 1976 and find that spatial gradients which are nearly independent of particle rigidity and species dominate the time histories. There are 57 rounded events with gradients on each side, 17 spatially dominated decays of flare associated temporal events and 9 broad minima. These events fill about 70% of the total time period and ~ 70% are associated with solar wind streams. The e-folding lengths of the gradients average ~ 20° heliographic longitude and the rounded events have soft spectra and are Helium rich. These events are consistent with coronal propagation from a central source by a mechanism independent of particle species and energy.

INTRODUCTION

The observed time profile of spatially ordered solar particle events may be dramatically altered by velocity structure in the solar wind. If the interplanetary trajectory of the plasma is approximated by radial expansion at constant velocity then the high coronal emission longitude of the solar wind may usually be estimated to within ~ 10° (Nolte and Roelof, 1973; Gold and Roelof, 1977). However, during rapid velocity increases the extrapolations of emission longitude become more uncertain because of the acceleration of plasma in the interplanetary stream interaction. The additional approximations of frozen-in magnetic fields, collimated convection of low energy particles (Roelof and Krimigis, 1973), and small radial gradients in long-lived energetic particle events (Roelof, 1976) imply that the emission longitude of the solar wind is also the interplanetary injection longitude of the energetic particles from the high corona. Thus, the observed solar wind velocity may be used to map the observed particle fluxes back to their emission longitudes and to reconstruct a profile proportional to the high coronal injection during long-lived particle events. This is not an instantaneous heliographic longitude profile but rather a longitude-time cut that advances at an overall rate of ~ 13.2° per day. Because of the mixture of longitude and time in single spacecraft measurements, other cues are required to separate spatially dominated events with a single spacecraft. The most important of these cues is the existence of solar wind "sweeps" (stream onsets) and "dwells" (stream decays). During a stream onset the heliographic connection longitude decreases rapidly since the ~ 13° per day longitude decrease resulting from solar rotation is combined with the rapid decrease in the westerly displacement (from the earth-sun line) of the high coronal connection caused by the velocity step. Thus sweeps emphasize the effects spatial gradients in the particle flux longitude profile while, because of their speed, they minimize temporal changes. Solar wind stream decays, on the other hand, cause the connection point to dwell in a narrow range of heliographic longitude since the increase in the westerly displacement of the connection point from the earth-sun line compensates for solar rotation. Thus, during a dwell the effects of spatial gradients are minimized and observed flux changes are predominantly temporal in nature. Therefore, if an energetic particle event is predominantly spatial, the observed time profile at earth may appear

stepped with rapid changes in the sweeps and plateaus during the dwells. The three dimensional structure of the high corona (Nolte *et al.*, 1977) and meridional gradients (Rhodes and Smith, 1976; Richter and Suess, 1977) may also produce detectable features in the mapped-back profiles.

The relative longitudes of spatially dominated energetic particle events and solar wind streams can so severely affect the observed time profile that it may mimic a flare-associated, temporal event. Consider the energetic particle coronal injection profile in Figure 1a. If a solar wind sweep occurs at the onset of the event as in Figure 1b, most of the energetic particle increasing longitude gradients (west side) may be compressed into a very short time while the energetic particle decreasing longitude gradient (east side) may be undistorted and thus mimic a smooth temporal decay. However, if the sweep occurs near the peak of the energetic particle profile as in Figure 1c, the observed time history may appear as the reverse of a flare associated event.

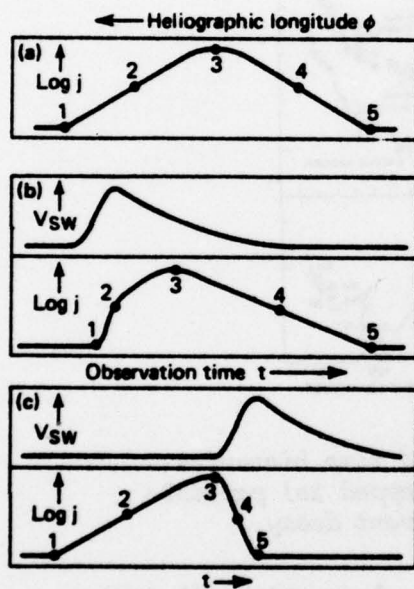


Figure 1a Coronal energetic particle injection profile,

Figure 1b Observed flux time history when solar wind sweep occurs near onset,

Figure 1c Observed flux history when solar wind sweep occurs near peak.

SELECTION AND CHARACTERISTICS OF EVENTS

We have examined the $\sim 1-5$ MeV/nuc data from the APL/JHU experiments on IMP-7 and 8 from launch in September 1972 through mid May 1976 to identify the large scale spatial structures including corotating energetic particle increases, broad recurrent minima and spatially dominated portions of the decays of solar flare associated events. Heliographic longitude profiles were constructed using solar wind velocity data from the MIT and LASL plasma experiments on IMP-7 and 8. Spatially dominated structures were identified by: (1) smooth connection longitude profiles, (2) the existence of solar wind sweeps and dwells within the event to clearly separate temporal evolution and spatial gradients, (3) recurrent source longitude profiles with nearly equal intensities, (4) the absence of relativistic electron events (> 0.22 MeV). Ignoring the easily recognized small flare-associated events (less than factor of ~ 10 flux rise lasting less than ~ 0.1 of the spatial event time) we have identified 83 spatially dominated events including 57 rounded peak profiles, 9 broad minima and 17 spatially dominated decays of temporal solar events. The decays of flare-associated events are often

dominated by their coronal injection profile since some events with stepped time histories have mapped profile with simple exponential longitude gradients (once the distortions produced by solar wind structure are removed by the mapping). The gradient in 7 September 1973 event decay shown in Figure 2 has an e-folding length of $\sim 18^\circ$ (Roelof *et al.*, 1975), typical of values in the class ($\sim 10^\circ$ to $\sim 30^\circ$ with the majority near 20°). The 9 spatially dominated minima in the data all have well-defined gradients on their eastern and western edges and 6 are recurrent features. Their average duration is 12 ± 8 days.

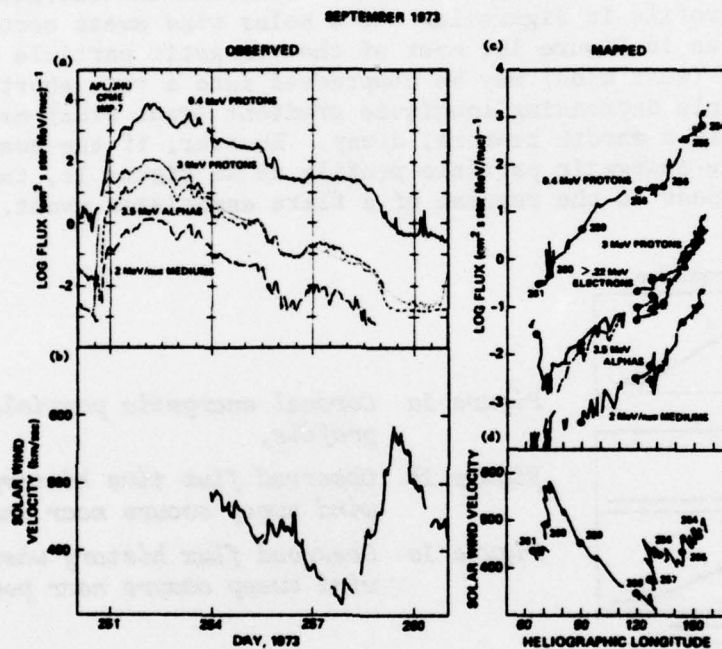


Figure 2a) Energetic particle and 2b) solar wind time histories for the 7 September 1973 flare event. Mapped 2c) particle and 2d) solar wind profiles during the event decay.

The largest group of events is the rounded peak class which all tend to have broad flux maxima and nearly exponential rises and decays. Figure 3 shows an example of an inverted time history event of the type described in Figure 1c. The rounded events tend to be Helium rich with α/p and α/CNO ratios significantly greater than the average of all events during this period (see Zwickl *et al.*, this Conference). Furthermore, the composition is generally uniform throughout the event with similar profiles in the 0.64 to 1.17 MeV/nuc Helium and ~ 2 MeV/nuc mediums. The spectra of the rounded events are quite soft with the differential spectral exponent γ for protons in the 3.2 to 6.2 MeV range rarely as low as 3.5 while between 0.40 and 0.75 MeV the γ usually ranged between 1.5 and 3.0. The 3.2 to 6.2 MeV γ was hardest at the event peak and softer in the rises and decays during about 70% of the events with sufficient fluxes to compute statistically significant hourly averaged spectra. This spectral softening in the wings of the event is consistent with coronal particle propagation azimuthally out from a central source. However, the variation of the proton spectral index apparently is a secondary effect in affecting the very strong and nearly energy-independent spatial gradients. The azimuthal gradients surrounding the event peaks have e-folding lengths ranging from $\sim 10^\circ$ to $\sim 30^\circ$ with the mean near 20° . This is the same range as observed during the spatially dominated

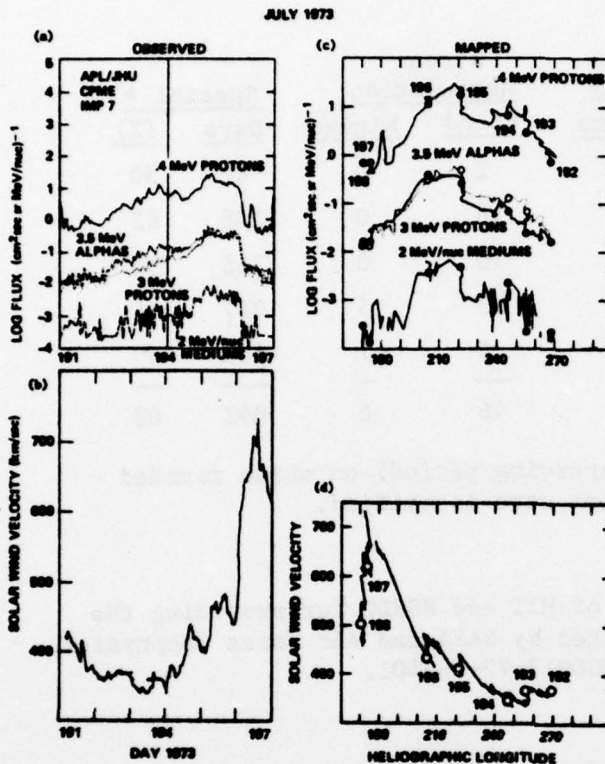


Figure 3 Observed and mapped energetic particles and solar wind during a rounded event with a sweep near the flux peak similar to Figure 1c.

decays of temporal events. Rounded spatial events are often associated with solar wind streams as has been pointed out by *Gold et al. (1975a)*. The events tend to fill the streams, starting in the sweep and extending through the dwell at the eastern edge of the stream. This is in contrast to the stream interaction events seen in the outer solar system by Pioneers 10 and 11 (*Barnes and Simpson, 1976*) which are sharply peaked in the stream interaction regions. Thus we consider it unlikely that these spatial events are due to interplanetary acceleration processes beyond 1 AU. Table 1 summarizes the observations and solar wind stream associations for each of the event types.

CONCLUSIONS

Energetic particle fluxes at 1 AU were spatially dominated ~ 70% of the time between September 1972 and May 1976. Excluding the spatially dominated decays of temporal events, ~ 70% of the events were associated with solar wind streams during this period which was characterized by very well-ordered stream structure. The striking exponential gradients appear with similar ranges of e-folding length in the rounded events, decay events and on the edges of the broad minima. Furthermore, these events have similar structures over at least an order of magnitude in energy and over the range of ions from protons at least through oxygen. *Gold et al. (1975a,b)*, *Roelof et al. (1975)* and *Roelof (1976)* have examined individual spatially dominated decays and rounded events during the Skylab period and compared them with solar x-ray photographs and H_α maps of low coronal polarity structure. They found no distinctive signatures in the coronal structures underlying the longitudes of the smooth energetic particle gradients. The examination of more than 3 years of data strengthens the evidence and shows that during the decline and minimum of the solar cycle the dominant propagation process in the corona is nearly energy rigidity and species independent.

TABLE 1

Year	Data Days	Number of Events			Stream Association		Spatial *	
		Rounded Profiles	Decay Gradients	Broad Minima	Round	Minima	Days	(%)
1972	80	4	2	0	2	0	40	50
1973	365	17	6	0	16	0	255	62
1974	365	13	5	2	10	0	215	59
1975	360	16	3	6	13	5	267	74
1976	135	7	1	1	5	1	108	80
72-76	1305	57	17	9	46	6	892	68

* Total number of days (and fraction of observing period) on which rounded profiles, decay gradients and broad minima were identified.

ACKNOWLEDGEMENTS

We are grateful to Dr. A. Lazarus of MIT and NSSDC for providing the solar wind data. This research was supported by NASA and Air Force Geophysics Laboratory under Task I of Navy Contract N00017-72-C-4401.

REFERENCES

- Barnes, C. W. and J. A. Simpson, Evidence for interplanetary acceleration of nucleons in corotating interaction regions, *Astrophys. J. Lett.*, 210, L91, 1976.
- Gold, R. E., S. M. Krimigis, E. C. Roelof, A. S. Krieger and J. T. Nolte, Relation of large-scale coronal x-ray structure and cosmic rays: 3. Low-intensity solar particle events with enhanced ~ 3 MeV helium and medium fluxes associated with solar wind streams, *Proc. 14th International Cosmic Ray Conf. (Munich)* 5, 1710, 1975a.
- Gold, R. E., E. C. Roelof, J. T. Nolte and A. S. Krieger, Relation of large-scale coronal x-ray structure and cosmic rays: 5. Solar wind and coronal influence on a Forbush decrease lasting one solar rotation, *Proc. 14th International Cosmic Ray Conf. (Munich)* 3, 1095, 1975b.
- Gold, R. E. and E. C. Roelof, Inference of the equatorial high coronal magnetic field polarity from interplanetary measurements, submitted to *Solar Phys.*, 1977.
- Nolte, J. T., A. S. Krieger, E. C. Roelof and R. E. Gold, High coronal structure of high velocity solar wind streams, *Solar Phys.*, in press, 1977.
- Nolte, J. T. and E. C. Roelof, Large-scale structure of the interplanetary medium. I: High coronal source longitude of the quiet-time solar wind, *Solar Phys.*, 33, 241, 1973.
- Rhodes, E. J., Jr. and E. J. Smith, Evidence of a large-scale gradient in the solar wind velocity, *J. Geophys. Res.*, 81, 2123, 1976.
- Richter, A. K. and S. T. Suess, Modeling the meridional solar wind flow in the midcorona, *J. Geophys. Res.*, 82, 593, 1977.
- Roelof, E. C. and S. M. Krimigis, Analysis and synthesis of coronal and interplanetary energetic particle, plasma and magnetic field observations over three solar rotations, *J. Geophys. Res.*, 78, 5375, 1973.

- Roelof, E. C., R. E. Gold, S. M. Krimigis, A. S. Krieger, J. T. Nolte, P. S. McIntosh, A. J. Lazarus and J. D. Sullivan, Relation of large-scale coronal x-ray structure and cosmic rays: 2. Coronal control of interplanetary injection of 300 keV solar protons, *Proc. 14th International Cosmic Ray Conf. (Munich) 5*, 1704, 1975.
- Roelof, E. C., Solar particle emission in *Physics of Solar Planetary Environments, Proc. of the International Symposium on Solar-Terrestrial Physics (Boulder)*, ed. D. J. Williams, American Geophysical Union (Washington, D. C.), 1, 214, 1976.
- Zwicky, R. D., S. M. Krimigis, R. E. Gold and T. P. Armstrong, Observations of enhanced abundances of He through Fe nuclei during solar events, 1972 to 1976, *Proc. 15th International Cosmic Ray Conf. (Ploudiv)*, 1977.

CORONAL STRUCTURE OF THE APRIL 10, 1969 SOLAR FLARE PARTICLE EVENT

R. E. Gold, E. P. Keath and E. C. Roelof
Applied Physics Laboratory/The Johns Hopkins University
Laurel, Maryland 20810 USA

R. Reinhard
Space Science Department, ESTEC, Noordwijk, Netherlands

The April 10, 1969 flare particle event and its associated solar wind disturbance have been re-examined by combining Pioneers 6-9 and Explorer 34 observations of ~ 10 MeV protons with measurements of solar wind plasma on the same spacecraft. The particle fluxes and plasma velocities are mapped back to the Sun and compared at the same time of observation to give the instantaneous coronal emission profiles of flare-accelerated protons and solar wind. While the plasma preferentially escapes over the flare site with a half width of ~ 50°, the bulk of energetic particles escapes from a quiet coronal region, almost 100° to the west of the flare site. The particle profiles reveal strong exponential longitudinal gradients in the corona, which persist up to 14 days after the flare.

1. INTRODUCTION

Time intensity profiles observed by spacecraft in the interplanetary medium are difficult to interpret in that they show the intermixed effects of temporal and spatial variations because the high coronal spacecraft connection longitude of the interplanetary magnetic field lines changes continuously, due to the rotation of the Sun (Reid, 1964; Roelof and Krimigis, 1973). Superimposed on the continuous change are irregular changes of the connection longitude due to the high variability of the solar wind velocity. However, in the decay of a solar wind stream, the decrease of the solar wind velocity tends to move the connection longitude westward, thus cancelling the effect of the Sun's rotation. The spacecraft is then connected to the same heliolongitude for some time and observes the temporal change dj/dt at that heliolongitude. On the other hand, when the solar wind increases strongly, the connection longitude will shift rapidly eastward, and then we observe the particle intensity over ~ 30° of heliolongitude in a very short time so that we sample primarily the longitudinal gradient $dj/d\phi$.

The clearest separation of temporal and spatial variations is provided by simultaneous measurements by several spacecraft at different heliolongitudes. The first 4 months of 1969 is perhaps one of the most fruitful time periods for such a study: numerous particle flares with intense fluxes were observed by 5 spacecraft, Pioneers 6-9 and Explorer 34, distributed more or less uniformly over more than 180° around the Sun, with good data coverage of both particle flux and solar wind plasma measurements. This provides a unique opportunity to study the inter-relationship between the emission longitude profiles of energetic protons and solar wind plasma.

In the present paper we give a detailed analysis of the April 10, 1969 event. This event was previously studied by McCraoken *et al.* (1971), who have already pointed out the existence of unusual spatial gradients in the energetic particle fluxes. Their work is complemented here by adding Explorer 34 data and solar wind plasma data of the 5 spacecraft so that we can map the observed

particle fluxes and solar wind velocities back to the Sun and thus study the coronal control of plasma and energetic particle emission.

2. OBSERVATIONS

The April 10, 1969 flare was observed at 0400 UT just beyond the east limb in McMath plage 10035 (recurrence of McMath plage 9994). The same active region produced all major particle events since March 21 (March 21, 0154 UT, E16°; March 27, 1341 UT, W68°, March 30, 0248 UT, ~W105°).

Figure 1 shows the 7.5–45 MeV proton fluxes observed by the UTD detectors on Pioneers 6–9 and the > 10 MeV proton fluxes observed by the APL/JHU detector on Explorer 34, together with the locations of the 5 spacecraft in the ecliptic as seen from the north. Pioneers 6–9 data points are taken from McCracken *et al.* (1971); in addition some unpublished Pioneer 8 and 9 data were available.

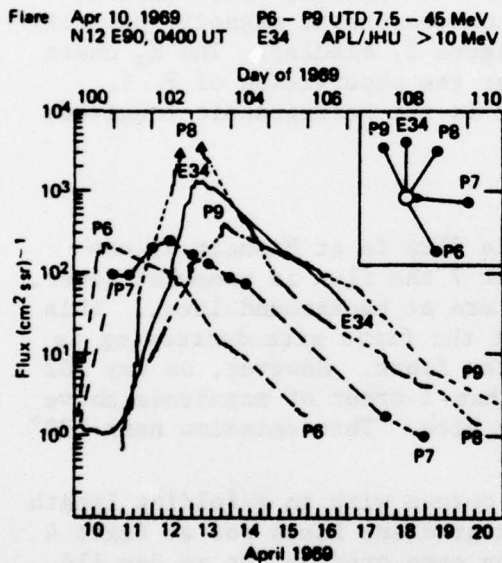


Figure 1 Energetic particle fluxes for the April 10, 1969 event observed by Pioneers 6–9 and Explorer 34. The insert shows spacecraft positions in the ecliptic as seen from north; the bubble indicates the flare site.

In the extended version of this paper (Reinhard *et al.*, 1977b) it is shown that the difference of the energy windows and the different electron sensitivity of the detectors on the Pioneers and Explorer 34 partly cancel, the degree depending on the proton and electron spectral indices and the ρ/e ratio. The resulting uncertainty is less than a factor of 1.5, which is negligible compared to the coronal particle gradients discussed below.

The April 10 event has a number of unusual features:

(1) The onset of the proton fluxes at Pioneer 8, Explorer 34 and Pioneer 9 is delayed by almost a day.

(2) The fluxes of Pioneer 7 show a second increase starting on April 11.

(3) After April 12 the fluxes at Pioneer 8, Explorer 34 and Pioneer 9 are persistently 1–3 orders of magnitude higher than at Pioneer 6 and 7, which are better connected to the flare site.

(4) The intensity difference persists until very late in the event, in contrast to more conventional views of diffusive equilibrium (the whole solar system being uniformly filled with particles late in the event).

Note that features (3) and (4) could only be verified by making use of multi-spacecraft observations.

3. THE METHOD

The method used to separate spatial from temporal variations and to deduce the coronal gradients as a function of time is straight-forward. First, all the particle fluxes are mapped back to the high corona using the approximations of non-accelerating radial solar wind transport with frozen-in magnetic field lines (Nolte and Roelof, 1973a,b) and, that the interplanetary gradients of particle intensity along individual interplanetary field lines are relatively small (Roelof, 1976). Second, the coronal particle intensities are connected at the same time of observation giving the *instantaneous coronal emission profile*. This is done for the labelled times for particle fluxes (Figure 2, bottom) and in the same way for solar wind velocities (Figure 2, top). It is then possible to study the temporal development of the coronal emission profiles, to compare the emission profiles of particle fluxes and solar wind plasma, and, finally, to compare the emission profiles with the global chromospheric magnetic polarity structure as visible on the H_{α} synoptic chart (Figure 2, middle). The H_{α} chart for Rotation 1546 was prepared by S. Wayland under the supervision of P. S. McIntosh of NOAA/ERL. Also indicated in Figure 2 is the heliographic longitude of the flare location.

4. INTERPRETATION

On day 101 (April 11) the peak particle flux is at Pioneer 6, connected closest to the flare longitude. At Pioneer 7 the flux is somewhat lower, while Pioneer 8, Explorer 34 and Pioneer 9 still are at background level. This is consistent with the idea that the peak flux at the flare site decreasing is gradually with time and also with distance from the flare. However, on day 102 (April 12) the peak flux is at 170° and is more than 1 order of magnitude above the flux observed by Pioneer 7 close to the flare site. This emission near 170° remains enhanced all through the decay.

There is a persistent gradient in the corona with an e-folding length of $\sim 35^{\circ}$ to the east and $\sim 18^{\circ}$ to the west. This gradient lasts for at least 4 days (102-106) and there is some indication of the same gradient up to day 114, 14(!) days after the flare, when the fluxes finally reach background. This is strong evidence for continued interplanetary injection of these particles, and the problems of storing ~ 10 MeV particles lead to the conclusion that there could be extended acceleration throughout the period. Extended acceleration is unlikely to take place at 170° , because there is no active region nearby. The dominant active region after April 10 is McMath plage 10035 at 85° heliographic longitude producing all the flares $\geq 1N$. This implies continuous transport of particles from the site of acceleration to the site of release, i.e., over $\sim 100^{\circ}$ of longitude. On the other hand, the smooth exponential decay of the fluxes from April 13 until April 20 would favor the idea of a storage region with loss of particles into the denser lower corona and escape into interplanetary space.

The solar wind plasma emission profiles are shown in the upper panel. The shaded region on the right around 330° shows a recurrent and quasi-stationary solar wind stream and the adjacent region from 270° to 210° has been quiet for several rotations. Over the active region the solar wind velocity is enhanced on day 95, it has decayed on day 97, and is again enhanced on day 99 with a decrease thereafter. These are probably temporal solar wind variations associated with solar flare events on day 92 and 95, for which energetic protons are only seen by Pioneer 6, which is closest to the active region 9994/10035. The solar wind velocity is decaying on day 101 until the solar wind disturbance from

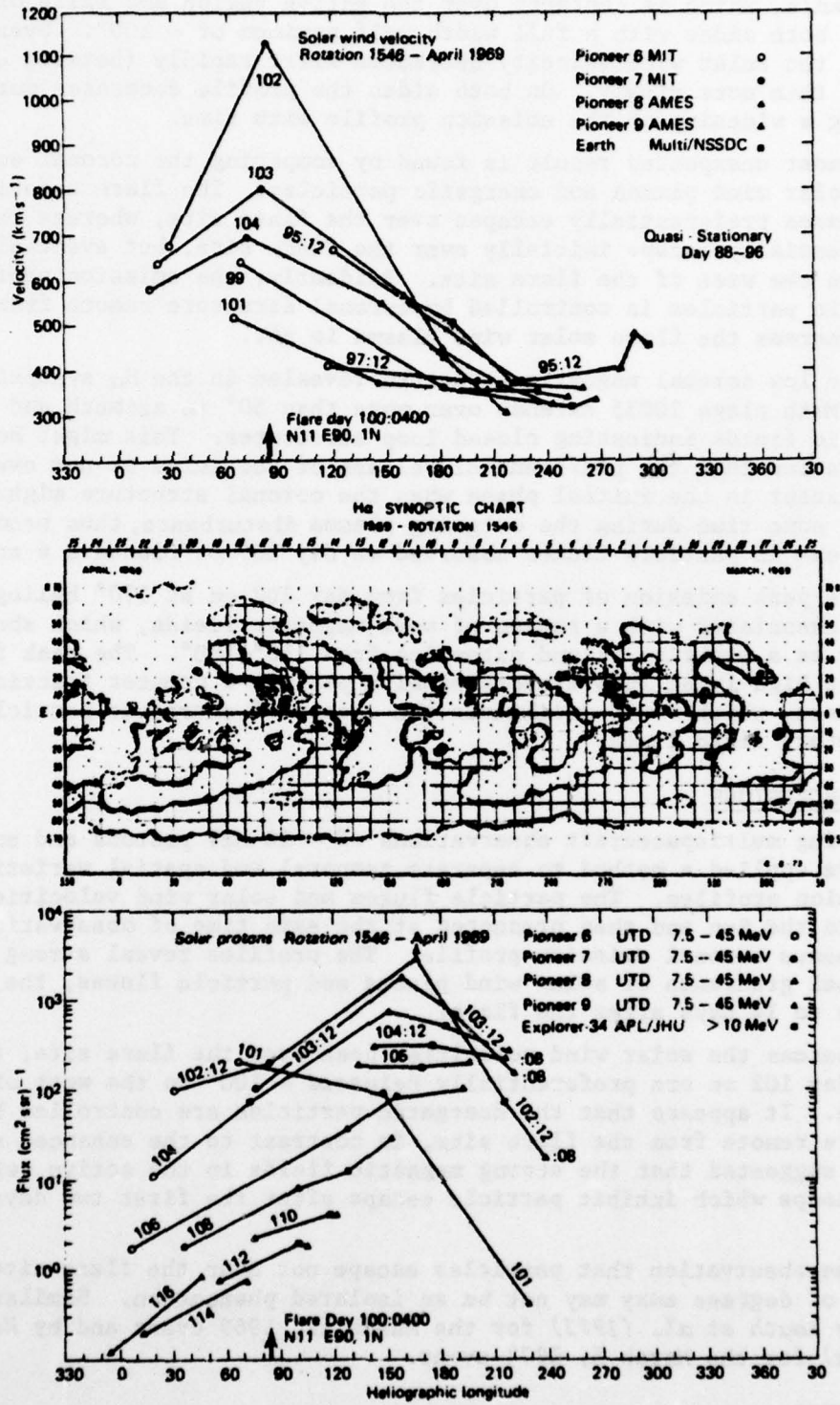


Figure 2 Coronal solar wind velocity emission profiles (upper panel), H_{α} synoptic chart (center panel) and coronal particle flux emission profiles (lower panel). Numbers on the emission profiles give the time of the observations (days:hours).

the April 10 flare arrives on day 102. The solar wind emission profile has a peak of 1134 km/s, which is centered over the active region and falls off symmetrically to both sides with a full width half maximum of $\sim 100^\circ$. Over the active region the solar wind velocity decreases first rapidly (between days 102 and 103), and then more slowly. On both sides the profile decreases more slowly, thus producing a widening of the emission profile with time.

A most unexpected result is found by comparing the coronal emission profiles of solar wind plasma and energetic particles. The flare associated solar wind plasma preferentially escapes over the flare site, whereas the particles preferentially escape initially over the flare site, but eventually almost 100° to the west of the flare site. Evidently, the emission profile of flare energetic particles is controlled by coronal structure remote from the flare site, whereas the flare solar wind plasma is not.

The low coronal magnetic structure revealed in the H_α synoptic chart shows that McMath plage 10035 extends over more than 50° in azimuth and has strong magnetic fields indicating closed loop structures. This might be related to the observation that the preferential release of particles is not over the flare site, except in the initial phase when the coronal structure might have been open for some time during the outgoing plasma disturbance, thus producing the initial peak in particle fluxes observed on day 100 on Pioneers 6 and 7.

The peak emission of particles from day 102 on at 170° heliographic longitude is associated with a region of weak magnetic fields, which shows up on the H_α map as a negative island extending from 150° - 180° . The weak fields would indicate high lying loop structures with perhaps a greater fraction of open field lines, which would facilitate the escape of energetic particles out to interplanetary field lines.

5. CONCLUSIONS

Using multispacecraft observations of ~ 10 MeV protons and solar wind plasma we have applied a method to separate temporal and spatial variations of coronal emission profiles. The particle fluxes and solar wind velocities are mapped back to the Sun and then presented at the same time of observation giving the instantaneous coronal emission profile. The profiles reveal strong longitudinal coronal gradients of solar wind plasma and particle fluxes, the latter persistent up to 14 days after the flare.

Whereas the solar wind velocities peak over the flare site, the particles from day 102 on are preferentially released $\sim 100^\circ$ to the west of the active region. It appears that the energetic particles are controlled by coronal structure remote from the flare site, in contrast to the enhanced solar wind. It is suggested that the strong magnetic fields in the active region form closed loops which inhibit particle escape after the first two days of the event.

The observation that particles escape not over the flare site but several tens of degrees away may not be an isolated phenomenon. Similar results were found by *Keath et al. (1971)* for the March 12, 1969 event and by *Reinhard et al. (1977a)* for the March 5, 1972 event.

ACKNOWLEDGEMENTS

Work done at APL/JHU was supported by the Atmospheric Research Section of the National Science Foundation (Grant ATM76-23816) and by the Air Force Geophysics Laboratory under Task ZF10 of Contract N00017-72-C-4401 with the Department of the Navy. Solar wind data from the Pioneer and Explorer spacecraft were provided by the National Space Science Data Center.

REFERENCES

- Keath, E. P., R. P. Bukata, K. G. McCracken and U. R. Rao, *Solar Phys.*, 18, 503, 1971.
- McCracken, K. G., U. R. Rao, R. P. Bukata and E. P. Keath, *Solar Phys.*, 18, 100, 1971.
- Nolte, J. T. and E. C. Roelof, *Solar Phys.*, 33, 241, 1973a.
- Nolte, J. T. and E. C. Roelof, *Solar Phys.*, 33, 483, 1973b.
- Reid, G. C., *J. Geophys. Res.*, 69, 2659, 1964.
- Reinhard, R., V. Domingo, C. Perron, K.-P. Wenzel, *this Conference*, 1977a.
- Reinhard, R., R. E. Gold, E. P. Keath and E. C. Roelof, *J. Geophys. Res.*, (to be submitted), 1977b.
- Roelof, E. C., *Proc. of the Int. Symposium of Solar-Terrestrial Physics (Boulder)*, D. J. Williams (ed.), American Geophysical Union, 1, 214, 1976.
- Roelof, E. C. and S. M. Krimigis, *J. Geophys. Res.*, 78, 5375, 1973.

THE RELATIONSHIP BETWEEN JOVIAN ELECTRONS AND SOLAR WIND STREAM STRUCTURE

R. E. Gold, S. M. Krimigis and E. C. Roelof
Applied Physics Laboratory/The Johns Hopkins University
Laurel, Maryland 20810 USA

R. W. Fillius
University of California, San Diego
La Jolla, California 90237 USA

The relationship between the observed time histories of Jovian electrons and solar wind velocity differs dramatically depending on the position of the observer in the solar system. Near Earth observations of > 0.22 MeV Jovian electrons by the APL/JHU experiments on IMP-7 and 8 during 1972-1975, a period of stable recurrent solar wind, reveals 19 of 26 events in good association with solar wind streams. This pattern of positive correlation with solar wind streams is also observed in 3-6 MeV data from 1965-1972 during well-defined electron events. During their pre-encounter periods Pioneers 10 and 11 were nearly radially aligned with Jupiter and direct magnetic connection was highly unlikely. Jovian electrons ≥ 5 MeV in the UCSD experiments on Pioneers 10 and 11 were anticorrelated with solar wind velocity from $\sim 3-4$ AU until encounter. Reconstructions of the large-scale interplanetary magnetic field suggest that the near-Earth events result from direct connection with the Jovian magnetotail and corotation of quasi-trapped populations while for Pioneer events electrons propagate out from the magnetosphere to a solar wind stream interaction, in along the interaction, then in to Pioneer on undisturbed field lines.

INTRODUCTION

We present new evidence on the intriguing question of interplanetary propagation of relativistic Jovian electrons, using data from the UCSD detectors on Pioneers 10 and 11 and the JHU/APL instruments on IMP-7 and 8. The observation of Jovian electrons with the Pioneer 10 spacecraft (*Chenette et al.*, 1974; *Teegarden et al.*, 1974) also provided the explanation for the "quiet time electron increases" that had been observed for many years with near-earth spacecraft. *Teegarden et al.* (1974) noted that the Jovian electron "season" of ~ 4 months every 13 months roughly corresponded to the period of nominal solar wind connection to Jupiter. The interplanetary conditions and the mode of propagation for these particles has not been established but *Gotwols et al.* (1976) have pointed out an association with solar wind structure.

Pioneers 10 and 11 began observing Jovian electrons within 1 to 2 AU inside the orbit of Jupiter (*Teegarden et al.*, 1974; *Chenette et al.*, 1974, *Conlon*, 1977). Yet, both Pioneers were nearly radially aligned with Jupiter during this period and therefore could not be directly connected to Jupiter by the average large-scale interplanetary magnetic field structure. Jovian electron events observed by the Pioneer spacecraft inside 5 AU are also associated with solar wind structure (*Gotwols et al.*, 1976) but exhibit a different relationship with the streams from that of the near-earth events. All of these events rise to their peaks late in the decay of solar wind streams while some continue into the rise of the following stream. This suggests that the stream interactions play a vital role in Jovian electron transport in these events.

Thus the near-earth events and the Pioneer events inside 5 AU appear to be associated with different transport mechanisms and their relationship with solar wind velocity structure is the key to these differences.

NEAR-EARTH OBSERVATIONS

We have examined the near earth electron events with the APL/JHU experiments on IMP-7 and 8 and have imposed three strict criteria for Jovian electron identification: (1) non-impulsive, rounded time histories with slow rises and decays (> 1 day); (2) significant increases in both the > 0.22 MeV and > 0.8 MeV electron channels; (3) hard spectra indicated by a channel ratio $[(0.22 \leq E_e \leq 0.50 \text{ MeV}) / (0.50 \leq E_e \leq 0.8)]$ less than 3.0 corresponding to a differential power law spectral exponent $\gamma \leq 1.8$. These criteria may actually exclude some genuinely Jovian electron events ≥ 0.22 MeV but the surviving events clearly exhibit the ~ 13 month periodicity indicative of the Earth-Jupiter geometry reported by *Krimigis et al. (1975)* in a preliminary study and they are uncorrelated with ~ 5 MeV protons, assuring that they are not of solar origin.

We have examined the period from October 1972 through 1975 and identified 26 Jovian events using the strict criteria listed above. Figure 1 shows three consecutive events during the remarkable series in 1974. This is a composite record of the events taken from the interplanetary sections of the IMP orbits to minimize contributions from magnetospheric electron bursts (*Sarris et al., 1976*) which are clearly recognized as the spikes in the > 0.22 MeV channel and the ratio. A complete list of the 26 events, their spectral ratios and relationship with low energy protons appears in *Gold et al. (1977)*. It is also clear from Figure 1 that other, less restrictive, selection criteria or detectors in different energy regions might select different events or sections of events (such as the excluded period from day 89 through most of day 94 in the center of the figure); however, the 26 strictly selected events are sufficient for a comparison with solar wind data.

These 26 events have been compared with solar wind velocity data from the MIT and LASL plasma experiments on IMP-7 and IMP-8. Nineteen of the 26 events have a good association with solar wind streams, 5 have fair associations and 2 are only poorly associated as explained below. Figure 2 shows the solar wind velocity data for the events in 1973 and 1974 and the periods during which Jovian electrons were observed are indicated by the shaded areas. Broken edges in the shading such as on day 210 of 1973 indicate that the edge of the event

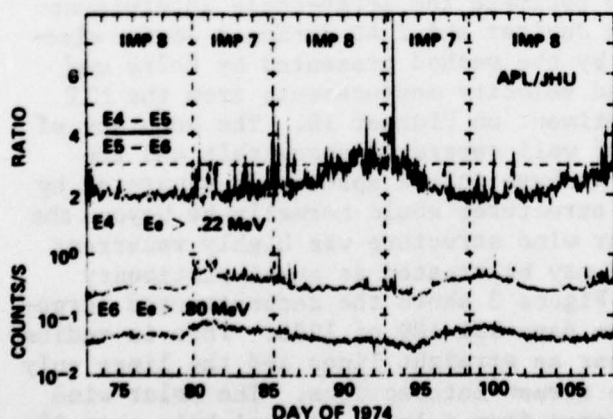


Figure 1 Three Jovian electron events and the spectral ratio.

was poorly defined. This may result from the presence of solar electron fluxes such as the solar event onset on day 210, or from intense magnetospheric activity. The solar wind association categories of good, fair and poor can best be explained using examples from Figure 2. By "good" we mean that the electron event was contained within a single stream (as in the day 135 of 1974 event), while some of these events are "very good" and tend to fill the stream (as in the event beginning on day 147 of 1973). The Jovian electron increase starting on day 346 of 1973 was rated "fair" since it covered most of 2 small streams and the event that began on day 22 of 1974 was rated "poor" since

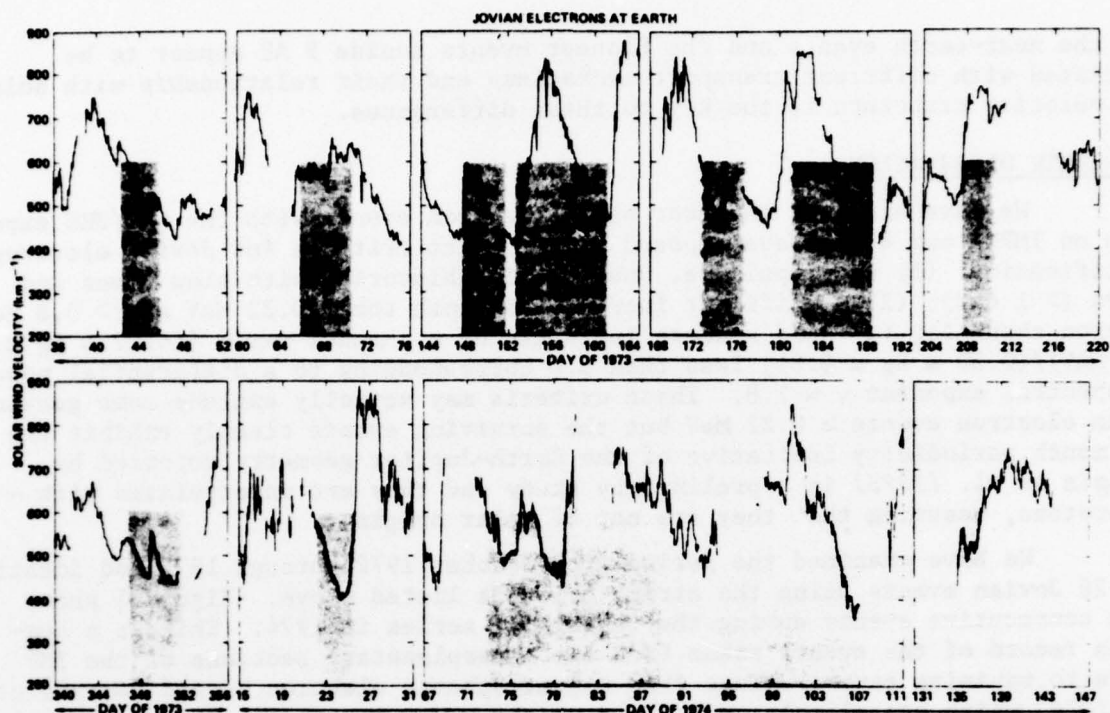


Figure 2 Solar wind velocity during 1973 and 1974 with times of Jovian electron events shaded.

it began late in one stream and probably ended shortly after the rise of the following stream.

The good association between Jovian electron events near earth and solar wind streams is not confined to the 1972 to 1975 period. We have compared the incidence of Jovian electrons with solar wind stream structure between 1965 and 1972 and we find the large, well-defined electron events exhibit a good association with solar wind streams during these years as well. A pattern that emerges throughout the solar cycle is the propensity for Jovian electrons to appear in stable, recurrent solar wind streams suggesting that well ordered interplanetary structure may modulate Jovian electron propagation.

In order to demonstrate how solar wind structure may affect Jovian electron transport to earth we next try to estimate the large-scale interplanetary magnetic field (IMF) structure between Jupiter and 1 AU during a Jovian electron event. The fields are reconstructed by the method presented by *Nolte and Roelof (1973)* using simultaneous solar wind velocity measurements from the MIT experiment on IMP-7 and the NASA/Ames experiment on Pioneer 10. The accuracy of the reconstruction depends on the number of well separated spacecraft and the stability of the structure. In this case we have only 2 spacecraft separated by ~ 4 AU so that reconstruction of evolving structures would normally be beyond the scope of the technique. However, the solar wind structure was highly recurrent during 1973 through 1975 so the solar wind may be treated as quasi-stationary and corotating to a first approximation. Figure 3 shows the reconstructed large-scale IMF for the electron increase seen on days 181-189 of 1973. This is radius-longitude plot in which ideal spirals appear as straight lines and the lines only bend where the plasma is decelerated as in stream interactions. The solar wind stream with its peak velocity on day 182 comes from a large coronal hole near 0° and is quite stable over the next 4 solar rotations, thus confirming the corotating approximation. The shaded areas indicate the time of the Jovian electron

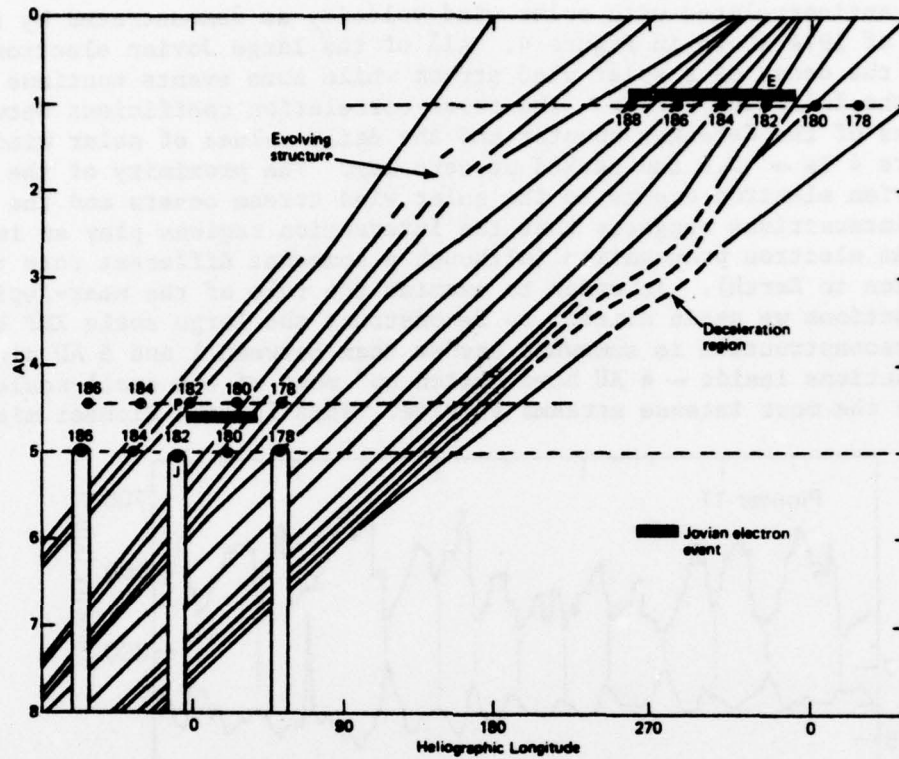


Figure 3 Reconstruction of the large-scale interplanetary magnetic field structure inferred from Pioneer 10 and IMP-7 solar wind measurements. Jovian electron events at Earth and Pioneer 10 are shaded.

event at Earth (days 181-189) and at Pioneer 10 (days 179-182). The approximate large-scale field directly connects the earth with the flank of the Jovian magnetotail ~ 2.5 AU out from the planet. The Jovian electron event at Earth nearly fills the solar wind stream, although the onset follows a solar electron event decay and its timing is therefore somewhat uncertain. However, the event clearly ends on day 189 when the Earth field line intersects the leading edge of the following high speed stream interaction. It is interesting to note that the extrapolations of the stream interactions on each side of the "smooth" field lines connecting earth to Jupiter intersect near 10 AU. Thus quasi-trapping of the electrons appears possible. Figure 3 suggests two possibly complementary methods for Jovian electrons to reach the near-Earth environment. Electrons emitted from the down flank of the magnetosphere may reach earth directly and quasi-trapped populations may corotate from their injection region at the Jovian magnetosphere to the longitude of Earth.

PIONEER OBSERVATIONS INSIDE 5 AU

Jovian electrons were observed by the Pioneer spacecraft prior to Jovian encounter starting at about 3 to 4 AU. During this period the spacecraft were nearly radially aligned with Jupiter and therefore could not be directly connected to Jupiter by the average large-scale magnetic field structure. We have examined the pre-encounter Jovian electron events with the Cerenkov counts of the UCSD experiments on both Pioneers 10 and 11 which respond to electrons > 5 MeV and protons > 0.5 GeV. A comparison of the electron event profiles with the NASA/Ames solar wind velocity data from the same spacecraft reveals a markedly different pattern than that observed at Earth. The pre-encounter electron events

are strongly anticorrelated with solar wind velocity as demonstrated by the data for 200 days of 1974 shown in Figure 4. All of the large Jovian electron events rise late in the decay of a solar wind stream while some events continue into the rise of the following stream. The cross correlation coefficient between daily averages of the Cerenkov counter and the daily values of solar wind velocity in Figure 4 is ~ -0.6 and peaked at zero lag. The proximity of the pre-encounter Jovian electron events to the solar wind stream onsets and the associated stream interactions suggests that the interaction regions play an important role in Jovian electron propagation (although a somewhat different role than in the propagation to Earth). In order to examine the role of the near-Jupiter stream interactions we again attempt to reconstruct the large scale IMF beyond 5 AU. This reconstruction is somewhat easier than between 1 and 5 AU since stream interactions inside ~ 4 AU have "eaten up" most of the small scale structure and only the most intense streams survive. Thus for the Pioneer missions

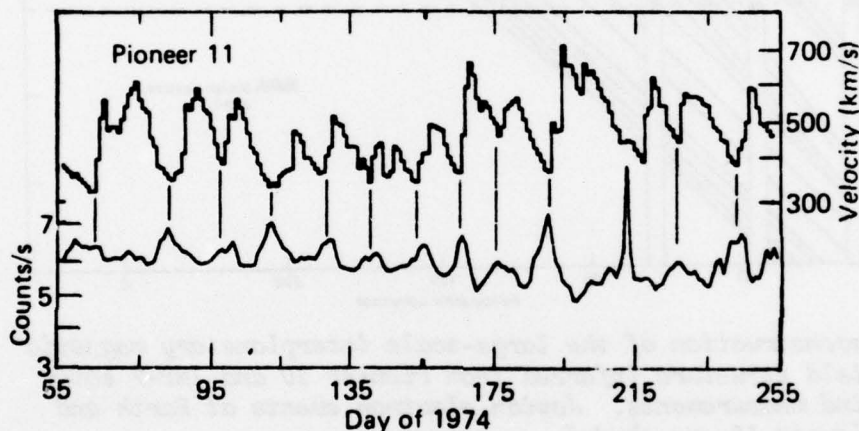


Figure 4 Daily averages of the UCSD Cerenkov counter and daily solar wind velocity points.

which were characterized by quasi-stationary solar wind structure we may approximate the large-scale IMF structure beyond the spacecraft by simple extrapolating the Pioneer velocity as stream lines. Figure 5 shows the reconstructed large-scale interplanetary magnetic field during the Pioneer 10 event of day 190-192, 1973. This field structure suggests that the Jovian electron transport route is out along the undisturbed field lines to the interaction region (at r_2 in the figure) in along the interaction to r_1 and then back to the spacecraft on undisturbed field lines (arrows in Figure 5).

CONCLUSIONS

We have shown that Jovian electron events are intimately associated with solar wind structure, but that the association depends on spacecraft location. Jovian electron events near earth are positively correlated with solar wind velocity and the reconstructed large-scale IMF suggests that the electrons are transported to earth along "undisturbed" field lines within the stream by direct connection and/or corotation of quasi-trapped populations. The pre-encounter Pioneer 10 and 11 events are anticorrelated with solar wind velocity and the reconstructed fields during these events suggest a propagation mode along undisturbed field lines out to the stream interaction region, in along the interaction then on undisturbed field lines to Pioneer. This mode of transport may also operate to initiate the Jovian electron season at earth prior to the period of direct connection. This discussion of propagation of Jovian electrons with large mean free paths has necessarily been brief and no justifying

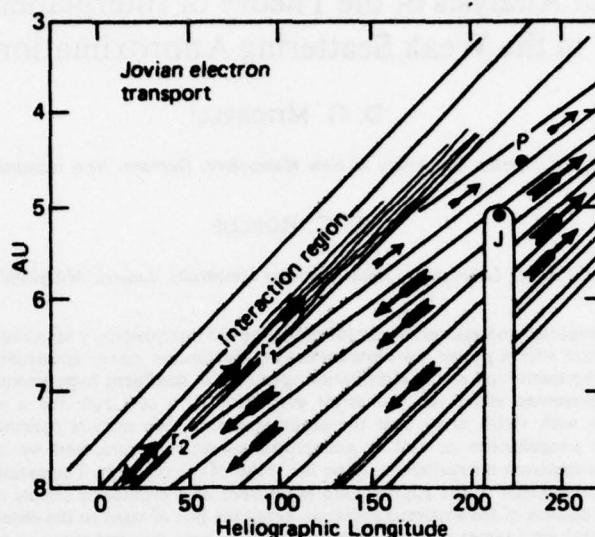


Figure 5 Reconstruction of the large scale interplanetary magnetic field structure during the day 190-192, 1973 event at Pioneer 10.

arguments or comparisons with other models (Jokipii, 1976; Conlon, 1977) have been presented. However, complete discussions do appear in the full papers (Gold et al., 1977; Gold and Roelof, 1977).

ACKNOWLEDGEMENTS

We are grateful to A. Lazarus of MIT, NSSDC and J. Wolfe of NASA/Ames for providing the solar wind velocity data. The research at APL was supported by NASA and Air Force Geophysics Laboratory under Task I of Navy Contract N00017-72-C-4401. The research at UCSD was supported by NASA.

REFERENCES

- Chenette, D. L., T. F. Conlon and J. A. Simpson, *J. Geophys. Res.*, **79**, 3351, 1974.
- Conlon, T. F., *J. Geophys. Res.*, submitted to, (University of Chicago, Enrico Fermi Institute Preprint 77-12), 1977.
- Gold, R. E., B. L. Gotwols, S. M. Krimigis and E. C. Roelof, *J. Geophys. Res.*, submitted to, (JHU/APL Preprint 76-07), 1977.
- Gold, R. E. and E. C. Roelof, *J. Geophys. Res.*, submitted to, (JHU/APL Preprint 76-08), 1977.
- Gotwols, B. L., R. E. Gold, S. M. Krimigis and E. C. Roelof, *EOS*, **57**, 292, 1976.
- Jokipii, J. R., *Geophys. Res. Lett.*, **3**, 281, 1976.
- Krimigis, S. M., E. T. Sarris and T. P. Armstrong, *Geophys. Res. Lett.*, **2**, 561, 1975.
- Nolte, J. T. and E. C. Roelof, *Solar Phys.*, **33**, 483, 1973.
- Sarris, E. T., S. M. Krimigis and T. P. Armstrong, *J. Geophys. Res.*, **81**, 2341, 1976.
- Teegarden, B. J., F. B. McDonald, J. H. Trainor, W. R. Webber and E. C. Roelof, *J. Geophys. Res.*, **79**, 3615, 1974.

A Mathematical Analysis of the Theory of Interplanetary Scintillation in the Weak Scattering Approximation

D. G. MITCHELL¹

Department of Physics, University of New Hampshire, Durham, New Hampshire 03824

E. C. ROELOF

Applied Physics Laboratory, Johns Hopkins University, Laurel, Maryland 20810

We present a simplified analytic technique for modeling the interplanetary scintillation of radio sources of finite angular size with a power law electron density fluctuation power spectrum. The simplification results from the representation of the scintillation spectrum in confluent hypergeometric functions. The approximations presented allow fast numerical evaluation of a spectrum for a weak scattering but extended medium with <10% error over the entire spectrum. We include parameters describing anisotropic electron irregularities as well as anisotropic source structure, and we derive explicitly the dependence of the spectrum normalization upon the scales of the medium. The parametric description of the domains of convergence of the approximate expansions also provides a simple conceptualization of the relative contributions of the scattered radiation along the line of sight to the observed spectrum. This is particularly useful for sources of finite angular size. We apply this technique to previously published observations.

INTRODUCTION

Interplanetary scintillations (IPS) of radio sources have been recognized for over a decade as a probe both of the interplanetary medium and of radio source structure. The interpretation of experimental results is model dependent and has been complicated by the necessity for lengthy numerical computations involved in comparing these models with the data. The analysis presented here, based on a power law electron density fluctuation power spectrum, results in a greatly simplified mathematical formulation (in the weak scattering approximation) which allows extensive study with comparative ease of the effects of many parameters on the spectrum of IPS. In particular, we present a detailed quantitative analysis of the effect of finite source size on IPS for a power law electron fluctuation spectrum.

Earlier work on the interpretation of IPS spectra invoked a Gaussian spectrum for electron density irregularities [e.g., *Salpeter*, 1967], following the seminal work on ionospheric scintillations by *Booker et al.* [1950], *Tatarskii* [1971], summarizing his general work on scattering of electromagnetic waves in a random medium (published in Russian in 1959 and 1967), introduced power law irregularity spectra containing both an inner and an outer scale (which would depress the spectrum at high and low wave numbers, respectively). It was known that the spectrum of irregularities in the interplanetary magnetic field displayed a power law dependence [*Coleman*, 1967], as did variations in solar wind flux [*Intriligator and Wolfe*, 1970].

A power law irregularity spectrum was suggested by a number of authors: *Cronyn* [1970a], *Hollweg* [1970], *Jokipii* [1970], *Jokipii and Hollweg* [1970], and *Lovelace et al.* [1970]. These authors argued for a power law dependence on the basis of an increasing realization that not only could the IPS data be fitted with a power law but also the directly measurable spectrum of

the other solar wind parameters were found to exhibit a power law dependence. *Cronyn* [1972] presented evidence that in fact the electron irregularity spectrum measured by radio scintillation was consistent with the power law dependence of the solar wind ion irregularity spectrum measured at much lower wave numbers by satellites. Later spacecraft measurements in the frequency range which contributes to the IPS directly showed a power law dependence [*Unti et al.*, 1973; *Unti and Russell*, 1976].

The functional form of the power law applied to IPS has several variations: an exact isotropic power law (k^{-2}), suggested by *Jokipii* [1970], *Jokipii and Hollweg* [1970], *Lovelace* [1970], and *Young* [1971]; a form including parameters for elongation of the irregularities ($\alpha k_x^2 + \beta k_y^2 + k_z^2$)⁻², suggested by *Cronyn* [1970a, 1972], *Lovelace* [1970], and *Rufennach* [1972]; a parameter for an outer scale to limit the power at low wave numbers ($k_o^2 + k^2$)⁻², suggested by *Cronyn* [1970a], *Matheson and Little* [1971], and *Callahan* [1974]; and a form with a parameter for an inner scale ($k_o^2 + k^2$)⁻² exp ($-k^2/k_i^2$), suggested (not always in this strict functional form) by *Hollweg* [1970], *Jokipii and Hollweg* [1970], *Matheson and Little* [1971], and *Rickett* [1973]. The same functional form, a Gaussian cutoff exp ($-k^2\Omega^2L^2$), was used by *Salpeter* [1967], *Young* [1971], and *Houminer* [1973] as a visibility function for sources with Gaussian brightness distributions of finite angular radius (Ω) for thin screens at a distance L from the receiver. The latter application has meaning in terms of the diffraction pattern, not in terms of the density irregularities themselves.

Much of the discussion of these parameters has been covered by other authors, perhaps most completely and concisely (though semiquantitatively) by *Matheson and Little* [1971].

In this paper we include all of the above effects in our formulation, and in addition, we are able to include in our analytical representation two anisotropy effects discussed by *Cronyn* [1970b]: (1) the elongation of electron irregularities along the projection of the solar wind vector and (2) an anisotropic intensity distribution for a source of finite size [*Dennison*, 1969].

¹ Now at Applied Physics Laboratory, Johns Hopkins University, Laurel, Maryland 20810.

All the above physical effects for the IPS spectrum from a weak scattering thin screen may be formulated in terms of the confluent hypergeometric function (CHGF), as we pointed out earlier [Mitchell *et al.*, 1973; Mitchell and Roelof, 1975]. This formulation not only leads to a highly simplified representation of the thin-screen spectrum but also greatly facilitates the computation of the spectrum and scintillation index for scattering from an extended medium [Young, 1971]. We present analytic expressions giving the thin-screen spectrum within an error of <10% over all frequencies, and we discuss the dependence at meter observing wavelengths of the IPS spectrum and the scintillation index on elongation angle and source size for the extended interplanetary medium.

NORMALIZED ELECTRON DENSITY WAVE NUMBER SPECTRUM

We consider first the normalization of a physically acceptable form for an electron density power spectrum which exhibits a power law dependence on wave number (k) in the range affecting interplanetary scintillations. A form common in the literature is

$$F(k, r) = F_0(r)k^{-q} \quad (1)$$

This form cannot be normalized. The integral of $F(k, r)$ over all k space should equal the variance of the electron density fluctuation (δN^2), but clearly, this integral diverges for (1) at the limit $k \rightarrow 0$ for $q \geq 3$ or at the limit $k \rightarrow \infty$ for $q \leq 3$. Therefore two modifications of (1) have been proposed which eliminate these divergences: an 'outer scale' k_o [Cronyn, 1970a; Matheson and Little, 1971; Callahan, 1974] and an 'inner scale' k_i [Hollweg, 1970; Jokipii and Hollweg, 1970; Matheson and Little, 1971; Rickett, 1973]. For comparison with scintillation spectrums obtained at meter wavelengths the two scales appear to be unobservable. The observed spectrum is depressed by Fresnel diffraction at wave numbers above the wave number expected for an outer scale [Cronyn, 1970a], while at meter wavelengths an inner scale would be masked by the effects of the finite angular size of sources, on the assumption that the inner scale is at least as small as the gyroradius of thermal protons. The instrumental effect of a finite receiver passband [Budden and Uscinski, 1972] would also be dominated by finite angular size effects. We shall therefore emphasize source size effects over medium-scale effects in our discussion of the IPS spectrum.

However, even though the inner and outer scales may not affect the shape of observed scintillation spectrums, we now show that the inner and outer scales do have a significant effect on the normalization of the spectrum (and hence on the absolute values of the scintillation index), i.e., the unknown spatial function $F_0(r)$ in (1). Various studies [e.g., Cronyn, 1970b; Roadhead, 1971; Young, 1971] have fitted the run of scintillation index with elongation angle to the function $F_0 \propto r^{-n}$ with $n \approx 4$. This is a reasonable result under the assumptions $\delta N \propto N$ and $N \propto r^{-2}$. Nonetheless, the r dependence of F_0 is due not only to (δN^2) but also to the spatial variation of either the inner or the outer scale. To show this, we generalize (1) to a form which can be normalized:

$$F(k) = F_0(k_o^2 + k^2)^{-q/2} \exp(-k^2/k_i^2) \quad (2)$$

Tatarskii [1971] has noted that the three-dimensional spatial autocorrelation function corresponding to this spectrum with $k_i \rightarrow \infty$ involves a modified Bessel function of the second kind of order $(3 - q)/2$. A straightforward transformation of the integral of (2) over k space by using the variable $t = k^2/k_o^2$ yields

$$\langle \delta N^2 \rangle = \pi^{3/2} F_0 k_o^{3-q} U\left(\frac{3}{2}, \frac{5-q}{2}, \frac{k_o^2}{k_i^2}\right) \quad (3)$$

where U is the CHGF defined by the integral [Abramowitz and Stegun, 1964]

$$\Gamma(a)U(a, b, z) = \int_0^\infty dt e^{-t} t^{a-1} (1+t)^{b-a-1} \quad (4)$$

with the provision that z and a have positive real parts.

To be physically meaningful, the outer scale must greatly exceed the inner scale ($k_o^2 \ll k_i^2$), so we may take the small-argument limit of the CHGF:

$$\lim_{z \rightarrow 0} U(a, b, z) = \frac{\Gamma(b-1)}{\Gamma(a)} z^{1-a} \quad b > 1 \quad (5a)$$

$$\lim_{z \rightarrow 0} U(a, b, z) = \frac{\Gamma(1-b)}{\Gamma(1+a-b)} \quad b < 1 \quad (5b)$$

There is a logarithmic dependence for $b = 1$. Therefore the normalization of the electron density spectrum depends on the range of the power law index q :

$$F_0 = \frac{\langle \delta N^2 \rangle}{\pi} \frac{2^{-1/2}}{\Gamma[(3-q)/2]} k_i^{q-3} \quad q < 3 \quad (6a)$$

$$F_0 = \frac{\langle \delta N^2 \rangle}{\pi^{3/2}} \frac{\Gamma(q/2)}{\Gamma[(q-3)/2]} k_o^{q-3} \quad q > 3 \quad (6b)$$

The inner scale k_i appears in the normalization for a hard spectrum $q < 3$, since otherwise, the integral for (δN^2) diverges as $k \rightarrow \infty$. In the more commonly observed case of $3 < q < 4$, F_0 depends rather weakly on the outer scale k_o ; if $k_o \propto r^2$, while $(\delta N^2) \propto r^2$, then $F_0 \propto r^{2+2(q-3)}$. Thus although the observational fits obtained for $F_0(r)$ do not necessarily imply that (δN^2) has the same r dependence as $F_0(r)$, studies of the variation of scintillation index with elongation angle over a 'quiet' interplanetary medium [Cronyn, 1972] would be substantially correct in associating the derived radial dependence of $F_0(r)$ with that of (δN^2) . On the other hand, when weak scattering is caused by localized turbulence, as occurs in a solar wind shock or stream-stream interaction, the turbulence spectrum will be expected to display an outer scale with a strong r dependence (due to the finite extent of the disturbed region), so that the term k_o^{q-3} could be of significant physical importance in interpreting the value of the scintillation index in these special cases.

ANISOTROPY EFFECTS FOR DENSITY IRREGULARITIES AND SOURCE STRUCTURE

Two effects result from anisotropies, the first in the source, the second in the medium. The geometry for IPS observations is shown in Figure 1, along with the relevant trigonometric relationships. There are two orthogonal triads ($\hat{x}, \hat{y}, \hat{z}$) and ($\hat{f}, \hat{g}, \hat{s}$). The \hat{z} direction is the line of sight to the source, while the \hat{f} direction is radial (and hence also the nominal direction of the solar wind). The \hat{x} direction is the projection onto the plane of the sky of the radial solar wind velocity vector crossing the line of sight a distance r from the sun and L from the earth; i.e., the plane defined by \hat{x} and any \hat{f} along the line of sight contains all radial solar wind vectors crossing the source. The \hat{g} direction completes the right-handed triad ($\hat{x}, \hat{y}, \hat{z}$), while the \hat{s} direction completes the other orthogonal triad ($\hat{f}, \hat{g}, \hat{s}$).

Cohen *et al.* [1967] examined the possibility that anisotropic

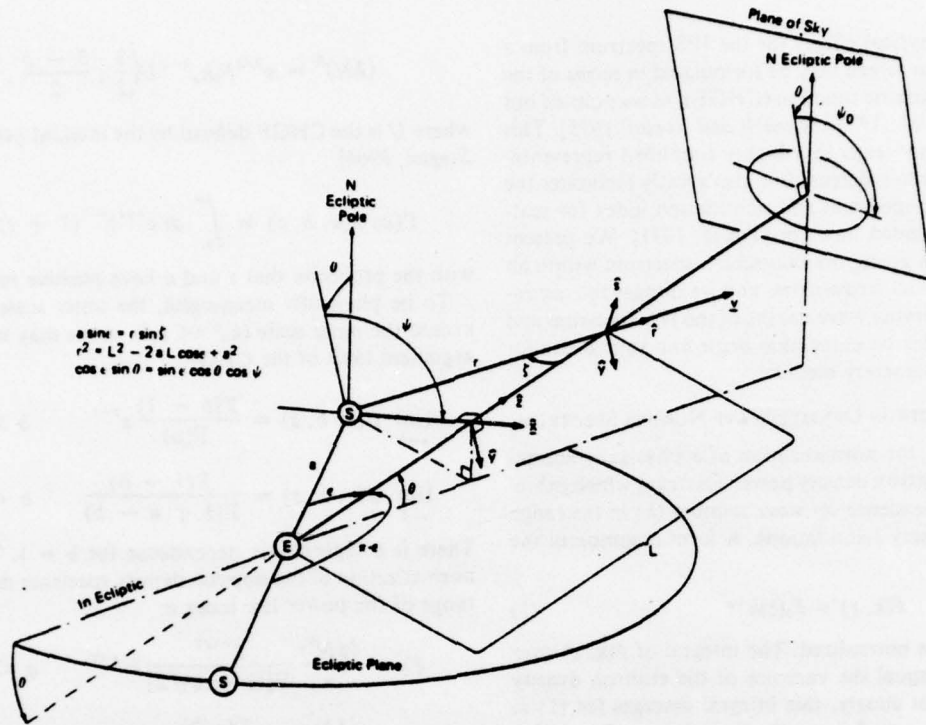


Fig. 1. Geometry for scintillation observations of an anisotropic radio source through a medium with anisotropic irregularities. The source at elongation angle ϵ and ecliptic latitude θ is approximated by an ellipsoidal intensity distribution in the plane of the sky, with the semimajor axis making an angle ψ_0 with the projection of the ecliptic north direction onto that plane. Scattering occurs at a distance L out along the line of sight (\hat{z}) from the earth (E) where irregularities are assumed to be axisymmetric about a radial (\hat{r}) solar wind vector V from the sun (S). The projection of V onto the plane of the sky gives the direction \hat{x} , and then $\hat{y} = \hat{z} \times \hat{x}$, and $\hat{s} = \hat{r} \times \hat{y}$. The angle ψ is measured between \hat{x} and the ecliptic north projection onto the plane of the sky. If for some elongation angle ϵ the source axis lies along the projection of V (so that $\psi = \psi_0$), it will also do so 6 months later at an elongation angle $\pi - \epsilon$.

source structure could significantly affect scintillation power. In order to investigate the effect on the scintillation spectrum we model the source anisotropy by assuming that its intensity distribution is ellipsoidal with a semimajor axis making an angle ψ_0 in the plane of the sky with the projection of the north ecliptic axis. Figure 1 reveals that the semimajor axis will coincide with the x axis when the elongation angle ϵ and the ecliptic polar latitude θ satisfy the simple relation

$$\tan \epsilon = \tan \theta \cos \psi_0, \quad \theta < \epsilon < \pi - \theta \quad (7)$$

i.e., when the general angle ψ equals ψ_0 . If this alignment can occur at all, it occurs twice, at intervals of $\frac{1}{2}$ year, since if ϵ_0 is the solution for the positive semimajor axis ψ_0 , then $\pi - \epsilon_0$ is a solution for $\psi_0 + \pi$, the negative semimajor axis. A pair of alignments may also occur for the semiminor axes.

Within the formalism which we present below, we can treat such an anisotropic source only when its principal axes (major or minor) lie in the \hat{x} direction. However, these special cases will serve to illustrate the strong effect of source anisotropy. We then obtain the source 'filter function' as the squared Fourier transform of the brightness distribution across the source [Salpeter, 1967]. An anisotropic Gaussian angular distribution in plane-of-the-sky coordinates

$$I(\omega_r, \omega_s) = I_0 \exp \left(-\frac{\omega_r^2}{\beta \Omega^2} - \frac{\beta \omega_s^2}{\Omega^2} \right) \quad (8)$$

has the integrated total intensity $\pi \Omega^2 I_0$, and leads to a filter function dependent upon β (the ratio of the semimajor axis to the semiminor axis) and the mean angular radius of the source,

Ω , i.e., the apparent size of the source. See the comprehensive discussion by Cohen and Cronyn [1974] of apparent source size.

$$f(k_x, k_y) = \exp [(-\frac{1}{2}\Omega^2 L^2)(\beta k_x^2 + \beta^{-1} k_y^2)] \quad (9)$$

Now we turn to the suggestion that the electron density irregularities may also be anisotropic [Dennison, 1969]. The simplest assumption is that they are elongated along the direction of the solar wind vector. Although they are more difficult to measure than proton anisotropies, solar wind electron anisotropies also appear to be aligned along the interplanetary magnetic field vector [Hundhausen et al., 1970; Feldman et al., 1975], but the additional geometrical complication would again be beyond the formalism which we shall use.

We therefore generalize (1) and (2) for forms dependent not on k but on the vector $\kappa = (\gamma_0 k_x, k_y, k_z)$. Thus a value of $\gamma_0 > 1$ corresponds to irregularities elongated along the solar wind vector. The only effect on the normalization from this generalization is to multiply F_0 in (3) by the factor $\gamma_0^{-1/2}$. However, the anisotropy projected on the plane of the sky will not be γ_0 , since \hat{r} and \hat{x} do not generally coincide (Figure 1). The projection can be obtained by rewriting the quadratic form κ^2 under a rotation through the angle ζ :

$$\kappa^2 = (\gamma_0 \sin^2 \zeta + \cos^2 \zeta) k_x^2 + (\gamma_0 - 1) \sin 2\zeta k_x k_z + (\gamma_0 \cos^2 \zeta + \sin^2 \zeta) k_z^2 + k_y^2 \quad (10)$$

The appropriate anisotropy factor γ in the x - y plane (which will depend on ϵ and L) is given by the coefficient of k_x^2 (since $k_x = 0$ for the phase spectrum projected onto the x - y plane), so

using the relationships from Figure 1 among ζ , ϵ , and l (where l is L expressed in astronomical units), we obtain

$$\gamma(\epsilon, l) = 1 + (\gamma_0 - 1)(V_{\perp}/V)^2 \quad (11)$$

since, by the same relationships, we find the projection of the solar wind onto the plane of the sky ($V_{\perp} = V \sin \zeta$) to be

$$V_{\perp}/V = \sin \epsilon (1 - 2l \cos \epsilon + l^2)^{-1/2} \quad (12)$$

THIN-SCREEN SCINTILLATION SPECTRUM FOR A FINITE DIAMETER SOURCE

The weak scattering approximation to the scintillation power dP from an interval dL in the frequency range ($\nu, \nu + d\nu$) was given by *Cronyn* [1970b] and *Young* [1971]. A sample thin-screen power spectrum dP/dL is shown in Figure 2 in order to identify the nomenclature that we shall use in the following discussion. In the notation of the previous sections,

$$dP(\nu) = \frac{dL}{V_{\perp}} (2\pi r_e \lambda)^2 \int_{-\infty}^{\infty} dk_y F(\gamma k_x, k_y, 0) \cdot 4 \sin^2 \left(\frac{k_x^2 + k_y^2}{k_f^2} \right) f(k_x, k_y) \quad (13)$$

where the scintillation spectrum $F(k)$ is given by (2), the finite source filter function f by (9), and the transverse solar wind velocity V_{\perp} by (12); the remaining term in the integrand is the Fresnel filtering function, which depends on the Fresnel wave number $k_f = (4\pi/\lambda L)^{1/2}$. Here λ is the observing wavelength, and r_e is the classical radius of the electron. The connection between scintillation frequency and wave number is $k_x V_{\perp} = 2\pi\nu$. We shall neglect any inner- or outer-scale effects on the shape of the spectrum, since they are most likely less important parameters at meter wavelengths than the parameters that we will retain. Then a convenient representation of dP is obtained in terms of the two dimensionless variables

$$S = \frac{k_x^2}{k_f^2} = \frac{\pi \lambda a^2}{V^2} \frac{k(1 - 2l \cos \epsilon + l^2)}{\sin^2 \epsilon} \quad (14)$$

$$S_1 = \frac{\beta}{k_f^2 \Omega^2 L^2} = \left(\frac{\lambda}{4\pi a} \right) \frac{\beta}{\Omega^2 l} \quad (15)$$

where $a = 1$ AU and $l = L/a$. Note that only S contains the frequency and velocity dependence, while S_1 contains all information on apparent source size and structure. The variables S and S_1 are the squares of scintillation frequency ν and the characteristic frequency of the source structure, respectively,

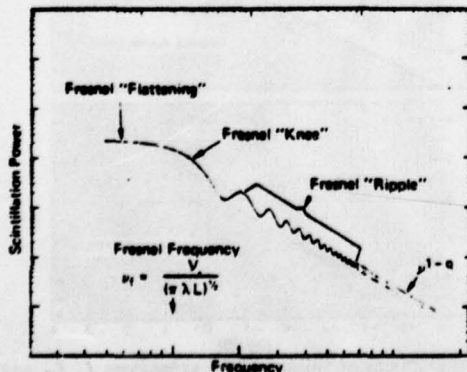


Fig. 2. Characteristic signatures of Fresnel diffraction in a computed thin-screen interplanetary scintillation spectrum for a point source ($\Omega = 0$) and a pure power law electron irregularity spectrum ($q = 3.6$) with a solar wind velocity of 400 km s^{-1} .

both being expressed as ratios to the 'Fresnel frequency' $\nu_f = k_f V_{\perp}/2\pi$.

A simple transformation of the variable of integration from k_x to t (by writing $k_x^2 = k_f^2 \gamma S t$) and the expression of the Fresnel filtering function in complex exponentials lead directly to the following expressions involving the CHGF given by (4):

$$dP = \frac{dL}{V_{\perp}} (2\pi r_e \lambda)^2 \left(\frac{\gamma_0}{\pi} \right)^{1/2} k_f^{1-q} F_0(r) \cdot \exp(-\beta S/2S_1) J(S, S_1; \gamma, q) \quad (16)$$

$$J(S, S_1; \gamma, q) = (\gamma S)^{(1-q)/2} \left\{ U\left(\frac{1}{2}, \frac{3-q}{2}, \frac{\gamma S}{2S_1}\right) - \text{Re} \left[e^{-i2S} U\left(\frac{1}{2}, \frac{3-q}{2}, \frac{\gamma S}{2S_1} + i2\gamma S\right) \right] \right\} \quad (17)$$

The normalization factor F_0 is given by (6a) and (6b).

For the purpose of generality, we have included in (A12) and (A13) of the appendix the effects on (16) and (17) of the inner and outer scales, which are described by the variables $S_o = (k_o/k_f)^2$ and $S_i = (k_i/k_f)^2$, respectively. We can see, however, that the Fresnel filtering effect obscures any flattening of the scintillation spectrum at low frequencies if $S_o \ll 1$, i.e., if $k_o^2 \lambda L \ll 4\pi$. For meter wavelengths and $L \leq 1$ AU this condition is easily satisfied for $k_o < 10^{-2} \text{ km}^{-1}$, i.e., outer scales larger than $0.1 R_E$. Even though an inner scale larger than 0.3 km is unlikely [*Cronyn and Mitchell*, 1974], the effect of an inner scale is masked at meter wavelengths by the independent effect of a finite source angular diameter if $S_i \gg S_1$, i.e., if $k_i \Omega L > 1$. Since meter wavelength angular diameters are often $> 0.1^\circ$ [*Readhead and Hewish*, 1974], the inequality is satisfied for $L > 0.1$ AU if $k_i > 10^{-1} \text{ km}^{-1}$. Therefore an inner scale would have to be at least as large as the thermal proton gyroradius at 1 AU to be observable for a source size of $\sim 0.1^\circ$. The Ogo 5 spectrums analyzed by *Unti and Russell* [1976] show no evidence of an inner scale larger than one tenth of a gyroradius.

Although the effects of the inner and outer scales may be more significant at shorter observing wavelengths (since the Fresnel wave number varies as $k_f \propto \lambda^{-1/2}$, and the effective source size approximately as $\Omega \propto \lambda^{-2}$), they are apparently negligible at meter wavelengths. Therefore we have suppressed the terms S_o and S_i in the remainder of our discussion of scattering from irregularities with a power law wave number spectrum. Recall, however, that even though the outer scale will have little effect on the shape of the scintillation spectrum, it may still play a significant role in the normalization of the spectrum, as was discussed above following (6a) and (6b).

Thus as was pointed out by *Mitchell et al.* [1973] and *Mitchell and Roelof* [1975], the computation of the weak scattering spectrum reduces to evaluation of the CHGF for complex arguments. *Young* [1971] presented excellent expansions for all frequency ranges of the spectrum; however, the coefficients are calculated by a best fit method for only one value of the index $q = 4$. *Woo* [1975] has made use of the CHGF technique in the analysis of multifrequency scintillation observations. The usefulness of (17) lies in the simple behavior of the CHGF for small and large arguments. For small arguments, power series expansions are appropriate, while for large arguments, asymptotic forms are well known. However, both of these expansions fail badly for arguments approaching unity. Fortunately, we were able to derive a much improved modified asymptotic expansion for large arguments which is valid even for argu-

ments close to unity. Therefore we can present expansions containing only a few terms which approximate the scintillation spectra over most of the frequency range with errors no larger than 10%.

Consider first the CHGF of complex argument $U(\frac{1}{2}, (3 - q)/2, \xi + i\eta)$. In the appendix the expansions are derived, and error contours for the real and imaginary parts of U are shown in Figures 9a and 9b as a function of ξ and η for the large-argument expansion for the parameter $3.2 \leq q \leq 4$. It is seen that $\text{Re } U$ is given to better than 5% accuracy for $\xi \geq 0.1, \eta \geq 0.1$, while $\text{Im } U$ (which is an oscillating function of η) is given to better than 10% accuracy for $\xi \geq 1, \eta \geq 1$. The errors were calculated by comparing the expansions with exact numerical evaluations of the CHGF (see the appendix).

However, (17) contains the difference of two CHGF's, so that there are three expansion regions:

Region I

$$\xi \ll 1 \quad \eta \ll 1$$

Region II

$$\xi \ll 1 \quad \eta \geq 1$$

Region III

$$\xi \geq 1 \quad \eta \text{ arbitrary}$$

The results of expanding the two CHGF's in (17) and of expressing the arguments of the CHGF as $\xi = \gamma S/2S_1$ and $\eta = 2\gamma S$ are then

$$J_I = 2^{(q+1)/2} \frac{\Gamma[(S-q)/2]}{(q-1)(q-3)\pi^{1/2}} \left\{ (4S_1)^{(1-q)/2} - \left(1 + \frac{1}{16S_1^2}\right)^{(1-q)/2} \left(\cos \frac{q-1}{2} \Theta + 2S \sin \frac{q-1}{2} \Theta\right) + \frac{2\gamma S q}{q+1} \left[(4S_1)^{-(1+q)/2} - \left(1 + \frac{1}{16S_1^2}\right)^{(1+q)/2} \cdot \cos \frac{q+1}{2} \Theta + O(S^2) \right] + \frac{\Gamma[(q-1)/2]}{\Gamma(q/2)} (\gamma S)^{(1-q)/2} \cdot \left[\frac{2}{\gamma^2} + \frac{4}{(q-3)\gamma} + \frac{6}{(q-3)(q-5)} \right] + O(S^{(7-q)/2}) \right\} \quad (18)$$

$$J_{II} = (\gamma S)^{(1-q)/2} \left[\frac{\Gamma[(q-1)/2]}{\Gamma(q/2)} - \omega_{02}^{-1/2} \cos(2S + \theta_0) - (0.1875)q\omega_{12}^{-5/2} \cos(2S + 5\theta_1) - (0.1563)q\omega_{12}^{-7/2} \cos(2S + 7\theta_1) - (0.1367)q\omega_{12}^{-9/2} \cos(2S + 9\theta_1) - (0.2051)q(q-1)\omega_{22}^{-9/2} \cos(2S + 9\theta_2) - \dots \right] \quad (19)$$

$$J_{III} = J_{II} - \frac{\Gamma[(q-1)/2]}{\Gamma(q/2)} (\gamma S)^{(1-q)/2} + (\gamma S)^{(1-q)/2} \left[\omega_{01}^{-5/2} + (0.1875)q\omega_{11}^{-5/2} + (0.1563)q\omega_{11}^{-7/2} + (0.1367)q\omega_{11}^{-9/2} + (0.2051)q(q-1)\omega_{21}^{-9/2} + \dots \right] \quad (20)$$

where $\tan \Theta = 4S_1$ and $\tan 2\theta_n = 2\gamma S/\omega_{n1}$, while

$$\omega_{n1} = \frac{\gamma S}{2S_1} + \frac{q}{2} + n \quad \omega_{n2}^2 = (2\gamma S)^2 + \omega_{n1}^2 \quad (21)$$

If q is an odd integer, there are analogous expansions with logarithmic terms and digamma functions replacing the gamma functions. However, we have retained the pairs of terms which combine to give the logarithmic behavior, so that the expansions remain accurate even as q approaches odd integral values.

Expansion I is in the small-argument range of both CHGF's of (17), so since the errors of both CHGF's are of the same sign, they tend to be minimized in the J function, which essentially takes their difference. The same is also true of expansion III, where both CHGF's are in the large-argument range. However, in expansion II the first CHGF in (17) is in the small-argument range, while the second is in the large-argument range. Thus the errors do not subtract, and for this reason, the greatest accuracy was obtained by keeping only the lowest-order terms in the small-argument expansion.

We show in Figure 3a the domains of validity for the three expansions in a $\log(2S)$ - $\log(4S_1)$ plane. Note that $\eta = 2S$ and $\xi = 2S/4S_1$ when $\gamma = 1$ (as we assume here). Therefore the conditions bounding the three regions take a very simple form: $\eta = 1$ becomes $\log 2S = 0$ (the ordinate axis), $\xi = 1$ becomes a line through the origin with positive unit slope, and $\xi \ll 1$ becomes a line above and parallel to that of $\xi = 1$. From examination of (18)-(20) it is seen that region I gives the flat portion of the spectrum below the Fresnel frequency ($S = 1$), while region II gives the characteristic ν^{1-q} decay beyond the Fresnel frequency with the additive 'Fresnel ripple' $\cos(2S + \theta_0)$. Region III is dominated by the exponential damping term $\exp(-\beta\xi)$ in (16) due to the finite source angular size, resulting in a Gaussian round-off which steepens the ν^{1-q} decay at high frequencies. Regions Ia, IIa, and IIIa indicate transitions between expansions. The high-frequency attenuation of the spectrum due to finite source size will be illustrated in detail in the discussion below of Figures 4-6.

Error contours at the 10% level were prepared for the J functions by again comparing the expansions (18)-(20) with exact numerical calculations of the CHGF (see the appendix). The result for $q = 3.6$ is presented in Figure 3b in the same $\log 2S$ - $\log 4S_1$ parameter space as was used in Figure 3a (on the

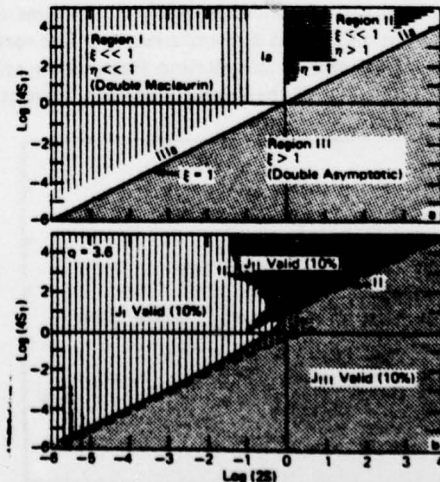


Fig. 3. (a) Domains of validity of the expansions $J_I, J_{II},$ and J_{III} (see text) for the two confluent hypergeometric functions making up the spectral function $J(S, S_1; \gamma, q)$. (b) Computed accuracy contours within which the expansions $J_I, J_{II},$ and J_{III} approximate $J(S, S_1; 1, 3.6)$ to within 10%.

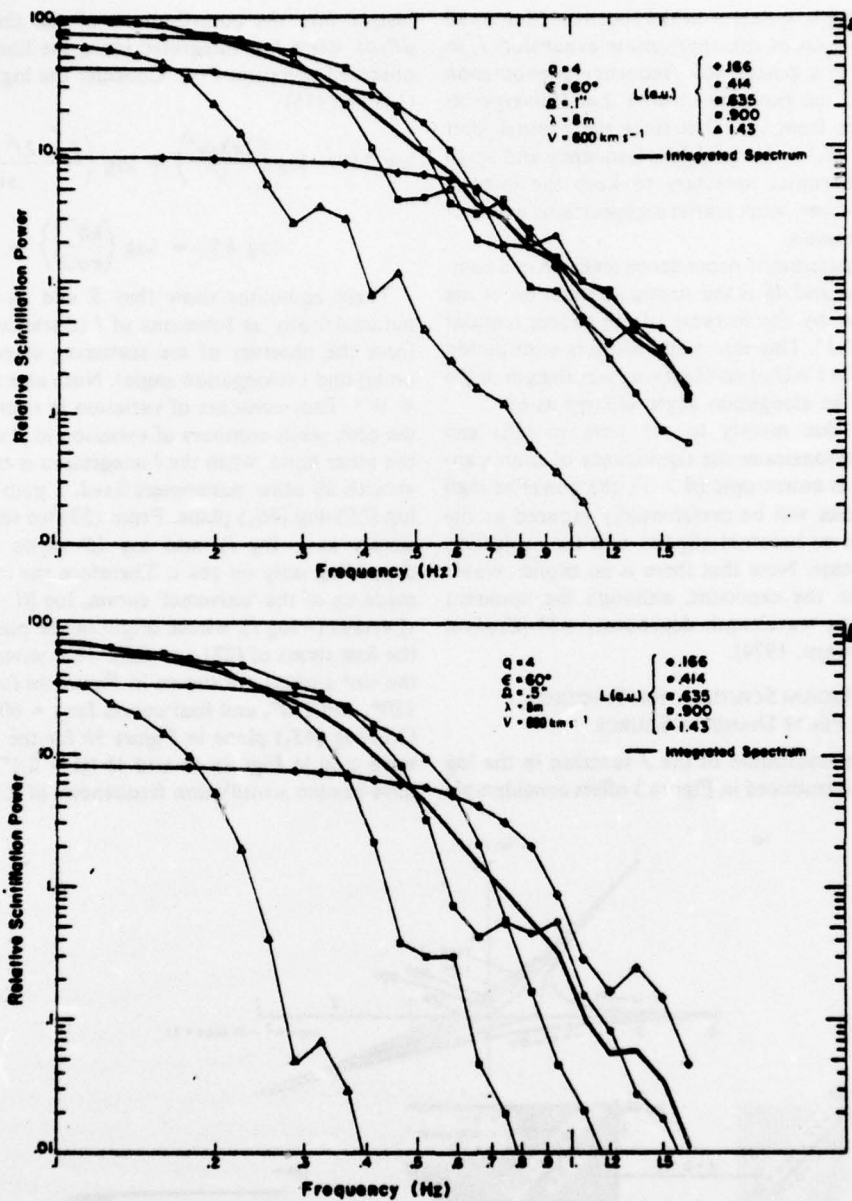


Fig. 4. Thin-screen spectra calculated for five distances L (out along the line of sight) by using expansions J_I , J_{II} , and J_{III} . Their relative normalization is given by $F_0 \propto r^{-4}$, although the absolute normalization of F_0 is arbitrary. The integrated scintillation power, integrated along the line of sight for each frequency with $F_0 \propto r^{-4}$, is given by the heavy solid line. (a) A relatively 'small' source radius $\Omega = 0.1^\circ$. (b) A larger source $\Omega = 0.5^\circ$, demonstrating the strong suppression of the high-frequency power from more distant screens.

assumption that the irregularities are isotropic, so $\gamma = 1$). The domains of validity of the three expansions overlap, covering the whole space. Therefore the expansions (18)–(20) completely describe the IPS thin-screen weak scattering power spectrum within an error always less than 10% (for $q = 3.6$). The error contours are, of course, a function of q ; actually, we found that the 10% criterion is satisfied over a range at least as large as $3.2 \leq q \leq 4.0$.

The main effect of anisotropic irregularities ($\gamma \neq 1$) is easily seen from (18)–(20). Both expansion J_{II} and expansion J_{III} describe the spectrum at frequencies higher than the Fresnel frequency, where the power falls off at least as fast as ν^{-2} . However, the leading term in J has the coefficient $\gamma^{1-q/2}$, so that dP/dL varies as $\approx \gamma^{1-q/2}$, due to the factor $\gamma_0^{1/2}$ in (16).

Thus irregularities elongated along the solar wind vector ($\gamma_0 > 1$) further depress this portion of the spectrum, while the converse is true for $\gamma_0 < 1$. For example, Dennison [1969] suggests a value for $\gamma \approx 3.2$ for the projection along the solar wind direction lines. When $q = 3.6$ is chosen, the spectrum for $\nu > \nu_f$ will be $\approx 40\%$ of the value that it would have for isotropic irregularities.

Figures 4a and 4b present sample calculations, using (18)–(20), of thin-screen spectra at different distances L along the line of sight to a source at elongation $\epsilon = 60^\circ$. Here it was assumed that $F_0 \propto r^{-4}$ in (2). The power law index was taken as $q = 4$, the anisotropy parameters were taken as $\gamma = \beta = 1$, and the calculations were carried out for two angular radii, $\Omega = 0.1^\circ$ and $\Omega = 0.5^\circ$. The flattening of the spectra

due to Fresnel filtering is apparent in the spectrums for small values of L . Examination of the appropriate expansion J_1 in (18) shows that this is a general low-frequency phenomenon for $q < 5$. For $q > 5$ the expansion shows that J diverges as $S^{2-q/2}$, but it is seen from (13) that since the Fresnel filter function approaches $(k_x^2 + k_y^2)^2$ for low frequency and small k_v , an outer scale becomes necessary to keep the integral defined as $\nu \rightarrow 0$. However, weak scattering spectrums with $q > 5$ appear to be uncommon.

The most striking parametric dependence revealed in a comparison of Figures 4a and 4b is the strong attenuation of the high-frequency power by the increase of the source angular radius from $0.1''$ to $0.5''$. This essentially restricts scintillation above 0.2 Hz to within 1 AU at an observing wavelength in the meter range, even at an elongation angle as large as 60° .

The reduction is due mainly to the term in (16) $\exp(-\beta S/2S_1)$, which demonstrates the significance of source anisotropy. If a source is anisotropic ($\beta > 1$), the power at high scintillation frequencies will be preferentially reduced as the major axis of the source becomes aligned with the projection of the solar wind vector. Note that there is no explicit wavelength dependence in the exponent, although the apparent angular size should be wavelength dependent, $\propto \lambda^2$ [Cronyn, 1970b; Cohen and Cronyn, 1974].

EXTENDED MEDIUM SCINTILLATION SPECTRUM FOR A FINITE DIAMETER SOURCE

The parametric representation of the J function in the $\log(2S)$ - $\log(4S_1)$ plane introduced in Figure 3 offers considerable

insight into the contributions of the thin-screen spectrums dP/dL when it is integrated along the line of sight to give the observed spectrum $P(\nu)$. Consider the logarithmic versions of (14) and (15):

$$\log 2S = \log \left(\frac{2\pi\lambda a \nu^2}{V^2} \right) + \log \left(\frac{l - 2l^2 \cos \epsilon + l^3}{\sin^2 \epsilon} \right) \quad (22)$$

$$\log 4S_1 = \log \left(\frac{\lambda \beta^{1/2}}{\pi a \Omega^2} \right) - \log l \quad (23)$$

These equations show that S and S_1 can be represented parametrically as functions of l (distance along line of sight from the observer of the scattering screen, in astronomical units) and ϵ (elongation angle). Note also that $S \propto \nu^2$, while $S_1 \propto \Omega^2$. Thus contours of variation in ν are horizontal lines on the plot, while contours of variation in Ω are vertical lines. On the other hand, when the l integration is carried out from 0 to ∞ with all other parameters fixed, a path is traced out in the $\log(2S)$ - $\log(4S_1)$ plane. From (23) we see that $\log 4S_1$ varies simply as $(-\log l)$, and $\log 2S$ varies as a function of l , depending only on $\cos \epsilon$. Therefore the integration paths are made up of the 'universal' curves, $\log [(l - 2l^2 \cos \epsilon + l^3)/\sin^2 \epsilon]$ versus $(-\log l)$, whose origin in the plane is determined by the first terms of (22) and (23). The universal curves (without the $\sin^2 \epsilon$ term) are shown in Figure 5a for $\epsilon = 30^\circ, 60^\circ, 90^\circ, 120^\circ$, and 150° , and four curves for $\epsilon = 60^\circ$ are laid on the $\log(2S)$ - $\log(4S_1)$ plane in Figure 5b for the same parameters as were used in Figures 4a and 4b ($\Omega = 0.1''$ and $\Omega = 0.5''$). We have chosen scintillation frequencies of 0.1 and 1.0 Hz for the

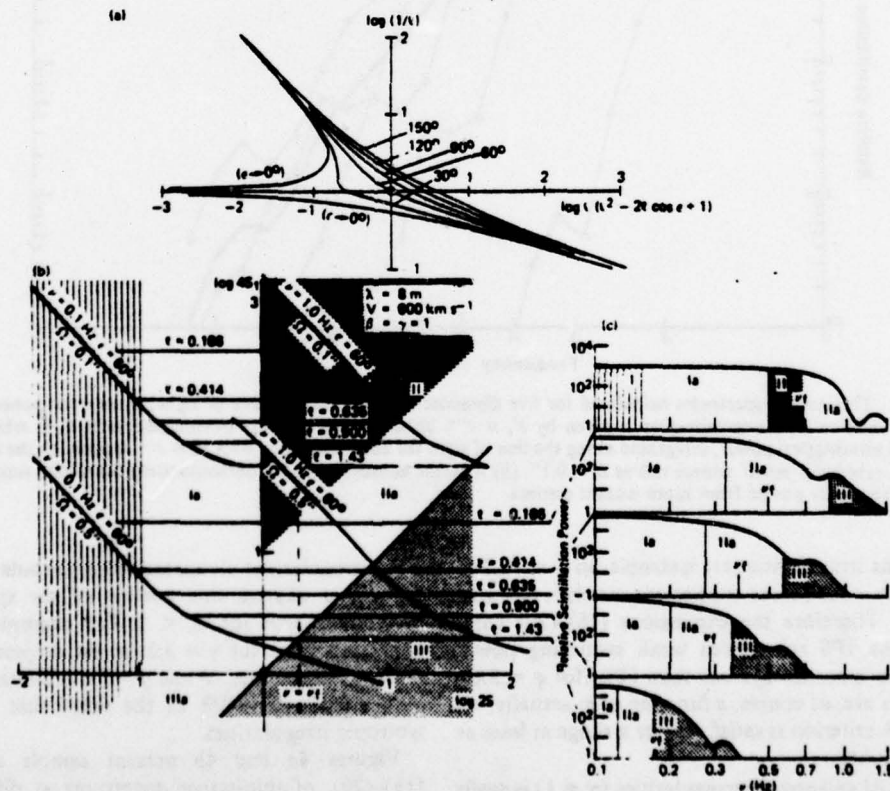


Fig. 5. (a) 'Universal curves' giving the contour in the $\log(2S)$ - $\log(4S_1)$ plane for an integration along the line of sight at constant frequency. (b) Universal curve for line-of-sight integrations at $\epsilon = 60^\circ$ located in the $\log(2S)$ - $\log(4S_1)$ plane for all combinations of scintillation frequencies of 0.1 and 1.0 Hz and source angular radii of $0.1''$ and $0.5''$. The regions indicated are the same as those in Figure 3a. The spectrums fall in the transition regions Ia and IIa, in which expansions J_1 and J_{III} (respectively) are actually valid for $q = 3.6$ (Figure 3b). (c) Thin-screen spectrums from Figure 4c sketched to illustrate how their form can be deduced from the regions intersected by the $l = \text{const}$ lines in Figure 5b.

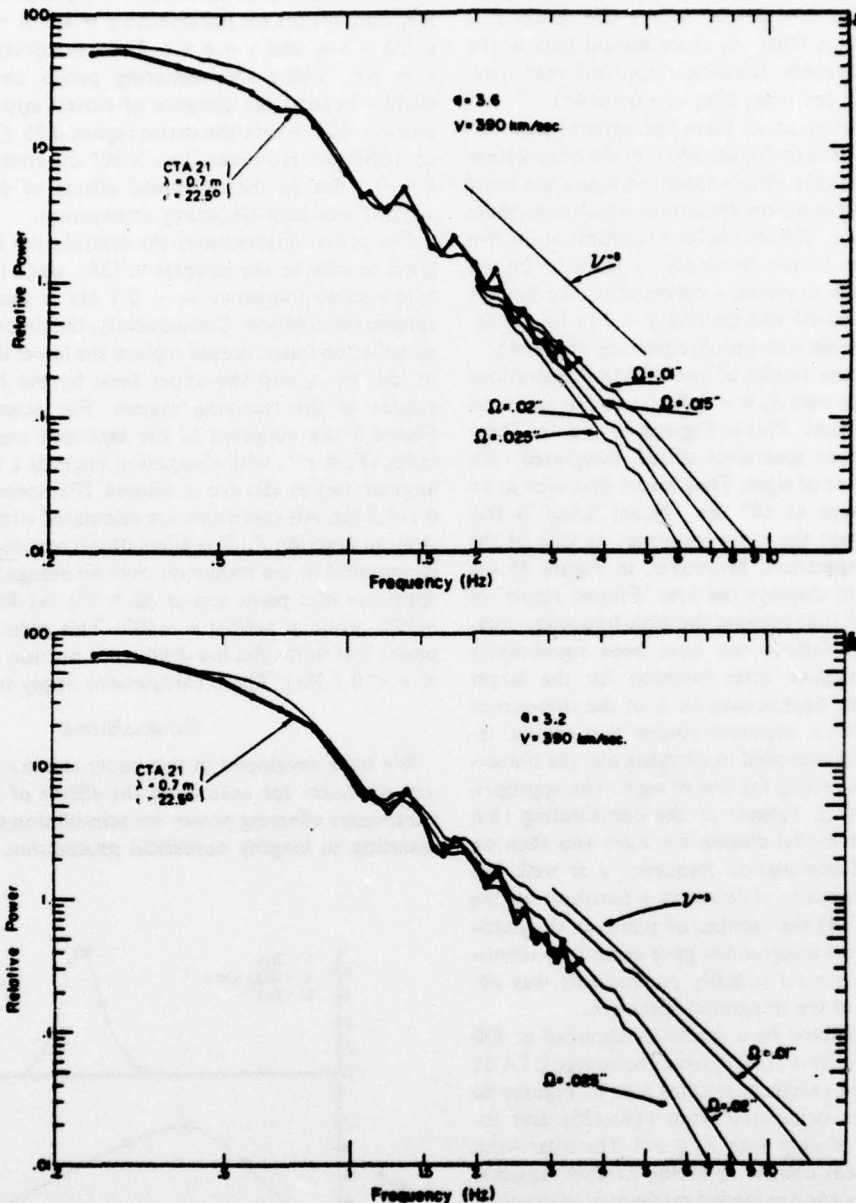


Fig. 6. Scintillation spectrum of CTA 21 observed at 430 MHz [Lovelace *et al.*, 1970] is indicated by the heavy line. Light lines give the theoretical weak scattering spectra for various source apparent angular radii (Ω). An integration of thin-screen spectra along the line of sight was carried out by assuming $F_s = r^{-3}$, and the solar wind speed was chosen at $V = 390 \text{ km s}^{-1}$ to best-fit the Fresnel structure. The electron irregularity spectrum power law index was chosen as (a) $q = 3.6$, which produces an asymptotic high-frequency dependence $\nu^{-3.6}$, and (b) $q = 4.0$, going as $\nu^{-4.0}$ (for a point source). It is clear that q and Ω cannot both be determined unambiguously by comparison with a single spectrum.

illustration, and the l values corresponding to those used in Figures 4a and 4b are indicated as constant values of S , along the integration path curves.

Since a change in frequency represents a horizontal displacement of the origin of the universal curves in Figure 5b, one can simply slide the entire l curve horizontally to determine how the contribution to the observed frequency spectrum from each l changes qualitatively as a function of frequency. For instance, by comparing the curves on the plot with the corresponding thin-screen spectra in Figures 4a and 4b we can demonstrate this process. The two lower curves correspond to the spectra in Figure 4b. Looking first at the curve for $\nu = 0.1 \text{ Hz}$ in Figure 5b, we see that all five screens are in

the Fresnel flattened region. Now as we go to $\nu = 1.0 \text{ Hz}$, the first screen is in region II, the power law region of the spectrum, while the remaining four are attenuated by the finite source size in the exponentially damped region III and are thus severely depressed.

Now, staying at $\nu = 0.1 \text{ Hz}$, let us change to a smaller source radius. A change in Ω corresponds to a vertical displacement of the universal l curve. Thus using the same l curve as was used before but displacing it vertically to the position of the upper curve in Figure 5b, we can see qualitatively the profound effect that the source size has on each screen's contribution and thus on the shape of the observed spectrum. The first four screens are now in the power law region II, and only the last

(farthest out) screen is still affected by the source angular diameter. The total effect of a smaller source size results in a much greater contribution from the more distant part of the medium (compare the second-, third-, and fourth-screen spectrums in Figure 4a with the same ones in Figure 4b).

Thus with no calculation at all (save the determination of the placement of the l curve on Figure 5b from the observation parameters) one can quickly obtain from the figure the basic shape of the individual thin-screen spectrums which contribute to the observed spectrum. The shapes for spectrums at the five l values are sketched in Figure 5c simply by marking on the frequency axis where the universal l curves cross the boundaries of regions I, II, and III and the line $S = 2$ in Figure 5b. Figure 5c may be compared with the spectrums in Figure 4b.

We present finally some results of line-of-sight integrations for an extended medium with $F_0 \propto r^{-4}$. First, we call attention to the 'integrated spectrums' $P(\nu)$ in Figures 4a and 4b. These are simply the thin-screen spectrums dP/dL integrated with respect to L along the line of sight. They reveal that even at an elongation angle as large as 60° the Fresnel 'knee' is still defined and falls at about the same frequency as that of the dominant thin-screen spectrum. Moreover, in Figure 4b the integrated spectrum still displays the first 'Fresnel ripple' of the closest screen ($l = 0.166$) because the high-frequency components of the screens further out have been significantly attenuated by the Gaussian filter function for the larger source. The complicated dependence on L of the thin-screen spectrums, including finite apparent source size effects, requires that some care be exercised in carrying out the numerical integration of dP/dL along the line of sight. The appropriate choice of locations (L values) of the contributing thin screens depends on the model chosen for $F_0(r)$ and then on elongation angle ϵ and scintillation frequency ν as well. We adopted the ad hoc procedure of choosing a partition for the integral and then doubling the number of points in the partition. If the two numerical integrations gave essentially identical results, the latter integral (doubly partitioned) was accepted as our estimate of the integrated spectrum.

Another example is offered by a spectrum obtained at 430 MHz (0.7 m) by Lovelace *et al.* [1970] from the source CTA 21 at 22.5° elongation. The spectrum is compared in Figures 6a and 6b with spectrums calculated from (18)–(20) and integrated along the line of sight with $F_0 \propto r^{-4}$. The solar wind velocity (390 km s^{-1}) was chosen to fit the Fresnel maxima. Young [1971] obtained a good extended medium fit with velocities of $\approx 400 \text{ km s}^{-1}$ for a point source and $q = 4$ (a Kolmogoroff spectrum). Comparison of Figures 6a and 6b reveals that the CTA 21 spectrum is well fitted (including Fresnel oscillations) with two different sets of parameters: either a power law index $q = 3.6$ and a source radius $\Omega = 0.015^\circ$ or $q = 3.2$ and $\Omega = 0.025^\circ$. This ambiguity demonstrates the difficulty of deriving source or medium parameters from fits to a single spectrum. The attenuation of the high-frequency scintillation power obtained by increasing the source radius (Ω) is indistinguishable (over the limited frequency range of the power law portion of the spectrum) from the result of increasing the power law index (q).

A cruder but more easily obtained measure of scintillation activity is the scintillation index (m), which may be written in terms of its differential contributions along the line of sight as

$$\frac{dm^2}{dL} = \int_0^\infty d\nu \frac{dP(\nu)}{dL} \quad (24)$$

These differential contributions are presented in Figure 7 as a function of ϵ for the parameters $q = 4.0$, $\Omega = 0.1^\circ$, $V = 400 \text{ km s}^{-1}$, $\lambda = 8 \text{ m}$, and $\gamma = \beta = 1$. There is a drastic change between $\epsilon = 30^\circ$, where the scattering power comes mainly from slightly beyond the distance of closest approach ($l = 0.866$), and $\epsilon = 60^\circ$, where the entire region $0.25 \leq l \leq 1.25$ makes a contribution. However, for $\epsilon > 90^\circ$ the contributions are from $l < 0.5$ due to the combined effects of density falloff and angular size high-frequency attenuation.

For actual observations the scintillation index is not calculated exactly as the integral in (24), since the array response below some frequency $\nu_0 \sim 0.1 \text{ Hz}$ is usually due to ionospheric scintillation. Consequently, the theoretically computed scintillation index should replace the lower limit of the integral in (24) by ν_0 and the upper limit by the high-frequency response of the receiving system. For example, we show in Figure 8 the variation of the extended medium scintillation index ($F_0 \propto r^{-4}$) with elongation angle as a function of source angular radius (Ω) for a filtered IPS spectrum restricted to 0.1–1.5 Hz. All spectrums are calculated with the same normalization function F_0 . The effect of the particular filter used here is apparent in the reduction over all elongation angles for the spectrum of a point source ($\Omega = 0^\circ$). At 40° the reduction is $\sim 30\%$, while at 160° it is $\sim 50\%$. This reduction is due to the power lost in the flat low-frequency portion of the spectrum ($0 < \nu < 0.1 \text{ Hz}$). These calculations apply to $\lambda = 8 \text{ m}$.

CONCLUSIONS

We have developed in this paper the mathematical formalism necessary for examining the effects of varying the many parameters affecting power law scintillation spectrums without resorting to lengthy numerical procedures. The most signifi-

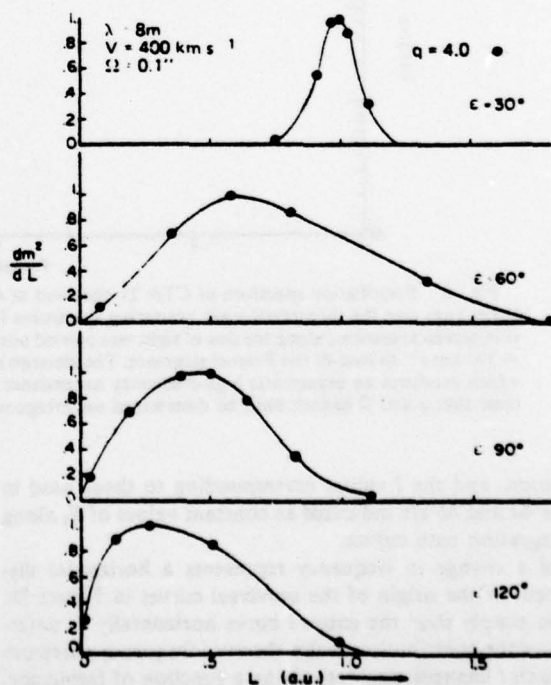


Fig. 7. Contributions to the square of the scintillation index m^2 (the total area under the frequency spectrum), from thin screens of thickness dL at distances L along the line of sight. The dependence is shown for four elongation angles for a medium with $F_0 \propto r^{-4}$, and the functions dm^2/dL are normalized to unity at their maximum value.

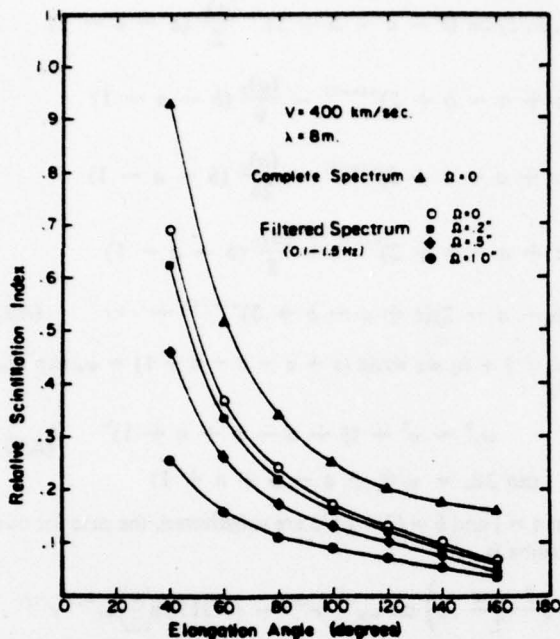


Fig. 8. Effect of instrumental filtering of the scintillation spectrum for various angular sizes as a function of source elongation angle. The nonuniform reduction of the index for the finite size sources is similar to the reduction shown for $\Omega = 0^\circ$ (which varies from $\sim 30\%$ at $\epsilon = 40^\circ$ to $\sim 50\%$ at $\epsilon = 160^\circ$).

cant parameter for meter wave observations is the apparent source angular size. We have shown that the normalization of the spectrum depends on the characteristic outer scale of the turbulence in the medium as well as on the electron density variance itself. This dependence on outer scale should usually be too weak to affect the interpretation of the elongation angle variation of the scintillation index, although the dependence may be significant when scattering is localized in small-scale structures such as solar wind stream-stream interactions. We have included anisotropy effects, both of a finite size source and of the irregularity structure. We have also introduced in the discussion of the extended medium a graphical construction which allows a quick qualitative modeling of the contribution to the frequency spectrum from different parts of the scattering medium. An outgrowth of this simplification is that one can integrate the spectrums over arbitrary frequency ranges. Therefore data acquisition system filters can be simulated, and their effect on the scintillation index modeled.

As is indicated in the comparison with the data of *Lovelace et al.* [1970], the parameters cannot be uniquely determined through modeling a single spectrum. The most ambiguous part of the model is the essentially free function which determines the strength of the turbulence along the line of sight through the medium. The comparison of a large number of observed spectrums with the extensive calculations is now made possible by the simplified mathematical expansions presented in this paper. We hope first to test the limits of weak scattering theory and then, working within those limits, to examine the spatial structure of turbulence in the solar wind.

APPENDIX

Although the confluent hypergeometric function (CHGF) may be defined by the integral (4) under restricted conditions,

its more general definition is in terms of Kummer's CHGF $M(a, b, z)$ [Abramowitz and Stegun, 1964].

$$U(a, b, z) = \frac{\pi}{\sin \pi b} \left[\frac{M(a, b, z)}{\Gamma(1+a-b)\Gamma(b)} - z^{1-b} \frac{M(1+a-b, 2-b, z)}{\Gamma(a)\Gamma(2-b)} \right] \quad (A1)$$

$$M(a, b, z) = \sum_{n=0}^{\infty} \frac{(a)_n z^n}{(b)_n n!} \quad (A2)$$

$$(a)_n = a(a+1) \cdots (a+n-1) \quad (a)_0 = 1 \quad (A3)$$

If b is an integer, than (A1) contains a logarithmic term $M(a, b, z) \ln z$, which results from the near cancellation of terms of the form z^{1-a+n} from the second Kummer function with the power series in z from the first. The full logarithmic solution is given by *Abramowitz and Stegun* [1964], but we found that if we grouped the canceling terms together, we could use (A1) for b values very close to integers. Therefore (A1) and (A2) provide us with the expansion for small arguments used in J_1 and J_{11} (equations (18) and (19)) for almost all values of b .

For $|z| \gg 1$, *Abramowitz and Stegun* [1964] give the asymptotic expansion

$$U(a, b, z) \sim z^{-a} \sum_{r=0}^{\infty} \frac{(a)_r (1+a-b)_r}{n!} (-z)^{-r} + O(|z|^{-R-1}) \quad (A4)$$

We found, however, that this expansion was inadequate to provide overlapping domains of convergence to accuracies of $\sim 10\%$ with the small-argument expansion (A1). Therefore we returned to the integral definition (4) and noted that the conventional asymptotic expansion may be obtained by expanding the term in the integrand $(1+t)^{b-a-1}$ using the binomial theorem. With this motivation we rewrote the same term as

$$[e^t + (t+1-e^t)]^{b-a-1} = \sum_{n=0}^{\infty} \frac{\Gamma(b-a)}{\Gamma(n+1)\Gamma(b-a-n)} \cdot (t+1-e^t)^n e^{(b-a-1-n)t} \quad (A5)$$

and expanded using the binomial theorem. The terms

$$(t+1-e^t)^n = (-1)^n \left(\frac{t^2}{2} + \frac{t^3}{3} + \dots \right)^n = \frac{t^{2n}}{(-2)^n} \sum_{m=0}^{\infty} K_{nm} t^m \quad (A6)$$

are of the order of unity for $n=0$ but are $O(t^{2n})$ for $n \geq 1$. Since the main contribution from the integrand in (4) comes from small values of t for $\text{Re } z \gg 1$, the higher-order (t^{2n}) terms should be negligible. The coefficients K_{nm} in (A6) are easily found to satisfy $K_{0m} = \delta_{0m}$, $K_{1m} = 2/(m+2)!$ and

$$K_{n+1,m} = 2 \sum_{l=0}^{\infty} \frac{K_{nl}}{(2+m-l)!} \quad (A7)$$

Substitution of (A6) into the defining integral (4) yields

$$U(a, b, z) = \sum_{n=0}^{\infty} \sum_{m=0}^{\infty} \frac{K_{nm}}{(-2)^n n!} (b-a-n)_n \cdot (a)_{n+m} (z+a-b+n+1)^{-(a+n+m)} \quad (A8)$$

The first few terms are

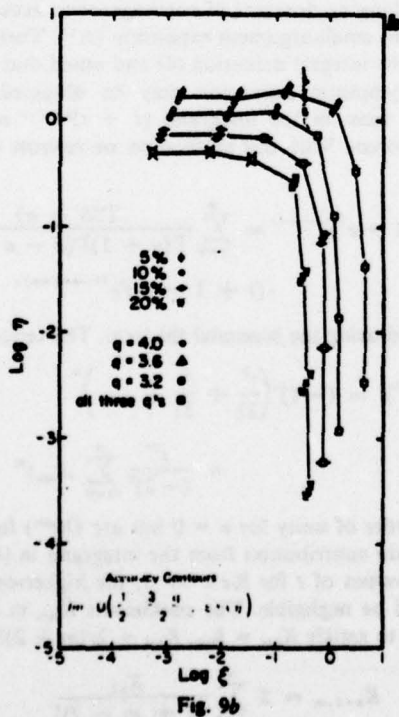
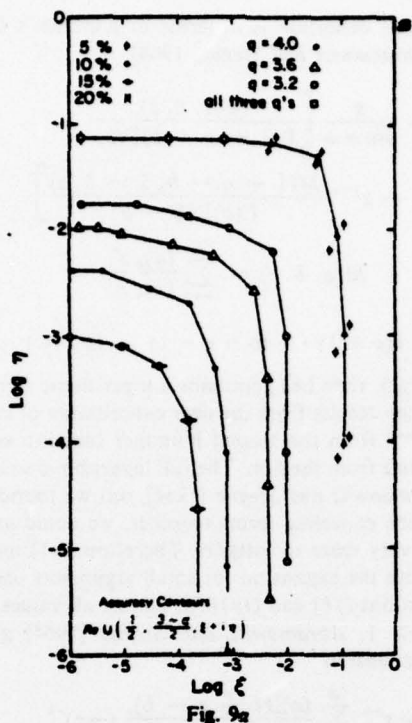


Fig. 9. Accuracy contours for the modified asymptotic expansion for $U(a, b, z)$ derived in the appendix compared with direct numerical computations of the confluent hypergeometric function. When z is expressed as $\xi + i\eta$ and $a = \frac{1}{2}$ and $b = (3 - q)/2$ are taken, the contours are presented for accuracies of 5, 10, 15, and 20% for q equal to 3.2, 3.6, and 4.0. The expansion gives $U(a, b, \xi + i\eta)$ to better than the indicated accuracy in all regions to the right and above a given contour for (a) the real part and (b) the imaginary part.

$$\begin{aligned}
 U(a, b, z) &\approx (z + a - b + 1)^{-a} \frac{(a)_n}{2} (b - a - 1) \\
 &\cdot (z + a - b + 2)^{-(a+2)} - \frac{(a)_n}{6} (b - a - 1) \\
 &\cdot (z + a - b + 2)^{-(a+3)} - \frac{(a)_n}{24} (b - a - 1) \\
 &\cdot (z + a - b + 2)^{-(a+4)} + \frac{(a)_n}{8} (b - a - 1) \\
 &\cdot (b - a - 2)(z + a - b + 3)^{-(a+4)} + \dots \quad (A9)
 \end{aligned}$$

For $z = \xi + i\eta$ we write $(z + a - b + n + 1) = \omega_n \exp i\theta_n$, where

$$\begin{aligned}
 \omega_n^2 &= \eta^2 + (\xi + a - b + n + 1)^2 \quad (A10) \\
 \tan 2\theta_n &= \eta / (\xi + a - b + n + 1)
 \end{aligned}$$

When $a = \frac{1}{2}$ and $b = (3 - q)/2$ are substituted, the case for our spectrum is

$$\begin{aligned}
 U\left(\frac{1}{2}, \frac{3-q}{2}, z\right) &\approx \omega_n^{-1/2} e^{i\theta_n} + (0.3175) \left(\frac{q}{2}\right) \omega_1^{-7/2} e^{i7\theta_1} \\
 &+ (0.375) \left(\frac{q}{2}\right) \omega_1^{-5/2} e^{i5\theta_1} + (0.2734) \left(\frac{q}{2}\right) \omega_1^{-9/2} e^{i9\theta_1} \\
 &+ (0.8203) \left(\frac{q}{2} + 1\right) \left(\frac{q}{2}\right) \omega_2^{-9/2} e^{i9\theta_2} + \dots \quad (A11)
 \end{aligned}$$

This series converges very rapidly, even for $\xi \sim 1$ or $\eta \sim 1$, due to the presence of n in the expression (A10) for ω_n .

We have compared the expansion (A11) with numerical calculations of $U(\frac{1}{2}, (q - 3)/2, \xi + i\eta)$ using sufficiently high order terms in the power series (A1) to assure convergence. The error contours for $\text{Re } U$ and $\text{Im } U$ are shown in Figures 9a and 9b, respectively. It may be seen that $\text{Re } U$ is still given to within $< 10\%$ error, even though ξ and η are $O(10^{-2})$, while despite its oscillating nature, $\text{Im } U$ may still be computed to 10% accuracy even when ξ and η are of the order of unity. The unmodified asymptotic expansion (A4) only holds for ξ and η considerably larger than unity.

Finally, for completeness, we present the general expressions for the weak scattering thin-screen scintillation spectrum due to the electron density irregularity spectrum (2). These expressions are the generalizations of (16) and (17) and contain the effects of outer and inner scales represented by the wave numbers k_o and k_i in (2) in terms of the variables $S_o = (k_o/k_r)^2$ and $S_i = (k_i/k_r)^2$, respectively, where $k_r = (4\pi/\lambda L)^{1/2}$.

$$\begin{aligned}
 dP &= \frac{dL}{V_\perp} L r_o^2 \lambda^2 (\delta N^2) \gamma_o^{1/2} S_o^{-3} \frac{\Gamma(q/2)}{\Gamma[(q-3)/2]} \\
 &\cdot \exp \left[-\left(\frac{\beta}{2S_i} + \frac{\gamma}{S_i}\right) S \right] J(S, S_i; \gamma, q) \quad (A12)
 \end{aligned}$$

$$\begin{aligned}
 J(S, S_i; \gamma, q) &= (\gamma S + S_o)^{(1-q)/2} \left\{ U\left[\frac{1}{2}, \frac{3-q}{2}, \left(\frac{1}{2S_i}\right.\right.\right. \\
 &+ \left.\left.\left.\frac{1}{S_i}\right)(\gamma S + S_o)\right] - \text{Re} \left[e^{-i2\theta} U\left(\frac{1}{2}, \frac{3-q}{2}, \left(\frac{1}{2S_i}\right.\right.\right. \right. \\
 &+ \left.\left.\left.\frac{1}{S_i} + 2i\right)(\gamma S + S_o)\right] \right\} \quad (A13)
 \end{aligned}$$

In order to display explicitly the dependence of dP upon the

electron density variance we have substituted (6b) for $F_d(r)$ in (A12), corresponding to $q > 3$. The case for $q < 3$ is easily obtained from (6a).

Acknowledgments. D.G.M. gratefully acknowledges support from the graduate school of the University of New Hampshire during the summer of 1972 and support from the University of Iowa under National Science Foundation grant DES-73-06559. E.C.R. acknowledges partial support for this work from NASA grants NGR-30-002-097 to the University of New Hampshire and NSG-7055 to the Applied Physics Laboratory of the Johns Hopkins University as well as Air Force Cambridge Research Laboratories, Air Force Systems Command, contract F19628-73-C-0070 (although support by the latter sponsor does not necessarily imply endorsement). This work was initiated while we were guests of D. J. Williams of the Space Environment Laboratory, NOAA/ERL, and we have benefited from extensive discussions with J. T. Nolte (now at American Science and Engineering Inc.) and W. M. Cronyn and S. D. Shawhan of the University of Iowa.

The Editor thanks W. M. Cronyn and D. N. Matheson for their assistance in evaluating this paper.

REFERENCES

- Abramowitz, M., and I. A. Stegun, *Handbook of Mathematical Functions*. U.S. National Bureau of Standards, Washington, D. C., 1964.
- Booker, H. G., J. A. Ratcliffe, and D. H. Shinn, Diffraction from an irregular screen with applications to ionospheric problems, *Phil. Trans. Roy. Soc. London, Ser. A*, 242, 579, 1950.
- Budden, K. G., and B. J. Uscinski, The scintillation of extended radio sources when the receiver has a finite bandwidth, *Proc. Roy. Soc., Ser. A*, 330, 65, 1972.
- Callahan, P. S., Interpretation of columnar content measurements of the solar wind turbulence, *Astrophys. J.*, 187, 185, 1974.
- Cohen, M. H., and W. M. Cronyn, Scintillation and apparent angular diameter, *Astrophys. J.*, 192, 193, 1974.
- Cohen, M. H., E. J. Gundermann, and D. E. Harris, New limits on the diameters of radio sources, *Astrophys. J.*, 150, 767, 1967.
- Coleman, P. J., Jr., Wave-like phenomena in the interplanetary plasma: Mariner 2, *Planet. Space Sci.*, 15, 953, 1967.
- Cronyn, W. M., The analysis of radio scattering and space probe observations of small scale structure in the interplanetary medium, *Astrophys. J.*, 161, 755, 1970a.
- Cronyn, W. M., Radio scattering in the interplanetary medium, Ph.D. dissertation, Univ. of Md., College Park, 1970b.
- Cronyn, W. M., Density fluctuations in the interplanetary plasma: Agreement between space probe and radio scattering observations, *Astrophys. J.*, 171, L101, 1972.
- Cronyn, W. M., and D. G. Mitchell, Interplanetary electron density power spectrum (abstract), *Eos Trans. AGU*, 55, 411, 1974.
- Dennison, P. A., Observations of fine structure in the interplanetary medium, *Planet. Space Sci.*, 17, 189, 1969.
- Feldman, W. C., J. R. Asbridge, S. J. Bame, M. D. Montgomery, and S. P. Gary, Solar wind electrons, *J. Geophys. Res.*, 80, 4181, 1975.
- Hundhausen, A. J., S. J. Bame, J. R. Asbridge, and S. J. Sydorik, Solar wind properties: Vela 3 observations from July 1965 to June 1967, *J. Geophys. Res.*, 75, 4643, 1970.
- Hollweg, J. V., Angular broadening of radio sources by solar wind turbulence, *J. Geophys. Res.*, 75, 3715, 1970.
- Houminer, A., Power spectrum of small-scale irregularities in the solar wind, *Planet. Space Sci.*, 21, 1367, 1973.
- Intriligator, D. S., and J. H. Wolfe, Preliminary power spectra of the interplanetary plasma, *Astrophys. J.*, 162, L187, 1970.
- Jokipii, J. R., On the 'thin-screen' model of interplanetary scintillations, *Astrophys. J.*, 161, 1147, 1970.
- Jokipii, J. R., and J. V. Hollweg, Interplanetary scintillations and the structure of solar wind fluctuations, *Astrophys. J.*, 160, 745, 1970.
- Lovelace, R. V. E., E. E. Salpeter, L. E. Sharp, and D. E. Harris, Analysis of observations of interplanetary scintillations, *Astrophys. J.*, 159, 1047, 1970.
- Matheson, D. N., and L. T. Little, Radio scintillations due to plasma irregularities with a power law spectrum: The interplanetary medium, *Planet. Space Sci.*, 19, 1615, 1971.
- Mitchell, D. G., and E. C. Roelof, Spatial dependence of weak-scattering contribution to interplanetary scintillations (abstract), *Eos Trans. AGU*, 56, 439, 1975.
- Mitchell, D. G., J. T. Nolte, and E. C. Roelof, Asymptotic expansion for interplanetary scintillation spectra including Fresnel filtering (abstract), *Eos Trans. AGU*, 54, 1197, 1973.
- Readhead, A. C. S., Interplanetary scintillation of radio sources at metre wavelengths, 2. Theory, *Mon. Notic. Roy. Astron. Soc.*, 155, 185, 1971.
- Readhead, A. C. S., and A. Hewish, Fine structure in radio sources at 81.5 MHz, 3. The survey, *Mon. Notic. Roy. Astron. Soc.*, 78, 1, 1974.
- Rickett, B. J., Power spectrum of density irregularities in the solar wind plasma, *J. Geophys. Res.*, 78, 1543, 1973.
- Rufenach, C. L., Power law wave number spectrum deduced from ionospheric scintillation observations, *J. Geophys. Res.*, 77, 4761, 1972.
- Salpeter, E. E., Interplanetary scintillations, 1. Theory, *Astrophys. J.*, 147, 433, 1967.
- Tatarskii, V. I., *The Effects of the Turbulent Atmosphere on Wave Propagation*, translated from Russian by Israel Program for Scientific Translations, U.S. Department of Commerce, U.S. National Technical Information Service, Springfield, Va., 1971.
- Unti, T. W. J., and C. T. Russell, On the causes of spectral enhancements in solar wind power spectra, *J. Geophys. Res.*, 81, 469, 1976.
- Unti, T. W. J., M. Neugebauer, and B. E. Goldstein, Direct measurements of solar wind fluctuations between 0.0048 and 133 Hz, *Astrophys. J.*, 180, 591, 1973.
- Woo, R., Multi-frequency techniques for studying interplanetary scintillations, *Astrophys. J.*, 201, 238, 1975.
- Young, A. T., Interpretation of interplanetary scintillations, *Astrophys. J.*, 168, 543, 1971.

(Received June 24, 1974;
accepted May 26, 1976.)

Solar Wind, Energetic Particles, and Coronal Magnetic Structure: The First Year of Solar Cycle 20

J. T. NOLTE

American Science and Engineering, Inc., Cambridge, Massachusetts 02139

E. C. ROELOF

Applied Physics Laboratory, Johns Hopkins University, Laurel, Maryland 20510

Coronal magnetic field structure is investigated by using solar and interplanetary magnetic polarity measurements and by using observations of solar wind plasma and energetic particles during the first 8 months of 1965. When it is compared by using all data available during this period, interplanetary polarity (mapped back to the high corona by using observed solar wind velocities) correlates best with mid-latitude solar polarity. However, when it is compared at only those times when energetic particles were present in the interplanetary medium and again at times of fast solar wind, the best correlation is with equatorial solar polarity. From these results we infer that energetic particles and fast solar wind escape preferentially from equatorial coronal magnetic structures which are open, while the more usual equatorial structures at this time are closed.

1. INTRODUCTION

In the past few years a number of studies have demonstrated that coronal magnetic field structures strongly influenced the propagation of solar wind [Krieger *et al.*, 1973; Roelof, 1974; Neupert and Pizzo, 1974; Nolte, 1974; Nolte *et al.*, 1976, 1977] and low-energy solar charged particles [Roelof and Krimigis, 1973; Gold *et al.*, 1974; Nolte, 1974] close to the sun (within $\sim 20 R_{\odot}$) near solar maximum and during the declining phase of the solar cycle. Here we wish to investigate the relationship between coronal magnetic field structure and solar wind and energetic particle propagation during the period immediately following the minimum of solar cycle 19. It will be most interesting to see if these relationships are found again following the next solar minimum.

During the last solar minimum there were no direct X ray or EUV observations of coronal structure available. We therefore use a statistical examination of magnetic polarities to study the coronal fields. The analysis procedure, described in detail in section 2, utilizes H α neutral lines (which have been shown by McIntosh *et al.* [1976] to be representative of coronal structures) to define the chromospheric and low-coronal polarities. These are then compared with interplanetary polarities mapped back to the sun by using observed solar wind velocities.

The problem of the quantitative statistical determination of the relationship between the polarities of solar and interplanetary magnetic fields has received considerable attention, first in a study by Ness and Wilcox [1964] and also in subsequent papers by Wilcox and a number of co-workers. Such a relationship provides statistical information on the source and propagation of the solar wind [Wilcox, 1968] that may be compared with direct observations [Krieger *et al.*, 1973] and also provides a framework for the discussion of the propagation of low-energy solar protons, since, as Roelof and Krimigis [1973] have shown, these particles follow interplanetary field lines with negligible perpendicular diffusion.

The cross-correlation study which we are presenting consists of three main parts. In section 3 the method of McIntosh and Roelof [1972] is applied to the time period from January to

August 1965 (near solar minimum), and the latitude dependence of the correlation between interplanetary and chromospheric field polarities is determined. In the following two sections, using the same technique on selected subsets of the data, we demonstrate that both energetic solar protons and fast solar wind streams come preferentially from coronal magnetic field configurations different from those primarily responsible for the general latitudinal pattern in the correlation found in section 3. These cross-correlation results may be interpreted in terms of predominantly 'open' and 'closed' equatorial coronal magnetic structures such as were suggested theoretically by Pneuman [1973] and observationally by Altschuler *et al.* [1972], Krieger *et al.* [1973], and Timothy *et al.* [1975].

2. DATA AND ANALYSIS METHOD

The time period covered by this study is January–August 1965. For this time period, synoptic charts of chromospheric polarity, inferred from H α filtergrams, are available [McIntosh and Nolte, 1975] as well as interplanetary field polarity measurements from Mariner 4 [Coleman *et al.*, 1967] and unpublished solar wind velocity data from the same spacecraft, which have been supplied through the courtesy of A. J. Lazarus of Massachusetts Institute of Technology and John Davis of American Science and Engineering, Inc.

The H α synoptic charts used to indicate solar magnetic field polarity have been constructed by using the method described by McIntosh [1972]. Briefly, this technique consists of marking the locations of well-defined structures (filaments and filament channels in the weak field regions and plage corridors, fibril patterns, and arch filaments in and around the strong fields of active regions) observed in H α filtergrams on a synoptic chart. These well-defined locations provide the basis for inferring the chromospheric magnetic field polarity pattern.

We have divided the H α synoptic charts into 10° bins in latitude and in longitude and have assigned a polarity to each bin, positive or negative if one polarity is dominant ($>75\%$ of the area), otherwise mixed. In the correlation analysis, mixed polarities will be considered to be half positive and half negative. We assign an interplanetary polarity (also positive, negative, or mixed) to each 10° in solar longitude by mapping back

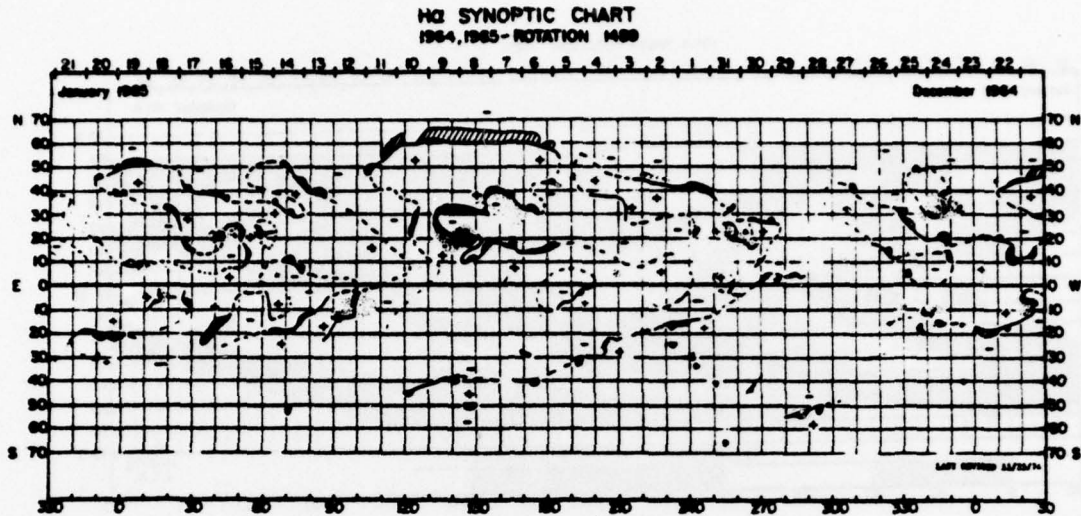


Fig. 1. A sample H α synoptic chart, Carrington rotation 1489. Filaments are indicated by shading, plage corridors and filament channels by solid lines, and other (weak) structures or lines inferred from continuity from previous or subsequent rotations by dashed lines. The date of central meridian passage is indicated at the top, and Carrington longitude at the bottom of the chart. Polarities are inferred from sunspot groups and comparison with the Mount Wilson magnetograph records.

the interplanetary polarity observed at Mariner 4 [Coleman *et al.*, 1967] to the high-coronal connection points of the interplanetary field lines, using solar wind velocity data from Mariner 4 (J. Davis, private communication, 1976).

Following Snyder and Neugebauer [1966], we estimate the emission longitude from the approximation of radial constant velocity plasma flow. Although the actual trajectories involve both the effects of corotation inside the Alfvén radius and acceleration in the interplanetary medium, this 'extrapolated quasi-radial hypervelocity' (EQRH) approximation gives an estimate of the high-coronal solar wind emission longitude good to $\leq 10^\circ$ [Nolte and Roelof, 1973a, b]. We will use the EQRH terminology to emphasize that it is source locations and not trajectories of the plasma flow which we are estimating.

We have done the study twice, once using only those bins from the H α charts whose polarity (positive, negative, or mixed) is defined by nearby H α structures (within 20° of the bin) and a second time using an 'extrapolation' for the chromospheric polarity to regions $\sim 20^\circ$ beyond the nearest H α structure. This extrapolation consists of closing all neutral lines except in polar regions, based wherever possible on the assumption of continuity of magnetic structure from one solar rotation to the next.

A sample H α chart for the first rotation of this study (Carrington rotation 1489) is shown as Figure 1 [from McIntosh and Nolte, 1975]. The corresponding chart with estimated polarities included is the first panel of Figure 2a. On this chart and the other charts showing the estimated polarities in Figures 2a-2c, polarity is indicated by the shading (dark is negative, white positive). The interplanetary polarities mapped back to the high corona by using the EQRH solar wind technique are indicated at the bottom of the shaded maps. The source longitudes of energetic particles and fast solar wind, which are used to select subsets of the data in sections 4 and 5, are also marked on these maps. Vertical lines between the interplanetary polarity strip and the H α chart indicate the connection longitudes of large-scale interplanetary field lines

populated with 0.5-MeV protons at Mariner 4. These energetic particle events are discussed in detail in a companion paper [Nolte and Roelof, 1977]. The source locations of fast solar wind are marked by horizontal lines.

We determine the latitudinal dependence of the relationship between solar and interplanetary magnetic polarities by forming the cross-correlation coefficient between the interplanetary polarity and the H α polarity in each 10° swath in latitude. In constructing the correlation coefficients a mixed polarity in either data set compared with a definite polarity in the other is considered to be a chance occurrence (half agreement, half disagreement), and mixed polarity in both sets is considered to be full agreement, except in the following case. If both mixed polarity assignments are due to a definite change in polarity (in interplanetary polarities a sector boundary, in H α a north-south-oriented neutral line), the polarities are considered to be in full agreement only if both halves of the bin agree and in full disagreement if the polarities in the two halves of the bin disagree. Details of the statistical method are discussed in the appendix. For polarity correlations there is a simple relationship among chi-square, the correlation coefficient ρ , and the number of independent measurements: $\chi^2 = N\rho^2$.

3. COMPREHENSIVE CROSS-CORRELATION STUDY

The results of the study using all data available during this entire period are shown in Figure 3. The general pattern of the latitude dependence of the correlation coefficient ρ is the same in both studies (using the definite or estimated H α polarities). In fact, the correlation coefficients from the two different studies are nearly equal in each latitude swath, demonstrating that the extrapolated closure of neutral lines has not distorted the statistics. There is no point for 50° - 60° S in the definite H α polarity study owing to lack of definite neutral line structure south of 50° latitude.

As is shown by Chapman and Bartels [1940], once the cross correlation has been calculated, the statistical significance may be determined by estimating the number of independent measurements from an 'appropriate' length (or time) scale. Gold

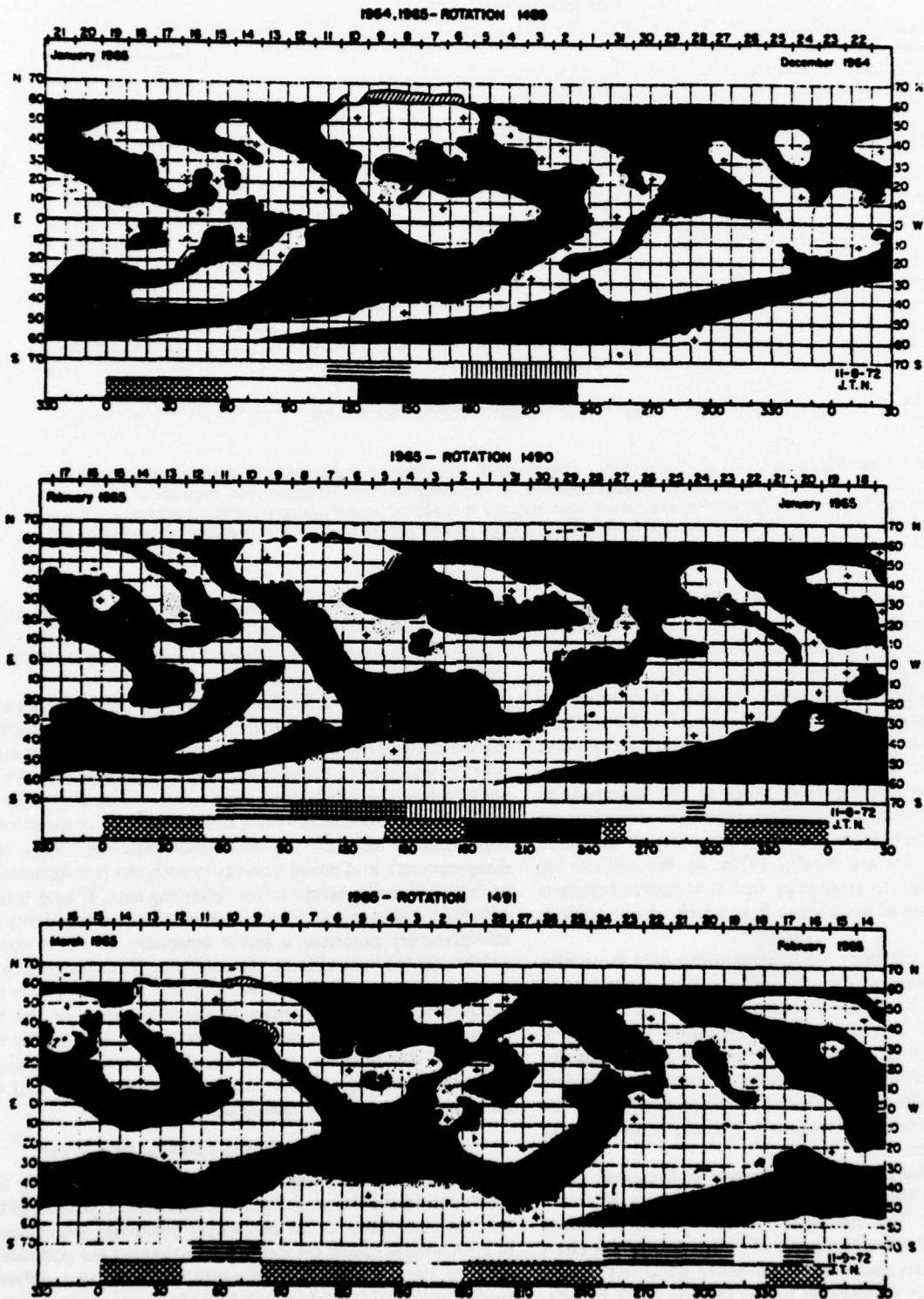


Fig. 2a. The $H\alpha$ synoptic charts for rotations 1489-1491 with all neutral lines at latitudes below 60° closed. White areas are positive (out of the sun) polarity, dark negative. The interplanetary polarity, mapped back to the high-coronal connection longitude, is indicated at the bottom: again white is positive, dark negative; the crosshatching represents mixed interplanetary polarity. Above the interplanetary polarity stripe, sources of fast solar wind (velocity greater than 400 km/s) are indicated by horizontal lines, and sources of enhanced 0.5-MeV proton flux by vertical lines.

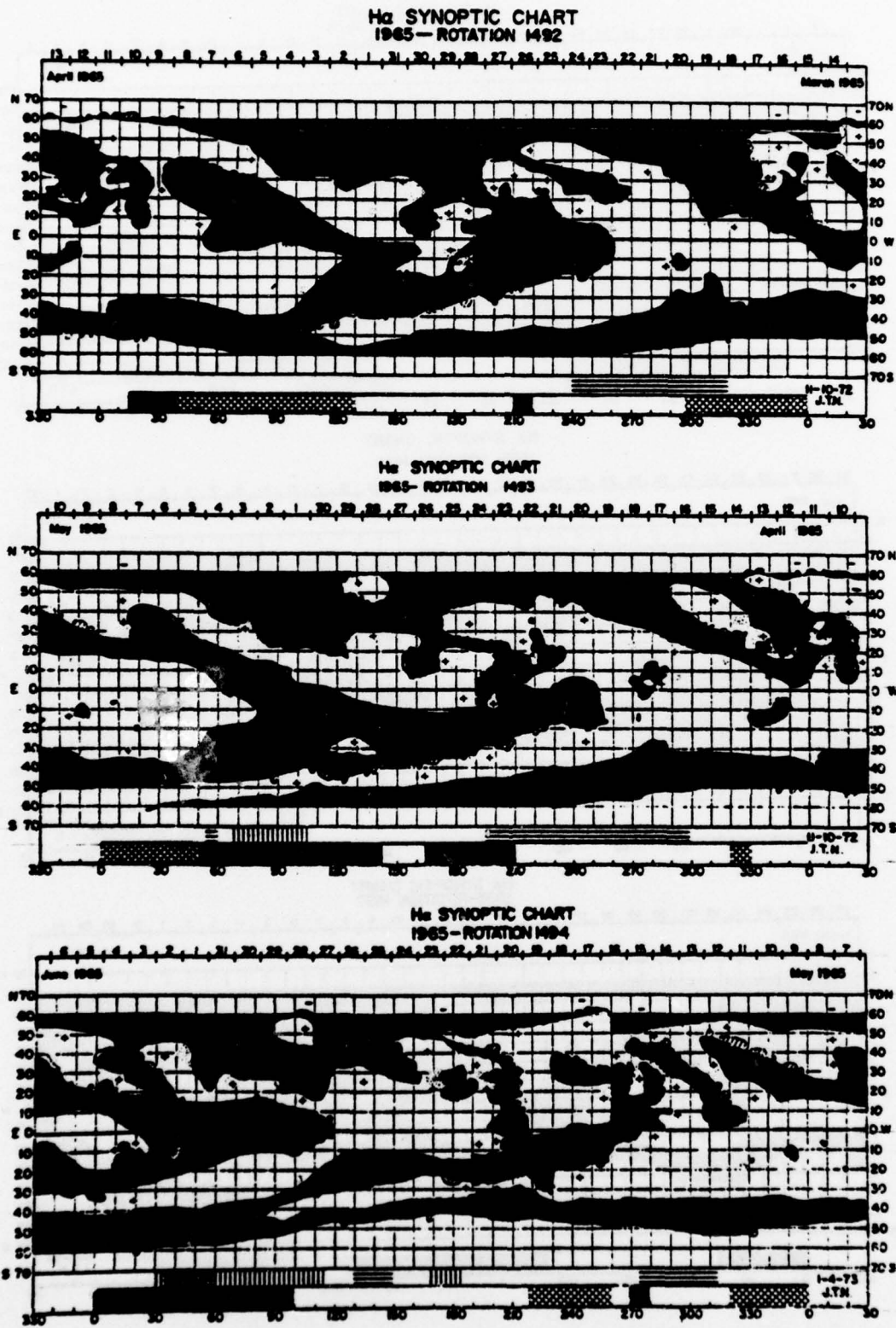


Fig. 2b. Same as Figure 2a but for rotations 1492-1494.

NOLTE AND ROELOF: SOLAR WIND, PARTICLES, AND CORONAL STRUCTURE

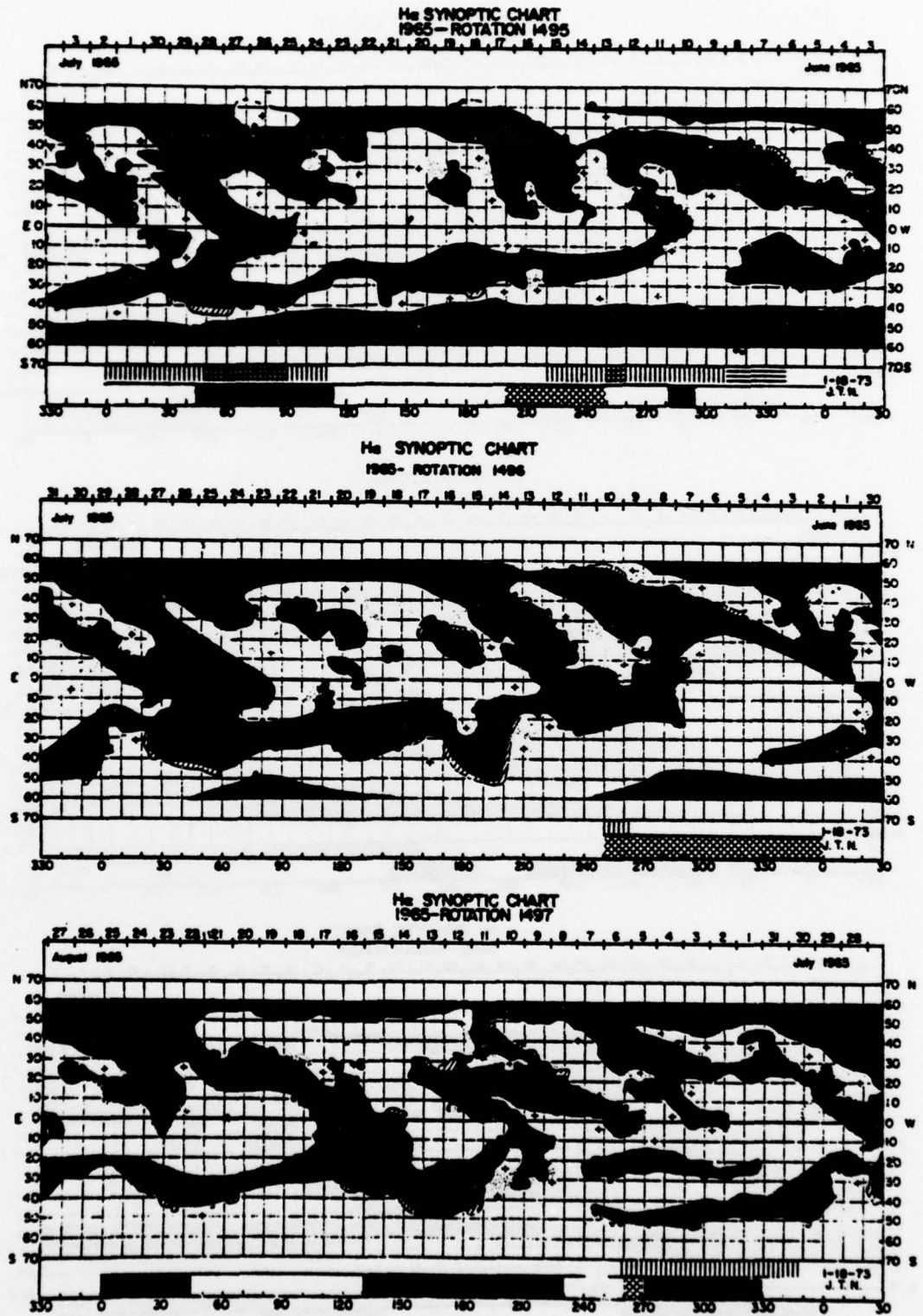


Fig. 2c. Same as Figure 2a but for rotations 1495-1497.

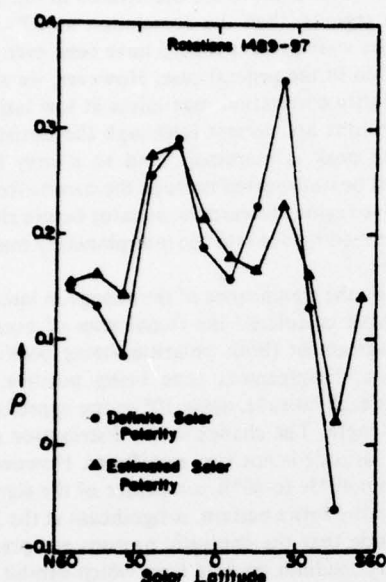


Fig. 3. The cross-correlation coefficient as a function of latitude for nine solar rotations in 1965. The correlation coefficients at each latitude are quite similar for the two studies (definite and estimated solar polarities). Therefore either method may be used to determine the pattern of the latitude dependence of the correlation, since the estimated closure of neutral lines has not distorted the statistics.

and Roelof [1976] have shown that the autocorrelation length is an appropriate length to use. This is somewhat less than 30° for the $H\alpha$ polarities at latitudes of 10° – 30° N, so that the cross correlation at these latitudes is significant at the 1% level; 287 10° bins of $H\alpha$ estimated polarity were used, of which we took one third to be independent measurements.

Schatten *et al.* [1969], using data from nine solar rotations from June 1965 through February 1966, were able to obtain a significant cross correlation of mid-latitude solar fields calculated at a 'source surface' $0.5 R_s$ above the photosphere with the interplanetary field observed near the earth. Their results indicate that the pattern found in this study (the best correlation of interplanetary polarity with solar polarity at latitudes removed from the equator) persisted throughout 1965.

A similar tendency for correlation of interplanetary with both northern and southern mid-latitude solar fields was deduced by Wilcox and Ness [1967] from a different line of reasoning. They compared the autocorrelation of latitude swaths of photospheric polarity for three different rotations (during Carrington rotations 1474–1477) but also near solar minimum. The patterns in the solar field autocorrelation at 10° , 15° , and 20° N and 20° S are similar to the interplanetary pattern; i.e., they also find a good agreement between interplanetary and solar field autocorrelation at northern solar latitudes and a weaker agreement between interplanetary and southern solar autocorrelations. This tendency for mid-latitude correlation in two additional studies using different techniques for different time periods suggests that the correlation is physically significant. It is of particular interest to consider why the southern cross-correlation peak is observed, since solar activity was very weak in the southern hemisphere near solar minimum. One interpretation consistent with both this possible southern influence on the interplanetary polarity and the relative absence of strong field solar active regions in the southern hemisphere at this time is that the large-scale mid-

latitude chromospheric fields (both northern and southern) influence the equatorial interplanetary polarity rather than the small-scale strong fields in mid-latitude solar active regions.

To test this interpretation, we have examined the cross correlation between interplanetary polarity mapped back to the corona and the polarities of solar active regions (as indicated by the occurrence of $H\alpha$ plages) at latitudes between 10° and 30° N. The correlation coefficient of 0.19 is smaller than the coefficients for both 10° – 20° N ($\rho = 0.30$) and 20° – 30° N ($\rho = 0.26$). Since the $H\alpha$ plage regions also occupy less than one fourth of the longitudes at these latitudes, it is clear that the correlation previously found between mid-latitude solar polarity and interplanetary polarity is not due primarily to any agreement between active region and interplanetary polarity (at the same longitude). This result also quantitatively supports the interpretation of Scherrer *et al.* [1972] that their best correlation (by using a solar area about one fourth of the disk) is due to large-scale regions rather than to strong field regions.

4. POLARITY CROSS CORRELATION DURING TIMES OF ENHANCED ENERGETIC PARTICLE FLUX

The next part of this study is motivated by the realization that low-energy (~ 0.5 MeV) solar protons are often not observable in the data from Mariner 4 for this same time period [Krimigis, 1969], even though these particles are often associated with centers of activity rather than with specific solar flares [Fex *et al.*, 1968; Krimigis, 1969; Krimigis *et al.*, 1971; McDonald and Daxai, 1971; Pick, 1972; Roelof and Krimigis, 1973]. The joint 27-day recurrence of particle streams and their associated active regions does not imply that the particles observed are injected onto interplanetary field lines directly above the active regions. On the contrary, it appears that there is considerable coronal transport of energetic particles [e.g., Reinhard and Roelof, 1973; Reinhard and Wibberenz, 1974]. For instance, Fan *et al.* [1968] found that particle fluxes above detector threshold from a single solar active region could be observed near 1 AU over a spread of $\sim 180^\circ$ in heliocentric longitude.

Recently, more detailed evidence of injection of low-energy solar particles into the interplanetary medium at locations far removed from the active region accelerating source has been presented by Gold *et al.* [1973] and Inman *et al.* [1973], who find at two different times in 1967 that the energetic particles observed during an entire solar rotation were predominantly produced by a single active region and transported in the solar corona to the foot of the interplanetary field lines leading to the earth. Since these particles can be transported for large distances (at times completely around from the backside of the sun) and there have almost always been active regions visible on the sun, even in 1965 (near solar minimum), 0.5-MeV protons might have been expected to be almost continually present in the interplanetary field. Therefore the absence of particles during much of this time period could indicate that they escape the corona preferentially from certain equatorial magnetic field configurations.

As a first indication that this is true, we note that during the general study, 60% of the measured interplanetary polarities were positive, while during the particle events, 65% of the interplanetary polarities were negative. Although the statistical significance of this result is somewhat uncertain, owing to the tendency for recurrence of the particle increases, this observation suggests that the 0.5-MeV protons had a strong

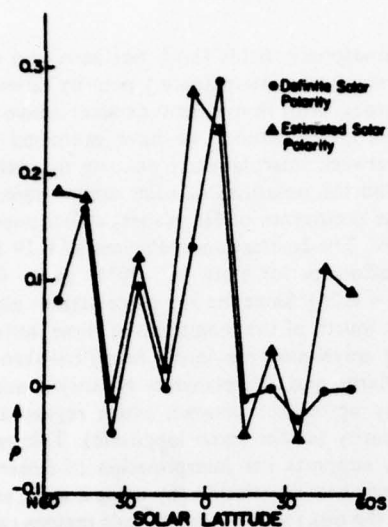


Fig. 4. Same as Figure 3 but restricted to times during the same nine solar rotations when fluxes of 0.5-MeV solar protons at Mariner 4 exceeded $0.5 \text{ (cm}^2 \text{ s sr)}^{-1}$. The correlation as a function of latitude now peaks strongly near the solar equator.

tendency to escape from a coronal field configuration different from the usual configuration in 1965.

These particles must escape into the interplanetary medium on field lines which are open or directly connected from interplanetary space to the chromosphere and photosphere. Therefore if the correlation between mid-latitude solar and interplanetary polarities which we found in the previous section is interpreted as an indication of direct connection of fields and if the particles are accelerated in the mid-latitude active regions (as is usually assumed), then at those times when particles were observed we expect an even better correlation than in the general case.

It is therefore reasonable to ask whether the polarity correlation differs in any significant way at times when low-energy solar protons are observed from times when they are absent. To answer this question, we have repeated the polarity correlation study, restricting it to times when 0.5-MeV solar protons were present in the interplanetary medium at flux levels of $0.5 \text{ (cm}^2 \text{ s sr)}^{-1}$. These times totaled only one sixth of the entire period (54 $10^\circ \text{ H}\alpha$ bins or about 18 independent points).

The results of this study are shown in Figure 4. The change in the latitude dependence from the study using all the data from the same period is quite striking. The correlation now peaks strongly near the equator. The maximum correlation is not very significant, owing to the reduced number of data points; however, the equatorial correlation coefficient has increased from 0.18 to 0.28 ($\chi^2 = 1.4$ for 18 independent points) and is now comparable to the maximum correlation coefficient (at $10^\circ\text{--}20^\circ\text{N}$) found in the study of this entire period.

More important than the absolute significance of the equatorial correlation found when particles were present is the change in the latitude dependence from the study of the entire time period. Not only has the equatorial correlation coefficient increased but the correlation at $10^\circ\text{--}20^\circ\text{N}$ and $20^\circ\text{--}30^\circ\text{S}$ (the maxima of the previous study) has almost completely disappeared. This result reinforces the inference drawn at the end of section 3 that there is no direct connection of field lines from the mid-latitude active regions to the equatorial interplanetary field (at the same longitude).

If 0.5-MeV solar protons are accelerated in the mid-latitude solar active regions, then the correlation at $10^\circ\text{--}30^\circ\text{N}$ when these particles were present should have been even better than the correlation in the general case. However, we actually find that the polarity correlation maximizes at low latitudes when energetic protons are present (although the statistical significance of the peak is marginal), and so it may be that the protons must be transported through the corona from the mid-latitude active regions toward the equator before they encounter field lines leading out into the interplanetary medium in the ecliptic plane.

To quantify the significance of the change in latitude dependence, we have calculated the frequencies of occurrence expected for agreement (both polarities being positive or both negative) and disagreement (one being positive, the other negative) for each latitude, using 30° as the approximate auto-correlation length. The change in the distribution of frequencies at each latitude is not very significant. However, the sum of the χ^2 from 40°N to 40°S , a measure of the significance of the change in the entire pattern, is significant at the 2% level.

We conclude that the energetic protons are present in the interplanetary medium on field lines which exhibit a different pattern of correlation with the chromospheric-low-coronal magnetic polarities. Since the chromospheric neutral lines which were used to define the solar polarities are indicators of coronal magnetic structure [McIntosh *et al.*, 1976], this difference implies that the protons escape preferentially from a different kind of magnetic structure, or at least from a different arrangement, than that which produces the good correlation at mid-latitudes in the general study of section 3.

One further aspect of both the study for the entire period and the study restricted to times when particles were observed is worth noting. In both studies there is an enhanced correlation between high-latitude fields, primarily $40^\circ\text{--}60^\circ\text{N}$, and the interplanetary polarity. Since the polarity regions at these latitudes usually extend uninterrupted for many tens of degrees in longitude, these high-latitude field regions represent in a sense the large-scale solar field. The observed correlation therefore is not necessarily interpreted as indicative of the direct influence of these high-latitude fields on the polarity of the interplanetary field in the ecliptic on the scale of $\sim 10^\circ$ appropriate for this study; rather, this correlation is another indication of the general correlation between very large scale solar fields and the interplanetary polarity such as is found by

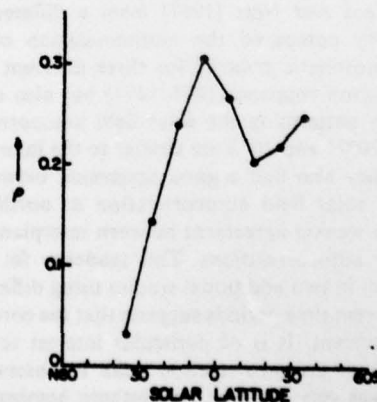


Fig. 5. Same as Figure 3 but restricted to times when solar wind velocity exceeded 400 km/s. As in Figure 4, the correlation peaks strongly near the equator.

Scherrer *et al.* [1972] (averaging over about one fourth of the solar disk) and by Severny *et al.* [1970] using daily solar average field measurements.

5. POLARITY CROSS CORRELATION DURING TIMES OF ENHANCED SOLAR WIND VELOCITY

In several recent studies it has been shown that high-speed solar wind streams are related to coronal magnetic structure (see the references cited in the introduction). We have therefore used the same cross-correlation analysis as in the preceding sections during the same time period in 1955 but restricted to only those times when the solar wind velocity observed at Mariner 4 was greater than 400 km s⁻¹. We note that Nolte *et al.* [1976] used 500 km s⁻¹ to divide solar wind observations into fast and slow categories. However, in 1965, velocities observed by Mariner 4 rarely exceeded 500 km s⁻¹, and no streams having velocity of 600 km s⁻¹, such as were quite common in 1973, were seen. Times when velocity was greater than 400 km s⁻¹ comprise about one fifth of the data. The latitude dependence of ρ for this study is shown in Figure 5. We have carried this study only to 40° latitude north and south because the higher latitudes seem to reflect the large-scale field correlations (see section 4).

The latitudinal pattern found here peaks near the solar equator, as is expected if high-speed solar wind streams are associated with open (radial) coronal magnetic field configurations. The maximum correlation coefficient (0.29) is comparable to the maximum coefficients found in the first two parts of this study.

A comparison of expected and observed frequencies for this study using the same method as was used in section 4 yields a similar result. The changes in the frequencies at each latitude are again not very significant, but the sum of these χ^2 , an indicator of the change in pattern, is significant at the 5% level.

The interplanetary polarity during the fast solar wind streams was positive in 79% of the longitude bins. This dominance of positive polarity may not be significant, however, since the data are dominated by the recurrence of a single fast solar wind stream which originated near Carrington longitude 300° for six solar rotations (1490–1495). Over half of the longitude bins having solar wind faster than 400 km/s were from this one recurrent stream.

However, this dominance of the data by one recurrent series, which makes the quantitative interpretation of statistical inferences somewhat uncertain, does emphasize the principal result of this section: fast solar wind does tend to come from a coronal magnetic field configuration different from the 'average' configuration in 1965.

Before we proceed with the interpretation of this result, it is necessary to discuss a significant distortion of the time sequence of interplanetary data resulting from the application of the EQRH approximation to solar wind streams. Since in 1965 these streams represent only a small fraction (less than one fifth) of the entire period, it is not necessary to correct for this distortion in either of the previous two sections (see below for a further discussion of particle events during solar wind streams).

This distortion is simply the rapid shift in calculated connection longitude during the rising portion of the solar wind velocity time history and the slower than usual change during the decrease in velocity. During the rise the calculated connection longitude often shifts by more than 10° in the 3 hours over which both magnetic field and solar wind velocity are

averaged, although the accuracy of the connection longitudes calculated during rising velocities is less certain than that during stream peaks or decays, since the rise consists of compressed (and accelerated) plasma from the stream-stream interaction. However, during the decrease, which actually defines the eastern boundary of the stream source in the corona [Nolte *et al.*, 1977], the connection point may move as little as 10° in several days (though this usually includes a decrease to velocities below 400 km/s). The interplanetary polarity pattern is also much more likely to be distorted locally in the stream-stream interaction during the rise in velocity than in the rarefaction during the decrease [e.g., Nolte and Roelof, 1973b]. Thus the net effect of the application of the EQRH approximation to solar wind streams in the polarity cross correlation is to emphasize the most uncertain interplanetary polarity measurements (during the velocity increase) while deemphasizing the measurements at just those times when the EQRH approximation source locations are expected to be best, i.e., in the rarefaction following the peak of the high-speed stream [Nolte and Roelof, 1973b].

To compensate for this distortion, we have repeated the study of this section (restricted to times of fast solar wind), now weighting each longitude bin by the length of time that the EQRH approximation connection longitude of the interplanetary field at Mariner 4 remained in that bin. The results of this weighted study are shown in Figure 6.

The pattern now peaks much more strongly near the solar equator, at a level of significance comparable to the maximum significance in the comprehensive study: $\chi^2 = 7.8$; $Q(\chi^2) = 0.005$. The maximum correlation coefficient ($\rho = 0.53$) is much larger than any in the previous studies reported here. This striking improvement in the equatorial correlation due to the weighting described above provides strong evidence that the

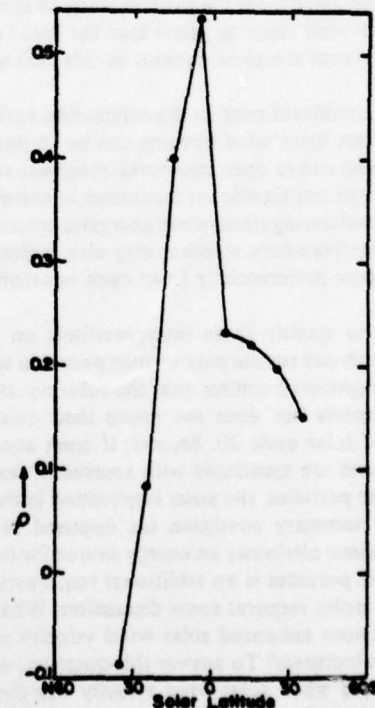


Fig. 6. Cross-correlation coefficient versus solar latitude for times of fast solar wind but with each longitude bin being weighted for the length of time the connection longitude remained in that bin.

interpretation of the unweighted study is correct; fast solar wind exhibited a very strong tendency to come from a different kind of coronal magnetic field structure from the usual configuration during the first 8 months of 1965. As was the case for the energetic protons, this observational result immediately implies that the coronal magnetic field exerted a strong effect on the solar wind.

This result is easily interpreted in terms of open and closed magnetic field configurations near the solar equator such as are suggested by *Pneuman* [1973], who also argues that solar wind should escape preferentially from open coronal magnetic field configurations. This argument is substantiated by the work of *Noci* [1973]. He considered the energy budget in coronal 'holes' and concluded that these magnetically open structures should be sources of strong solar wind. *Krieger et al.* [1973] provide observational support for this idea, finding that the source of a recurrent high-speed solar wind stream is indeed the equatorial regions of a coronal hole observed in an X ray image of the sun. The X ray photograph (taken on November 24, 1970) exhibited a sickle-shaped nonmeridional hole extending from 30°N to the south polar hole. Yet the estimated source of the peak stream velocity fell at the minimum of the densitometer trace 4' wide taken at the equator. Further evidence for a direct physical connection between coronal holes and high-speed solar wind is presented by *Nolte et al.* [1976], who found the best correlation ($\rho = 0.96$) at latitudes less than 10° between coronal hole area and the maximum velocity observed near 1 AU in the associated solar wind stream.

We therefore interpret the good correlation at low latitudes during times of high-speed solar wind as an indication that fast solar wind tends to come from open structures which extend nearly radially from equatorial regions of the chromosphere out through the corona to the interplanetary medium in the ecliptic plane. The significant change in the pattern of the latitude dependence from the general study to the time-weighted fast solar wind study suggests that the usual coronal field configuration near the solar equator at this time was different, i.e., closed.

Since the significant peak in the correlation near the equator at times of fast solar wind streams can be so naturally interpreted as being due to open equatorial magnetic structures, we suggest that the less significant maximum in correlation at low latitudes found during times when energetic protons were present in the interplanetary medium may also indicate that these particles escape preferentially from open equatorial magnetic structures.

We wish to qualify these interpretations on two counts. First, although our results may be interpreted in terms of open or closed magnetic structures near the solar equator, this consistency supports but does not prove their existence at the beginning of solar cycle 20. Second, if open equatorial magnetic structures are associated with sources of fast solar wind and energetic particles, the strict implication is that open field lines are a necessary condition (as opposed to a sufficient condition), since obviously an energy source for the solar wind and energetic particles is an additional requirement.

One final point requires some discussion: What is the relationship between enhanced solar wind velocity and 0.5-MeV solar proton increases? To answer this question, we have studied those times when solar wind velocity was over 400 km/s and 0.5-MeV protons were observed at Mariner 4. This data set consists of only eleven 10° bins in longitude and is therefore inadequate to produce a statistically significant cross cor-

relation. However, it is worth noting that the occurrence of both enhanced solar wind and energetic protons in these 11 longitude bins could have been due to chance; since 54 out of 287 bins 'contained' particles and 59 out of 287 had enhanced solar wind, a chance relationship between solar wind and particles would result in 11 bins with both. Furthermore, the solar protons are present in interplanetary field regions which have dominant negative polarity, while the dominant polarity in the fast solar wind streams is positive. It therefore seems likely that fast solar wind and energetic solar protons escape preferentially from different coronal regions. This topic is discussed further in the next section.

We note that the situation in 1965 was substantially different from what it was at the end of 1963 as reported by *Wilcox and Ness* [1965]. At that time both recurrent energetic particle streams and solar wind streams appeared to be closely tied to the magnetic sectors, as was indeed the case again in 1973-1974 during the decline of the latest solar cycle [*Gold et al.*, 1975].

6. MERIDIONAL CORONAL STRUCTURE

We have suggested above that the change in the latitudinal dependence of the cross correlation of interplanetary with chromospheric polarity when the study is restricted to times when energetic particles and/or fast solar wind was observed is an indication of a different coronal magnetic field structure. We now wish to examine this hypothesis further.

The different coronal field structures will be identified here by their statistical 'meridional polarity signatures' in the chromosphere. This polarity signature is defined by three chromospheric polarities, northern (10°-20°N), equatorial (0°-10°S), and southern (20°-30°S), for each longitude bin. For instance, the longitude bin 70°-80° of rotation 1489 in Figure 1 would have the signature (+, -, +). We use this signature to investigate the relationship of different coronal configurations to the interplanetary medium. We note that coronal holes associated with high-speed solar wind streams are often meridional structures near the equator, i.e., have considerable extent in latitude [*Krieger et al.*, 1973; *Nolte et al.*, 1976].

The data from each of the four studies (comprehensive and times of enhanced particle flux, fast solar wind, and fast solar wind with each longitude bin weighted by the time the connection point remained there) have been divided again into three subsets, based on the agreement, half agreement (one polarity mixed), or disagreement of the interplanetary and equatorial polarities. Then for each of these 12 subsets and also for the four totals the frequencies of occurrence of the four independent chromospheric polarity signatures have been determined, i.e., (+, -, -) is considered to be equivalent to (-, +, +), since we are primarily concerned with the topology of the field lines. Then, using the hypothesis that the total from the comprehensive study is the set from which all subsets are randomly drawn, we have also calculated an expected frequency for each case. Since the longitude bins in these subsets are seldom adjacent, we consider each bin to be an independent measurement. These expected and observed frequencies are shown in Figure 7 for the only two signatures where the values of χ^2 are large enough for statistical significance: for both cases, $Q(\chi^2) < 0.003$. The polarity structures in these two cases are also shown schematically in Figure 7. The four arrow diagrams can be interpreted as follows.

In the first case (from the comprehensive study), if the interplanetary and equatorial polarities disagree, it is significantly more likely than chance that both northern and south-

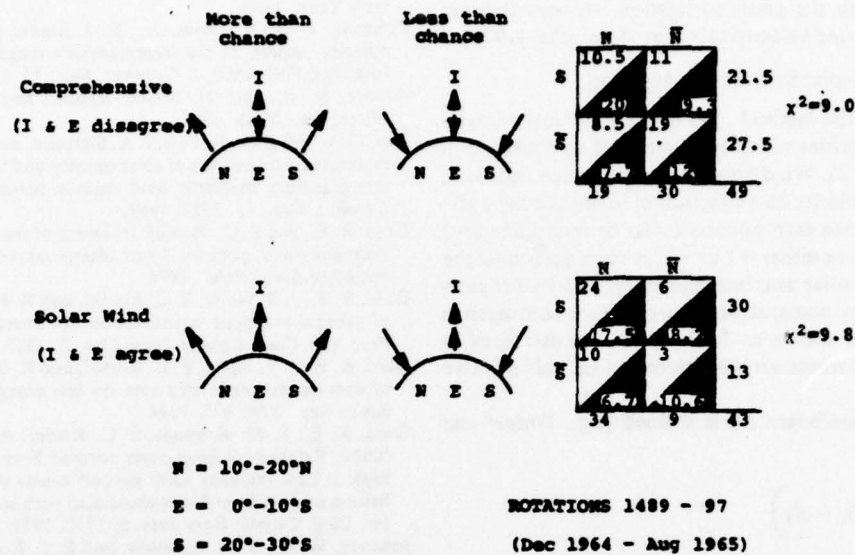


Fig. 7. Comparison of chromospheric polarity signatures with interplanetary polarity for those structures which show significantly different statistical properties from normal. The top diagrams illustrate that if the interplanetary polarity disagrees with the equatorial polarity, it is more likely than usual that both northern and southern polarities agree with the interplanetary field. The bottom diagrams demonstrate that when the interplanetary and equatorial polarities agree in a fast solar wind stream, it is more likely that the source is a large unipolar region (stretching from northern to southern mid-latitudes) than a small polarity cell.

ern polarities disagree with the equatorial polarity (and agree with the interplanetary polarity). On the other hand, it is less likely than chance that all three solar polarities agree with each other but disagree with the interplanetary polarity. Both of these situations seem reasonable. At those times when the interplanetary field is not connected directly to the chromospheric fields near the equator it must still connect somewhere nearby (within a few tens of degrees).

The other case is also quite reasonable. If there is fast solar wind and if the interplanetary and equatorial polarities agree, it is more probable than usual that all three solar polarities agree and less probable that both northern and southern polarities disagree with the equatorial polarity. That is, fast solar wind propagating directly out from an equatorial solar region is more likely to come from a large, presumably open, unipolar field region than from a small polarity cell. This result is in agreement with the correlation between coronal hole area and solar wind velocity found by Nolte *et al.* [1976]. However, we have no way of directly establishing whether the open structures inferred in this paper are coronal holes or not.

The lack of direct observations of the corona during the last solar minimum does leave several important questions unanswered. What happens to the large holes seen just prior to solar minimum? Are the holes after minimum different or do the solar boundary conditions (and with them the area versus velocity correlation) change? Finally, are the recurrent energetic particle and solar wind streams during the year immediately after solar minimum related to coronal holes or to some other kind of coronal structure?

7. SUMMARY AND CONCLUSIONS

We have investigated coronal magnetic structure as indicated by chromospheric magnetic polarities and interplanetary polarities mapped back to the high corona using observed solar wind velocities during nine solar rotations in 1965 (just after solar minimum). We found in the general case

that the interplanetary polarity correlated best with mid-latitude solar polarity. This correlation was due more to large-scale magnetic fields than to the strong fields in the mid-latitude solar active regions.

We have also performed the same correlation analysis for the same time period but restricted it to only those times when energetic particles were present in the interplanetary medium, and again to only times of enhanced solar wind velocity. Both of these conditions are indications of open coronal magnetic field structures. We found that both energetic particles and fast solar wind exhibited a strong tendency to come from a different magnetic structure than that which was normal at this time, as evidenced by its polarity signature. In both cases the correlation was best between interplanetary and equatorial solar polarities.

These results, together with a more detailed examination of the meridional polarity signature, can be interpreted in terms of equatorial coronal magnetic structures being open or closed. That is, the usual equatorial structure during this period tended to be closed. Energetic particles observed in the ecliptic plane escaped preferentially from equatorial fields which were more open, but particles were not present in all open equatorial structures. Finally, fast solar wind in the ecliptic plane originated from open equatorial structures larger in meridional extent ($30^{\circ}N$ to $30^{\circ}S$) than were required for preferential escape of energetic particles. This association of

TABLE 1. Two-by-Two Contingency Table for Polarity

		Interplanetary Polarity		
		+	-	
Solar Polarity	+	n_{++}	n_{+-}	S_+
	-	n_{-+}	n_{--}	S_-
		I_+	I_-	N

large open equatorial structures with fast solar wind appears to be consistent with the good correlation between coronal hole area and solar wind velocity found by Nolte *et al.* [1976].

APPENDIX: STATISTICAL METHOD

We describe here the method used in the statistical analysis of the magnetic polarities which were assigned as discussed in the text (see section 2). We divide the H α polarities into sets, each consisting of polarity as a function of longitude for a 10° swath in latitude. Since each polarity (solar or interplanetary) can be considered to be either +1 or -1, we can determine the correlation between solar and interplanetary polarity for each 10° latitude swath by constructing a two-by-two contingency table. An example is shown as Table 1. As was discussed in section 2, mixed polarities are considered to be half positive and half negative.

The correlation coefficient ρ_{IS} is defined [e.g., Draper and Smith, 1966] by

$$\rho_{IS} = \left(\sum_{i=1}^N (I_i - \bar{I})(S_i - \bar{S}) \right) \left[\left(\sum_{i=1}^N (I_i - \bar{I})^2 \right)^{1/2} \left(\sum_{i=1}^N (S_i - \bar{S})^2 \right)^{1/2} \right]^{-1} \quad (A1)$$

where $\bar{I} = (I_+ - I_-)/N$ and $\bar{S} = (S_+ - S_-)/N$ are the means. Noting that $I_+ = n_{++} + n_{+-}$, $N = I_+ + I_-$, and similar relations from Table 1, straightforward algebra shows that

$$\rho_{IS} = \frac{n_{++}n_{--} - n_{+-}n_{-+}}{(I_+I_-S_+S_-)^{1/2}} \quad (A2)$$

From the contingency table we can also estimate the statistical significance. Beginning with the definition of χ^2 ,

$$\chi^2 = \sum_{i,j=1}^2 \frac{(O_{ij} - E_{ij})^2}{E_{ij}} \quad (A3)$$

and determining E_{ij} from

$$E_{ij} = (I_i S_j / N) \quad (A4)$$

it is again a relatively simple algebraic manipulation to show that $\chi^2 = N\rho^2$. This χ^2 has 1 degree of freedom, since the margins (I_+ , S_+) provide three independent constraints on the four frequencies in the table. Here N must be the number of independent data points [Chapman and Bartels, 1940], which can be estimated from the characteristic scale of the autocorrelation function [Gold and Roelof, 1976]. The statistical significance of the correlation can then be found from tabulated values of the probability integral of the χ^2 distribution [e.g., Pearson and Hartley, 1970].

Acknowledgments. This paper is based on the Ph.D. dissertation of one of us (J.T.N.). This work was supported by Department of Commerce contract NOAA03-3-022-41 and by NASA contract NGR-30-002-097. This work was finished with support at American Science and Engineering, Inc., from NASA under contract NAS8-27758 and at the Johns Hopkins University Applied Physics Laboratory from the Air Force Geophysics Laboratory under task ZF10 of contract N00017-72-C-4401, Department of the Navy.

The Editor thanks W. M. Neupert and K. Schatten for their assistance in evaluating this paper.

REFERENCES

Altschuler, M. D., D. E. Trotter, and F. Q. Orall, Coronal holes, *Solar Phys.*, 26, 354, 1972.

Chapman, S., and J. Bartels, *Geomagnetism*, Oxford University Press, New York, 1940.

Coleman, P. J., L. Davis, Jr., E. J. Smith, and D. E. Jones, The polarity pattern of the interplanetary magnetic field during solar rotations 1798-1808, *J. Geophys. Res.*, 72, 1637, 1967.

Draper, N. R., and H. Smith, *Applied Regression Analysis*, John Wiley, New York, 1966.

Fan, C. Y., M. Pick, R. Pyle, J. A. Simpson, and D. R. Smith, Protons associated with centers of solar activity and their propagation in the interplanetary magnetic field regions corotating with the sun, *J. Geophys. Res.*, 73, 1555, 1968.

Gold, R. E., and E. C. Roelof, Inference of the equatorial high coronal magnetic field polarity from interplanetary measurements, submitted to *Solar Phys.*, 1976.

Gold, R. E., J. T. Nolte, E. C. Roelof, and R. Reinhard, The influence of coronal magnetic structures on low energy solar proton events, *Proc. Int. Conf. Cosmic Rays 13th*, 2, 1367, 1973.

Gold, R. E., J. T. Nolte, E. C. Roelof, and R. Reinhard, The influence of coronal magnetic structure on low-energy solar proton events, *Space Res.*, XIV, 477, 1974.

Gold, R. E., S. M. Krimigis, E. C. Roelof, A. S. Krieger, and J. T. Nolte, Relation of large-scale coronal X-ray structure and cosmic rays, 3. Low-intensity solar particle events with enhanced ~3 MeV helium and medium fluxes associated with solar wind streams, *Proc. Int. Conf. Cosmic Rays 14th*, 5, 1710, 1975.

Innanen, W. G., S. M. Krimigis, and E. C. Roelof, Coronal injection profile of low energy protons during solar rotation 1517 (abstract), *Eos Trans. AGU*, 54, 1165, 1973.

Krieger, A. S., A. F. Timothy, and E. C. Roelof, A coronal hole and its identification as the source of a high-velocity solar wind stream, *Solar Phys.*, 29, 505, 1973.

Krimigis, S. M., Observation of low energy solar protons with Mariners 4 and 5, Trudy mezunarodnogo seminara, in *Proceedings of the Ioffe Physico-Technical Institute*, edited by G. E. Kocharov, pp. 43-86, Academy of Sciences of the U.S.S.R., Leningrad, 1969.

Krimigis, S. M., E. C. Roelof, T. P. Armstrong, and J. A. Van Allen, Low-energy (≥ 0.3 MeV) solar particle observations at widely separated points (>0.1 AU) during 1967, *J. Geophys. Res.*, 76, 5921, 1971.

McDonald, F. B., and U. D. Desai, Recurrent solar cosmic ray events and solar M regions, *J. Geophys. Res.*, 76, 808, 1971.

McIntosh, P. S., Solar magnetic fields derived from hydrogen alpha filtergrams, *Rev. Geophys. Space Phys.*, 10, 837, 1972.

McIntosh, P. S., and J. T. Nolte, H-alpha synoptic charts of solar activity during the first year of solar cycle 20, *Upper Atmos. Geophys. Rep.* 41, NOAA World Data Center A for Solar-Terr. Phys., Boulder, Colo., 1975.

McIntosh, P. S., and E. C. Roelof, H α structure: An improved correlation between the solar and interplanetary magnetic fields (abstract), *Eos Trans. AGU*, 53, 1113, 1972.

McIntosh, P. S., A. S. Krieger, J. T. Nolte, and G. S. Vaiana, Association of X-ray arches with chromospheric neutral lines, *Solar Phys.*, 49, 57, 1976.

Ness, N. F., and J. M. Wilcox, Solar origin of the interplanetary magnetic field, *Phys. Rev. Lett.*, 13, 461, 1964.

Neupert, W. M., and V. Pizzo, Solar coronal holes as sources of recurrent geomagnetic disturbances, *J. Geophys. Res.*, 79, 3701, 1974.

Noci, G., Energy budget in coronal holes, *Solar Phys.*, 28, 403, 1973.

Nolte, J. T., Inter-relationship of energetic particles, plasma and magnetic fields in the inner heliosphere, Ph.D. dissertation, Univ. of N. H., Durham, 1974.

Nolte, J. T., and E. C. Roelof, Large-scale structure of the interplanetary medium, 1, High coronal source longitude of the quiet-time solar wind, *Solar Phys.*, 33, 241, 1973a.

Nolte, J. T., and E. C. Roelof, Large-scale structure of the interplanetary medium, 2, Evolving magnetic configurations deduced from multi-spacecraft observations, *Solar Phys.*, 33, 483, 1973b.

Nolte, J. T., and E. C. Roelof, Coronal magnetic structure and energetic solar particle events during the first year of solar cycle 20, submitted to *J. Geophys. Res.*, 1977.

Nolte, J. T., A. S. Krieger, A. F. Timothy, R. E. Gold, E. C. Roelof, G. Vaiana, A. J. Lazarus, J. D. Sullivan, and P. S. McIntosh, Coronal holes as sources of solar wind, *Solar Phys.*, 46, 303, 1976.

Nolte, J. T., A. S. Krieger, E. C. Roelof, and R. E. Gold, High coronal structure of high velocity solar wind stream sources, *Solar Phys.*, in press, 1977.

Pearson, E. S., and H. O. Hartley (Eds.), *Biometrika Tables for Statis-*

- sicians*, vol. 1, 3rd ed., Cambridge University Press, New York, 1970.
- Pick, M., Permanent sources of particle emission from the sun, in *Solar Terrestrial Physics*, part 1, edited by E. R. Dyer, pp. 61-71, D. Reidel, Dordrecht, Netherlands, 1972.
- Pneuman, G. W., The solar wind and the temperature-density structure of the solar corona, *Solar Phys.*, **28**, 247, 1973.
- Reinhard, R., and E. C. Roelof, Drift and diffusion of solar flare protons in the corona, *Proc. Int. Conf. Cosmic Rays 13th*, **2**, 1378, 1973.
- Reinhard, R., and G. Wibberenz, Propagation of flare protons in the solar atmosphere, *Solar Phys.*, **36**, 473, 1974.
- Roelof, E. C., Coronal structure and the solar wind, in *Solar Wind Three*, edited by C. T. Russell, p. 98, University of California Press, Los Angeles, 1974.
- Roelof, E. C., and S. M. Krimigis, Analysis and synthesis of coronal and interplanetary energetic particle, plasma, and magnetic field observations over three solar rotations, *J. Geophys. Res.*, **78**, 5375, 1973.
- Schatten, K. H., J. M. Wilcox, and N. F. Ness, A model of interplanetary and coronal magnetic fields, *Solar Phys.*, **6**, 442, 1969.
- Scherrer, P. H., J. M. Wilcox, and R. Howard, The mean photospheric magnetic field from solar magnetograms: Comparisons with the interplanetary magnetic field, *Solar Phys.*, **22**, 418, 1972.
- Severny, A., J. M. Wilcox, P. H. Scherrer, and D. S. Colburn, Comparison of the mean photospheric magnetic field and the interplanetary magnetic field, *Solar Phys.*, **15**, 3, 1970.
- Snyder, C. W., and M. Neugebauer, The relation of Mariner II plasma data to solar phenomena, in *Solar Wind*, edited by R. J. Mackin and M. Neugebauer, pp. 25-32, Pergamon, New York, 1966.
- Timothy, A. F., A. S. Krieger, and G. S. Vaiana, The structure and evolution of coronal holes, *Solar Phys.*, **42**, 135, 1975.
- Wilcox, J. M., The interplanetary magnetic field: Solar origin and terrestrial effects, *Space Sci. Rev.*, **8**, 258, 1968.
- Wilcox, J. M., and N. F. Ness, Quasi-stationary corotating structure in the interplanetary medium, *J. Geophys. Res.*, **70**, 5793, 1965.
- Wilcox, J. M., and N. F. Ness, Solar structure of the interplanetary sector structure, *Solar Phys.*, **1**, 437, 1967.

(Received September 13, 1976;
accepted January 28, 1977.)

CORONAL HOLES AS SOURCES OF SOLAR WIND

J. T. NOLTE, A. S. KRIEGER, A. F. TIMOTHY*

American Science and Engineering, Inc., Cambridge, Massachusetts U.S.A.

R. E. GOLD, E. C. ROELOF

Johns Hopkins University/Applied Physics Laboratory, Laurel, Maryland U.S.A.

G. VAIANA

Center for Astrophysics, Cambridge, Massachusetts U.S.A.

A. J. LAZARUS, J. D. SULLIVAN

Massachusetts Institute of Technology, Cambridge, Massachusetts U.S.A.

and

P. S. McINTOSH†

National Oceanic and Atmospheric Administration, Boulder, Colorado U.S.A.

(Received 16 December 1975)

Abstract. We investigate the association of high-speed solar wind with coronal holes during the Skylab mission by: (1) direct comparison of solar wind and coronal X-ray data; (2) comparison of near-equatorial coronal hole area with maximum solar wind velocity in the associated streams; and (3) examination of the correlation between solar and interplanetary magnetic polarities. We find that all large near-equatorial coronal holes seen during the Skylab period were associated with high-velocity solar wind streams observed at 1 AU.

1. Introduction

Recently progress has been made on the identification of the low coronal sources of some particular solar wind streams observed near 1 AU through the association of high-speed solar wind with 'coronal holes': regions of greatly reduced X-ray, EUV and metric radio emission. The direct association of a recurrent, high-velocity solar wind stream with a coronal hole observed in soft X-rays from a sounding rocket was made by Krieger *et al.* (1973). Neupert and Pizzo (1974) found enhanced geomagnetic activity following the central meridian passage of large, near-equatorial coronal holes, using a superposed epoch analysis of EUV data from OSO-7. They interpret this result to be an indication of the association of high-speed streams with coronal holes. Krieger *et al.* (1974), in a preliminary

* Present address: National Aeronautics and Space Administration, Washington, D.C. U.S.A.

† Harvard College Observatory-Smithsonian Astrophysical Observatory.

‡ A substantial portion of this work was done while a visiting scientist at American Science and Engineering.

The U.S. Government is authorized to reproduce and sell this report. Permission for further reproduction by others must be obtained from the copyright owner.

analysis of data from the first part of the Skylab period, have also found an association between coronal holes and high-speed solar wind streams. The correspondence which they found was not one-to-one, however.

We explore the range of validity of this previously postulated association between coronal holes and high-speed solar wind streams using three different approaches. First we make a direct association of high-velocity streams and coronal holes during the Skylab period. We find three recurrent high-speed streams associated with the three largest near-equatorial holes. We then compare coronal hole area and maximum velocity in the associated stream, and find a highly significant correlation ($\rho = 0.96$). Finally, we form the cross-correlation between solar and interplanetary magnetic polarities, and demonstrate that the principal positive correlation found at this time is due to high-velocity streams associated with coronal holes.

From these results, we conclude that all *large*, near-equatorial coronal holes seen during Skylab are the sources of high-speed solar wind streams in the ecliptic plane, with the interplanetary magnetic polarity in the stream agreeing with the solar polarity beneath the hole.

2. Association of Coronal Holes and High Speed Solar Wind

Coronal holes are regions of greatly reduced X-ray, EUV and metric radio emission (Munro and Withbroe, 1972; Neupert and Pizzo, 1974; Dulk and Sheridan, 1974; Timothy *et al.*, 1975). These structures are regions of low density and/or temperature, and apparently occur in weak, open, diverging, unipolar magnetic field regions (Altschuler *et al.*, 1972; Krieger *et al.*, 1973; Vaiana *et al.*, 1973; Timothy *et al.*, 1975).

Coronal holes have also been found to be associated with recurrent high-velocity solar wind streams (Krieger *et al.*, 1973; Neupert and Pizzo, 1974; Krieger *et al.*, 1974). In this paper we concentrate on a further investigation of this association for the Skylab period.

We present the data base for this study in Figures 1 and 2. In Figure 1, the hourly averages of the solar wind velocity observed by the MIT plasma experiments on IMP 7 and 8 are plotted against the estimated source location of the observed plasma for solar rotations 1601-1610. This plot was generated for comparison with solar images. Therefore, longitude increases from left to right, and time runs from right to left. The first hourly average of each day is a heavy dot, and every other dot is labeled by day of the month in which the solar wind observation was taken.

Source locations were calculated as if the solar wind velocity were constant and in the radial direction all the way from the Sun to 1 AU. Recently, Nolte and Roelof (1973) have argued that this approximation, first used by Snyder and Neugebauer (1966), gives the source longitude in the *high* corona, near the altitude of the Alfvénic critical point, estimated by Weber and Davis (1967) to be

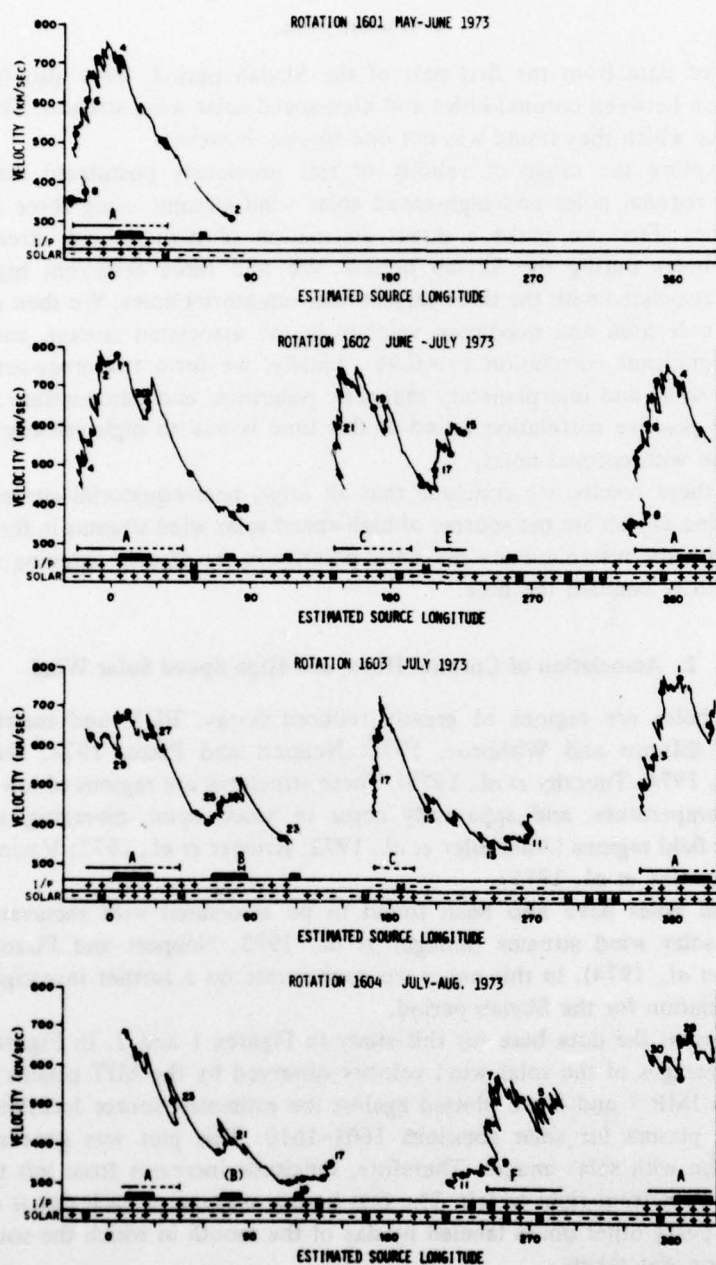
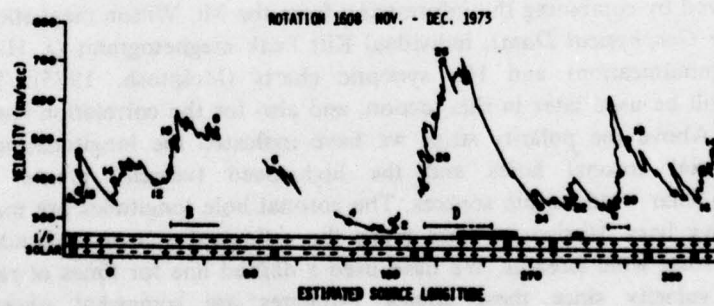
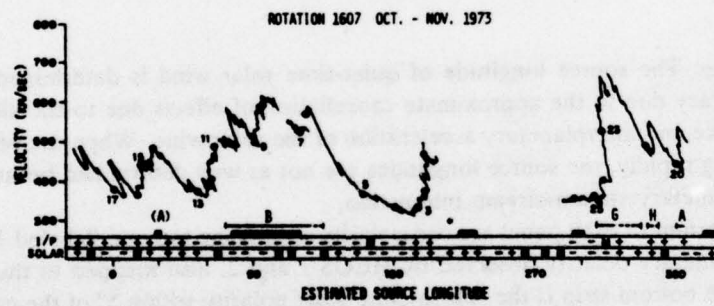
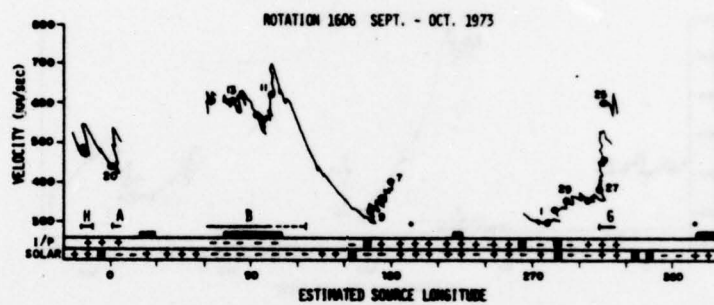
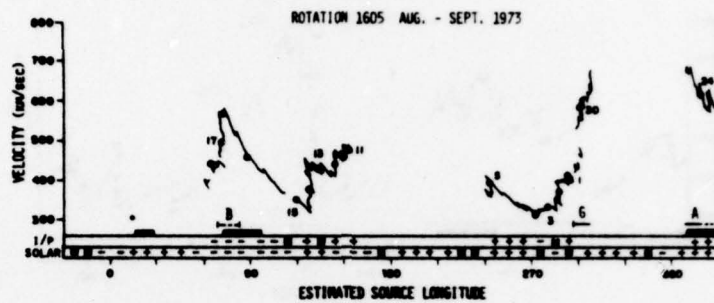


Fig. 1. Hourly averages of solar wind velocity plotted against estimated source longitude for Carrington rotations 1601-1610. The first point of each day is indicated by a heavy dot, and alternate days are indicated. At the bottom are indicated the 10° averages of interplanetary (*I/P*) and solar magnetic polarity. Above these polarity strips, near-equatorial coronal hole locations are indicated by the heavy bars, and the high-speed solar wind stream sources are labeled by letters. Estimated extent in longitude of the stream sources is marked by the horizontal lines, which are dashed during times of rapidly rising velocity. Short vertical lines mark the estimated edges of the sources whenever the solar wind data are complete.



CORONAL HOLES AS SOURCES OF SOLAR WIND

307

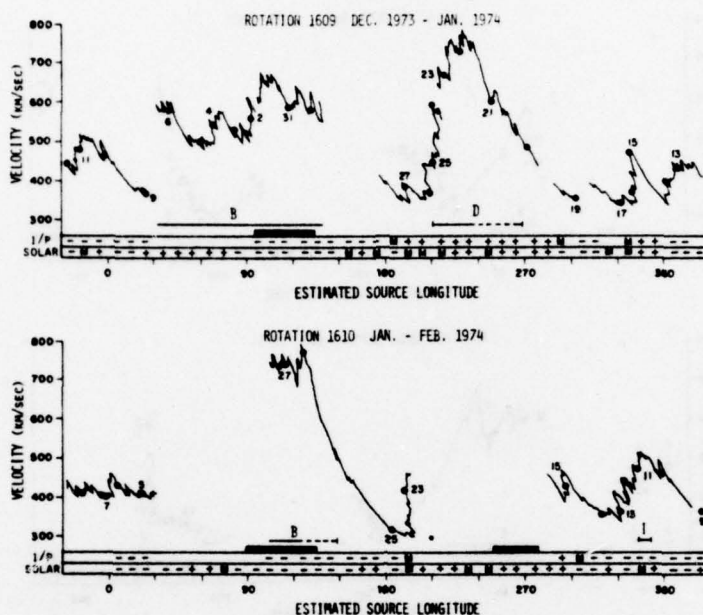


Fig. 1 (Continued)

at $20\text{--}50R_{\odot}$. The source longitude of quiet-time solar wind is determined with $\sim 10^{\circ}$ accuracy due to the approximate cancellation of effects due to the altitude of the source and interplanetary acceleration of the solar wind. When the velocity is increasing rapidly, the source longitudes are not as well determined because of the interplanetary stream-stream interaction.

At the bottom of each panel are two polarity strips. The top one (labeled *I/P*) is the interplanetary polarity observed by HEOS 1 and 2, also mapped to the high corona. The bottom strip is the sub-satellite solar polarity within 5° of the ecliptic plane, derived by combining the information from the Mt. Wilson magnetic field atlas (*Solar Geophysical Data*), individual Kitt Peak magnetograms (J. Harvey, private communication) and $H\alpha$ synoptic charts (McIntosh, 1975). These polarities will be used later in this section, and also for the correlation study in Section 4. Above the polarity strips we have indicated the longitudes of the near-equatorial coronal holes and the high-speed (velocity greater than 500 km s^{-1}) solar wind stream sources. The coronal hole longitudes are marked by the heavy bars. Horizontal lines mark the estimated source longitudes of high-speed solar wind streams. We have used a dashed line for times of rapidly increasing velocity since these source estimates are somewhat uncertain. Whenever the solar wind data are complete, the estimated edge of the stream source is marked by a short, vertical line. Note that many of the streams (e.g., stream A on rotations 1602 and 1603; stream B on rotations 1609 and 1610) are

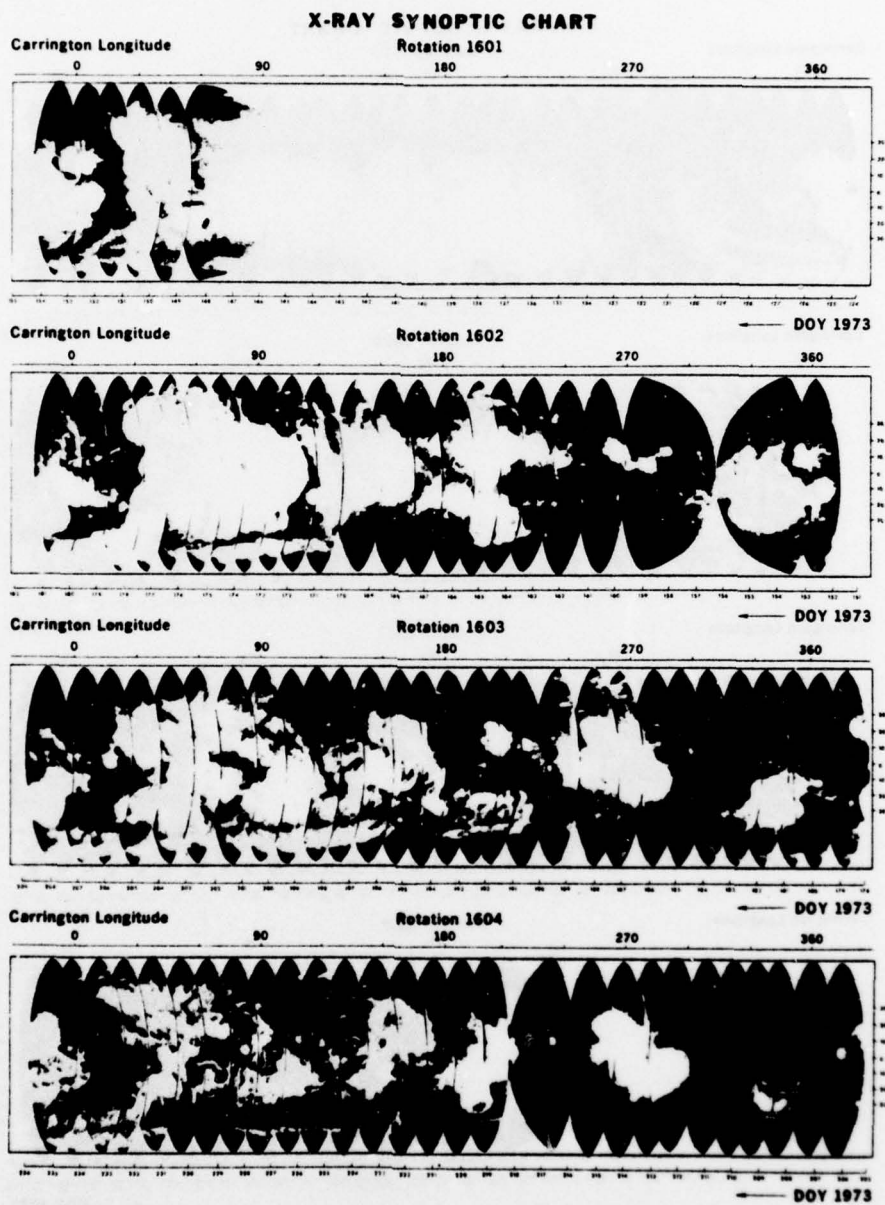


Fig. 2. X-ray synoptic charts for Carrington rotations 1601-1608, made from lunes from 256 s exposures, 2-32, 44-54 Å X-ray images taken by the AS&E spectrographic telescope on Skylab.

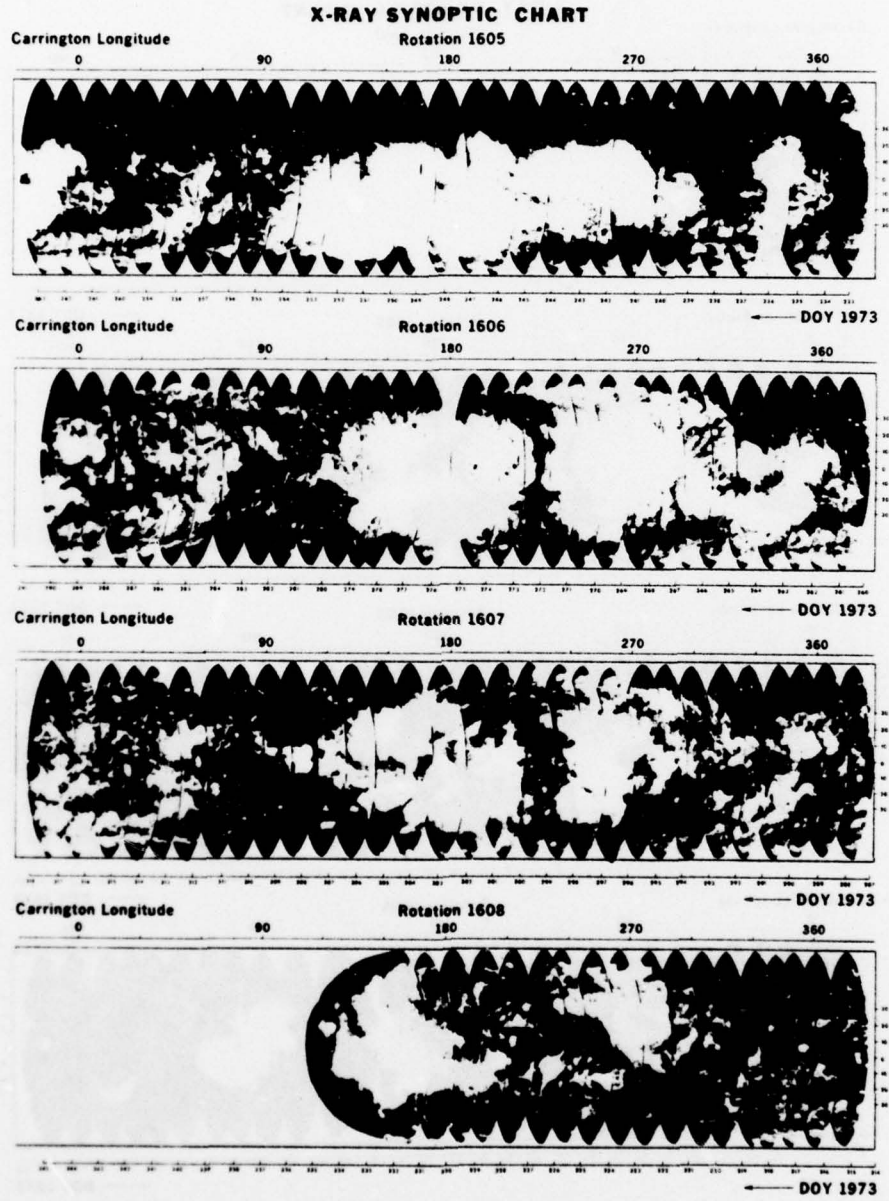


Fig. 2 (Continued)

quite broad, with velocities near the maximum for more than 10° , or approximately one day.

The approximate high coronal source locations of the fastest part of the streams are listed in Table I. Asterisks mark those rotations preceding or following the observations of a high-speed stream when there were no IMP 7 or 8 data because the spacecraft were in the magnetosphere. Streams are labeled in sequence by their estimated source longitude.

Figure 2 is an X-ray synoptic chart, showing the low coronal emission structure. This chart was made by cutting and overlapping lunes from the centers of daily X-ray images taken by the AS&E telescope on Skylab. We have chosen the longest exposures (256 s) in the thinnest filter, to show the coronal holes most clearly. In Figure 2, the coronal holes are seen as black regions surrounded by lighter regions. The coronal hole boundaries are usually sharply defined. Note that Figure 2 is not a projection, and therefore demonstrates locations only to a few degrees. For more precise locations of coronal hole boundaries, see Nolte *et al* (1975).

Due to a filter wheel failure, there were no coronal hole observations from November 27 to December 26, 1973. Between December 26 and February 7, 1974, there are images available, but they are of poorer quality due to a misaligned shutter blade. Therefore, the X-ray synoptic chart extends only from rotation 1601–1608. For the later period, we have been able to identify the large hole seen near 90° on rotations 1609 and 1610. Moreover, the hole visible at 240° on rotation 1608 also appears on rotation 1610. However, we have not attempted to identify new, small coronal holes from the December 26 to February 7 data. Table II lists the CMP days of the near-equatorial coronal holes, which are also identified by number and approximate location in heliographic longitude.

There were five recurrent high-speed streams during this period, labeled on the plots in Figure 1. The first was stream A, plotted near 0° on rotations 1601–1604 (with perhaps a remnant on 1606). Stream B began to develop on rotation 1603, and was observed coming from the region between 60° and 100° through rotation 1607. On 1608, it seemed to decrease, but came back strongly on 1609 and 1610,

TABLE I
Estimated source longitudes of high speed solar wind streams

Rotation	A	B	C	D	E	F	G	H	I
1601	0								
1602	0		160		220				
1603	10	80	175				*		
1604	10	(70)	*			250	*		
1605	*	70					310		
1606	0	100		*			315		
1607		100		*			310	340	
1608		60(*)		210			320		
1609		100		230					
1610		120		*					345

TABLE II
Near equatorial coronal holes during Skylab

Solar rotation	Hole number (Longitude)					
	1 (15)	2 (90)	3 (120)	4 (240)	5 (260)	6 (300)
1601	May 31	May 28				
1602	June 27	June 22	June 21		June 9	
1603	July 25	July 20	July 17			
1604	Aug. 21	Aug. 16	Aug. 13			
1605	Sept. 16	Sept. 12				
1606	Oct. 14	Oct. 9		Sept. 28		
1607	Nov. 10	Nov. 5		Oct. 25		Oct. 20
1608				Nov. 21		Nov. 16
1609		Dec. 29				
1610		Jan. 24		Jan. 14		

extending as far west as 130° . Stream C was seen with an apparent source location between 150° and 180° on rotations 1602 and 1603. Stream D might have been present near 200° on rotation 1607, and became quite strong on 1608 and 1609. It was not observable on rotation 1610 due to magnetospheric transit of the spacecraft. The last recurrent stream was stream G, plotted between 300° and 320° on rotations 1605–1608.

Of these, all except stream C had extrapolated sources near equatorial coronal holes during at least part of their lifetimes. However, stream G contained a positive polarity interplanetary magnetic field, while the solar polarity under coronal hole 6 (the nearby hole) was negative. Such an association is inconsistent with the observation of coronal holes as open magnetic structures. Therefore, we conclude that coronal hole 6 was not the source of stream G. For the other three recurrent streams (A, B and D), the polarity of the interplanetary field in the stream agrees with the solar polarity beneath the nearby coronal hole (CH1, 2 and 4 respectively), as can be seen from the polarity data presented in Figure 1.

It is interesting at this point to compare our preliminary results with the study by Krieger *et al.* (1974). We have extended their analysis to three additional solar rotations, and have also included the polarity of the interplanetary and solar magnetic fields. Yet the conclusion is the same: there is apparently a good association between some recurrent high-speed solar wind streams and some equatorial coronal holes. In particular, we have associated streams A, B and C with coronal holes 1, 2 and 4 respectively. Yet the correspondence is not one-to-one, in that streams C and G are not associated with near-equatorial coronal holes and no high-speed streams are associated (during the period of this study) with coronal holes 3 and 6. There were no solar wind observations to compare with hole 5.

The association of three recurrent, high-speed streams with coronal holes which we have presented above justifies examination of the relationship between

streams and holes in greater detail. This study will provide an explanation for the lack of high speed streams associated with coronal holes 3 and 6.

As for the other streams, it is possible to suggest several potential sources for either. One possibility is that these streams originate from extensions of the polar holes, which extend toward the equator from the south near 180° on rotations 1602 and 1603, and from the north near 330° on rotations 1605–1608. The magnetic polarities are in agreement with these associations (negative in stream C and positive in stream G), and the extensions are near the estimated stream source longitudes (compare Figures 1 and 2).

In support of this suggestion, Hundhausen (1975, private communication) has reported that the hole extending northward from the south polar hole near 270° on rotation 1602 reached north of the solar equator at higher altitudes, as seen in images taken by the HAO white light coronagraph on Skylab. He finds this hole to be associated with a very high-speed solar wind stream observed by the Vela satellites. This stream was substantially slower by rotation 1603 when the MIT plasma detector on IMP 7 was in position to see the stream.

Thus it is possible that all recurrent high-speed solar wind streams are associated with coronal holes. However, since the association is somewhat ambiguous for streams C and G, we restrict our attention in the remainder of this paper to solar wind streams associated with near-equatorial coronal holes.

3. Hole Areas and Stream Velocities

If the holes actually are the sources of the solar wind streams, there should be observable relationships between hole parameters and stream parameters. Since we do not know in detail how the solar wind and magnetic field are transported out through the corona and interplanetary medium, it is preferable to choose parameters which do not depend strongly on the detailed propagation of solar wind, particularly through the corona.

For a hole parameter, we use the area of the hole within 10° of the ecliptic plane, measured from full disk X-ray images obtained near CMP of the hole. This is a reasonable parameter to choose for a comparison, since the (near-equatorial) area of the hole should be fairly directly related to any integral measure of the solar wind stream.

For a solar wind stream parameter, we have chosen to use the maximum hourly average of velocity observed in the stream. The leading edge of the high-speed stream must be decelerated as it sweeps up slower 'ambient' plasma. Therefore, if the stream is small in longitudinal extent, it may not survive to 1 AU. In this way, the maximum velocity observed at 1 AU may be, to a degree, an integral measure of the stream.

In Figure 3 we show the peak velocity plotted against coronal hole area within 10° of the ecliptic plane for the three holes we found to be associated with recurrent high velocity solar wind streams during the period of Skylab

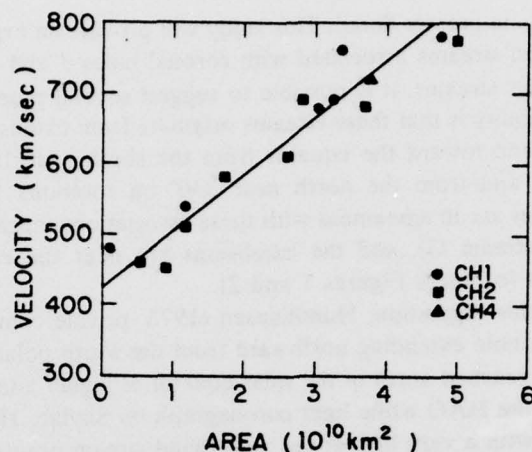


Fig. 3. Maximum solar wind velocity vs. area of the associated coronal hole within 10° of the ecliptic plane. The 'least squares' straight line is also shown.

observations. The velocities are the largest velocities observed with a high coronal source near the hole (within 20°), when the magnetic polarity observed in the interplanetary space was the same as that lying under the hole. It is apparent from the figure that coronal hole area and maximum velocity in the associated solar wind stream are related. This is also verified by the high correlation coefficient of 0.96 between these two data sets. Using standard statistical methods, we find a least-squares fit linear relationship between maximum velocity V in km s^{-1} and hole area A in 10^{10} km^2 given by:

$$V = (80 \pm 2)A + 426 \pm 5.$$

This least-squares straight line is shown in Figure 3.

Most of the points in Figure 3 are from two coronal holes (numbers 1 and 2), with only one point from hole 4 due to the frustrating, ubiquitous data gaps. All the points lie on the same line. Two conclusions can be drawn from this fact. Coronal hole area is related to maximum stream velocity for both holes which we have observed on several rotations. Furthermore, the relationship is the same for both holes, and probably for a third hole as well.

Note, however, that the least-squares straight line predicts a velocity of 426 km s^{-1} for a hole area of 0. This is substantially higher than the lowest solar wind velocities ($\sim 300 \text{ km s}^{-1}$) which have been observed. Velocities less than 426 km s^{-1} are found during the time of our study also. Additionally, the velocities predicted by the least-squares straight line for coronal holes 3 and 6 are significantly higher than the highest velocities observed in the three cases where a comparison between coronal hole area and solar wind velocity could be made for these holes. This is shown in Table III. However, it is clear that holes 3 and 6 are not expected to be sources of high velocity ($> 500 \text{ km s}^{-1}$) solar wind.

TABLE III
Predicted and observed velocities associated with coronal holes 3 and 6

Hole	Rotation	Area (10^{10} km ²)	Predicted velocity	Observed maximum velocity
3	1604	0.22	444	320
6	1607	<0.05 ^a	426	350
6	1608	0.65	478	400

^a This was a small hole, located principally between 10° and 20° south of the ecliptic plane.

At the large hole area, high-velocity end of the curve, there is an additional example from a coronal X-ray image obtained on 26 June 1974 during a rocket flight. This hole was more than 2.5 times larger in near-equatorial area than the largest hole seen during Skylab (J. Davis, private communication). However, the velocity of the associated solar wind stream was less than 800 km s^{-1} (W. Feldman, private communication).

We conclude that the linear relationship between near-equatorial coronal hole area and maximum velocity in the associated stream does not hold for very small holes or very large holes. Instead, at both very small and very large coronal hole areas, the solar wind stream peak velocity can be less than that predicted by the linear relationship.

In Figures 4 and 5 we look at the relationship for the two well-observed hole-associated streams in more detail. We have plotted both velocity and area

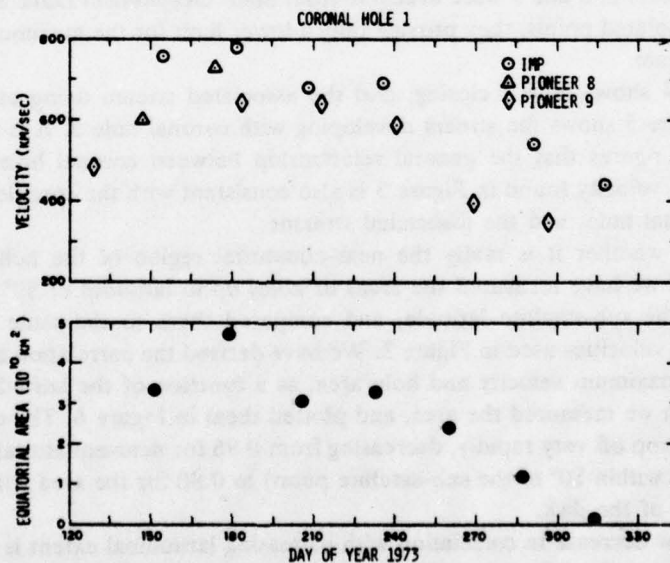


Fig. 4. Top panel: Solar wind velocity from CH1 vs. time for the last part of 1973. (The time scale is the same as the bottom panel.) Pioneer 8 and 9 points are lower limits, since the data are incomplete. Bottom panel: Area of CH1 within 10° of the ecliptic plane vs. time.

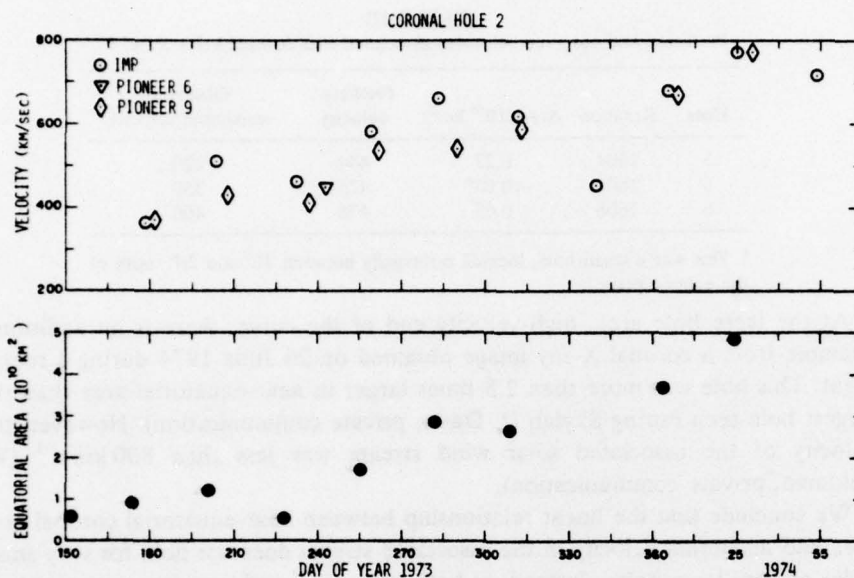


Fig. 5. Same as Figure 4, but for CH2.

against time for each hole separately here. To fill in the temporal evolution of the streams as well as possible, we have also added to the IMP data whatever data from Pioneers 6, 8 and 9 were available from *Solar Geophysical Data*. Since these data are isolated points, they provide only a lower limit for the maximum velocity in the stream.

Figure 4 shows hole 1 closing, and the associated stream dying at the same time. Figure 5 shows the stream developing with coronal hole 2. It is clear from these two figures that the general relationship between coronal hole area and solar wind velocity found in Figure 3 is also consistent with the specific evolution of individual holes and the associated streams.

To test whether it is really the near-equatorial region of the hole which is important, we have measured the areas of holes up to latitudes of 50° north and south of the sub-satellite latitude, and compared these to the same maximum solar wind velocities used in Figure 3. We have derived the correlation coefficients between maximum velocity and hole area, as a function of the latitudinal range over which we measured the area, and plotted them in Figure 6. The correlation does not drop off very rapidly, decreasing from 0.96 for near-equatorial hole area (measured within 10° of the sub-satellite point) to 0.80 for the area within 50° of the center of the disk.

This slow decrease in correlation with increasing latitudinal extent is consistent with the suggestion (Section 2) that some recurrent high speed streams seen near 1 AU originate from the polar holes. This result does not provide convincing evidence, however. The high correlation at wide extend in latitude could be due

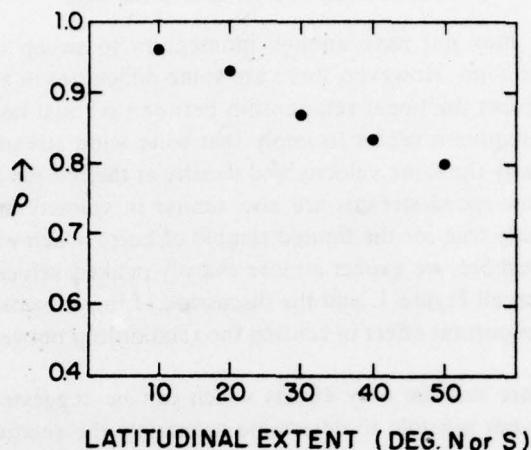


Fig. 6. Correlation coefficient between maximum solar wind velocity and coronal hole area for areas measured within different latitude limits from the ecliptic plane.

to a simpler relationship. A hole which is large near the equator tends to be large over a wider range in latitude also. In fact, we have examined the correlation between equatorial area and area over wider latitude ranges and have found that it is sufficient to account entirely for the correlation observed in Figure 6.

We turn next to the interpretation of the linear relationship between coronal hole area and maximum velocity in the associated solar wind stream. There are two aspects which are particularly noteworthy: the correlation is very good ($\rho = 0.96$), and the relationship is the same for both well-observed holes.

There are two possible explanations for this result. Either the coronal parameters which determine the solar wind acceleration and propagation near the Sun are systematically related to the size of the coronal hole, or the excellent correlation between hole area and maximum velocity in the associated stream is a result of solar wind propagation effects between the Sun and 1 AU (or a combination of both).

One possible systematic effect related to the size of the coronal hole is suggested by the work of Durney and Pneuman (1975). They find that the solar wind velocity calculated at 1 AU is smaller for a magnetic field configuration which diverges more rapidly near the Sun. If this is the case, since the field (at least near the center) of a large hole probably diverges less than that from a small hole, the velocity of a stream from a large hole would be greater, if the other parameters (temperature, density, etc.) were the same. Another alternative source might be a systematic variation in energy transport into the corona from below, perhaps due to a variation in magnetic field strength with hole area.

One possible effect due to propagation of the stream which depends on its spatial extent (mentioned above) is the deceleration of the leading edge of a high speed stream as it sweeps up slower 'ambient' plasma. Thus streams associated

with small holes may not have enough momentum to sweep up the preceding low-velocity solar wind. However, there are some difficulties in assuming that this effect alone produces the linear relationship between coronal hole area and peak velocity. This assumption seems to imply that solar wind streams from all holes observed had nearly the same velocity and density at the release altitude, and that the preceding slow speed streams are also similar in velocity and density. (This may be coincidentally true for the limited sample of holes which we have observed, however.) Furthermore, we expect a more sharply peaked velocity profile than is often observed (recall Figure 1, and the discussion of the streams) if the deceleration is the most important effect in causing the relationship between hole area and peak velocity.

Clearly these are not the only effects which can be suggested to explain the result. Also, it is not possible to determine accurately the relative importance of source effects and propagation effects in producing the high correlation from measurements of the solar wind stream at 1 AU only. A direct test of whether the deceleration effect is significant can come from comparisons of solar wind measurements at substantially different heliocentric radii.

The high correlation provides no direct information on the physical mechanism which results in the relationship between coronal holes and solar wind streams. However, it certainly does show that it is most likely that the solar wind streams are associated with the coronal holes themselves, and not with the boundaries of the holes or with the conditions of activity near the boundaries as Kasinsky and Tomozov (1975) have suggested.

4. Magnetic Polarity Correlation

In the previous section, we have demonstrated a strong correlation between one coronal hole parameter (area) and one solar wind parameter (maximum velocity in the associated stream). However, since a high correlation does not necessarily imply a direct physical connection, it is desirable to test this association in an independent way.

Since the magnetic field may very well be the dominant factor in solar wind propagation deep in the corona (see for example, Durney and Pneuman, 1975) we have also investigated the relationship between solar and interplanetary magnetic fields during this time period. In order to minimize distortions due to the coronal and interplanetary magnetic dynamical effects on the magnetic field strength and direction, we have chosen to investigate the correlation between the magnetic field polarities observed on the Sun and near 1 AU.

Studies of the statistical correlation between interplanetary and solar magnetic polarities were pioneered by Wilcox and Ness (1967). Statistically significant correlations were found in this work, and in subsequent studies by Schatten *et al.* (1969), Scherrer *et al.* (1972), Gold *et al.* (1974) and Nolte (1974), applying a variety of methods to different time periods. However, no simple completely general relationship has been discovered.

The data used in this study are the two polarity strips which were shown in Figure 1. These are the interplanetary polarities mapped back to the high corona, and the solar polarity derived from magnetograms and $H\alpha$ synoptic charts. We have defined these polarities as functions of longitude, with 10° resolution.

We then calculated the cross-correlation as a function of lag in longitude. Mixed polarities have been ignored. The results are shown in Figure 7. The maximum correlation is 0.50 at a lag of $+10^\circ$. This is interpreted as an indication that the estimated connection point (using the constant radial velocity approximation) of an interplanetary magnetic field line to the solar surface may be $\sim 10^\circ$ to the east of the actual connection longitude. There is also a strong tendency for recurrence indicated by the four peaks all greater than 0.37, at intervals of 350° or 360° .

In order to investigate the relationship between these results and high-speed streams, we have done the same studies on subsets of the data. These subsets are listed in Table IV. Figure 8a shows the correlation vs. lag for only the interplanetary magnetic field carried by high-speed (velocity $> 500 \text{ km s}^{-1}$) solar wind. The peak correlation at a lag of 10° is improved to 0.71. The recurrence of many high-speed streams is evident in this figure also.

Figure 8b shows the correlation vs. lag for the data not used in Figure 8a; that is, for interplanetary data at times when the velocity was less than 500 km s^{-1} . It is possible to discern the largest positive correlation peak (0.41) at a lag of $+10^\circ$, and also recurrence peaks at the same lags as in Figure 8a. However, it is apparent that the principal positive correlation at this time was due to the high-speed streams, which also demonstrate a strong tendency to recur.

We have checked the association of high-speed solar wind streams and coronal holes found in Section 2 by correlating only the interplanetary polarities in the hole-associated high-speed streams, namely streams A, B and D, with the solar

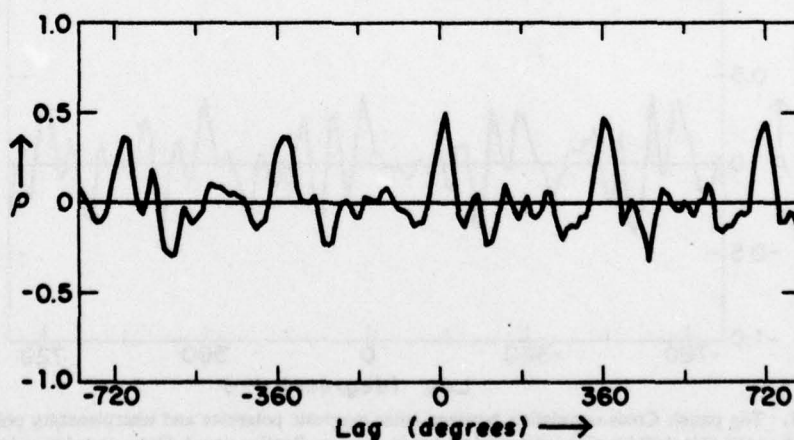


Fig. 7. Cross-correlation between solar and interplanetary magnetic polarities vs. lag in degrees for the Skylab period.

TABLE IV
Correlation subsets

Figure	Data used
7	All
8a	Fast solar wind only ($V > 500 \text{ km s}^{-1}$)
8b	Slow solar wind only ($V < 500 \text{ km s}^{-1}$)
9a	Fast solar wind from coronal holes only
9b	Slow solar wind and fast solar wind not from equatorial holes

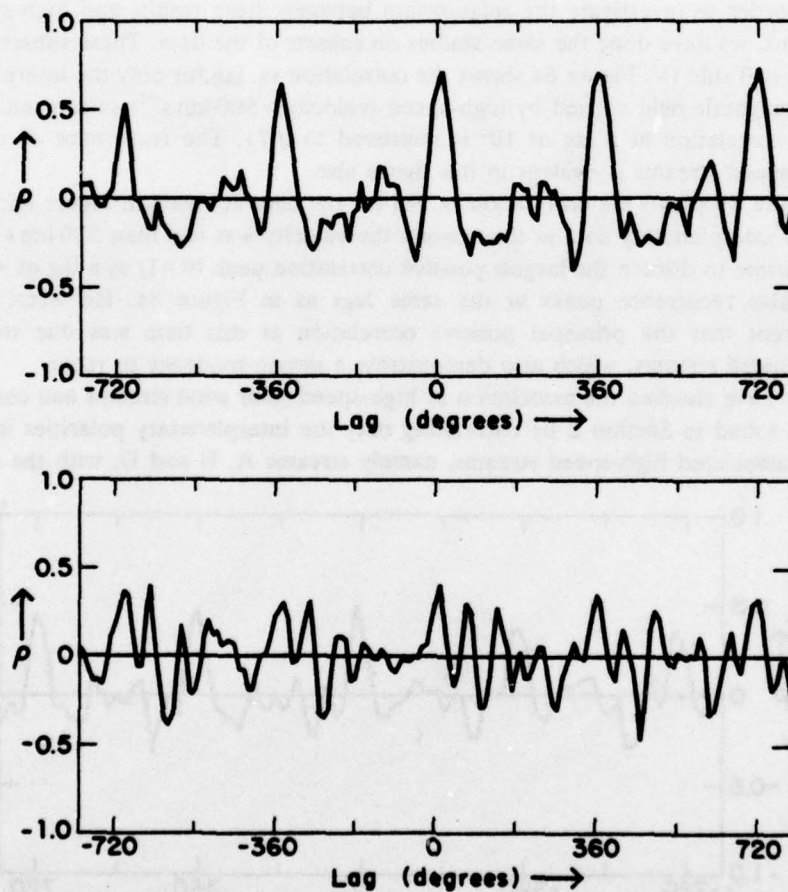


Fig. 8. Top panel: Cross-correlation between solar magnetic polarities and interplanetary polarities in high speed ($V > 500 \text{ km s}^{-1}$) solar wind vs. lag in degrees. Bottom panel: Cross-correlation between solar magnetic polarities and interplanetary polarities in low speed ($V < 500 \text{ km s}^{-1}$) solar wind vs. lag in degrees.

polarity. The results are shown in Figure 9a. Both the peak correlation at $+10^\circ$ lag (0.84) and the tendency toward recurrence are even greater than for all the high-speed solar wind (Figure 8a). The correlation vs. lag for all the rest of the data (Figure 9b) looks quite similar to that found for the slower solar wind in Figure 8b, but with a slightly lower maximum correlation coefficient of 0.37.

Figure 9 demonstrates two important features of coronal magnetic structure during this period. First, the high correlation (0.84) between interplanetary polarity in hole-associated high-speed streams and solar polarity indicates that the magnetic field maps out quite simply from large coronal holes. This very good correlation is consistent with the idea that the magnetic field structure of coronal holes is open. Second, the lack of a highly significant correlation in the rest of the data shows that the relationship between interplanetary and low coronal magnetic

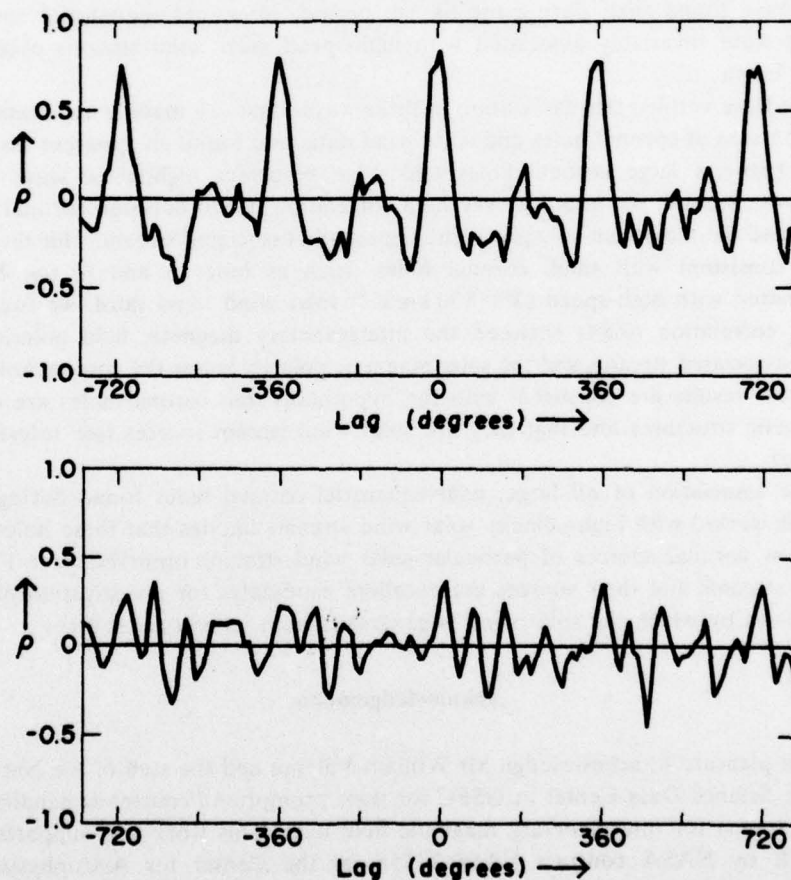


Fig. 9. Top panel: Cross-correlation between solar magnetic polarities and interplanetary polarities in high speed ($V > 500 \text{ km s}^{-1}$) solar wind from coronal holes vs. lag in degrees. Bottom panel: Cross-correlation between solar magnetic polarities and interplanetary polarities in low speed ($V < 500 \text{ km s}^{-1}$) solar wind and also high speed solar wind not from coronal holes vs. lag in degrees.

fields is not so simple when the solar wind is not associated with a large, equatorial coronal hole.

Comparison of Figures 8a and 9a suggests that fast solar wind streams not associated with coronal holes do not map out in the same direct way as do the hole-associated streams. Additionally, Figure 9 shows that the principal cause of the significant positive correlation between solar and interplanetary polarities shown in Figure 7 is due to high-speed solar wind streams which are associated with coronal holes.

5. Summary and Conclusions

We have found that, during the Skylab period, *large*, near-equatorial coronal holes were invariably associated with high-speed solar wind streams observed near Earth.

We have verified this association in three ways. First, we made a non-statistical comparison of coronal holes and solar wind data, and found an apparent association between large coronal holes and some recurrent high-speed solar wind streams. Second, we found a very high correlation (0.96) between coronal hole area and the maximum velocity in the apparently associated stream. This result is also consistent with small coronal holes (such as holes 3 and 6) not being associated with high-speed ($V > 500 \text{ km s}^{-1}$) solar wind. And third, we found a good correlation (0.84) between the interplanetary magnetic field polarity in hole-associated streams and the solar magnetic polarity below the coronal holes.

These results are consistent with the hypotheses that coronal holes are open magnetic structures and that they are solar wind stream sources (see references above).

The association of *all* large, near-equatorial coronal holes found during the Skylab period with high-velocity solar wind streams implies that these holes are the low coronal sources of particular solar wind streams observed near 1 AU. Such streams and their sources are excellent candidates for investigation of the processes by which the solar wind is generated from its coronal sources.

Acknowledgements

It is a pleasure to acknowledge Mr William Valente and the staff of the National Space Science Data Center at GSFC for their prompt and courteous handling of our request for interplanetary magnetic field data. This work was supported at AS&E by NASA contract NAS8-27758, at the Center for Astrophysics by NAS8-31374, at MIT by contract NAS5-11062 and at APL by Research Contract F19628-73-C-0070 from Air Force Cambridge Research Laboratories, Air Force Systems Command (but does not necessarily reflect endorsement by the latter sponsor).

References

- Altschuler, M. D., Trotter, D. E., and Orrall, F. Q.: 1972, *Solar Phys.* **26**, 354.
- Dulk, G. A. and Sheridan, K. V.: 1974, *Solar Phys.* **36**, 191.
- Durney, B. R. and Pneuman, G. W.: 1975, *Solar Phys.* **40**, 461.
- Gold, R. E., Nolte, J. T., Roelof, E. C., and Reinhard, R.: 1974, in M. J. Rycroft and R. D. Reasenberg (eds.), *Space Research XIV*. Akademie Verlag, Berlin, p. 477.
- Kasinsky, V. V. and Tomozov, V. M.: 1975, Preprint, Academy of Sciences U.S.S.R., Siberian Branch, Siberian Institute of Earth Magnetism, the Ionosphere, and the Propagation of Radio Waves, Irkutsk.
- Krieger, A. S., Timothy, A. F., and Roelof, E. C.: 1973, *Solar Phys.* **29**, 505.
- Krieger, A. S., Timothy, A. F., Vaiana, G. S., Lazarus, A. J., and Sullivan, J. D.: 1974, in C. T. Russell (ed.), *Solar Wind Three*, p. 132.
- McIntosh, P. S.: 1975, *Upper Atmosphere Geophysics Report No. 40*, NOAA World Data Center A for Solar-Terrestrial Physics, Boulder, Colorado, U.S.A.
- Munro, R. H. and Withbroe, G. L.: 1972, *Astrophys. J.* **176**, 511.
- Neupert, W. M. and Pizzo, V.: 1974, *J. Geophys. Res.* **79**, 3701.
- Nolte, J. T. and Roelof, E. C.: 1973, *Solar Phys.* **33**, 241.
- Nolte, J. T., Krieger, A. S., Timothy, A. F., Vaiana, G. S., and Zombeck, M. V.: 1975, submitted to *Solar Phys.*
- Schatten, K. H., Wilcox, J. M., and Ness, N. F.: 1969, *Solar Phys.* **6**, 442.
- Scherrer, P. H., Wilcox, J. M. and Howard, R.: 1972, *Solar Phys.* **22**, 418.
- Severny, A., Wilcox, J. M., Scherrer, P. H., and Colburn, D. S.: 1970, *Solar Phys.* **15**, 3.
- Snyder, C. W. and Neugebauer, M.: 1966, in R. J. Mackin and M. Neugebauer (eds.), *Solar Wind*, Pergamon, New York, pp. 25-32.
- Timothy, A. F., Krieger, A. S. and Vaiana, G. S.: 1975, *Solar Phys.* **42**, 135.
- U.S. Department of Commerce, Environmental Science Services Administration: 1973, *Solar Geophysical Data*, 346-354.
- Vaiana, G. S., Krieger, A. S., and Timothy, A. F.: 1973, *Solar Phys.* **32**, 81.
- Weber, E. J. and Davis, L., Jr.: 1967, *Astrophys. J.* **148**, 217.
- Wilcox, J. M. and Ness, N. F.: 1967, *Solar Phys.* **1**, 437.

HIGH CORONAL STRUCTURE OF HIGH VELOCITY SOLAR WIND STREAM SOURCES

J. T. NOLTE and A. S. KRIEGER

American Science and Engineering, Inc., Cambridge, Mass., U.S.A.

and

E. C. ROELOF and R. E. GOLD

Applied Physics Laboratory, Laurel, Md., U.S.A.

(Received 14 June; in revised form 29 September, 1976)

Abstract. When solar wind plasma in the trailing (eastern) edge of a high-speed stream is mapped back to its estimated source in the high corona using the constant radial velocity (EQRH) approximation, a large range of velocities appears to come from a restricted range in longitude, often only a few degrees. This actually constitutes a sharp eastern coronal boundary for the solar wind stream source, and demands that the boundary have a three-dimensional structure. Using interplanetary data, we infer a systematic variation in 'source altitude' (identified approximately with the Alfvén point), with faster solar wind attaining its interplanetary characteristics at lower altitudes. This also affects the accuracy of the source longitude estimates, so that we infer a width in the high corona of $4-6^\circ$ for the source of the trailing edges of streams which appear to originate from a single longitude. We demonstrate that the possible systematic interplanetary effects (in at least some cases) are not large ($\leq 2^\circ$ in heliocentric longitude). The relatively sharp boundaries imply that high-speed streams are well-defined structures all the way down to their low coronal sources, and that the magnetic field structure controls the propagation of the plasma through the corona out to the vicinity of the Alfvén point ($\geq 20 R_\odot$).

1. Introduction

While the existence of the solar wind can be understood in terms of current theoretical models, the details of its origin in observable regions of the solar atmosphere ($< 10 R_\odot$ above the photosphere) and propagation beyond the observable corona out to spacecraft distances are not yet fully explained. It is therefore important to determine as much as possible about solar wind sources and propagation from spacecraft observations. Other useful information is contained in extrapolations and inferences from radio observations such as Type III bursts, e.g., Fainberg and Stone (1974) and references therein, and interplanetary scintillation close to the Sun, e.g., Coles *et al.* (1974).

Recently progress has been made on the identification of the low coronal sources of one type of high-speed stream, those associated with coronal holes (Krieger *et al.*, 1973; Neupert and Pizzo, 1974; Krieger *et al.*, 1974; Nolte *et al.*, 1976). The structure of these streams between a few solar radii and the closest spacecraft (usually near 1 AU) is not directly observable, however.

In this paper we use interplanetary measurements of solar wind plasma and magnetic fields to partially fill this gap by inferring some aspects of the structure of sources of

Solar Physics 51 (1977) 459-471. All Rights Reserved
Copyright © 1977 by D. Reidel Publishing Company, Dordrecht-Holland

The U.S. Government is authorized to reproduce and sell this report.
Permission for further reproduction by others must be obtained from
the copyright owner.

stationary (slowly evolving) high-speed solar wind streams in the high corona. We deal only with the structure at the eastern edge of the stream source, i.e., in the falling portion of the velocity time profile, because the coronal information at the leading edge of the stream is obscured by the interplanetary stream-stream interaction.

By 'sources of solar wind streams' we mean the high coronal sources, at the altitude where the solar wind takes on its interplanetary character. This 'source altitude' is the boundary between the solar corona and the interplanetary medium.

In a simplified sense, one could consider coronal plasma to be completely channeled by magnetic structures which rotate rigidly with the Sun. Interplanetary solar wind, on the other hand, is flowing very nearly radially, and carries the magnetic field along. In these terms, the 'source' of the interplanetary solar wind, or the region in which the solar wind undergoes the transition from coronal to interplanetary conditions, is clearly an extended zone which Nolte and Roelof (1973) estimated to be in the vicinity of the Alfvén radius.

There are also two more direct physical arguments for associating the boundary between the corona and the interplanetary medium with the Alfvén point. First, the direct transfer of angular momentum from the Sun to the plasma through the magnetic field ends at the Alfvén point, since plasma beyond this point can exert no torque on the Sun. Second, at the Alfvén point the energy of bulk flow of the plasma becomes greater than the magnetic field energy, so that channeling of the flow by the magnetic field is much less effective.

We therefore assume that the high coronal source altitude of interplanetary solar wind is approximately the Alfvén radius.

As a first approach, we determine the approximate source longitude of the solar wind plasma using the Extrapolated Quasi-Radial Hypervelocity (EQRH) approximation discussed by Nolte and Roelof (1973). The EQRH terminology is used to emphasize that the estimated source longitudes are the *high* coronal sources. In this approximation, first utilized by Snyder and Neugebauer (1966), source longitudes are calculated as if the solar wind velocity were radial and constant all the way from the Sun to the point of observation. The errors introduced by ignoring corotation and interplanetary acceleration approximately cancel each other, resulting in a good estimate for the longitude of the high coronal source of the solar wind.

We further investigate the structure of the high coronal source of high velocity streams by examining the interplanetary data for indications of systematic variations of the actual solar wind sources from the EQRH estimates. We find that at the edges of high velocity solar wind streams there is a variation in both altitude and longitude of the sources of plasma of different velocities, with higher velocity plasma originating from lower altitudes.

2. EQRH-Approximation Solar Wind 'Dwells'

Near 1 AU, a high-speed solar wind stream is typified by a rapid increase in velocity, followed by a slow decrease. During the decrease in velocity, the EQRH-

approximation source longitude of interplanetary plasma often remains nearly constant for a period of one to three days. These velocity structures, identified with sources of solar wind, have been called solar wind 'dwells' (Roelof and Krimigis, 1973; Gold *et al.*, 1974), since the approximate high coronal source location dwells at one longitude instead of moving across the solar surface at the normal solar rotation rate.

Solar wind streams, such as the example shown in Figure 1, often recur on several successive rotations, with only minimal differences in their amplitudes or structures. This implies that temporal variations in the source over a period of a few days are not significant. Additionally, due to the differences in transit time from the Sun to 1 AU, all the solar wind plasma observed during a dwell was emitted from the Sun at nearly the same time. Therefore, dwells in these streams are representative of the spatial structure

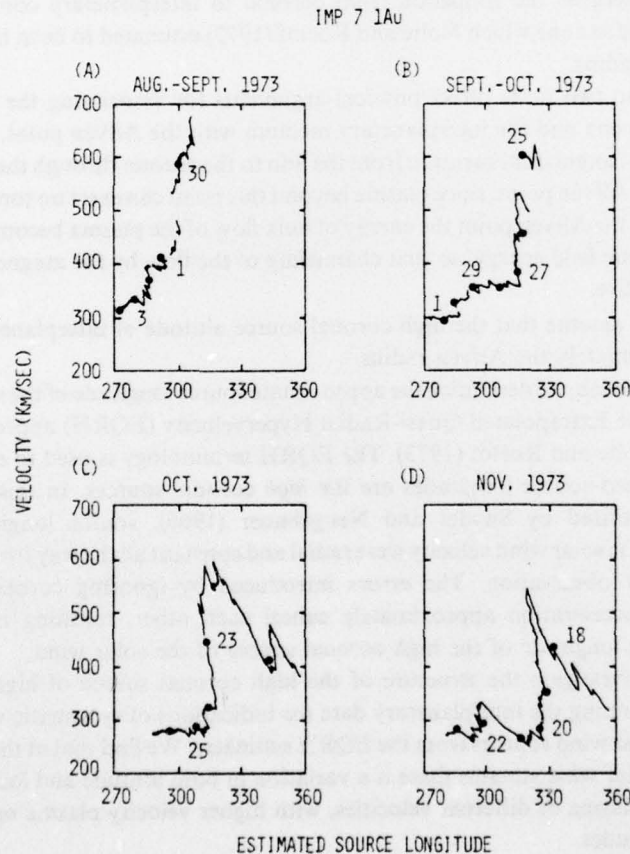


Fig. 1. Hourly averages of solar wind velocity plotted against estimated source longitude for a high-speed stream on four consecutive rotations. The first point of each day is indicated by a heavy dot, and alternate days are labeled. Note the near-vertical drop, or 'dwell' in source longitude, for two or three days at the eastern edge of each stream.

of the solar wind stream, rather than a temporal variation of the source. Here we shall use the interplanetary measurements of solar wind parameters to deduce some aspects of the longitudinal structure of the source of a stream of this type.

In Figure 1 we show four successive rotations of one of the high-speed streams seen by the MIT experiment on IMP 7 during the Skylab mission in 1973 (Nolte *et al.*, 1976). This recurrent high-speed stream was not associated with an equatorial coronal hole. However, it was selected as our principal example for this paper because this is the longest recurrence of a dwell which was well-observed on each rotation during that period. Hourly averages of the solar wind velocities measured by IMP 7 near Earth are plotted against the source longitudes estimated using the EQRH-approximation. In this figure, the first hourly average of each day is a heavy dot. Alternate days are identified by day of month. It is not clear whether IMP 7 observed the peak velocity in the stream in late August and September (Figures 1A and 1B), because the spacecraft was coming out of the magnetosphere. The basic structure of dwells is shown, however. There is some evolution in the shape of the dwell between late August and late September, with the estimated source longitude remaining more nearly constant in September. Also, during the four rotations, the estimated source location of the dwell drifts westward in Carrington longitude. On the last two rotations, when the peak velocity was definitely seen, the velocity decreases by a factor of 2, while the estimated source longitude remains constant, or even shifts slightly to the west during the dwell.

For comparison, in Figure 2 we show all four dwells in streams associated with equatorial coronal holes for which Nolte *et al.* (1976) had reasonably complete data. In their notation, Figures 2A and 2B are the stream from coronal hole 1 on the first two rotations of the Skylab mission, and Figures 2C and 2D are the stream from coronal hole 4 on two successive rotations near the end of the period. These dwells are similar, but less sharp than those of Figure 1, extending for $\sim 15^\circ$ in heliocentric longitude. On the basis of this very limited sample, it appears that there may be a difference between the high coronal source profiles for the two kinds of recurrent high-speed streams.

These figures imply that either there are large longitudinal gradients in the high corona in the solar wind parameters which affect the velocity at 1 AU, or there are systematic, velocity-dependent effects in the EQRH estimates. Since such large gradients have significant implications for both interplanetary and coronal studies of solar wind propagation and origin, we investigate the possibility of systematic effects.

Processes such as magnetic channeling which occur primarily below the source altitude obviously affect the estimation of high coronal source locations from interplanetary solar wind data only to the extent to which the interplanetary flow is affected. Therefore the systematic effects could be either a variation in the angular momentum at the source, or variation in the amount of interplanetary acceleration or deflection of the solar wind. Since most of the channeling by the magnetic fields is likely to occur close to the Sun, at altitudes below $\sim 3 R_\odot$ (Jackson, 1976), differences in angular momentum would be due to a variation in source altitude. We investigate the source latitude effect in the next section, but now show that interplanetary deflection is

not likely to have a significant systematic effect on the estimates of source longitudes.

Interplanetary effects in the trailing edges of high-speed streams between 1 and 5 AU have been discussed by Lazarus (1975). He finds some streams with substantially non-radial flow in even the trailing edge. These streams apparently interact strongly with the surrounding solar wind. Such interactions can explain the apparent shift of the source longitude back to the west as seen in Figures 1C and 1D. He also finds some streams (the one we show in Figure 1A in particular) where there is little interplanetary effect between 1 and 4.6 AU. Therefore, in such streams any systematic effects (such as pressure gradients) which might affect the shape of the dwell must be most effective near the Sun, since they are not effective beyond 1 AU.

In order to demonstrate the magnitude of these possible effects, we approximate the effects of a pressure gradient as simply an increase in the azimuthal velocity of the slow

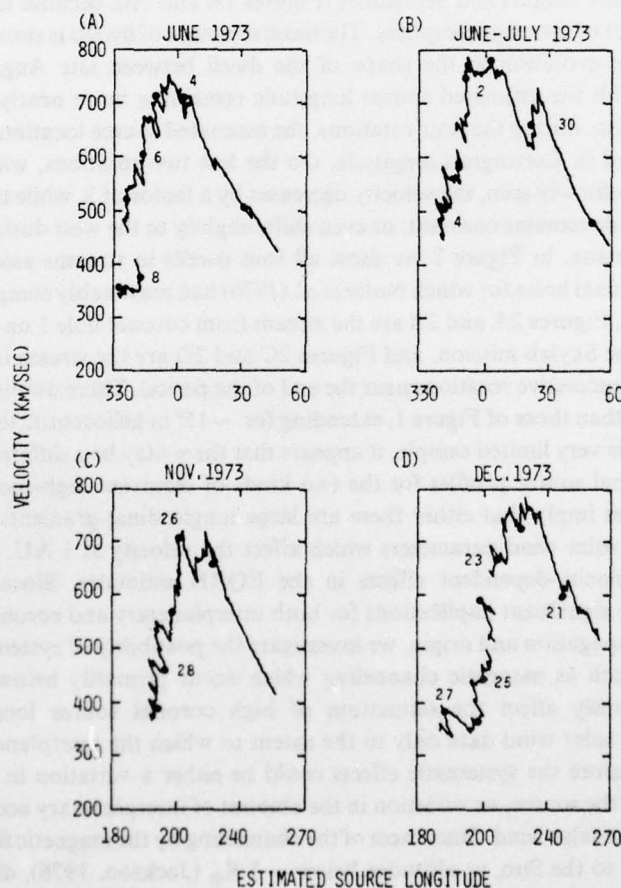


Fig. 2. Same as Figure 1, but for the solar wind streams associated with coronal holes.

solar wind at the source altitude, and assume that the plasma angular momentum (due to this increase) is conserved. As a numerical example, an increase of 10 km s^{-1} in azimuthal velocity at a source altitude of 0.1 AU ($\sim 20 R_{\odot}$) results in a total extra interplanetary rotation of only 1.5° for 350 km s^{-1} solar wind. This is a fairly large perturbation, since 10 km s^{-1} is approximately one-quarter of the corotation velocity at that altitude, and is also almost three times larger than the largest azimuthal velocity which Weber and Davis (1967) calculated (occurring in their model at $\sim 13 R_{\odot}$). For higher source altitudes, the effect is slightly reduced.

Based on this estimate, and on the results of Lazarus (1975), we tentatively conclude that systematic interplanetary effects during at least some dwells are less than 2° . Of course, the final test of this conclusion must come from a comparison of measurements of the same stream close to the Sun and at 1 AU.

3. Effect of Source Altitude Variation

Since interplanetary acceleration and deflection are apparently not substantial (in at least some dwells), there must be a source effect such that many velocities appear to originate from a single longitude. We demonstrate such an effect schematically in Figure 3. Figure 3A shows the EQRH-approximation streamlines for a hypothetical dwell following a high-speed stream. The streamlines are drawn on a plot of radius (r) vs longitude (ϕ) in rectangular coordinates. Therefore, the ideal spirals are straight lines. Because the source longitude does not change as the velocity changes, the dwell resembles a point source from which solar wind emanates at a variety of speeds. Figure 3B shows these EQRH streamlines together with a drawing of 'more realistic' streamlines which include corotation near the Sun, a smooth transition and interplanetary acceleration. Here we have assumed the same source altitude r_0 for all streamlines. Using the same interplanetary streamlines as in Figure 3B, we show the effect of reducing the source altitude with increasing velocity in Figure 3C. The effect shifts the 'actual' sources of faster solar wind to the west relative to slow solar wind sources. This appears to be a reasonable possibility, and we investigate the magnitude of the angular shift induced by a velocity-dependent source altitude in this section.

This investigation requires an estimate of the variation of the source altitude with velocity. As discussed above, we assume that the source altitude is near the Alfvénic critical point. We therefore estimate the variation of the Alfvén point implied by the variation of solar wind parameters measured at 1 AU during dwells.

We begin this analysis from the equations for conservation of magnetic flux and density. Since the interplanetary solar wind is divergent in dwells, we must use the forms of these equations appropriate for divergent flow:

$$B_r(r)r^s = B_0r_0^s, \quad (1)$$

$$n(r)V(r)r^s = n_0V_0r_0^s, \quad (2)$$

where s is greater than 2; r_0 is a reference level (e.g., 1 AU); and B_0 , n_0 and V_0 are the

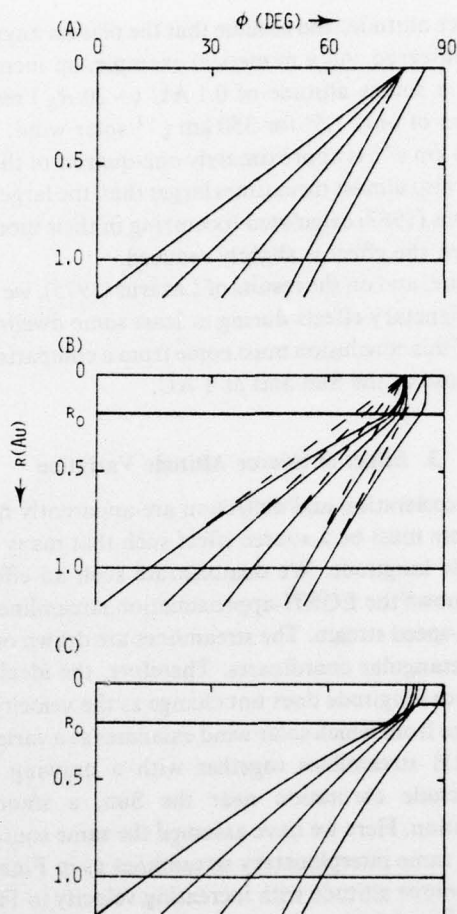


Fig. 3. The effect of variation of source altitude. (A) The EQRH-approximation streamlines on an r - ϕ plot (ideal spirals are straight lines). In the trailing (eastern) edge of the stream, all the plasma appears to be coming from a single longitude. (B) 'More realistic' streamlines (light solid lines) showing effects of corotation and interplanetary acceleration, assuming a constant source altitude. The EQRH-approximation streamlines from 3A are shown as the dashed lines. (C) 'More realistic' streamlines drawn with a varying source altitude. Sources of high velocity plasma are lower, and further west than the EQRH estimates.

values of B_r , n and V at r_0 . The Alfvén critical point condition (equal Alfvén and flow speeds) may be rewritten as

$$B_r^2(r_A) = 4\pi mn(r_A)V^2(r_A), \quad (3)$$

where r_A is the Alfvénic critical radius. Using (1) and (2) to express this in terms of the reference level parameters results in

$$\left(\frac{r_A}{r_0}\right)^s = \frac{B_0^2}{4\pi mn_0 V_0 V(r_A)}. \quad (4)$$

In this form the Alfvén points could be evaluated if the velocity of the solar wind as a function of radius were available. However, since the velocity model cannot be verified experimentally, and since the Alfvén point need not be exactly the source altitude, it is more appropriate to calculate the ratio of the Alfvén radii. This ratio is not strongly dependent on the velocity model, and is also a reasonable estimate for the variation of the source. We shall assume $V(r) \sim r^q$, where Burlaga (1967) used $q = \frac{1}{4}$ as a fit to Parker's (1963) curves. Then the ratio of the Alfvén altitudes for two different parts of the dwell may be expressed as:

$$\left(\frac{r'_A}{r_A}\right)^{s+q} = \frac{B_0^2 n_0 V_0^2}{B_0'^2 n_0' V_0'^2} \quad (5)$$

To estimate the variation in density n , we use some of the results of Diodato *et al.* (1974) and Formisano *et al.* (1974), who studied average properties of the solar wind. Although these results are long-term averages, at speeds above the ambient solar wind speed they are heavily weighted in favor of the dwells, due to the form of solar wind streams (fast rise, long dwell). The various results shown in these two papers can be expressed as $n \sim V^{-j}$, with $1 < j < 1.5$. This provides a reasonable range to use in Equation (5).

We use the interplanetary magnetic field strength measured by Heos 1 and 2 during the four dwells shown in Figure 1 to estimate the effect due to variation of the magnetic field (kindly supplied by the National Space Science Data Center at GSFC). The field strength plotted against time during these dwells is shown in Figure 4. We have plotted the magnitude of the field as positive if the garden hose component of the field was directed away from the Sun, and negative if toward.

This figure demonstrates that a reasonable estimate is that field strength is constant during dwells. There is no significant general trend evident in these plots. Another interesting point is evident in Figure 4C. There is a change in interplanetary magnetic polarity (*i.e.*, a sector boundary) during this dwell, which implies that the dwell must have some measurable extent in longitude.

In order to estimate the divergences we consider the cross-sectional area ΔA of a small flux tube as a function of radius. In the ecliptic plane ($\theta \cong 90^\circ$), at r_A ,

$$\Delta A(r_A) = Kr_A^2 = \Delta\theta_A \Delta\phi_A r_A^2, \quad (6)$$

where $\Delta\theta_A$ and $\Delta\phi_A$ are the heliocentric angles subtended by the area ΔA at r_A . Similarly, at r_0 ,

$$\Delta A(r_0) = Kr_0^2 = \Delta\theta_0 \Delta\phi_0 r_0^2. \quad (7)$$

Since the divergence at a rate greater than r^{-2} (due to velocity differences) is in ϕ , we write $\Delta\theta_0 = \Delta\theta_A$, and $\Delta\phi_0 = C\Delta\phi_A$, where C is a constant giving the azimuthal divergence from r_A to r_0 . Then

$$Kr_0^2 = C\Delta\theta_A \Delta\phi_A r_0^2 = CKr_A^{-2} r_0^2, \quad (8)$$

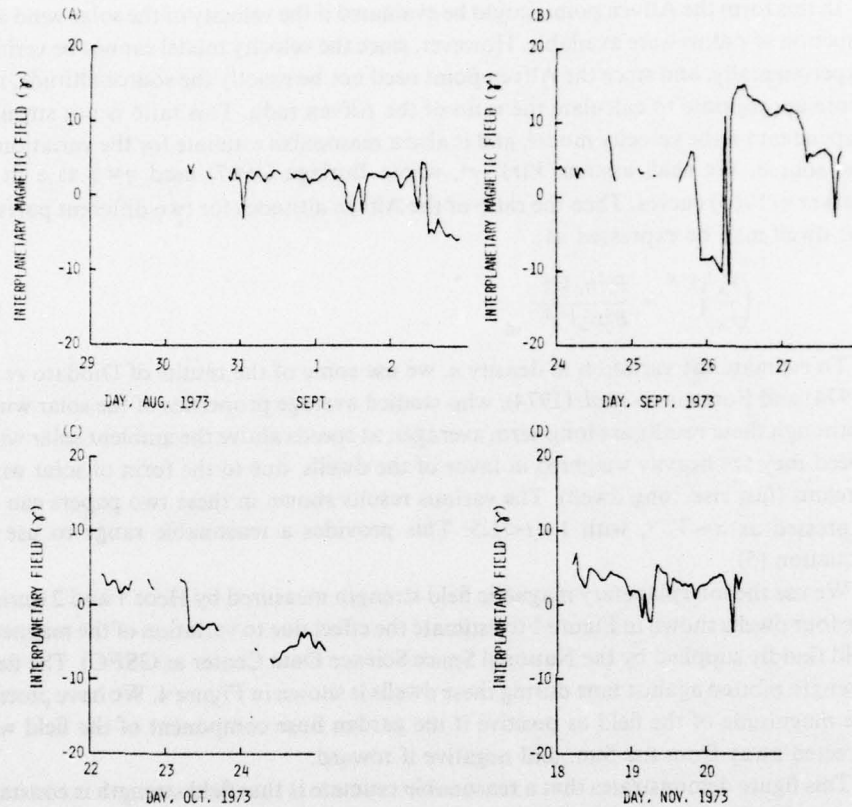


Fig. 4. Interplanetary magnetic field strength in the four dwells of Figure 1. There is no consistent systematic variation. Note the change in polarity on 23 October in Figure 4C.

so that

$$s = 2 + \frac{\ln C}{\ln \left(\frac{r_0}{r_A} \right)} \quad (9)$$

We estimate s using the following assumptions, noting also that s is not strongly dependent on the values of the parameters. The reference level r_0 is at 1 AU, and we use the Weber and Davis (1967) estimates for the critical radii of 15–50 R_\odot . We also note that the interplanetary magnetic field strength in dwells is not drastically lower than normal. Thus the actual longitudinal extent at r_A is at least a few degrees, while the extent at 1 AU is $\sim 30^\circ$. Thus C should be within the range 5–15. These constraints imply that $2.5 < s < 4$.

Putting these results into Equation (5), we find

$$\frac{r'_A}{r_A} = \left(\frac{V_0}{V'_0} \right)^k \quad (10)$$

with $0.1 < k < 0.4$. If $V_0 \cong 2V'_0$, as in the dwells in Figure 1,

$$1.07 < \frac{r'_A}{r_A} < 1.32. \quad (11)$$

Therefore, we conclude that the altitude of the Alfvén point, and also of the source altitude, increases by 7–32% as the velocity falls in the trailing edge of a solar wind stream. This implies that the high speed plasma carries less angular momentum away from the Sun than the slower plasma does, assuming that total angular momentum is determined by the Alfvén altitude.

4. High Coronal Structure of Solar Wind Stream Sources

The final step in our derivation of the shape in radius and longitude of the high coronal structure of stationary high-speed solar wind stream sources is the determination of the longitudinal extent of the dwell sources. For a dwell with no change in longitude in the EQRH-approximation, this is the variation in the estimated source locations due to the variation in altitude of r_A , and also includes the interplanetary effects ($\lesssim 2^\circ$) discussed in Section 2.

We start from Equation (5) from Nolte and Roelof (1973), which gives the longitude ϕ of the source location relative to the observer at 1 AU, rewritten in the notation of the present paper as

$$\phi = \left[1 - \left(\frac{r_A}{r_0} \right)^{3/4} \right] \frac{4r_0\Omega}{3V_0}, \quad (12)$$

where Ω is the sidereal rotation rate of the Sun. The variation $\Delta\phi$ due to corotation effects (assuming the same interplanetary acceleration model) introduced by using the same source altitude \tilde{r}_A for the entire dwell instead of the correct r_A for a particular point is

$$\begin{aligned} \Delta\phi &= \phi - \bar{\phi} = \left[\left(\frac{\tilde{r}_A}{r_0} \right)^{3/4} - \left(\frac{r_A}{r_0} \right)^{3/4} \right] \frac{4r_0\Omega}{3V_0} = \\ &= (1 - \alpha^{3/4}) \left(\frac{\tilde{r}_A}{r_0} \right)^{3/4} \frac{4r_0\Omega}{3V_0}, \end{aligned} \quad (13)$$

where $\alpha = r_A/\tilde{r}_A$. Putting in $V_0 = 600 \text{ km s}^{-1}$, if $\tilde{r}_A = 0.1 \text{ AU}$, the shift of the source of the slowest solar wind relative to that of the fastest is $\Delta\phi_{\text{max}} = 1.9^\circ$: if $\tilde{r}_A = 0.25 \text{ AU}$, $\Delta\phi_{\text{max}} = 3.7^\circ$.

The principal result is quite clear: the eastern edge of a high-speed stream can be very narrow in the high corona, often only a few heliocentric degrees. The approximate total systematic effect is less than 6° , $\sim 2^\circ$ due to interplanetary effects, $\lesssim 4^\circ$ due to source altitude variation.

It is interesting to compare the radial and azimuthal variations of the source altitude.

For a slow stream source altitude of 0.1 AU, the maximum longitudinal variation of 1.9° is $\sim 5 \times 10^5$ km, for a change in altitude of 3.6×10^6 km. If the source altitude is 0.25 AU, the longitudinal variation of 3.7° corresponds to 2.3×10^6 km, and implies a decrease of 9.1×10^6 km in altitude of the high-speed source. The variation in altitude is ~ 4 – 7 times the variation in longitude.

These variations actually provide us with the approximate shape of the source region of vertical dwells. As we noted above, it is possible that these dwells are more typical of recurrent streams not associated with an equatorial coronal hole. A schematic drawing of the source of a stream of this kind is shown in Figure 5A. The 'source altitude' is marked by a heavy line, with schematic solar wind streamlines as light lines. The western edge of the stream is drawn with the same shape as the eastern edge, and the high-speed stream is drawn arbitrarily as 20° wide.

On the basis of a limited data sample, dwells in streams not associated with equatorial coronal holes appear to be sharper than those in streams from equatorial holes. This must be considered when sources of these recurrent high-speed streams are suggested. For example, these streams may originate from extensions of the polar holes toward the equator (Nolte *et al.*, 1976). Then a detailed model of solar wind streams from coronal holes must explain why there is a sharper boundary of the stream observed when the spacecraft measuring the solar wind does not pass directly over the hole.

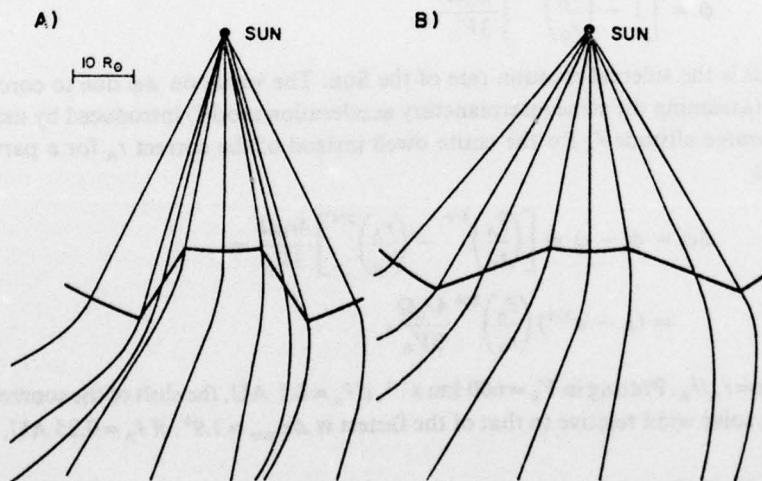


Fig. 5. A schematic drawing of the magnetic field near the source altitude. The varying source altitude is indicated as a heavy line, with nearly radial fields inside, and the beginning of the spiral field pattern outside for (A) a fairly sharp longitudinal gradient, and (B) a somewhat more gradual change. Note that the Sun is drawn approximately to scale. See text for estimates of size of the structures. It seems possible that (B) is appropriate for high-speed streams which come from equatorial coronal holes, while (A) shows the structure of other high-speed streams.

If this apparent difference is real, then the source of a stream from an equatorial coronal hole would appear as shown schematically in Figure 5B. The only difference between this and Figure 5A is a smaller gradient in longitude: the boundary of the stream is not as steep. The gradient is still quite large, however. There is an observed velocity difference of $\sim 350 \text{ km s}^{-1}$ for a source longitude variation of $\sim 20^\circ$. This gradient suggests an obvious explanation for at least part of the large latitudinal gradients such as have been inferred by Hundhausen *et al.* (1971) and Smith and Rhodes (1975), and observed by Coles *et al.* (1974). Whenever coronal holes extend from the poles to near, but not across, the solar equator, the ecliptic plane would be in the region of large gradients at the edge of the hole.

5. Conclusions

With this brief analysis we have demonstrated that the transition from a high-speed stream source to the ambient coronal conditions is quite rapid in longitude in the high corona. This sharp edge of the sources of quasi-stationary high-velocity solar wind streams is strongly suggested by the solar wind 'dwells' which appear in plots of solar wind velocity vs EQRH-approximation source longitudes.

We have investigated the possibility of a systematic velocity-dependent effect in the EQRH-approximation which would cause this boundary to appear sharper than it actually is. There are two possible sources of such a systematic effect. There could be a velocity-dependent interplanetary propagation effect, or the 'source altitude' could depend on velocity.

We have found that, for at least some dwells, it is not likely that there are significant interplanetary effects.

We have calculated the variation of the Alfvénic critical radius in solar wind dwells and found that the high velocity stream originates from a significantly lower altitude than the ambient solar wind. This variation was used to estimate the shape of the high coronal source of the solar wind stream. We note that this source of solar wind is the *physical* source; that is, the boundary between the high corona and the interplanetary medium.

The magnitude of the longitudinal effect due to source altitude variation is only $\sim 4^\circ$ in heliocentric longitude. We therefore conclude that there is a sharp longitudinal transition in the high corona between the high-speed stream source and the 'ambient' solar wind source at the eastern edge of the high-speed stream. Since there is no reason to believe that the western, unobservable edge is significantly different in the corona (i.e., the stream is symmetric), this implies that quasi-stationary high-speed streams are well-defined structures, with relatively sharp boundaries in the high corona.

It seems quite likely that the sharp eastern edge of the high-speed stream sources is caused by magnetic channeling in the corona. If this is so, high-speed streams must be well-defined structures all the way down to their ultimate sources in the very low corona.

Acknowledgements

It is a pleasure to acknowledge Mr William Valente and the staff of the National Space Science Data Center for their prompt and courteous handling of our request for interplanetary magnetic field data. In carrying out this research, the authors have benefited from their participation in the Skylab Solar Workshop Series on Coronal Holes. The Workshops are sponsored by NASA and NSF and managed by the High Altitude Observatory. This work was supported at AS&E by NASA under contract NAS8-27 758 and at JHU/APL by NASA and by Air Force Geophysics Laboratory under Task I of Navy contract N00017-72-C-4401.

References

- Burlaga, L. F.: 1967, *J. Geophys. Res.* **72**, 4449.
- Coles, W. A., Rickett, B. J., and Rumsey, V. H.: 1974, in C. T. Russell (ed.), *Solar Wind Three*, p. 351.
- Diodato, L., Moreno, G., Signorini, C., and Ogilvie, K. W.: 1974, *J. Geophys. Res.* **79**, 5095.
- Fainberg, J. and Stone, R. G.: 1974, *Space Sci. Rev.* **16**, 145.
- Formisano, V., Moreno, G., and Amata, E.: 1974, *J. Geophys. Res.* **79**, 5109.
- Gold, R. E., Nolte, J. T., Roelof, E. C., and Reinhard, R.: 1974, *Space Research XIV*, 477.
- Hundhausen, A. J., Bame, S. J., and Montgomery, M. D.: 1971, *J. Geophys. Res.* **76**, 5145.
- Jackson, B. V.: 1976, *Bull. Am. Astron. Soc.* **8**, 325.
- Krieger, A. S., Timothy, A. F., and Roelof, E. C.: 1973, *Solar Phys.* **29**, 505.
- Krieger, A. S., Timothy, A. F., Vaiana, G. S., Lazarus, A. J., and Sullivan, J. D.: 1974, in C. T. Russell (ed.), *Solar Wind Three*, p. 132.
- Lazarus, A. J.: 1975, invited review, *EOS* **56**, 438.
- Neupert, W. M. and Pizzo, V.: 1974, *J. Geophys. Res.* **79**, 3701.
- Nolte, J. T. and Roelof, E. C.: 1973, *Solar Phys.* **33**, 241.
- Nolte, J. T., Krieger, A. S., Timothy, A. F., Gold, R. E., Roelof, E. C., Vaiana, G., Lazarus, A. J., Sullivan, J. D., and McIntosh, P. S.: 1976, *Solar Phys.* **46**, 303.
- Parker, E. N.: 1963, *Interplanetary Dynamical Processes*, Interscience, New York.
- Roelof, E. C. and Krimigis, S. M.: 1973, *J. Geophys. Res.* **78**, 5375.
- Smith, E. J. and Rhodes, E. J.: 1975, *J. Geophys. Res.* **80**, 917.
- Snyder, C. W. and Neugebauer, M.: 1966, in R. J. Mackin and M. Neugebauer (eds.), *The Solar Wind*, Pergamon Press, N.Y., p. 25.
- Weber, E. J. and Davis, L., Jr.: 1967, *Astrophys. J.* **148**, 217.

SOLAR PARTICLE EMISSION

E. C. Roelof
The Johns Hopkins University/Applied Physics Laboratory
Johns Hopkins Road
Laurel, Maryland 20810

A variety of flare-associated and recurrent solar particle events are analyzed using the technique of "mapping" the fluxes back to the estimated high coronal longitude of the interplanetary field line passing through the spacecraft. Often it is possible to separate temporal from spatial effects as well as those of coronal and interplanetary propagation. Considerable regularity appears in the coronal injection profiles deduced during events in 1969, 1972 and 1973, implying extended acceleration of protons ~ 0.3 -7.5 MeV, helium and medium nuclei ~ 1 MeV/nuc and relativistic electrons. Clear associations are found in 1973 among energetic particle injection profiles, solar wind stream sources, and low coronal magnetic structure.

1. INTRODUCTION

Suppose we ask a very simple question: What is the coronal spatial dependence of the injection of energetic solar particles into the interplanetary medium? The answer given by theorists over the last decade was usually not simple. The emphasis was placed on the temporal behavior of the fluxes due to impulsive injection, interplanetary diffusion, (parallel and transverse to field lines) and adiabatic deceleration. The theoretical calculations were restricted to mathematically convenient longitude dependences of the injection profiles (e.g., point source or Gaussian distribution). Therefore little specific information on the actual injection profile could be derived from comparisons with data. Most theoretical treatments of interplanetary particle propagation over the last decade concentrated on protons of energies ≥ 10 MeV and relativistic electrons, where it was claimed there was agreement with theoretically predicted time histories. Yet even the earliest studies of ground level neutron monitor events found strong pitch angle anisotropies persisting into the maximum of some events, clearly at variance with diffusion with a mean-free-path $\lambda \ll 1$ AU (Meyer et al., 1956; Carrischoel, 1962; McCracken, 1962; Burlaga, 1967; Maurer et al., 1973). Evidence for non-diffusive propagation of protons < 10 MeV and non-relativistic electrons also accumulated from analysis of persistent anisotropies

(Lin, 1970; Krimigis et al., 1971; Roelof, 1973; Immenen and Van Allen, 1973; Roelof and Krimigis, 1973; Felser et al., 1975). Reinhard and Wibberenz (1975) argued that coronal and interplanetary propagation effects could be separated during the rise-to-maximum of 10-60 MeV proton events. In addition it became evident that these low-energy solar particles closely followed interplanetary field lines (Van et al., 1966; McCracken and Neugebauer, 1966; McCracken et al., 1968; Roelof and Krimigis, 1973; Kirsch and Munch, 1974; Domingo et al., 1976).

It would therefore seem prudent to consider a way of approaching the question of the coronal injection profile which invokes a minimum of a priori assumptions concerning interplanetary propagation. Since there is negligible transverse diffusion (at least at the lower energies), if we can estimate the longitude (and latitude) of the coronal foot-point of interplanetary field lines at the spacecraft, then we have sorted out a space/time cut of the event development ordered with respect to the spatial distribution of coronal injection. The required "mapping" technique was first proposed in a prescient study by Snyder and Neugebauer (1966) and applied to the Mariner 2 electron observations of Van Allen. The solar wind plasma was assumed (in the first approximation) to travel radially with constant velocity from the sun, carrying out with it the "frozen in" magnetic field lines. Thus the emission longitude of plasma with velocity V is taken to be the central meridian longitude at the time of plasma observation plus (r/V) , where r is the sidereal rotation rate at the solar equator and r is the spacecraft radius. The lack of immediate agreement of the inferred locations of plasma and electron origin with solar active regions, combined with the apparently extreme simplification of constant radial plasma trajectories, led the original authors themselves to raise questions concerning the validity of the mapping. The technique fell into disuse for several years. It was reapplied to the Mariner 2 plasma data by Courcier and Leblanc (1970), and Roelof (1972) demonstrated that the mapping ordered the apparently different (non-co-rotating) low energy particle histories observed by Pioneer 6 and at Earth from the July 7, 1966 flare event. The plasma mapping was applied to gross solar wind structure by Hundhausen (1972), while Krieger et al., (1973) established a detailed identification of the source of a recurrent solar wind stream with a coronal hole in a 1970 photograph from a rocket-borne American Science and Engineering focusing x-ray telescope. Theoretical justification for the "quasi-radial hypervelocity" (QRH) approximation beyond the MID critical points was presented by Sakurai (1971) and Matsuda and Sakurai (1972), while Nolte and Roelof (1973a, 1973b) argued that the "extrapolated" QRH (or EQRH) plasma trajectories, taken back as if to $r = 0$ (the center of the sun), actually gave an estimate (to within 10°) of the high coronal longitude and latitude of the origin of the solar wind plasma. The accuracy of the high coronal source longitudes (which they took care to distinguish from the fictitious EQRH trajectories) resulted from the near-cancellation of the two major effects on the actual plasma trajectory: acceleration of plasma beyond the critical points, and the tendency towards co-rotation inside the critical points. Beginning with the analysis of Roelof and Krimigis (1973), the EQRH mapping technique was applied to numerous particle events, some of which will be discussed below.

Once the observed particle fluxes are ordered in coronal connection longitude, there remains the problem of the relationship between the fluxes at the

spacecraft and the actual fluxes in the high corona. For the mapping technique to be useful in its simplest form, all that is required for comparison among multiple spacecraft is that the fluxes at the spacecraft be proportional to those on the same field line in the outer coronal, with the factor of proportionality being approximately independent of solar longitude. When data are available from only a single spacecraft, the mapped fluxes can only be interpreted as proportional to the coronal injection profile if the factor of proportionality is also nearly independent of time during the period of interest. The reason that the time constancy is often a good approximation is quite simply that lower energy particles are often injected for a period ~ 1 week, much longer than the time required to establish a quasi-equilibrium population along the injection interplanetary field line (Roelof and Krimigis, 1973). The longitude constancy can come about because of relatively homogeneous conditions along the interplanetary field lines encountered during the event, either because they are relatively undisturbed, or (at the other extreme) because they are similarly disturbed.

The uncertainty in the propagation factor affects the interpretation of the mapped fluxes, but does not affect the mapping itself. It seems that the most practical procedure is first to order the data in terms of connection longitude, and then to let the sun tell its own story. In actual practice, we always begin by regarding the plots of mapped particle fluxes as "spacecraft fluxes plotted at their high coronal injection longitude." We then find that on occasion we can deduce from the plots that the factor is approximately constant in longitude and/or time.

2. SINGLE SPACECRAFT ANALYSIS: SEPTEMBER 1973

During the decline of Solar Cycle 20 many low energy particle events exhibited simple coronal injection profiles. When the fluxes were mapped back to their estimated high coronal connection longitudes, they displayed a nearly exponential dependence on heliographic longitude $\exp(\phi/\phi_0)$, where $|\phi_0| \sim 10^\circ$ and both positive and negative values of ϕ_0 were found. Such a functional dependence is not unexpected. Reinhard and Roelof (1973) proposed a one-dimensional diffusion-drift-loss model to describe the gross characteristics of coronal particle transport

$$\frac{\partial N}{\partial t} + \frac{\partial}{\partial \phi} \left(\frac{N}{\tau_E} - \frac{\partial}{\partial \phi} \frac{1}{\tau_D} \frac{\partial N}{\partial \phi} + \frac{N}{\tau_L} \right) = 0 \quad (1)$$

The steady-state solution for the case of longitude-independent characteristic times for diffusion (τ_D), drift (τ_E) and loss (τ_L) in a source-free region is simply $\exp(\phi/\phi_0)$ where

$$\phi_0 = - \frac{\tau_L}{2\tau_E} \pm \left[\left(\frac{\tau_L}{2\tau_E} \right)^2 + \frac{\tau_L}{\tau_D} \right]^{1/2} \quad (2)$$

The choice of signs depends on the sign of the drift time τ_E and the relative location of the source region with respect to $\phi = 0$. A statistical analysis

216

of fits of the time-dependent solution of (1) to the rise-to-maximum of ≥ 10 MeV flare proton increases 1967-1969 leads to drift-diffusion-loss parameters which when substituted in (2) yield $|\phi_0| \sim 10^\circ$ (Reinhard and Roelof, 1976).

When such simple spatial coronal particle distributions exist, they are easily identified by observations from a single spacecraft if the solar wind velocity varies appreciably during the particle event. Such was the case for particles from the 2B flare (x-ray importance C1) 1212 UT, September 7, 1973 (day 250), and the time histories of solar particles and solar wind velocities measured on IMP-7 are shown in Figures 1a and 1b (respectively). The solar wind data are from the MIT detector and the particles from the JHU/APL detector and include: protons 0.3-0.5 MeV and 1.9-4.5 MeV; alphas 0.6-1.2 MeV/nuc; and medium nuclei ($Z \geq 3$) ~ 0.8 -3.2 MeV/nuc. IMP-7 was in the magnetotail on days 250 to 253, so no solar wind velocities are available from the spacecraft.

The similarity of the flux histories of the diverse particle species in Figure 1a reveals the spatial nature of the discontinuities in the curves. The changes are simultaneous on the 1-hour plotting scale, even though the transit times for 1 AU of the 0.4 MeV and 3 MeV protons differ by more than 3 hours, viz., the dip at 0000 UT, day 253 and the small peak at 2100 UT, day 255. This event was first discussed by Roelof et al., (1975).

The results of the mapping are shown in Figures 1c and 1d for the particle fluxes and solar wind velocities, respectively. The solar wind stream boundaries in the outer corona are evident in Figure 1d at heliographic longitudes $\sim 145^\circ$, $\sim 125^\circ$ and $\sim 70^\circ$. These "dwellings" in connection longitude have been identified with the eastern edges of solar wind source regions (Nolte et al., 1976a; 1976b). If the coronal injection profile is quasi-stationary in time on the scale of ~ 1 day, then the particle fluxes at Earth should remain approximately constant during the decay phase of the solar wind streams. This is indeed observed, as can be seen from Figure 1a in which the flux histories have flat "plateaus" during the dwells on days 255, 257 and 260. Further confirmation that we are indeed seeing a smooth coronal profile, distorted at Earth by the non-uniform eastward progression of connection longitudes, is found in the abrupt particle flux decreases in the middle of day 255 and at the beginning of day 259. These flux decreases correspond to the rapid eastward "sweep" of the connection longitude resulting from the increasing velocities at the leading edges of the two solar wind streams from 130° - 140° and 70° - 80° . The mapping is not strictly accurate when the plasma has undergone interplanetary deceleration, as at the stream leading edge (Nolte and Roelof, 1973b).

This event therefore demonstrates how, with the aid of variable solar wind velocities, the coronal injection profile can be unfolded from the particle flux history at Earth. The profile revealed in the September 7, 1973 event is approximately exponential over 80° of longitude and about 4 orders of magnitude in flux, implying $\phi_0 \sim 80^\circ/\ln 10^4 = 8.7^\circ$. That this profile is not restricted to the positive component of solar energetic particles is demonstrated by the mapped fluxes of near-relativistic electrons > 0.22 MeV (Figure 1c) which track the protons, alphas and mediums for the first two decades of intensity. This striking lack of dependence of these particle coronal injection profiles on charge or rigidity led Roelof et al., (1975) to suggest

217

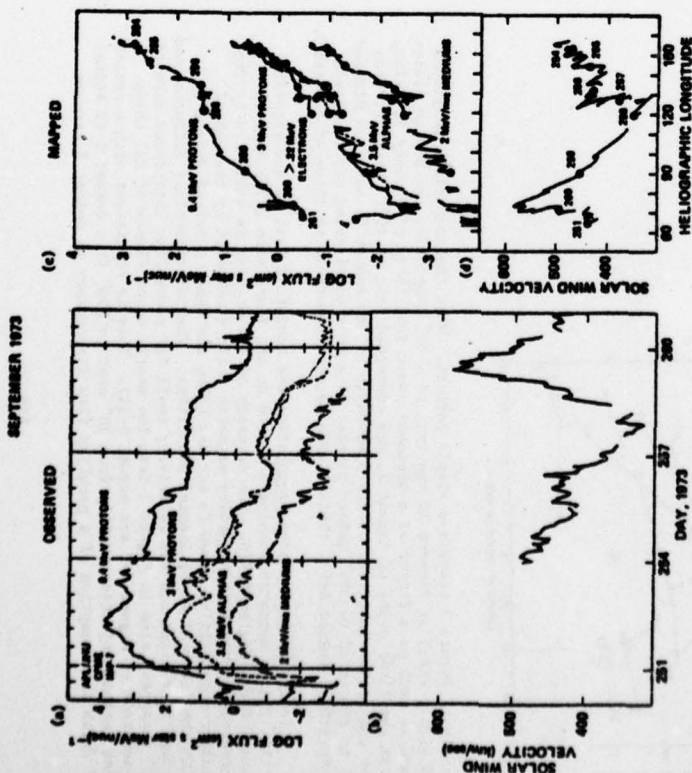


FIGURE 1
 TIME HISTORIES OF (a) ENERGETIC SOLAR PARTICLES AND (b) SOLAR WIND VELOCITY (MUT, IMP-7). CORONAL CONNECTION LONGITUDE MAPPING OF (c) PARTICLES FEATURES AND (d) SOLAR WIND VELOCITY.

that the coronal transport mechanism may involve electric fields, since the $E \times B$ drift is also independent of rigidity as well as the sign or magnitude of the charge.

What coronal structure lay under this injection profile? Examination of the American Science and Engineering x-ray photographs from Skylab for Carrington Rotation 1605 (Molte et al., 1976a) reveals a series of bright equatorial x-ray plagues extending eastward from the flare site (McMath Plage Region 12507, 188°, 818°) to the western edge of an equatorial coronal hole (CH2) at ~ 115°. There is considerable interconnection of the x-ray plagues by well-defined loop structure seen in emission. The first two decades of

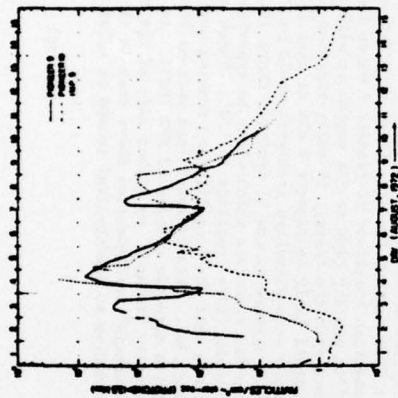


FIGURE 2
 TIME HISTORIES OF > 13.5 MeV PROTONS (GSPC/UBH) FROM THE THREE GREAT FLARES OF AUGUST 1972. PIONEER 9 (0.7 AU) AND PIONEER 10 (2.2 AU) WERE ON THE SAME RADIAL $\sim 46^\circ$ EAST OF EARTH.

the exponential profile (Figure 1c) lie over the plage region (120° - 160°), and the particle fluxes reach their minimums in the peak of the solar wind stream from CH2.

3. MULTIPLE SPACECRAFT ANALYSES: AUGUST 1972 AND APRIL 1969

Although the mapping technique can often establish (self-consistently) coronal spatial profiles for quasi-stationary solar wind streams and energetic particle populations, the use of coronal connection longitudes really comes into its own with observations from inter-calibrated detectors on well-separated spacecraft. A mapping analysis of the great flare particle events of August 2, 4 and 7, 1972 (Kochel et al., 1974), resolved the curious situation of three prompt impulsive increases being measured by Pioneer 9 at 0.7 AU and near the flare longitude, while IMP-5 some 45° to the west measured impulsive events only from the August 4 and 7 flares, and Pioneer 10, on the same radial as Pioneer 9 but at 2.2 AU, never really measured a sharp increase from any of the flares. The time histories of fluxes of ~ 13.5 MeV protons from the Goddard/University of New Hampshire detectors are shown in Figure 2.

In the lower panel of Figure 3 the spacecraft fluxes are mapped to their connection longitudes at the beginning of each day of August using the solar wind velocities from the Pioneers (Mihalov et al., 1974) and HEOS-2 (Grunwaldt et al., 1973). In the upper panel of Figure 3, a portion of the Hy Synoptic Chart for Carrington Rotation 1590 shows emission regions (No. 10 indicated by stipple) and absorption features (filaments, filament channels, etc.) which separate large-scale regions of different dominant magnetic polarity. The chart was prepared by S. C. Weyland of the University of New Hampshire under the supervision of P. S. McIntosh, NOAA/ERL. Comparison of the two

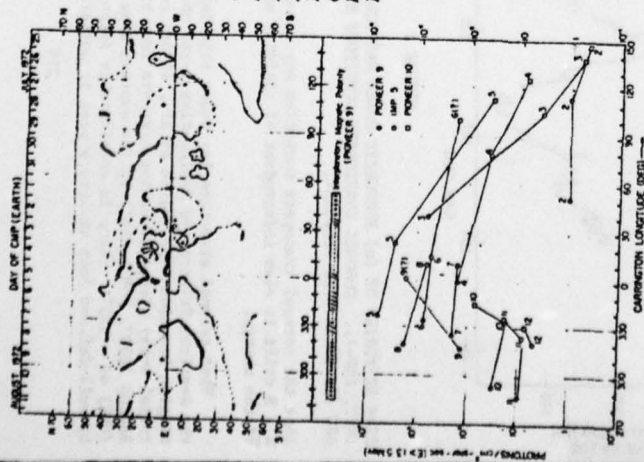


FIGURE 3

UPPER PANEL: H α SYNOPTIC CHART OF LARGE-SCALE CHROMOSPHERIC MAGNETIC POLARITIES (\pm), FLARE REGION IS MER 11976 (15 $^{\circ}$, N14). LOWER PANEL: MAPPED > 13.5 MeV PROTON FLUXES AT THE BEGINNING OF EACH DAY IN AUGUST AND MAPPED INTERPLANETARY FIELD POLARITIES (\pm , - AND MIXED//).

panels of Figure 3 reveals a simple pattern. When the connection longitude of either IMP-5 or Pioneer 10 was west of $\sim 60^{\circ}$ longitude, the proton fluxes were as much as a factor of a thousand lower than those of Pioneer 9, which, from the first event of August 2, was connected east of 60° . However, when the connection longitude of IMP-5 moves to 25° on August 5, and when Pioneer 10 is connected to 330° (after passage of a very complicated stream-stream interaction August 6-9), their fluxes become comparable to those of Pioneer 9.

Clearly coronal proton propagation was inhibited west of the extended active region magnetic complex centered on the flare site (15° , N10) in McMath Plage Region 11976. The accuracy of the mapping is validated by the agreement of the interplanetary magnetic field (indicated by the Pioneer 9 polarities shown in the bar below the upper panel of Figure 3), with the inferred H α equatorial polarities. The interplanetary azimuthal and radial flux gradients are relatively small for connection longitudes east of 90° (apparent also in Figure 2 from the nearly equal fluxes of all three spacecraft on August 6-7 and August 9-11). This is consistent with a rather flat coronal injection profile from 30° east to 290° from August 5 to August 12 (with the exception of a peculiar flux discrepancy on August 8 between

IMP-5 and Pioneer 9), even though the fluxes vary over two orders of magnitude during these 7 days. This behavior for fluxes mapping to east of 30° should be contrasted with the nearly exponential gradients west of 60° , the largest (August 3) having a characteristic $\phi \sim 100^{\circ}/\ln 1000 = 15^{\circ}$.

We now turn to a mapping analysis of another event covered by 5 spacecraft (Pioneers 6-9 and Explorer 34) spread over $\sim 180^{\circ}$ in longitude near 1 AU. The large proton event of 0400 UT April 10, 1969 from an east limb flare was analyzed by McCracken et al., (1971) who called attention to the large azimuthal gradients in interplanetary space. Fiek and Schatten (1972) suggested that the gradients could be due to coronal diffusion, and in a more recent study, Reinhard and Wibberenz (1975) have suggested that there was large scale coronal drift operating as well in the event.

The mapped 7.5-45 MeV proton fluxes for April 10-16 are shown in Figure 4a (taken from a forthcoming study of this period by R. E. Gold, E. F. Keath, R. Reinhard and myself). Fluxes from the different spacecraft have been connected by straight lines at the most closely agreeing times of the available observations. Aligned with the same longitude scale, the H α Synoptic Chart for Carrington Rotation 1546 (also prepared by S. C. Wayland and P. S. McIntosh) is shown in Figure 4b. The flare site is easily identified in McMath Plage Region 10035 at 85° longitude.

The mapped fluxes in Figure 4a show a maximum over the flare site around April 11:00 (similar to the August 2 and 4 events); however by April 12:12 the maximum is clearly defined at $\sim 170^{\circ}$, almost 90° west of the flare site. This maximum persists for another 4 days. The profiles to the east and west of the maximum can be approximated by exponentials with characteristic angles $\phi \sim 28^{\circ}$ and $\phi \sim 20^{\circ}$ for the east and west wings of the population during April 12-13. The slope of the western wing is remarkably constant over some 4 days, while that of the eastern wing steepens by April 15-16 to give $\phi \sim 10^{\circ}$. This difference between ϕ_E and ϕ_W is consistent with a westward coronal drift of the particles, as shown by Equation (2).

There is considerable justification for interpreting the mapped fluxes in Figure 4a as coronal profiles. Most obvious is the large displacement of the flux maximum from the flare site (after April 12:12). Secondly, when the connection longitude of Pioneer 7 makes the extraordinary sweep from 145° to 80° in one day (due to its encounter with a $> 1100 \text{ km s}^{-1}$ solar wind disturbance from the flare), it still measures essentially the same proton intensity on April 12:12 as Pioneer 6 did at that longitude on April 10:18. Such ordering by interplanetary transport would be rather fortuitous. And finally, there appears in the H α Synoptic Chart (Figure 4b) a candidate for a coronal magnetic structure which might be appropriate for transport of the particles from the flare longitude to 170° . There could have been a high magnetic arcade over the long filament running north-south and crossing the equator near 130° . This filament runs more-or-less continuously back into the active region magnetic complex of MFR 10035. At 170° longitude are two negative polarity "islands" on either side of the equator suggesting a possible open "fountain" configuration above them in the high corona which could have been conducive to preferential escape of solar particles.

AD-A045 021

JOHNS HOPKINS UNIV LAUREL MD APPLIED PHYSICS LAB

F/G 3/2

INTER-RELATIONSHIPS OF SOLAR AND INTERPLANETARY PLASMA, MAGNETI--ETC(U)

JUL 77 E C ROELOF; R E GOLD

N00017-72-C-4401

UNCLASSIFIED

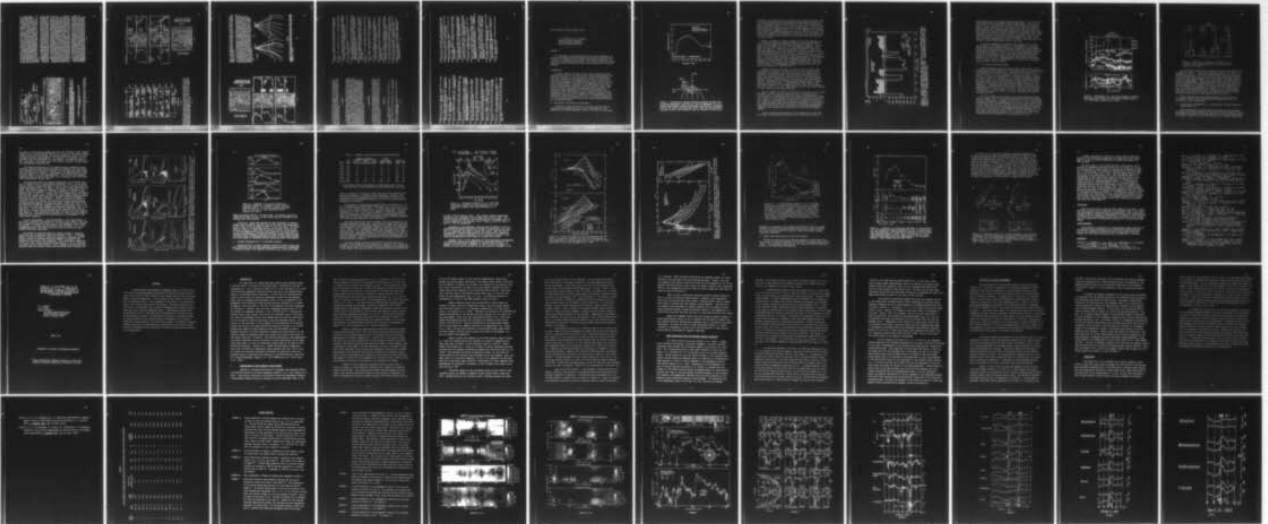
SCIENTIFIC-2

AFGL-TR-77-0166

NL

2 OF 2

AD
A045021



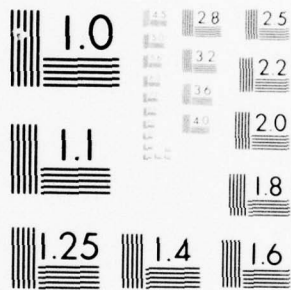
END

DATE

FILMED

11 -77

DDC



MICROCOPY RESOLUTION TEST CHART
NATIONAL BUREAU OF STANDARDS-1963-A

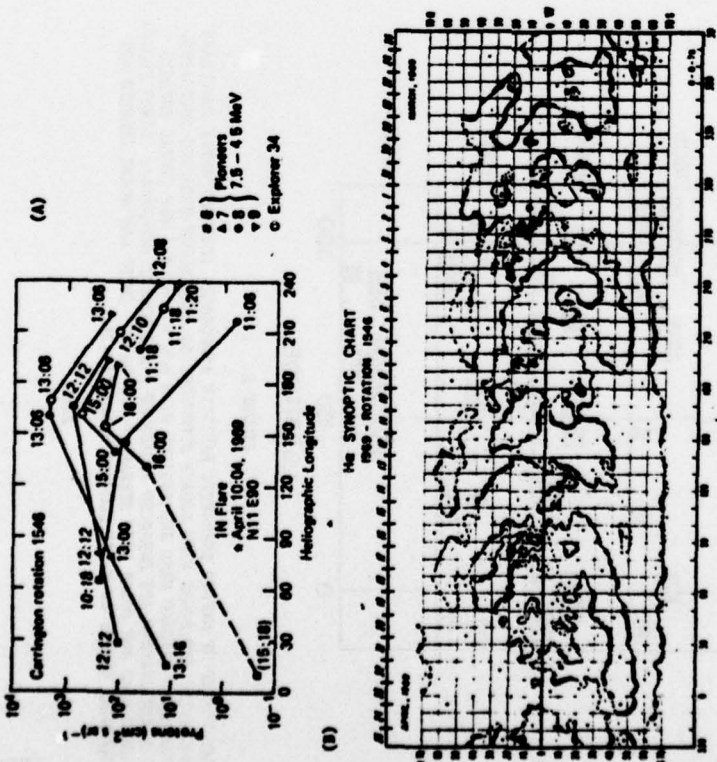


FIGURE 4
 (A) MAPPED LONGITUDINAL GRADIENTS OF FLARE PROTONS DURING APRIL 11-16, 1969 MEASURED BY THE PIONEER NETWORK (UTD) AND NEAR EARTH (JHU/APL). (B) He SYNOPSIS CHART SHOWING LARGE-SCALE CHROMOSPHERIC MAGNETIC POLARITIES (A) AT THE SAME HELIOGRAPHIC LONGITUDES AS THE PROTON FLARES.

4. RECURRENT ENERGETIC PARTICLE AND SOLAR WIND EVENTS
 MAY-DECEMBER 1973

The mapping of particle fluxes need not be limited to individual flare-associated events, as in the three events discussed above. It can also reveal

the global structure of recurrent particle injection regions. These regions can be identified not only by intensity increases, but also by changes in spectral index, abundance ratios, etc. An example, constructed from IMP-7 data during the Skylab period, is shown in Figure 5. This graphical summary of the results of Gold et al., (1975) was prepared by J. F. Wolfe of American Science and Engineering. For each rotation, the lower set of cross-hatched bars indicate the source longitudes of solar wind with velocities $> 500 \text{ km s}^{-1}$, while the inset blank bars mark the equatorial extent of x-ray coronal holes (compare Rotation 1605 with Figure 1d). The upper set of cross-hatched bars indicate populations of energetic helium nuclei with a proton-to-alpha ratio of $p/\alpha < 2$ (when compared at the same total energy of 2.7 MeV). The inset blank bars indicate mapped fluxes of enhanced medium nuclei ($Z \approx 3$). Very few of these helium and medium-rich regions are due to large flare activity. Most can be regarded as regions of "quiet time" energetic particle emission.

The most striking feature in Figure 5 is the recurrent region around 0° longitude for Rotations 1601-1604 of helium-rich and enhanced medium nuclei accompanying a coronal hole (CH1) associated solar wind stream. Another type of correspondence is found in the small recurrent solar wind stream around 315° on Rotations 1605-1608. A helium-rich region lies to the east of the stream on these rotations, and offers a fascinating demonstration of control of particle and plasma emission by coronal structure when examined in detail.

Figure 6 shows the JHU/APL helium fluxes $\sim 1 \text{ MeV/nuc}$ (lower panel) and the MIT solar wind velocities (upper panel) from IMP-7 mapped on Rotations 1605-1606. The helium-rich regions are indicated by cross-hatched bars. The center panel is an extract ($230^\circ-30^\circ$) from the He Synoptic Chart Atlas for the Skylab period (McIntosh, 1975). On the previous Rotation (1604) a flare occurred at 1313 UT on July 29 in the spotless McMath Plage Region 12461 at 270° , N14 and helium fluxes up to $1 \text{ (cm}^{-2} \text{ at MeV/nuc)}^{-1}$ were observed west of the flare site at 330° . On Rotation 1605 a Gaussian-like profile of a small helium event extended from 270° to 315° . This profile recurred on Rotation 1606. Moreover, the solar wind stream which appeared west of 300° for the first time on 1605 also recurs on 1606. The "dwell" or eastern boundary of the stream source appears closely aligned with the western limit of the helium profile (see arrows in Figure 6). This relationship persists on Rotations 1607 and 1608 shown in Figure 7. Data are not plotted east of 290° for 1607 because IMP-7 entered the magnetotail at that point, depriving us of solar wind measurements (and hence also of connection longitudes).

What is additionally remarkable over these four rotations is the coincidence of the common helium and plasma boundary with the equator-crossing longitude ($\sim 315^\circ$) of the neutral line marked by the well-developed He filament which was first established there on Rotation 1605. When this filament is distorted on Rotation 1609 by the emergence of strong magnetic fields in a new active region on the equator $\sim 305^\circ$, the helium fluxes do not rise above 10^{-3} , and the solar wind stream decays to 500 km s^{-1} while its eastern boundary shifts to 345° . This recurrent series of related structures in energetic particles, plasma and equatorial chromospheric magnetic fields demonstrates the persistence of coronal control over four solar rotations. It should be noted that it took 3-5 days to "trace out" either the stream

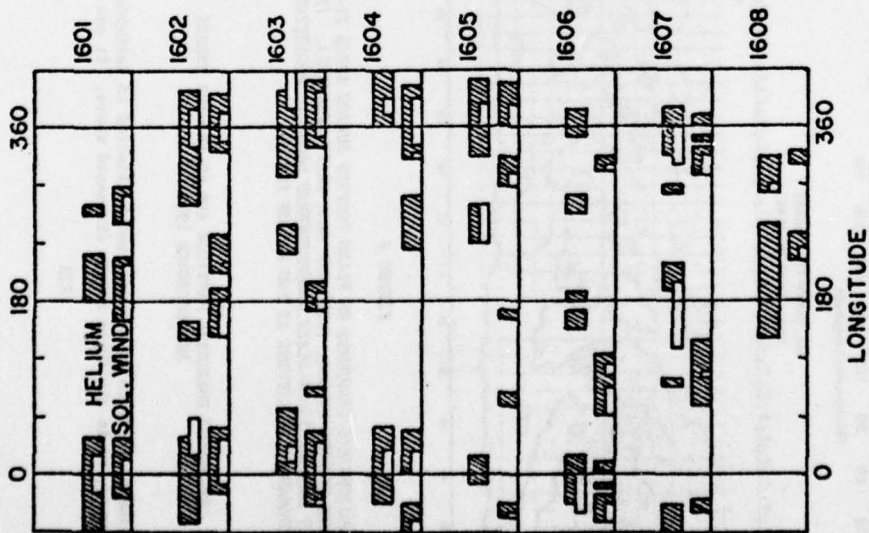


FIGURE 5

RELATIONSHIP OF MAPPED ENERGETIC PARTICLE ABUNDANCES (PREDOMINANTLY NON-FLARE ASSOCIATED) AND SOLAR WIND SOURCE STRUCTURE ON CARRINGTON ROTATION 1601-1608. UPPER CROSS-HATCHED BARS ARE REGIONS WITH $p/\alpha < 2$ AT 2.7 MeV (TOTAL ENERGY) AND BLANK INSERTS ARE ENHANCED FLUXES OF $Z \geq 3$ NUCLEI (JHU/APL). LOWER CROSS-HATCHED BARS ARE SOLAR WIND STREAMS $> 600 \text{ km s}^{-1}$ (MIT) AND BLANK INSERTS ARE EQUATORIAL EXTENT OF X-RAY CORONAL HOLES (ASAE).

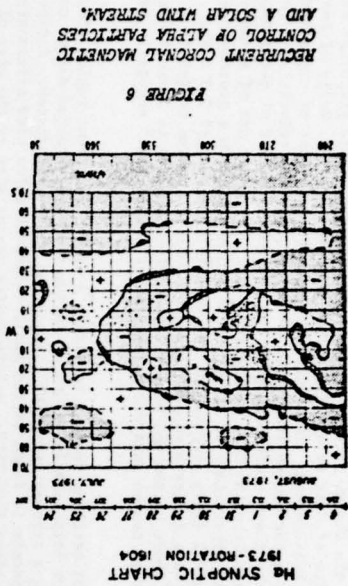
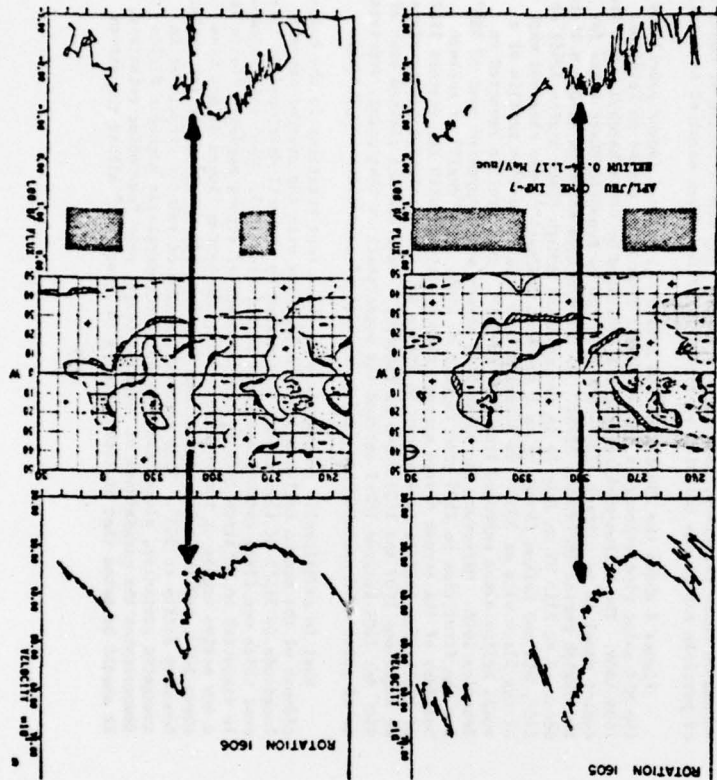


FIGURE 6
RECURRENT CORONAL MAGNETIC CONTROL OF ALPHA PARTICLES AND A SOLAR WIND STREAM.



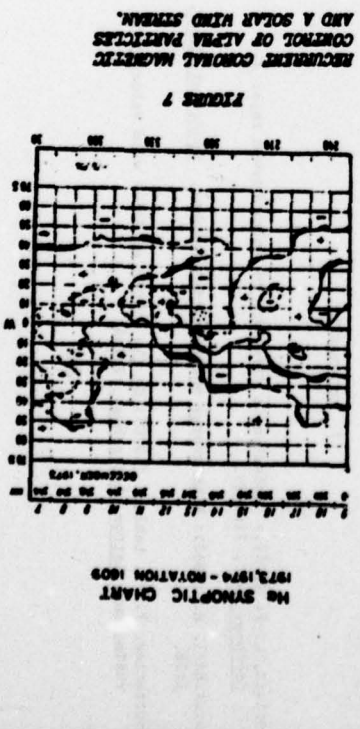


FIGURE 7
RECURRENT CORONAL MAGNETIC CONTROL OF ALPHA PARTICLES AND A SOLAR WIND STREAM.

source or the helium profile on each rotation, so even though the particle event is small in absolute flux and the solar wind peak velocity is not extraordinarily high (700 km s^{-1}), there are large structures, $\sim 50^\circ$ in longitudinal extent in the corona.

Not only is the longitude scale of the structures we have been discussing quite large, but the altitude scale is probably much grander than the several solar radii which we are accustomed to seeing in the excellent white-light coronagraph photographs from Skylab. To emphasize this point, Figure 8 shows two representations of the altitude dependence of the Alfvén critical point across the source region of high speed stream lines (Holte et al., 1976b). The critical radius was taken at $35 R_\odot$ in the highest speed portion of the stream, consistent with the estimates of Weber and Davis (1967). The sun is drawn to scale. The stream boundary altitude variation is a direct consequence of the narrowness of the "dwell" structures we have seen. Figure 8a represents the narrower dwell characteristic of the non-hole associated streams on Rotations 1601-1611, while Figure 8b corresponds to a typical hole-associated stream.

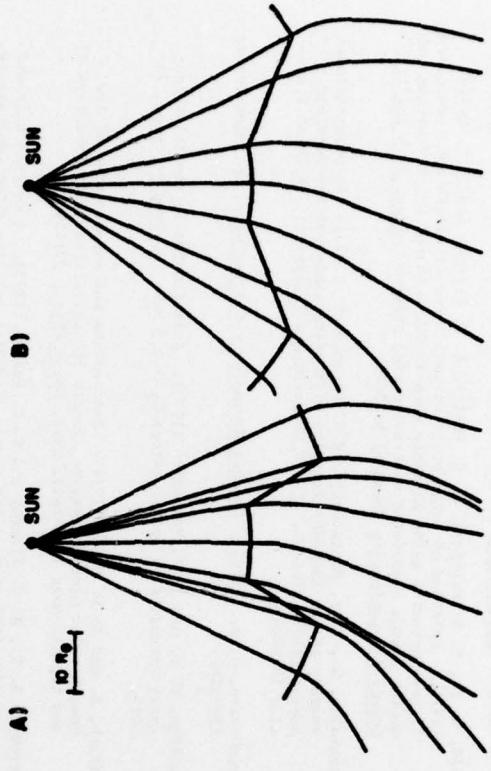
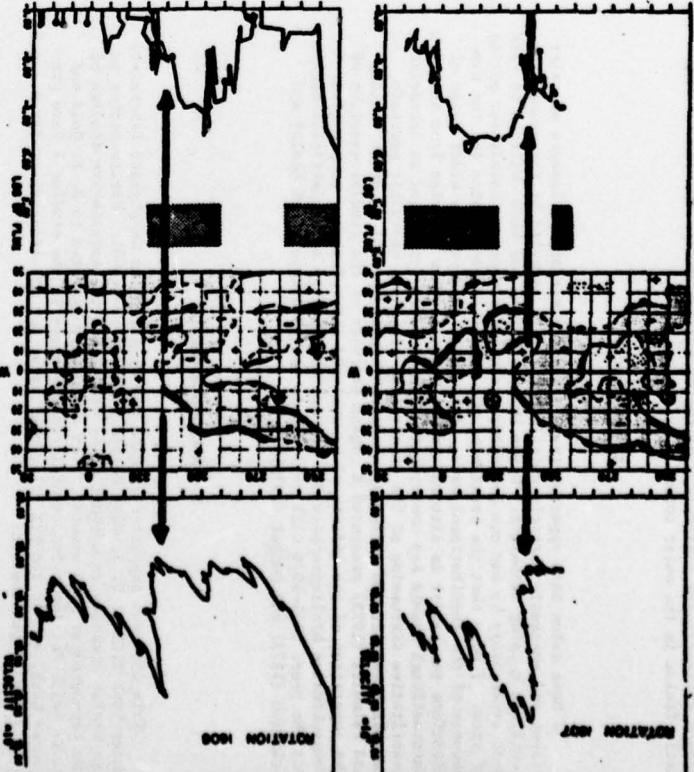


FIGURE 8
SCHEMATIC DRAWING OF SOLAR WIND STREAMLINES (WITH SUN TO SCALE) OF LONGITUDE DEPENDENCE OF ALFVÉN AND CRITICAL POINT IN SOURCE REGION OF HIGH SPEED STREAM (HOLTE, ET AL., 1976b).



226

Thus when we see associations of plasma, energetic particle, and low coronal structures such as those in Figures 5, 6 and 7, the alignments are probably established over altitude differences of $\sim 10^6$ km or 0.1 AU, the scale of the three-dimensional stream structures depicted in Figure 8. This places extraordinary constraints on the regularity of the topology of magnetic fields in the outer corona.

5. COMMENTS

I have taken this opportunity to present a variety of aspects of solar plasma and energetic particle emission which are revealed by the connection longitude mapping technique. Since this technique has been utilized to data most extensively by our own co-workers, the paper presents mainly our points of view. I hope that the breadth of the phenomena compensates for the narrowness of the institutional base. As a small attempt at a wider range of citations the reader is directed to two recent review articles from the 14th International Cosmic Ray Conference: Newkirk (1975) presented an extensive quantitative discussion of the constraints placed on energetic particle coronal transport and escape by the structure of coronal magnetic fields, and Palmeira (1975) presented a cogent overview of the crucial question of the separation of the effects of coronal and interplanetary propagation. Comprehensive bibliographies for low and high energy solar particles covering the years 1971-1974 will be found in the IUGG Reports of Roelof and Krimigis (1975) and Duggal (1975).

6. ACKNOWLEDGEMENTS

This work was supported by NASA and by Air Force Geophysics Laboratory under Task ZF10 of U. S. Navy Contract M00017-72-C-4401. Participation in the Skylab Workshop on Coronal Holes stimulated the correlative studies of the May-December 1973 events. I am especially indebted to R. E. Gold and J. T. Nolte for their fundamental contributions to the studies I have presented here, and to the MIT solar wind group for providing their IMP 7 and 8 data prior to publication.

7. REFERENCES

- Burlaga, L. F. (1967): Anisotropic diffusion of solar cosmic rays. J. Geophys. Res., 72:4449.
- Arachael, E. (1962): High energy solar-particle events. Space Sci. Rev., 1:78.
- Coururier, P., Y. Leblanc (1970): On the origin of solar wind velocity variations. Astron. Astrophys., 7:254.

228

Dwango, V., D. E. Page and K.-P. Wenzel (1976): October 1972 solar event — the third dimension in solar particle propagation. J. Geophys. Res., 81:43.

Duggal, S. P. (1975): Relativistic solar protons. Rev. Geophys. Space Phys., 13:1084.

Fan, C. Y., J. E. Lampert, J. A. Simpson and D. R. Smith (1966): Anisotropy and fluctuations of solar proton fluxes of energies 0.6-100 Mev measured on the Pioneer 6 space probe. J. Geophys. Res., 71:3289.

Flak, L. A. and K. H. Schatten (1972): Transport of cosmic rays in the solar corona. Solar Phys., 23:204.

Gold, R. E., S. M. Krimigis, E. C. Roelof, A. S. Krieger and J. T. Nolte (1975): Relation of large-scale coronal x-ray structure and cosmic rays 3. Low-intensity solar particle events with enhanced ~ 3 Mev helium and medium fluxes associated with solar wind streams. Proc. 14th Int'l. Cosmic Ray Conference (Munich) 5:1710.

Grünwaldt, H., M. D. Montgomery and H. Rosenbauer (1973): An observational summary of the large-scale solar wind disturbances of May-June and August 1972: HEOS-21. S-210 Measurements (Preprint) 7th ESLAB Symposium (Saugau).

Hundhausen, A. J. (1972): Coronal Expansion and Solar Wind, Springer-Verlag (Berlin).

Innanen, W. G. and J. A. Van Allen (1973): Anisotropies in the interplanetary intensity of solar protons $E_p > 0.3$ Mev. J. Geophys. Res., 78: 1019.

Kirsch, E. and J. W. Munch (1974): Intensities and anisotropies of low energy solar protons measured aboard the satellites AZUR, Explorers 35 and 41, November 1969-April 1970. Solar Phys., 39:459.

Krieger, A. S., A. F. Timothy and E. C. Roelof (1973): A coronal hole and its identification as the source of a high velocity solar wind stream. Solar Phys., 23:123.

Krimigis, S. M., E. C. Roelof, T. P. Armstrong and J. A. Van Allen (1971): Low energy (> 0.3 Mev) solar particle observations at widely separated points (> 0.1 AU) during 1967. J. Geophys. Res., 76:5921.

Lin, R. P. (1970): Observations of scatter-free propagation of ~ 40 keV solar electrons in the interplanetary medium. J. Geophys. Res., 75:2583.

McCracken, K. G. and N. F. Ness (1966): The collimation of cosmic rays by the interplanetary magnetic field. J. Geophys. Res., 71:3315.

McCracken, K. G., U. R. Rao and N. F. Ness (1968): Interrelationship of cosmic ray anisotropies and the interplanetary magnetic field. J. Geophys. Res., 73:4159.

229

- McCreech, E. C., V. R. Rao, R. P. Sakata and R. P. Keath (1971): The decay phase of solar flare events. Solar Phys., 18:100.
- McIntosh, P. S. (1975): K-alpha synoptic charts of solar activity for the period of Skylab observations May 1973-March 1974. Rep. WAC-40, World Data Center A, NOAA (Boulder, Colorado).
- Matveev, I. and I. Sekurui (1972): Dynamics of the azimuthally dependent solar wind. Cosmic Electrodyn., 3:97.
- Mauer, R. E., S. P. Duggal and M. A. Pomerantz (1973): Pitch angle distribution of solar flare particles in interplanetary space. J. Geophys. Res., 78: 29.
- Mayer, P., E. H. Parker and J. A. Simpson (1956): Solar cosmic rays of February 1956 and their propagation through interplanetary space. Phys. Rev., 104:748.
- Mihalov, J. D., B. S. Colburn, R. R. Colvard, R. F. Smith, C. P. Sonett and J. R. Wolfe (1974): Pioneer solar plasma and magnetic field measurements in interplanetary space during August 2-17, 1972. in Correlated Interplanetary and Magnetospheric Observations, ed. D. E. Page, D. Heidel (Dordrecht), 543.
- Meikir, G. Jr. (1975): Recent perspectives in solar physics: Elemental composition, coronal structure and magnetic fields, solar activity. Proc. 14th Int'l. Cosmic Ray Conf., 11:3594.
- Molte, J. T. and E. C. Roelof (1973a): Large-scale structure of the interplanetary medium. I: High coronal source longitudes of the quiet-time solar wind. Solar Phys., 33:241.
- Molte, J. T. and E. C. Roelof (1973b): Large-scale structure of the interplanetary medium. II: Evolving magnetic configurations deduced from multispacecraft observations. Solar Phys., 33:483.
- Molte, J. T., A. S. Krieger, A. F. Timothy, R. E. Gold, E. C. Roelof, G. Vidana, A. J. Lazarus, J. B. Sullivan and P. S. McIntosh (1976a): Coronal holes as sources of solar wind. Solar Phys., (in press).
- Molte, J. T., A. S. Krieger, E. C. Roelof and R. E. Gold (1976b): High coronal structure of high velocity solar wind streams. Solar Phys., (in press).
- Palmsira, R. A. R. (1975): Coronal and interplanetary propagation of solar cosmic rays. Proc. 14th Int'l. Cosmic Ray Conf., 11:3805.
- Palmer, I. D., R. A. R. Palmsira and F. R. Allum (1975): Monte Carlo model of the highly anisotropic solar proton event of 20 April 1971. Solar Phys., 46:449.
- Reinhard, R. and E. C. Roelof (1973): Drift and diffusion of solar flare protons in the corona. Proc. 13th Int'l. Cosmic Ray Conf., 2:1378.
- Reinhard, R. and E. C. Roelof (1976): A mathematical model for the coronal transport of flare particles. Submitted to Solar Phys.
- Reinhard, R. and G. Wibbeross (1974): Propagation of flare protons in the solar atmosphere. Solar Phys., 36:473.
- Roelof, E. C. (1972): Comment on large-scale magnetic fields and K-alpha patterns, Solar Wind, ed. P. J. Coleman, C. P. Sonett and J. M. Wilcox, NASA SP-308:1140.
- Roelof, E. C. (1973): New aspects of interplanetary propagation revealed by 0.3 MeV solar proton events in 1967. Proc. of the Solar-Terrestrial Relations Conference, University of Calgary, Canada, 411.
- Roelof, E. C. and S. M. Krimigis (1973): Analysis and synthesis of coronal and interplanetary energetic particle, plasma and magnetic field observations over three solar rotations. J. Geophys. Res., 78:5375.
- Roelof, E. C. and S. M. Krimigis (1975): Low energy solar cosmic rays: A bibliography. Rev. Geophys. Space Phys., 13:1092.
- Roelof, E. C., J. A. Lesiak, V. R. Webber, F. B. McDonald, B. J. Teegarden and J. H. Trainor (1974): Relation of coronal magnetic structure to the interplanetary proton events of August 2-9, 1972. in Correlated Interplanetary and Magnetospheric Observations, ed. D. E. Page, D. Heidel (Dordrecht), 563.
- Roelof, E. C., R. E. Gold, S. M. Krimigis, A. S. Krieger, J. T. Molte, P. S. McIntosh, A. J. Lazarus and J. D. Sullivan (1975): Relation of large-scale coronal x-ray structure and cosmic rays: 2. Coronal control of interplanetary injection of 300 keV solar protons. Proc. 14th Int'l. Cosmic Ray Conf., 5:1704.
- Sekurui, I. (1971): Quasi-radial hypervelocity approximation of the azimuthally dependent solar wind. Cosmic Electrodyn., 1:460.
- Snyder, C. W. and M. Neugebauer (1966): The relation of Mariner 2 plasma data to solar phenomena. in Solar Wind (ed. R. J. Mackin and M. Neugebauer), Pergamon Press, 25.
- Weber, E. J. and L. Davis, Jr. (1967): The angular momentum of the solar wind. Astrophys. J., 148:217.

SOLAR ENERGETIC PARTICLES BELOW 10 MeV

E. C. Roelof and S. M. Krimigis
Applied Physics Laboratory
The Johns Hopkins University
Laurel, Maryland 20810 USA

ABSTRACT

The information on solar acceleration and coronal propagation contained in low energy solar particle observations must be extracted from the effects of propagation in a dynamic interplanetary medium and the proximity of the Earth's magnetosphere. The resulting separation reveals long-lived coronal injection and strong spatial ordering of coronal propagation.

INTRODUCTION

The basic theme of this paper is that solar energetic particles undergo many and diverse processes between their acceleration and their detection; consequently, we must carefully identify the signatures of these many processes and then compensate our data for their effects before we can discover the essential physics of solar particle acceleration and propagation. We stress the *compensation*, since we now know that, although coronal, interplanetary and magnetospheric processes *distort* the information contained in the solar particle fluxes, these processes often do not destroy the information beyond recovery. We shall give several examples which demonstrate how essential this approach is, drawn from studies of: (1) relativistic solar electron propagation near 1 AU; (2) solar origin of enhanced abundances of low energy heavy nuclei and $\text{He}^3 \geq 2$ MeV/nucleon; (3) interplanetary propagation of > 10 MeV solar protons near 5 AU; (4) coronal propagation of > 7.5 MeV protons in a flare event; and (5) the decay phase anisotropies of > 300 keV protons.

1. Relativistic Solar Electron Anisotropies

In Figure 1 we show the fluxes of > 220 keV electrons from the large flare event beginning late on day 253 (September 10), 1974, measured on the JHU/APL experiment on IMP-7. If we were to find large,

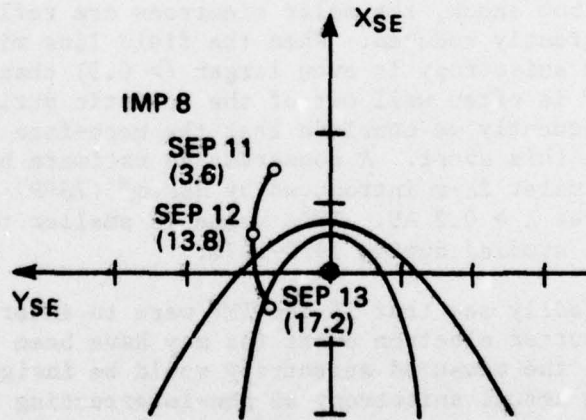
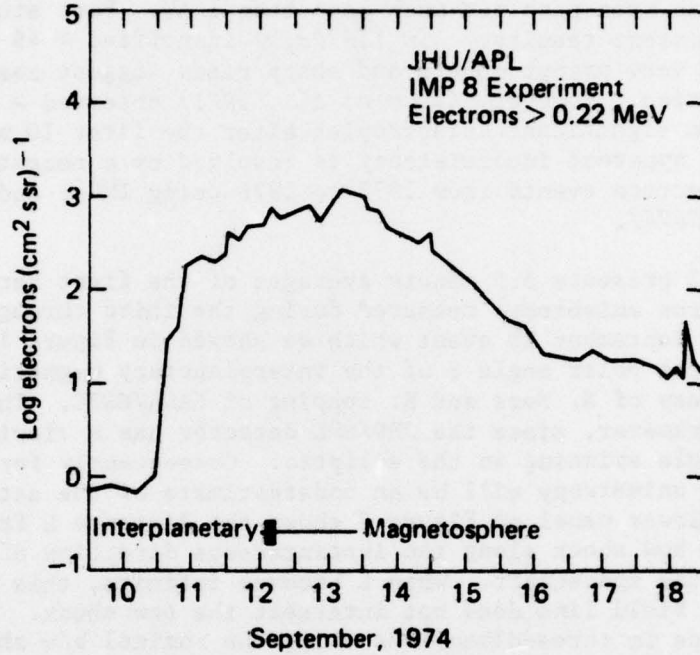


Figure 1. Relativistic electron intensity measured on IMP-8 from an eastern hemisphere flare 2121 UT, day 253 (September 10) 1974. Strong field-aligned outward anisotropies (distorted by reflection from the bow shock) persisted from onset until bow shock crossing. Distance of IMP-8 above ecliptic (Z_{SE}) is indicated on orbit plot.

persistent flux anisotropies in the early part of the event, that would be strong evidence for not only extended interplanetary injection, but also of a mean-free-path not much less than 1 AU. Past studies have given inconsistent results. *Lin (1976a,b)* identified > 45 keV electron events whose very prompt onsets and sharp rises suggest nearly scatter-free propagation. However, *Allum et al. (1971)* observed > 70 keV events which have no significant anisotropies after the first 10 minutes. We believe this apparent inconsistency is resolved by a recent analysis of > 220 keV electron events from 1972 to 1976 using IMP-7 and IMP-8 (*Ng and Roelof, 1977*).

Figure 2 presents 5.5 minute averages of the first harmonic (C1) of the electron anisotropy measured during the third through fifth hours of the September 10 event which we showed in Figure 1. The top panel shows the polar angle θ of the interplanetary magnetic field (IMF), courtesy of N. Ness and R. Lepping of NASA/GSFC. This is an important parameter, since the JHU/APL detector has a viewing cone of $22\frac{1}{2}^\circ$ half-angle spinning in the ecliptic. Consequently for $|\theta| \geq 22\frac{1}{2}^\circ$, the measured anisotropy will be an underestimate of the actual anisotropy. The lower panel of Figure 2 shows the distance L from the spacecraft to the bow shock along the instantaneous direction of the IMF measured on the spacecraft. When L becomes infinite, this means the extrapolated field line does not intersect the bow shock. The calculation is done in three-dimensions using the nominal bow shock configuration computed by *Fairfield (1971)*.

During the rise of the event, the IMF is quite variable, often swinging 90° in azimuth. The result is quite clear: when the IMF intersects the bow shock, the solar electrons are reflected and the anisotropy is greatly reduced. When the field line misses the bow shock, the true anisotropy is even larger (> 0.3) than that measured because the IMF is often well out of the ecliptic during unconnected periods. Consequently we conclude that the mean-free path is comparable to 1 AU in this event. A conservative estimate based on the anisotropy parameter $2\lambda/r$ introduced by *Roelof (1969)* and utilized by *Earl (1974)* gives $\lambda > 0.2$ AU. This value is smaller than those obtained in other events studied during 1972-1974.

One can readily see that if the IMF were to intersect the bow shock throughout a shorter electron event (as may have been the case in *Allum's* event), the measured anisotropy would be insignificantly small, even though the actual anisotropy on non-intersecting field lines could be so large as to approach the "scatter-free" propagation deduced by *Lin*. Thus, by use of IMF data on near-earth spacecraft we can identify the conditions under which strong electron anisotropies are reduced by reflection from the bow shock. Naturally, we also have learned something about the structure of interaction of the IMF and the magnetosheath.

The most striking characteristic of the September 10, 1974 electron event, revealed when we *compensate* for the bow shock effect, is

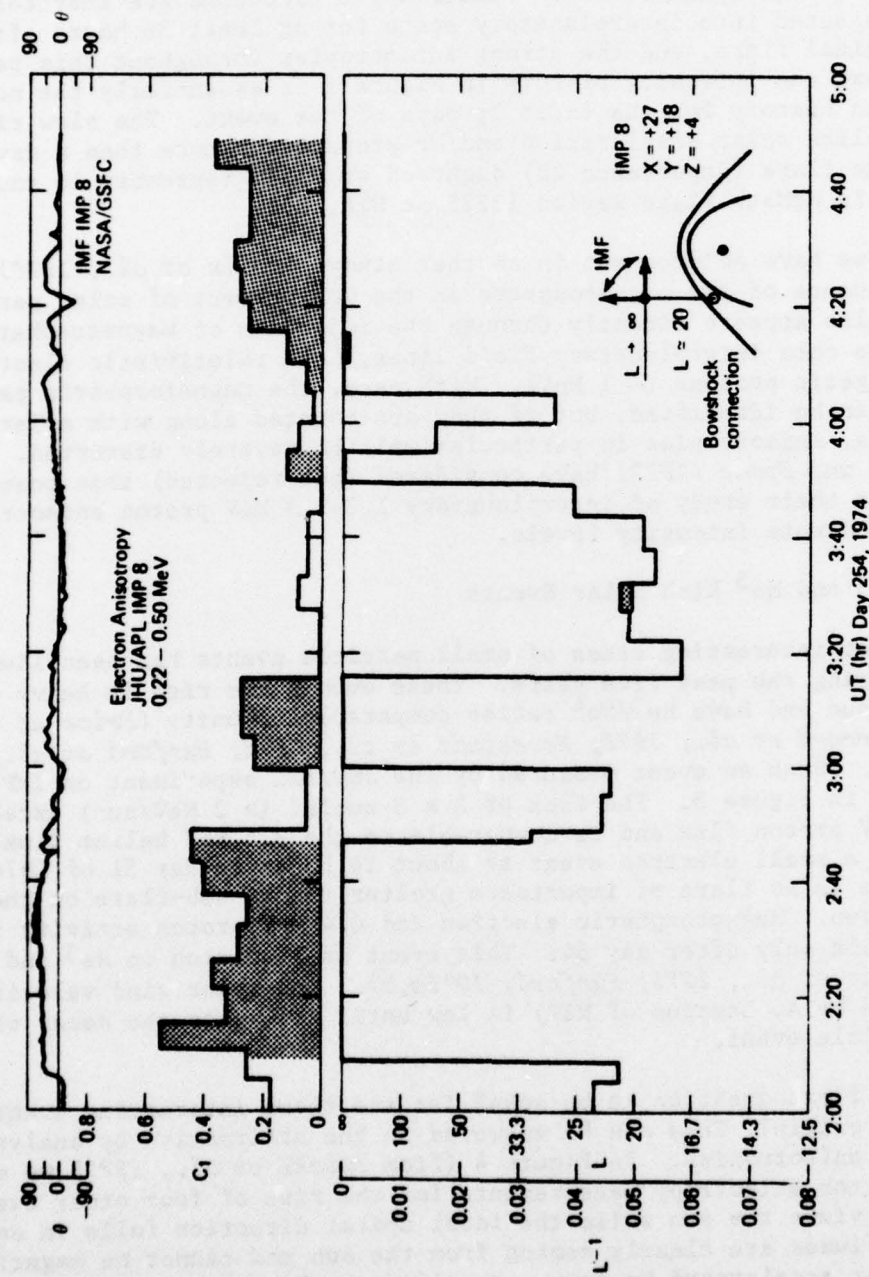


Figure 2. Effect on relativistic electron anisotropy (C_1) of intersection of interplanetary magnetic field line with the bow shock. L is distance in earth radii from IMP-8 to bow shock along extrapolated field line. Shaded periods indicate no intersection ($L \rightarrow \infty$). From Ng and Roelof (1977).

the duration of the relativistic electron anisotropy. The > 0.22 MeV electrons exhibit field-aligned outward anisotropies > 0.2 from the event onset (~ 2300 , September 10) until IMP-8 crosses the dusk bow shock (~ 1800 , September 12). Relativistic electrons are therefore being injected into interplanetary space for at least 36 hours after the original flare, and the strong anisotropies throughout this period imply that the intensity history in Figure 1 is essentially the coronal injection history for the first $1\frac{1}{2}$ days of the event. The slow rise then implies solar acceleration and/or storage for more than a day, since the flare (importance 2B) occurred at 2121, September 10 and was located in McMath Plage Region 13225 at N10, E61.

As we have pointed out in another study (*Sarris et al., 1976*), the influence of the magnetosphere on the measurement of solar particles also appears directly through the injection of magnetospheric particles onto interplanetary field lines, both relativistic electrons and energetic protons (~ 1 MeV). With care, the magnetospheric particles can be identified, but if they are counted along with solar particles, anisotropies in particular will be severely distorted. *Marshall and Stone (1977)* have considered (but rejected) this possibility in their study of interplanetary 1.3-2.3 MeV proton anisotropies at moderate intensity levels.

2. $Z \geq 3$ and He^3 Rich Solar Events

A most interesting class of small particle events has been identified during the past five years. These events are rich in heavy nuclei ≥ 1 MeV/nuc and have He^3/He^4 ratios comparable to unity (*Price et al., 1971; Garrard et al., 1973; Hovestadt et al., 1975; Hurford et al., 1975a,b*). Such an event measured by the JHU/APL experiment on IMP-8, is shown in Figure 3. The flux of $Z \geq 3$ nuclei (≥ 2 MeV/nuc) exceeds the 3 MeV proton flux and is comparable to the 3.5 MeV helium flux. There is a small electron event at about 14 hours on day 51 of 1974, but there is no flare of importance greater than a sub-flare on the visible sun. Magnetospheric electron and 0.4 MeV proton activity is appreciable only after day 54. This event is also rich in He^3 and Fe (*Hovestadt et al., 1975; Hurford, 1975a,b*). The solar wind velocity (provided by A. Lazarus of MIT) is low until well into the decay of the particle event.

The first question to be asked is: Are these interesting events solar in origin? This can be answered in the affirmative by analyzing the flux anisotropies. In Figure 4 (from *Zwickl et al., 1977*) we show the 8-sector anisotropy measurements for the rise of four other events. Sector 5 views the sun while the ideal spiral direction falls in sector 7. The fluxes are clearly coming from the sun and cannot be magnetospheric or accelerated by some unspecified mechanism beyond 1 AU. In fact, since the solar wind speed (Figure 3 top) is low ($< 350 \text{ km s}^{-1}$) and nearly steady during the event, it is unlikely that there is any stream-associated interplanetary acceleration inside 1 AU.

6

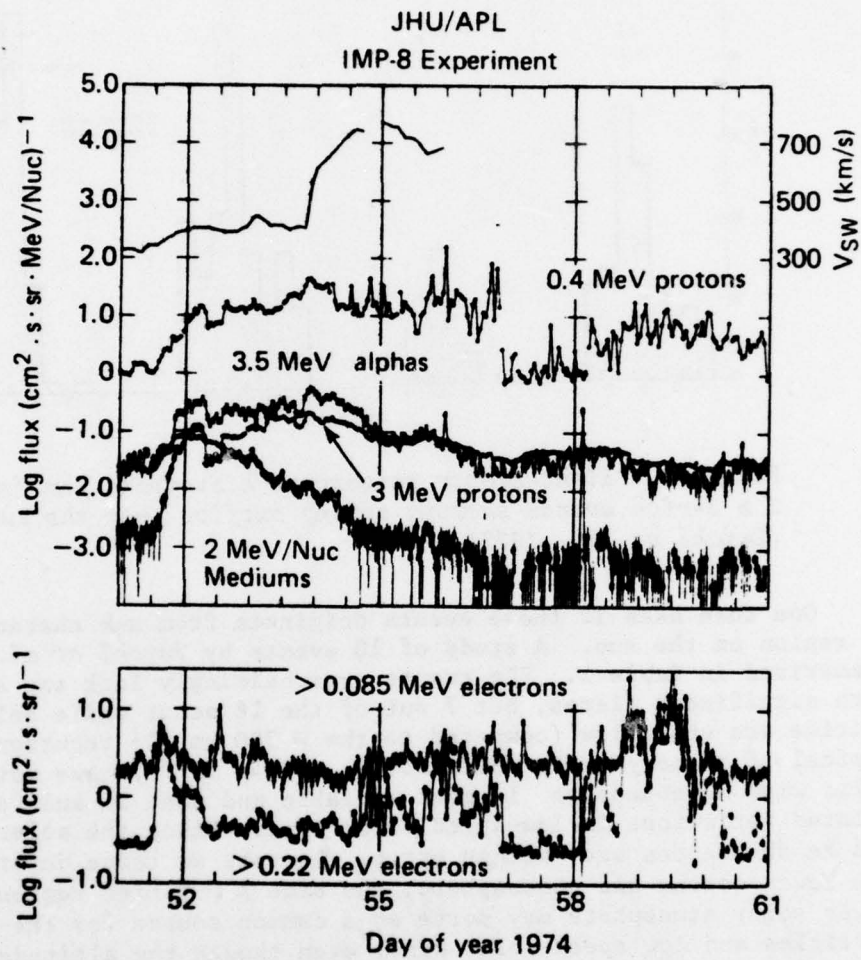


Figure 3. Intensities of ~ 1 MeV solar particles (JHU/APL) and solar wind velocity (MIT) measured on IMP-8 during a $Z \approx 3$ -rich event (Zwickl et al., 1977).

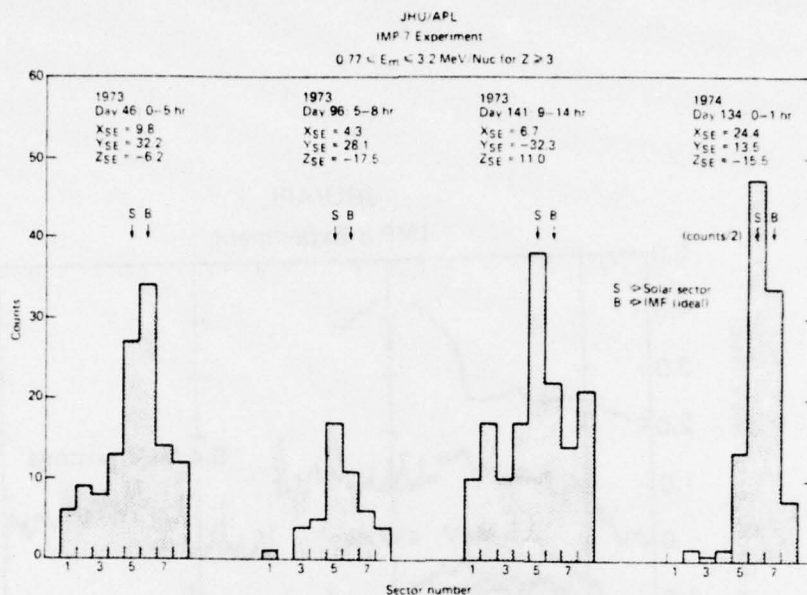


Figure 4. Eight-sector anisotropy histograms for four $Z \geq 3$ -rich events showing strong outflow from the sun. (Zwickl et al., 1977).

One then asks if these events originate from any characteristic type of region on the sun. A study of 10 events by Zwickl et al. (1977) is summarized in Table 1. The events overwhelmingly lack any association with significant flares, but 7 out of the 10 occur while solar wind velocities are quite low (compared to the $> 700 \text{ km s}^{-1}$ recurrent streams typical of these years). Bame et al. (1975, 1977), have noted that the solar wind He abundance is most variable and that Si and Fe show correlated variations in low-speed solar wind. Since the solar wind O, Si and Fe abundances are, within error, the same as those determined for the lower corona and photosphere, the same $Z \geq 3$ rich regions in the lower solar atmosphere may serve as a common source for the energetic particles and low speed solar wind, even though the altitudes of the particle acceleration and plasma heating may still differ.

Thus by identifying the low-speed signature of the solar wind during these events, we may have extracted a significant clue as to the nature of their acceleration.

3. Interplanetary Propagation of $> 10 \text{ MeV}$ Protons: Coronal Connection Effects Near 5 AU

Before discussing the observations in this and the next section, we briefly illustrate in Figure 5 how solar wind stream structure affects the longitude at which the IMF line from earth (or any spacecraft) enters the corona. During the rise of the velocity at the stream leading edge,

TABLE 1. $Z \geq 3$ RICH EVENTS FROM SEPTEMBER 1972 - JANUARY 1976

Event Duration	Flare Assoc.	Particle Data ¹				Solar Wind ² (km/s)	Connection Longitude (°)	Enrichment ³	
		$\gamma(P)$	$\gamma(A)$	$\gamma(Z)$	P/α				
72 302:00 - 304:00	?	2.4	2.0	1.4	25	360 - 410	S(1)	~ 40 → 15	Fe
73 46:00 - 47:18	?	2.7	3.2	2.0	5	325 - 380	D,S	30 → 10	Fe, ³ He
73 96:12 - 99:00	?	2.8	1.5	2.2	15	(?) - 425	D(1)	90 → 70	CNO
73 141:06 - 142:12	?	2.2	2.3	2.2	11	500 - 750	T	190 → 180	CNO
73 179:12 - 181:15	?	3.0	4.5	1.5	4	475 - 750	S,T	45 → 30	Fe, ³ He
73 248:15 - 250:12	?	2.5	3.6	2.9	4	375 - (?)	?(1)	250 → 230	Fe, ³ He
74 51:12 - 52:09	?	2.9	3.5	1.6	6	350 - 415	S	200 → 100	Fe, ³ He
74 127:08 - 130:15	1B,W38?	2.4	3.6	1.5	8	450 - 750	T	230 → 210	Fe, ³ He
74 133:15 - 136:12	2N,W66	3.6	3.6	1.2	25	350 - 410	S	180 → 140	Fe
74 335:12 - 336:12	?	3.1	—	1.6	34	320 - 350	S	60 → 40	Fe

¹ Particle data are derived from ~ 6 hour average at t_{max} . $\gamma(P)$, $\gamma(A)$, $\gamma(Z)$ refer to spectral index for 1.85-7.8 MeV protons, 1.74-11.5 MeV/nuc alpha, and 0.77-3.2 MeV/nuc $Z \geq 3$, respectively. P/α is the proton to alpha ratio at 1.74 to 4.3 MeV, and α/M is the alpha to $Z \geq 3$ ratio at 1.6 to 4.3 MeV.

² S = Solar wind stream onset and early portion of rise.

D = Solar wind stream decay with nearly constant high coronal connection longitude

T = Temporal solar wind stream superimposed on a large stream

i = Incomplete solar wind data

³ Fe and CNO rich designations are derived from scatter plots in Figure 2. ³He designations are taken from Hurford et al. (1975a,b) and Hovestadt et al. (1975).

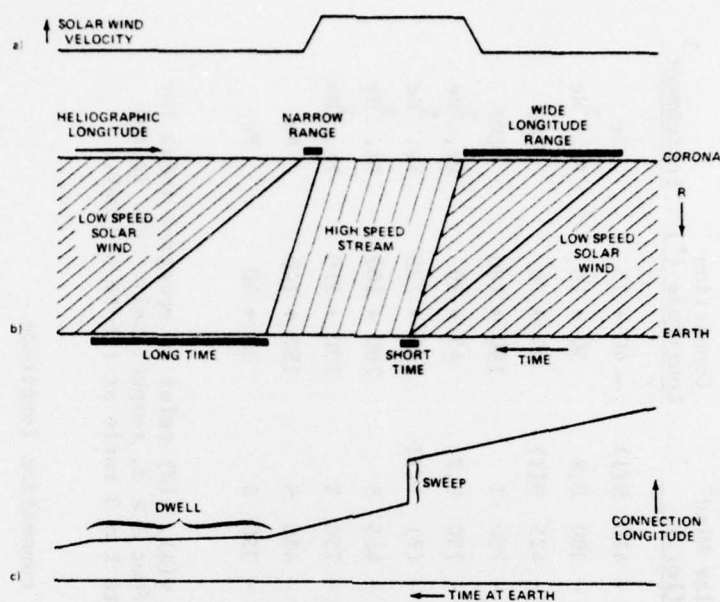


Figure 5. Effect of stationary solar wind stream structure on the coronal connection longitude of the interplanetary magnetic field lines at earth.

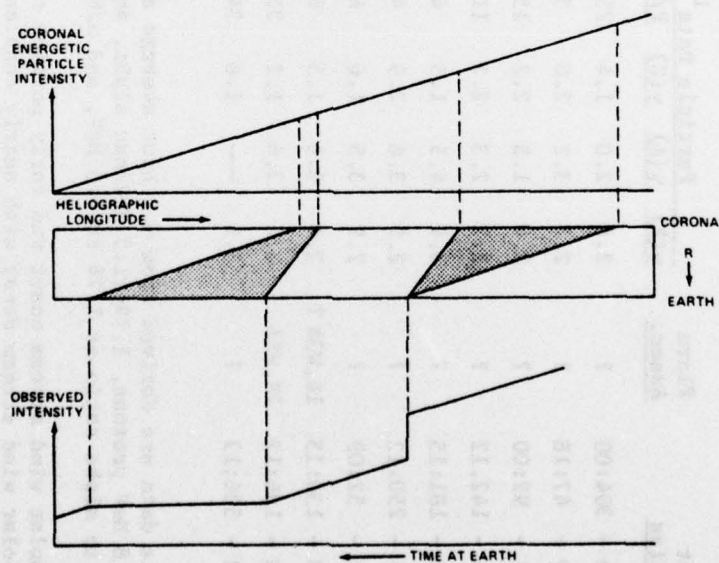


Figure 6. Reconstruction of a simple coronal longitude distribution from a time history of energetic particles at earth "deformed" by solar wind stream structure (Gold et al., 1977).

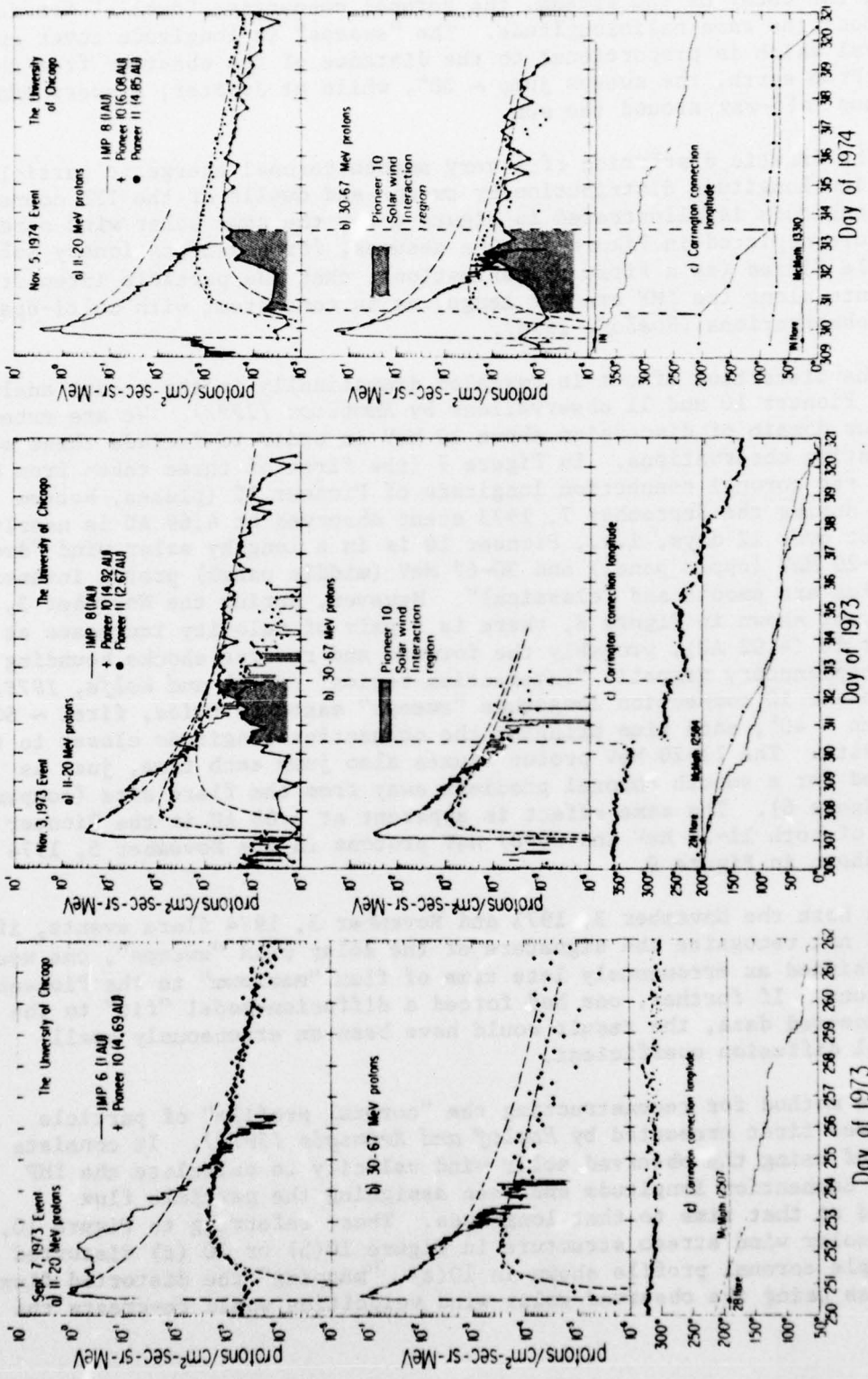
the source of the observed plasma (and hence the "frozen-in" IMF) "sweeps" rapidly over a large longitude interval to the east in the corona, whereas during the decay of the stream, the coronal connection "dwells" for days at almost the same heliolongitude. The "sweeps" in longitude cover an interval which is proportional to the distance of the observer from the sun. From earth, the sweeps jump $\sim 30^\circ$, while at Jupiter, a sweep easily can jump half-way around the sun.

The drastic distortion of a very smooth coronal energetic particle injection longitude distribution by sweeps and dwells of the IMF connection longitude is illustrated in Figure 6 for the same solar wind stream structure depicted in Figure 5. One assumes, for quasi-stationary solar particle fluxes (as a first approximation), that the particle intensity gradients along the IMF are not large, as is consistent with multi-spacecraft observations (*Roelof, 1976*).

The distortion effect is revealed dramatically in the recent analysis of Pioneer 10 and 11 observations by *Hamilton (1977)*. We are extending our domain of discussion above 10 MeV in order to include these most interesting observations. In Figure 7 (the first of three taken from his work), the coronal connection longitude of Pioneer 10 (pluses, bottom panel) during the September 7, 1973 event observed at 4.69 AU is nearly constant over 12 days, i.e., Pioneer 10 is in a lengthy solar wind "dwell". The 11-20 MeV (upper panel) and 30-67 MeV (middle panel) proton intensity histories are smooth and "classical". However, during the November 3, 1973 event shown in Figure 8, there is a pair of velocity increases at Pioneer 10 (4.92 AU), probably the forward and reverse shocks bounding an interplanetary magnetic "interaction region" (*Smith and Wolfe, 1976*). The Pioneer 10 connection longitude "sweeps" eastward twice, first $\sim 60^\circ$ and then $\sim 40^\circ$, each time bringing the connection longitude closer to the flare site. The 11-20 MeV proton fluxes also jump each time, just as expected for a smooth coronal gradient away from the flare site (compare with Figure 6). The same effect is apparent at 6.08 AU in the Pioneer 10 fluxes of both 11-20 MeV and 30-67 MeV protons in the November 5, 1974 event shown in Figure 9.

In both the November 3, 1973 and November 5, 1974 flare events, if one did not recognize the signature of the solar wind "sweeps", one would have assigned an erroneously late time of flux "maximum" to the Pioneer 10 protons. If further, one had forced a diffusion-model "fit" to the uncompensated data, the result would have been an erroneously small parallel diffusion coefficient.

The method for reconstructing the "coronal profile" of particle fluxes was first presented by *Roelof and Krimigis (1973)*. It consists simply of using the observed solar wind velocity to calculate the IMF coronal connection longitude and then assigning the particle flux observed at that time to that longitude. Thus, referring to Figure 10, if the solar wind stream structure in Figure 10(b) or 10(c) distorted the simple coronal profile shown in 10(a), "mapping" the distorted flux histories using the observed solar wind velocities would re-create the



Figures 7, 8 and 9. Intensity histories of three solar proton events observed near earth and in deep space (adapted from Hamilton 1977). Connection longitudes are estimated from observed solar wind velocities; shading marks times of large "sweeps" in longitude which affect particle time histories.

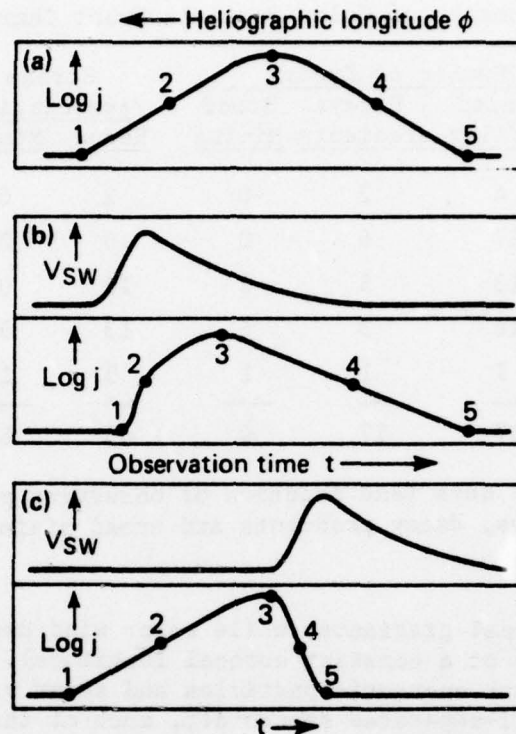


Figure 10. Examples of solar-wind/connection-longitude effects on a symmetric coronal particle injection profile: (a) velocity constant; velocity rise (b) early or (c) late in particle event. (Gold et al., 1977).

simple stationary profile. In other words, the computed connection longitudes provide the "key" to the coronal profile "encoded" by the varying solar wind velocity.

Gold et al. (1977) have carried out this "decoding" of particle events using the JHU/APL particle and the MIT solar wind measurements on IMP-7 and 8 from the launch of IMP-7 in 1972 into 1976. The result, shown in Table 2, of analyzing 1305 days of particle fluxes is that during an average of almost 70% of the time, particle flux histories at 1 AU are dominated by spatial distributions in the corona such as: rounded (quasi-stationary) longitude profiles; coronal gradients away from flare sites (established during the decay of flare event fluxes); and broad minima at longitudes between quasi-stationary distributions.

4. Coronal Propagation of > 7.5 MeV Flare Protons

Reconstruction of coronal longitude particle profiles using solar wind velocities from the same spacecraft requires special circumstances to separate spatial from temporal variations (e.g., solar wind sweeps

TABLE 2. Summary of Solar Particle Event Characteristics

Year	Data Days	Number of Events			Stream Association		Spatial *	
		Rounded Profiles	Decays Gradients	Broad Minima	Round	Minima	Days	(%)
1972	80	4	2	0	2	0	40	50
1973	365	17	6	0	16	0	255	62
1974	365	13	5	2	10	0	215	59
1975	360	16	3	6	13	5	267	74
1976	135	7	1	1	5	1	108	80
72-76	1305	57	17	9	46	6	892	68

* Total number of days (and fraction of observing period) on which rounded profiles, decay gradients and broad minima were identified.

identify longitudinal gradients, while solar wind dwells identify temporal flux changes at a constant coronal longitude). However, when observations of both energetic particles and solar wind velocity are available from well-separated spacecraft, much of the spatial/temporal ambiguities are removed.

Extraordinary circumstances existed in 1969, with Pioneers 6, 7, 8 and 9 distributed over nearly 180° . *McCracken et al. (1971)* and *Keath et al. (1971)* studied flare proton (> 7.5 MeV) events during this period, analyzing the events in terms of the spacecraft longitudes. Recently *Reinhard et al. (1977)* have added the JHU/APL > 10 MeV proton measurements from Explorer 34 and ordered the data in heliolongitude for the flare event of April 10, 1969 by calculating coronal emission longitudes from the solar wind measured on each spacecraft.

The time histories are shown in Figure 11 and one can note the considerable disparities among them. When they are "mapped back" as shown in Figure 12(a) for the initial three days of the event, the disparities order themselves into a remarkable transition (pointed out by *McCracken et al., 1971*), from intensities peaked over the flare site 7 hours after the flare, to a peak nearly two orders of magnitude $\sim 100^\circ$ west of the flare site. Beginning on April 13, the fluxes relax into a nearly perfect exponential longitude distribution with an e-folding scale $\sim 35^\circ$ late in the event. This is almost exactly the idealized longitude distribution shown in Figure 6.

The event becomes even more ordered when the time histories at constant coronal longitude are constructed in Figure 13 (a). These histories are as close as we can come with this technique to flux histories on the "same" field line discussed in idealized theoretical analyses such

14

Flare Apr 10, 1969 P6 - P9 UTD 7.5 - 45 MeV
 N12 E90, 0400 UT E34 APL/JHU > 10 MeV

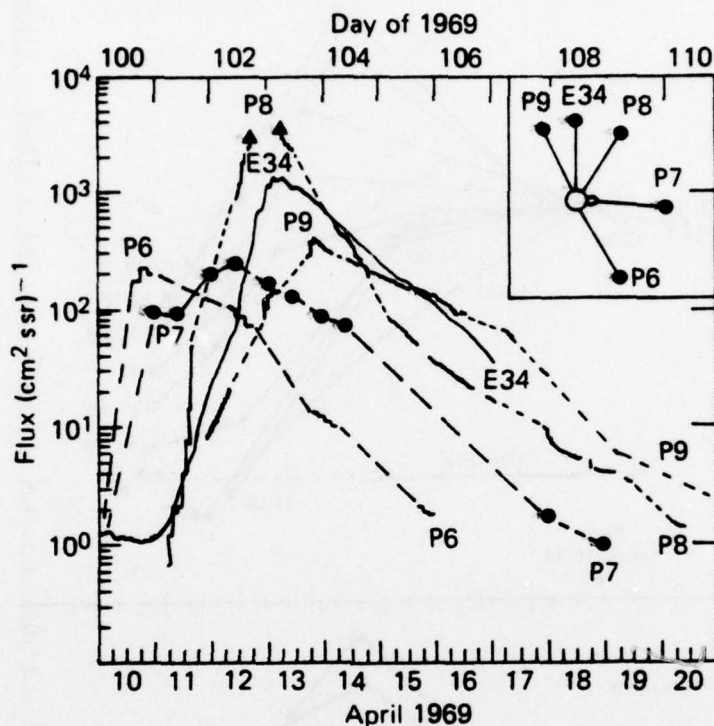


Figure 11. Intensity histories of a ~ 10 MeV solar proton event measured at five spacecraft over 180° longitude in April, 1969 (after McCracken et al., 1971).

as that of Ng and Gleeson (1976). They clearly reveal a second flux increase at all longitudes from the flare site at 60° to 180° . The decay histories are similar, and moreover they are strikingly well fit at each longitude by the function $(t-t_0)^{-k}$ where t_0 is 00 UT, April 11 and $k \approx 4$ for all longitudes.

Comparison of the spacecraft time histories of Figure 11 with the constant helio-longitude histories of Figure 13 demonstrates the necessity of "decoding" the former to obtain the latter. Many portions of the spacecraft histories nearly could be fit piece-wise by exponential distribution in coronal longitude, but all the while the decay at any fixed heliolongitude was much closer to a power law in time.

McKibben (1972), in his compilation of multi-spacecraft observations, fit piece-wise exponential segments to the spacecraft histories. An example, the flare event of December 16, 1967 is shown in Figure 14. However, we note that the breaks in the flux history on December 17 and

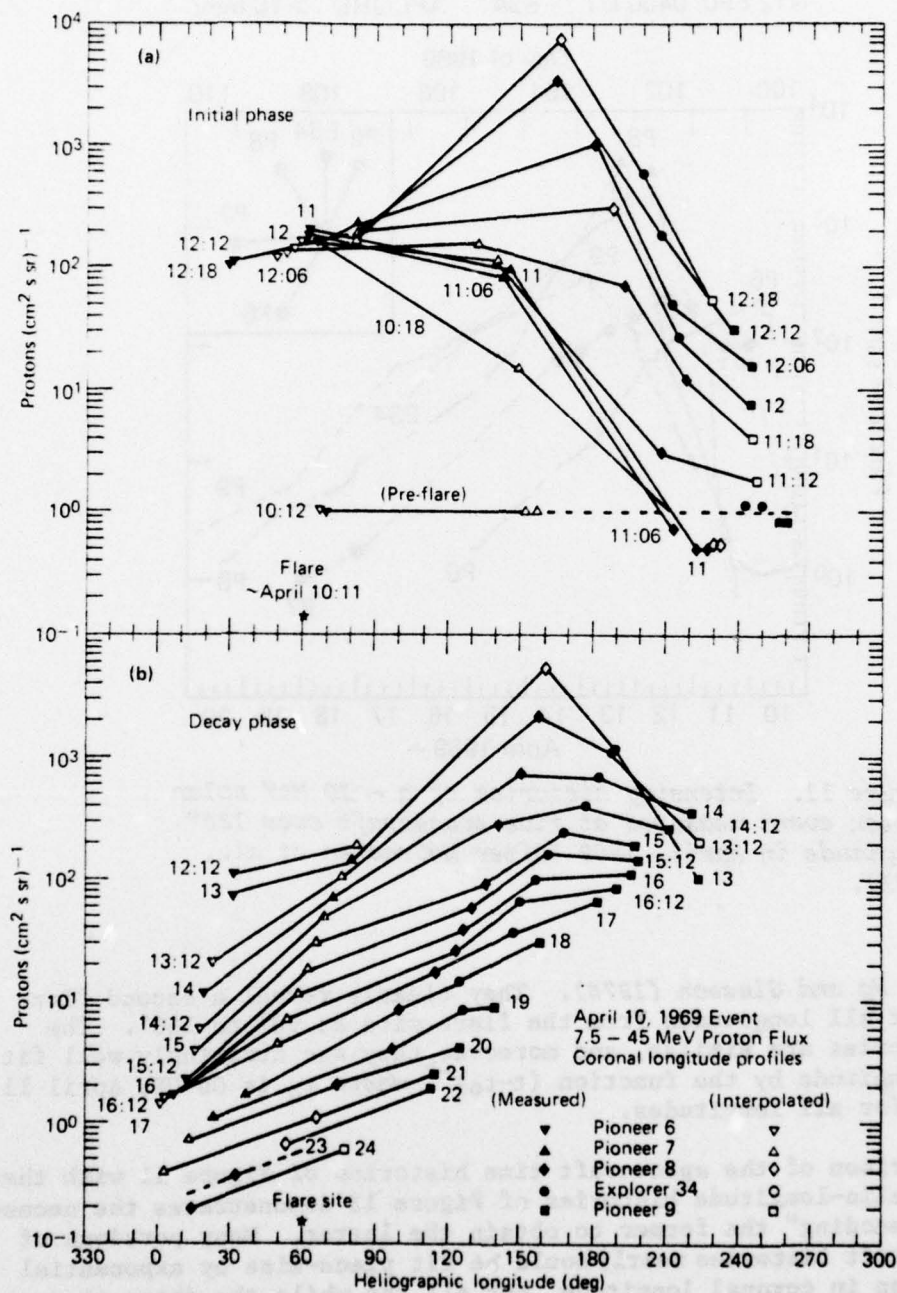


Figure 12. Coronal intensity profiles reconstructed from connection longitudes estimated from solar wind measurements on five spacecraft: (a) initial phase April 10-12, 1969; (b) decay phase April 13-24, 1969 (Reinhard et al., 1977).

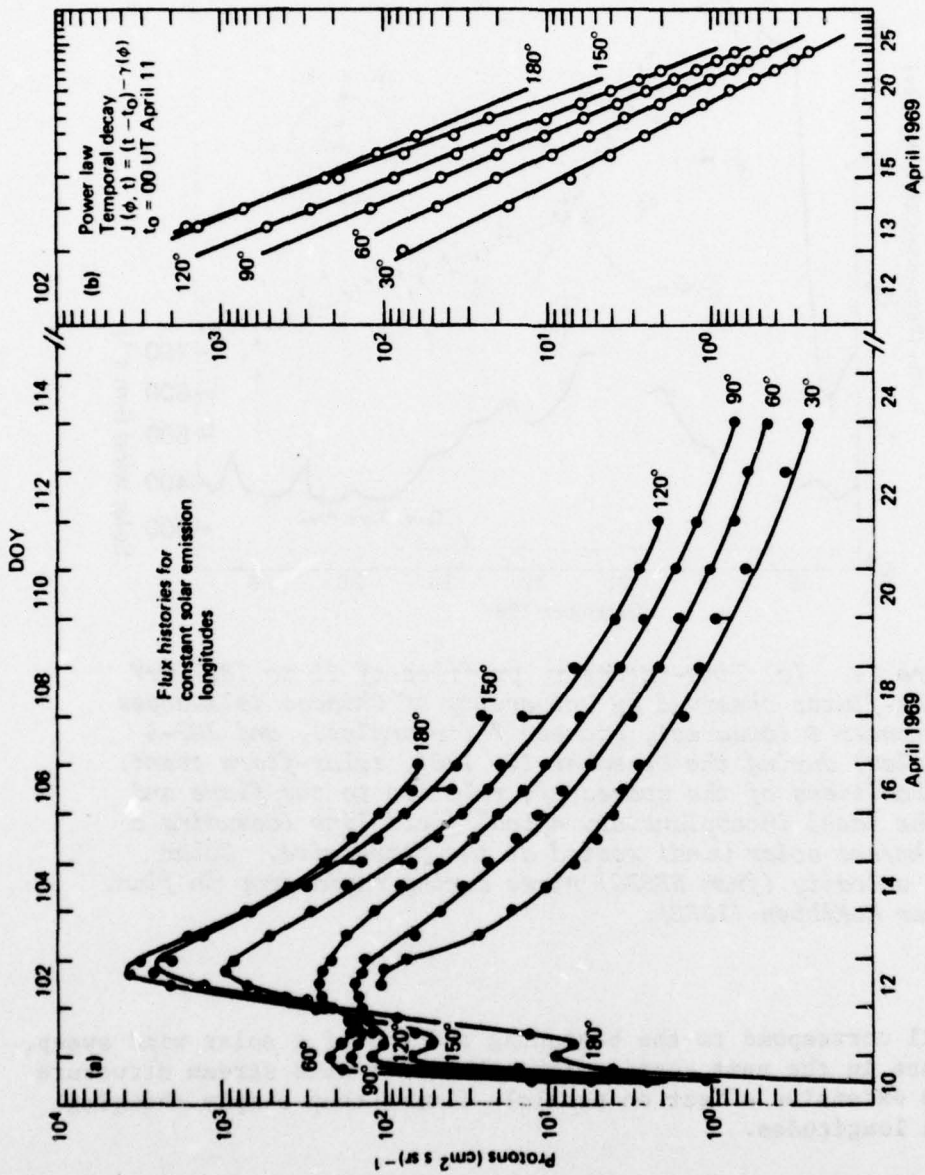


Figure 13. Coronal ~ 10 MeV proton intensity time histories (a) at fixed heliographic longitudes constructed from the coronal intensity profiles of Figure 12; (b) gives the same histories on a logarithmic time scale (Reinhard et al., 1977).

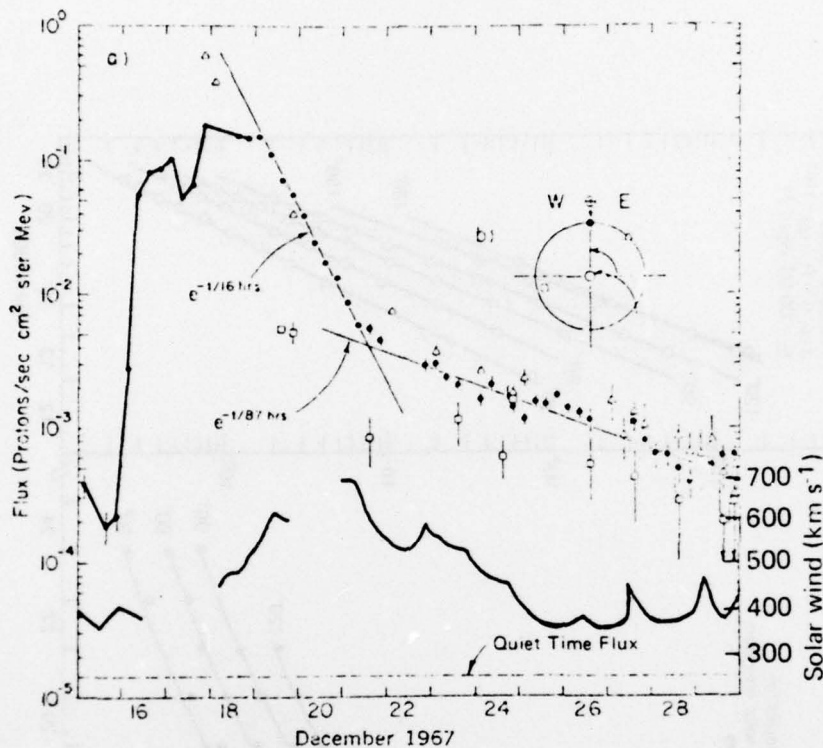


Figure 14. (a) Time-intensity profiles of 15 to 18.7 MeV proton fluxes observed by University of Chicago telescopes on Pioneer 6 (squares), Pioneer 7 (triangles), and IMP-4 (circles) during the December 16, 1967, solar-flare event. (b) Positions of the spacecraft relative to the flare and to the ideal interplanetary spiral field line (assuming a 400 km/sec solar wind) rooted at the flare site. Solar wind velocity (from NSSDC) rises during rapid drop in flux. After McKibben (1972).

December 21 correspond to the beginning and end of a solar wind sweep. We shall see in the next section that the solar wind stream structure has a more extensive effect on particle fluxes than simply changing connection longitudes.

5. Decay Phase Anisotropies of Solar Flare Events

We base this section on the extensive analysis of solar flare proton events ≥ 0.3 MeV from Explorer 35, 1967-1970, by *Innanen and Van Allen (1973)*. The statements concerning the two events we show here apply generally to all seven which they studied.

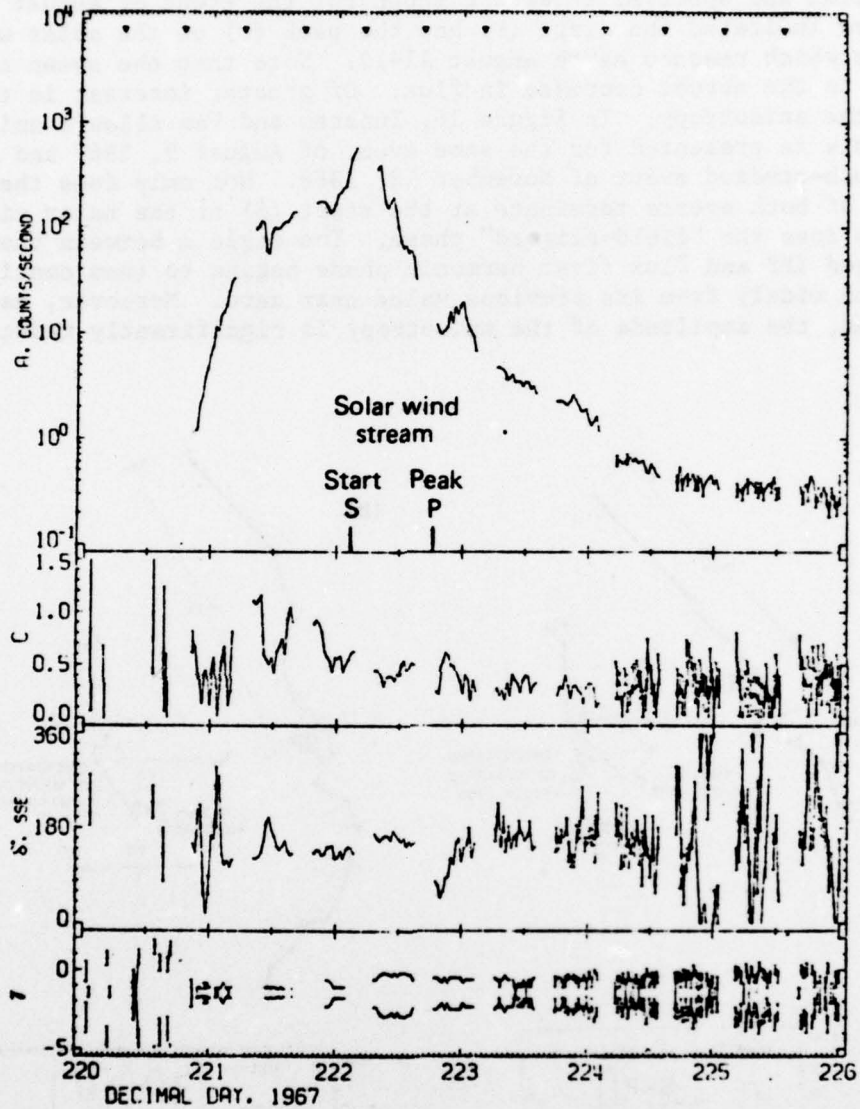


Figure 15. Intensity (A), anisotropy amplitude (C) and direction (δ), and differential spectral exponent (γ) for > 0.3 MeV protons from the University of Iowa detector on Explorer 35 for the flare event beginning August 9, 1967. Start (S) and peak (P) of the solar wind disturbance mark the discontinuity in the intensity history. After Imanen and Van Allen (1973).

In Figure 15, the flux, first harmonic anisotropy magnitude and direction and spectral index are shown for the event of August 9, 1967. We have indicated the start (S) and the peak (P) of the solar wind increase which reached earth August 11-12. Note that the sweep corresponds to the abrupt decrease in flux. Of greater interest is the effect upon the anisotropy. In Figure 16, Innanen and Van Allen's anisotropy analysis is presented for the same event of August 9, 1967 and also for the much-studied event of November 18, 1968. Not only does the "rise" phase of both events terminate at the start (S) of the solar wind increase but so does the "field-aligned" phase. The angle α between the 6-hour averaged IMF and flux first harmonic phase begins to (and continues to) deviate widely from its previous value near zero. Moreover, as can also be seen, the amplitude of the anisotropy is significantly reduced.

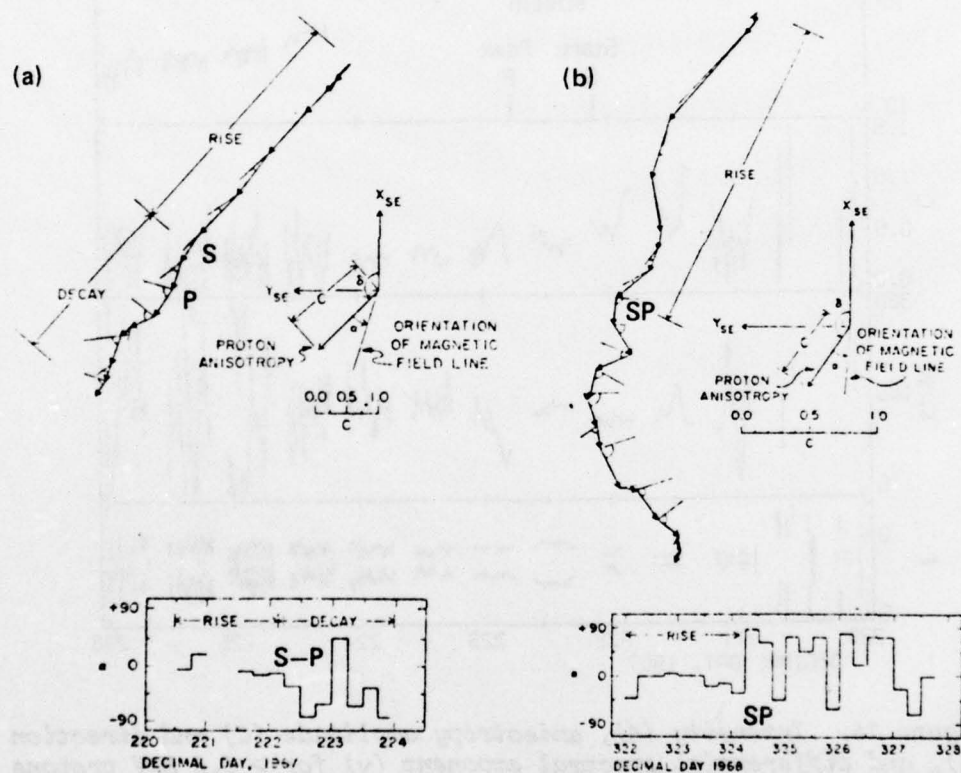


Figure 16. Anisotropy vector plot (6-hour averages in solar-ecliptic coordinates) of > 0.3 MeV protons (see Figure 15) with start (S) and peak (P) of solar wind disturbance corresponding to end of field-aligned phase ($\alpha = 0$). Events (a) August 9, 1967 and (b) November 18, 1968. After Innanen and Van Allen (1973).

A similar association is found in all seven events between the arrival of the flare-heated plasma and the transition to the "decay" phase in which the particle anisotropy is reduced and ceases to be field-aligned.

The decay phase of solar events has been a great puzzle, and no satisfactory explanation has been offered for the tendency of the particle anisotropy to become radial (or sometimes more easterly as seen in > 7.5 MeV protons), and essentially insensitive to the local direction of the IMF (Allum *et al.*, 1974). What has emerged here is that the arrival of the flare-heated solar wind disturbance, which is a *concomitant* of most flare events, actually controls the end of the "field-aligned rise" phase of the event and the transition to the "radial" and later "field-independent" phase. It is therefore not surprising that the diffusion model "fits" to the events using an undisturbed medium could not simultaneously match the intensity and anisotropy histories (Ng and Gleeson, 1971). What is actually happening is that the flare plasma stream-stream interaction with the slower ambient plasma ahead of it inhibits the propagation of particles through it, reducing the anisotropy behind it. The subsequent history of particles behind the interaction is often distorted by the change in flux when the fast solar wind "sweeps" the connection longitude to a region with different intensities than on those field lines in the preceding slow solar wind (see Figure 6).

CONCLUSIONS

There is little more to say; the data really tell the story. Solar energetic particles are so responsive to the dynamic state of the corona, the interplanetary medium and even the magnetosphere, that we make surer progress toward an eventual understanding of the origin of these particles by studying these concomitant interactions as carefully as the acceleration and "undisturbed" interplanetary propagation of the particles themselves.

ACKNOWLEDGEMENTS

This research was supported by the Atmospheric Research Section of the National Science Foundation (Grant ATM-76-23816) and by NASA and the Air Force Geophysics Laboratory under Contract N00017-72-C-4401 between The Johns Hopkins University and the Department of the Navy.

REFERENCES

- Allum, F. R., Palmeira, R. A. R., Rao, U. R., McCracken, K. G., Harries, J. R. and Palmer, I.: 1971, *Solar Phys.*, 17, 241.
 Allum, F. R., Palmeira, R. A. R., McCracken, K. G., Rao, U. R., Fairfield, D. H. and Gleeson, L. J.: 1974, *Solar Phys.*, 38, 227.

- Bame, S. J., Asbridge, J. R., Feldman, W. C., Montgomery, M. D. and Kearney, P. D.: 1975, *Solar Phys.*, 43, 1975.
- Bame, S. J., Asbridge, J. R., Feldman, W. C. and Gosling, J. T.: 1977, *J. Geophys. Res.*, 82, 1487.
- Earl, J. A.: 1974, *Astrophys. J.*, 188, 379.
- Fairfield, D. H.: 1971, *J. Geophys. Res.*, 76, 6700.
- Garrard, T. L., Stone, E. C. and Vogt, R. E.: 1973, in *High Energy Phenomena on the Sun*, R. Ramaty and R. G. Stone (ed.), NASA SP-342, 341.
- Gold, R. E., Krimigis, S. M. and Roelof, E. C.: 1977, *Proc. 15th International Cosmic Ray Conference (Plovdiv, Bulgaria)* in press.
- Hamilton, D. C.: 1977, *University of Chicago Preprint*.
- Hovestadt, D., Klecker, B., Vollmer, O., Gloeckler, G. and Fan, C. Y.: 1975, *Proc. 14th International Cosmic Ray Conference (Munich)*, 5, 1613.
- Hurford, G. J., Mewaldt, R. A., Stone, E. C. and Vogt, R. E.: 1975a, *Astrophys. J. Lett.*, 201, L95.
- Hurford, G. J., Stone, E. C. and Vogt, R. E.: 1975b, *Proc. 14th International Cosmic Ray Conference (Munich)*, 5, 1626.
- Innanen, W. G. and Van Allen, J. A.: 1973, *J. Geophys. Res.*, 78, 1019.
- Keath, E. P., Bukata, R. P., McCracken, K. G. and Rao, U. R.: 1971, *Solar Phys.*, 18, 503.
- Lin, R. P.: 1970a, *J. Geophys. Res.*, 75, 2583.
- Lin, R. P.: 1970b, *Solar Phys.*, 15, 453.
- Marshall, F. E. and Stone, E. C.: 1977, *Geophys. Res. Lett.*, 4, 1977.
- McCracken, K. G., Rao, U. R., Bukata, R. P. and Keath, E. P.: 1971, *Solar Phys.*, 18, 100.
- McKibben, R. B.: 1972, *J. Geophys. Res.*, 77, 3957.
- Ng, C. K. and Gleeson, L. J.: 1971, *Solar Phys.*, 20, 166.
- Ng, C. K. and Gleeson, L. J.: 1976, *Solar Phys.*, 46, 347.
- Ng, C. K. and Roelof, E. C.: 1977, *J. Geophys. Res.* (to be submitted).
- Price, P. B., Hutcheon, I., Cowsik, R. and Barber, D. J.: 1971, *Phys. Rev. Lett.*, 26, 916.
- Roelof, E. C.: 1969, in *Lectures in High Energy Astrophysics*, H. Ogelman and J. R. Wayland (ed.), NASA SP-199, 111.
- Roelof, E. C.: 1976, in *Physics of Solar Planetary Environments*, Proc. of the International Symposium on Solar-Terrestrial Physics (Boulder), D. J. Williams (ed.), American Geophysical Union, 1, 214.
- Roelof, E. C. and Krimigis, S. M.: 1973, *J. Geophys. Res.*, 78, 5375.
- Reinhard, R., Roelof, E. C. and Gold, R. E.: 1977, *J. Geophys. Res.*, (to be submitted).
- Sarris, E. T., Krimigis, S. M. and Armstrong, T. P.: 1976, *J. Geophys. Res.*, 81, 2341.
- Smith, E. J. and Wolfe, J. H.: 1976, *Geophys. Res. Lett.*, 3, 137.
- Zwickl, R. D., Krimigis, S. M., Gold, R. E., Roelof, E. C. and Armstrong, T. P.: 1977, *Proc. 15th International Cosmic Ray Conference (Plovdiv, Bulgaria)*, in press.

22

DISCUSSION

Morfill: When you extract the longitudinal intensity variation from your data (during solar wind streams) is the result consistent with a longitude-independent diffusion coefficient (in interplanetary space)?

Krimigis: Referring to the April 1969 event (Figure 13(b)), the decay phases at a given heliographic longitude all show a power-law time dependence with approximately the same exponent over longitudes from 30° to 150° . Since the influence of coronal propagation is minimized in this late phase ($> 3^d$ after the flare), the inference would be that there is no dependence on solar longitude for interplanetary propagation over these 120° .

Smart: In your Figure 3 you show a heavy ion event that occurs 1 or 2 days before the observation of a high speed solar wind stream. Is it possible the heavy ion event is the result of a high speed solar wind stream that "shorts out" the coronal propagation path (by producing a stream-stream interaction with the slower preceding solar wind), so that what you observed is the result of a solar wind switch?

Krimigis: We have given some thought to the possibility of such a "shorting out" of the connection longitude during an evolving flare-associated solar wind disturbance. However it is much less likely to occur in a co-rotating stream, and the velocity rise on day 53, 1974 (the event in Figure 3), is not flare-associated (Table 1). It is corotating, being part of the highly recurrent series which characterized 1974.

Wibberenz: The observer may be located at very different positions with respect to an interaction region, when a particle flare occurs. Why should this region hit the observer always late in the decay phase — in order to explain the easterly anisotropy?

Krimigis: By the "interaction region", I take it you mean the leading edge of the flare-associated solar wind disturbance. Since the flare also accelerated the energetic particles, the disturbance (which has a broad front in longitude), will usually reach earth 2 to 3 days after the particle increase, i.e., in the decay phase. The data reveal that it is at this time that the field-aligned anisotropy terminates; the 300 keV protons do not necessarily exhibit an "easterly anisotropy" after the solar wind disturbance.

Wibberenz: I would like to comment on the statement that the diffusion picture does not work if the anisotropies are large. For > 10 MeV protons the diffusion concept is generally valid, and large anisotropies merely indicate long-lasting solar injection. During an individual event the diffusion coefficient may vary by about a factor of 2.

Krimigis: Large anisotropies (> 0.50) cannot be consistent with diffusion-dominated transport. They imply that the time history is essentially the source injection history as long as the large

anisotropy persists. We seriously question whether the diffusion concept has truly been proven valid for > 10 MeV protons since the severe distortions introduced by coronal injection gradients and solar wind disturbances (Figures 12 and 14) have not been properly considered in fitting diffusion parameters to event time histories.

FLUXES OF > 50 keV PROTONS AND > 30 keV
ELECTRONS AT $\sim 35 R_e$. 4. ASSOCIATION OF
INTENSE BURSTS OF ENERGETIC PARTICLES IN
THE MAGNETOTAIL WITH THE EXPANSION PHASE
OF GEOMAGNETIC SUBSTORMS

E. C. Roelof
E. P. Keath
Takesi Iijima *

The Johns Hopkins University
Applied Physics Laboratory
Laurel, Maryland 20810

APRIL 1976

Submitted to Journal of Geophysical Research

* Senior Postdoctoral Research Associate on leave from
Geophysics Research Laboratory, University of Tokyo

ABSTRACT

Combining IMP-7 measurements of energetic protons (50-200 keV and 290-500 keV) with magnetograms from auroral zone and mid-latitude observations, we find that 13 high intensity proton bursts observed near the plasma-sheet in the dusk magnetotail $\sim 35 R_e$ during 1973 are directly associated with the expansion phase of large geomagnetic substorms at the western-most auroral zone station observing the disturbance. The sharp depression in H ($\Delta H > 400 \gamma$) is consistent with a western intrusion of the westward auroral electrojet deep into the premidnight sector. From detailed angular flux distributions with 20 s time resolution we conclude that the proton bursts are non-thermal in nature. The bulk flow of the bursts is tailward during the intensification of the auroral magnetic disturbance, and is sunward during the recovery phase at the western-most station. We suggest a possible physical connection via open magnetotail fieldlines of the electric fields driving the westward auroral electrojet and those accelerating the particles in the magnetotail.

1. INTRODUCTION

We report here our finding that all unusually high intensity bursts $\geq 10^6 (\text{cm}^2 \text{s ster})^{-1}$ of protons in the energy range $\sim 50\text{--}200$ keV in the dusk plasmashet at $\sim 35 R_e$ reported by Roelof et al. (1976) and Keath et al. (1976) occurred during geomagnetic substorms within what may be the intensification stage of the westward auroral electrojet. We show that the tailward-moving particle bursts (which are observed predominantly inside the dusk magnetopause) tend to accompany large decreases ($> 400 \gamma$) in the H-component of the geomagnetic field observed at high latitude stations estimated to be closest in magnetic local time (MLT) to the foot of the magnetic flux tube containing the spacecraft. Moreover, when there are subsequent sunward bursts of > 50 keV protons of comparable intensity $> 0.25 \times 10^6 (\text{cm}^2 \text{s ster})^{-1}$ following the tailward bursts, they usually occur during the withdrawal phase of the intrusion from the premidnight sector (even though there may still be intensification of the westward auroral electrojet in the post-midnight sector). Comparison of fine time-scale (~ 20 s) angular flux distributions of 50–200 keV protons with those in the range 290–500 keV reported by Sarris et al. (1976a) reveals that these very high intensity bursts are non-thermal in nature. Energetic electrons (> 30 keV) generally accompany the proton bursts, but the electron intensity variations agree only loosely with those of the protons on time scales less than ~ 5 minutes. The electron anisotropies, when measureable, are usually consistent with the direction of proton anisotropies (on the same loose time scale), so that the acceleration region might be the same for both protons and electrons. Sarris et al. (1976b) have described a magnetotail burst event in which the acceleration region extended less than $1 R_e$ at $35 R_e$. Our results are therefore consistent with models of substorms in which the expansion phase is associated with formation of near-Earth neutral lines within a thinned plasmashet (Hones et al., 1973; McPherron et al., 1973; Pytte et al., 1976).

2. OBSERVATIONS OF HIGH INTENSITY PROTON BURSTS

Recently we discussed observations of extremely high intensity bursts of 50–200 keV protons in the dusk plasmashet (Roelof et al., 1976; Keath et al., 1976). These bursts, detected by the National Oceanic and Atmospheric Administration/Applied Physics Laboratory Energetic Particle Experiment (EPE) on the

IMP-7 spacecraft, (near-circular orbit $\sim 35 R_e$, inclination $\sim 30^\circ$) had peak fluxes exceeding $10^6 (\text{cm}^2 \text{s sr})^{-1}$ and exhibited fluctuations on the time scale ~ 1 minute with an overall event duration ≤ 1 hour. Some sixteen burst events were found during the first year of IMP-7 observations (October 1972-October 1973). Although several events often occurred on the same orbit (and hence extended well into the plasmashet towards the midnight meridian from the dusk magnetopause), most events were detected in the region $11 < Y_{SM} < 22$ and $|Z_{SM}| < 5$ (in units of earth radii). In the magnetotail, IMP-7 is in the region $-25 R_e > X > -35 R_e$. We noted that the 50-200 keV high intensity proton events also extended into energies > 290 keV as measured by the APL/JHU Charged Particle Measurements Experiment (CPME) and discussed by Sarris et al. (1976a), and we also pointed out that the EPE high intensity events occurred under disturbed geomagnetic conditions $3 \leq K_p \leq 8$. The detailed parameters from which the above statements were derived were presented in Table 2 of Keath et al. (1976), and selected data are repeated in Table 1 of this paper. Descriptions of the EPE and CPME detectors will be found in the papers by Roelof et al. (1976) and Sarris et al. (1976a) respectively.

Table 1 contains all high intensity proton events observed on IMP-7 January through October 1973. We do not discuss the three events from 1972 that were in our original Table due to an insufficient amount of available magnetograms for October-December 1972. We give, for all the proton events, the start time, the peak observed flux in the 50-200 keV channel of the EPE detector, the 3-hour K_p value and the position of IMP-7 in solar magnetic (SM) coordinates in Earth radii. The new information in Table 1 includes the magnetic local time (MLT) of the auroral zone observatory (indicated by standard abbreviation) which recorded the furthest intrusion of the magnetic disturbance into the premidnight sector during the proton event as well as the maximum negative excursion of the H-component (to the nearest 100 γ) from its quiet value during the sporadic fluctuations in the intensification phase.

Figures 1a and 1b show the anisotropy history of burst Event 11 (0514 UT, October 3, 1973) reported by Roelof et al., (1976) for 50-200 keV protons from the EPE. Also shown are the 290-500 keV CPME angular distributions. The "arrival direction" is given in solar ecliptic coordinates, so that 0° corresponds to particles moving tailward, 180° moving towards the sun,

90° and 270° moving toward the dawn and dusk magnetopause, respectively. Despite the lesser angular resolution of the higher energy protons (8 sectors for the CPME vs. 16 sectors for the EPE), the contours for the multiple tailward events 0520-0540 UT in Figure 1a are very similar (although we note a larger dawn-to-dusk component in the 50-200 keV proton bursts). This burst event occurred close to the nominal neutral sheet ($Z_{SM} = 0.4 R_E$) and well inside the dusk magnetopause ($Y_{SM} = 17.5 R_E$). Its anisotropy history is representative of most of the high intensity events in Table 1.

Simple estimates reveal that the 290-500 keV protons cannot be thermal in origin, since even though they display very soft energy spectra with power-law indices $5 < \gamma < 7$, reasonable temperatures (< 20 keV) would imply $\gamma > 30$ (Sarris et al., 1976a). Therefore the similarity of the 290-500 keV angular distributions to the 50-200 keV protons implies that the latter are also non-thermal. This result was anticipated by Roelof et al. (1976) who showed that although the much more prevalent low-intensity 50 keV proton events $\leq 10^4 (\text{cm}^2 \text{s ster})^{-1}$ could be interpreted as the high energy thermal tail of fast plasma flow commonly observed in the magnetotail (e.g., Hones et al., 1976), the very high intensity > 50 keV proton bursts under discussion here formed a special class of events that could be non-thermal. We now can confirm this possibility.

Figure 1b shows the remainder of the burst sequence begun in Figure 1a. Often the tailward bursts are followed by a series of sunward bursts. These were seen on October 3, 1973 from about 0552 UT to 0618 UT. Return bursts often persist for ~ 1 hour at > 50 keV, but their intensities decrease and merge with the general low-intensity sunward flow reported by Keath et al. (1976). The anisotropy structure is generally similar, but note that the return bursts are not strictly time coincident at the two energies. Also, once again there is a cross-tail component, but now it is comparable at both energies and in the dusk-to-dawn direction. Unfortunately no IMP-7 magnetic field measurements are available to determine if this is simply flow along a field line with $\phi_{SE} \approx 150^\circ$.

As another example of the non-thermal nature of this class of high intensity bursts, we present in Figures 2a and 2b burst Event 1, March 26, 1973. Perhaps because of its location, Event 1 displays features not found

in the other burst events we have examined. As can be seen from Table 1, IMP-7 was closer to the nominal position of the dusk magnetopause than it was for the October 3, 1973 event ($Y_{SM} = 21.9 R_e$), but the spacecraft was further south of the nominal neutral sheet ($Z_{SM} = -4.8 R_e$). There is only a single high intensity burst at 1833 UT, and it is preceded by an isolated bi-directional burst at 1829 UT whose angular distribution resembles trapped particles with pitch angles $\sim 90^\circ$. This "precursor" is in striking contrast with the "drop-out" of fluxes at 0519-0520 UT which preceded the chain of large tailward bursts in the October 3 event (Figure 1a). The "precursor" appears to be an atypical feature which we have not found in other high intensity bursts. Also in contrast, the single tailward burst on March 26 shows no strong cross-tail component, although the return bursts display a strong dusk-to-dawn component at both energies. Magnetometer measurements were available for this event (R. Lepping and N. Ness, Private Communication, 1975). The field azimuth was rather steady at $\varphi_{SE} \approx 180^\circ$ during the hour 1830-1930 UT on March 26, therefore transverse flow occurred only during the sunward return bursts.

As discussed by Keath et al. (1976) and Sarris et al. (1976a), proton burst events are often accompanied by similar near-relativistic electron events at energies 30-90 keV and 0.22-2 MeV. Since these particles travel a path length of $\sim 100 R_e$ during the 5-second accumulation time of the IMP-7 instruments, their anisotropies are much smaller than the 50-200 keV protons (which travel only $\sim 3 R_e$ in 5 s). The electrons have ample time to distribute themselves inside of $35 R_e$ during a sample period, while the protons do not. Therefore we have concentrated on the protons as a diagnostic of the acceleration process. However, the electrons provide important information, and we illustrate this in Figure 3 for burst Event 2 (March 27, 1973, 0100-0300 UT). We have averaged the three sunward sectors (8, 9 and 10) with the three anti-sunward sectors (1, 2 and 3) for the 50-200 keV protons measured by the EPE. We have also averaged sectors 1 and 8 for the 30-90 keV electrons, since on the IMP-7 instrument, sectors 9-14 are desensitized by solar EUV flux.

These proton and electron "field-aligned" fluxes are plotted in Figures 3b and 3c, with periods of well-defined anisotropy indicated by bars labelled "sunward" or "tailward". A 30-200 keV proton anisotropy plot (in the same format as Figures 1 and 2) is given in Figure 3a. There is a general correspondence in proton and electron increases within a temporal resolution

of ~ 5 minutes. Where electron anisotropies are prominent enough for identification, they also agree with the proton anisotropies. However, note that the largest proton bursts at 0103 UT and 0112 UT are accompanied by two of the smaller 30-90 keV electron bursts, while the largest electron event, beginning 0204 UT, was accompanied by proton fluxes an order of magnitude lower than the events at 0103 UT and 0112 UT.

There is also a qualitative difference apparent between Figures 3b and 3c, in that the electron events display a smoother, quasi-exponential decay while the protons show abrupt decays, dropping several orders of magnitude within 20 seconds (the time between 5 second samples). None-the-less, the tendency toward agreement in general intensity and in changes of anisotropy directions implies a common acceleration region in the magnetotail for 30-200 keV protons and 30-90 keV electrons in these high intensity burst events.

These three examples reveal that even though the general sequence of these high-intensity bursts is one of tailward flow followed by sunward flow, the detailed structure contains more complexity than is conveyed in the general description. We leave the study of these significant details to a paper currently in preparation, and now turn to the association of these particle bursts with the development of magnetic substorms.

3. BURST ASSOCIATION WITH THE WESTWARD AURORAL ELECTROJET

In a recent study by our group (Sarris et al., 1976b), a single burst event was found during a fortuitous alignment of the IMP-6 and IMP-7 spacecraft which allowed the acceleration region of the burst to be localized. The > 50 keV proton flux in this event (October 16, 1973) was too small $< 0.6 \times 10^6 (\text{cm}^2 \text{s sr})^{-1}$ to be included in our list of high intensity events. We had pointed out that the 0520 UT October 3, 1973 tailward burst events occurred during the expansion phase of a substorm, as evidenced by a large decrease ($> 1000 \gamma$) in the H-component of the geomagnetic field at Point Barrow (Roelof et al., 1976). Examination of the H-component at a ring of auroral stations led Sarris et al. (1976b) to conclude that the October 16, 1973 event occurred during the maximum phase of a large auroral substorm ($\Delta H \sim 300 \gamma$), and the apparent earthward movement of the acceleration region in the magnetotail coincided with the active component of the westward auroral electrojet observed around midnight. The spacecraft were in the premidnight sector of the tail, but only $2 R_e$ from the midnight

meridian. The smallest value of Y_{SM} for the 13 events in Table 1 is $3.2 R_e$, with only 4 high intensity burst events occurring in the range $3 R_e < Y_{SM} < 10 R_e$; the remaining 9 occurred at $Y_{SM} > 10 R_e$.

We examined magnetograms which were available for the 13 high intensity burst events observed in 1973 by IMP-7 (See Table 1) and found that every event occurred during the intensification phase of substorms. Although a sufficient number of auroral magnetograms were not available for an unambiguous identification, we suggest that the disturbances may represent the intrusion of the westward auroral electrojet deep into the premidnight sector. These events therefore differ considerably from the usual appearance in substorms of the sharp intensification of the westward auroral electrojet; the more common intensifications are smaller in amplitude and occur in the premidnight or early postmidnight sectors. In Figure 4, we present the H-component traces from the auroral stations earliest in magnetic local time (MLT) which detected the apparent intensification of the westward electrojet. The MLT at the onset of the tailward bursts is given at the lower left of the panel for each trace. For all events, $\Delta H > 400 \gamma$. The occurrence of the 50-200 keV tailward proton bursts is indicated by individual bars, and the shading indicates the period over which high-intensity tailward bursts were observed. Also marked by individual bars outside the shading are the subsequent sunward bursts, whenever they were observed. The inset shows the (Y_{SM}, Z_{SM}) location of IMP-7 for each of the events, numbered in chronological order (the same as in Table 1).

We have also sketched on the inset the field-line mapping onto the $X = -10 R_e$ plane of the MLT and magnetic latitude of auroral zone field lines as given by Fairfield and Mead (1975) in their Figure 4. The mapping is calculated from a model (Mead and Fairfield, 1975) utilizing quadratic Taylor expansion coefficients of the field components which give a best fit to field vectors observed by spacecraft over the epoch 1966-1972 between 4 and $17 R_e$ (under non-quiet geomagnetic conditions, $K_p \geq 2$). It seems plausible, due to the flaring tendency of open field lines in the magnetotail, that if we project the actual spacecraft position ($X \sim -30 R_e$) on the YZ plane at $X = -10 R_e$, the indicated MLT should be a lower limit to the actual MLT of the foot of the field line from the IMP-7 orbit $X \approx -30 R_e$. We feel this very approximate limit serves as a useful indicator despite the stated lack of strict

validity of the Mead-Fairfield model beyond $17 R_e$. In any case, a more exact estimate seems inappropriate, since it is difficult to assign a well-defined field-line connection under the very disturbed conditions during which the high intensity proton events occur. We shall now see that these approximate spacecraft MLT connections (indicated in parentheses in each of the magnetogram panels of Figure 4), do tend to order the data.

The pattern of association becomes clear when one compares the MLT of the western-most available auroral station displaying the auroral system expansion signature with the rough estimate of the mapped spacecraft MLT from the inset in Figure 4. For Events 3, 6, 7, 8, 11, 12 and 13 the two MLT agree within 2 hours. Figure 4 is arranged so that these events are displayed in the lower 7 panels. Note, for instance, that for the very large Event 11 which occurred well over towards the dusk magnetopause ($Y_{SM} = 17.5 R_e$) that the westward electrojet was observed as far as 1710 MLT, well into the pre-midnight sector. Examination of the H-traces for these events reveals that the tailward proton bursts coincided closely with the intensification phase of the magnetic disturbance which often displayed large sporadic variations. Moreover, in five out of these seven events (the exceptions are Events 3 and 12), subsequent sunward bursts were detected in IMP-7, and all fell within the recovery phase of the magnetic disturbances.

For the remaining six events (1, 2, 4, 5, 9 and 10), the agreement between observatory and estimated spacecraft MLT is poorer, and this is reflected in the looser correspondence of the tailward burst times and the substorm intensification phase. This comparison is easily made from Figure 4, since the six events with poor MLT agreement fall in the upper two rows of the figure. One inference which could be drawn from all 13 events is that the intense proton bursts tend to be localized in the magnetotail on field lines mapping to the western-most extent of the development of the westward auroral electrojet. It is also true that the 6 events with poor MLT agreement are also the events which are among the closest to the dusk magnetopause. However Events 11 and 12 occur in the same location, but with better MLT agreement and also cleaner association with the intensification phase, so we are inclined to accept the physical significance of the MLT agreement of the approximate spacecraft field line connection and the western-most observation of the electrojet intensifications. We shall now document in some detail the nature of these geomagnetic events associated with energetic particle acceleration.

4. DISCUSSION OF GROUND MAGNETOGRAMS

From an inspection of the auroral electrojet activity indices (Allen et al., 1975) and an examination of individual geomagnetic records obtained in the northern hemisphere, we have determined that all events described in the previous section were observed during the intensification phase of magnetic substorms. We suggest that at these times the westward auroral electrojet was locally and sporadically intensified and travelled westward, intruding well into the premidnight sector. Figure 5 shows the ground-based magnetic disturbances for the large burst Event 11 beginning on ~ 0514 UT, October 3, 1973. The bursts are indicated by bars and shading as in Figure 4. This burst event seems to be directly associated with the auroral geomagnetic activity which was initially intensified about 0500 UT at longitudes ~ 2200-0000 MLT (Fort Churchill and Great Whate), and then expanded westward toward the evening hours as seen at Point Barrow (~ 1700 MLT). Especially at Point Barrow, which is estimated to be located close to the MLT meridian of the IMP-7 burst observation in the dusk side magnetotail (see inset to Figure 4), the geomagnetic activity was characterized by sporadic and intermittent intensification with a time scale of the order of ten minutes.

Simultaneous magnetic disturbances at low latitudes, shown in Figure 6, supplement and support the above-mentioned signature for the westward expansion of the westward auroral electrojet during the October 3 event. There is a westward progression of the region where a sharp increase of the H-component perturbation was occurring. This may be taken as an indication of westward movement at low latitudes of the return current of the westward auroral electrojet activity. The ΔH -increase was observed first in ~ 2100-0100 MLT sector (from Tucson toward San Juan) at ~ 0500 UT and ~ 10 minutes later at Honolulu (~ 1830 MLT). A time-delay of this magnitude was also seen for the peak time as well as the onset time of the ΔH -increase.

Figures 7, 8 and 9 show low-latitude magnetic records for four other burst events (Events 4, 6, 7 and 13). In each figure, the H and D component records are arranged from top to bottom as observed from the near-midnight region toward the evening region in MLT. The periods of tailward and sunward proton bursts are indicated as in Figure 4. In every case, a systematic time delay (with a magnitude of the order of ~ 10 minutes) for

the onset time and the peak-time of the ΔH -increase from the near-midnight toward the evening hours is observed associated with the expansion of the westward auroral electrojet (as tentatively identified by the signature illustrated in Figure 5 of the H-component record at auroral-zone observatories).

Although the westward progression of the low-latitude disturbances is consistent with the westward intrusion of the westward auroral electrojet the following points should be kept in mind. The magnetic disturbances observed at low latitudes show the integrated effect of the auroral electrojet system which connects the high-latitude ionosphere and the magnetotail via field-aligned currents. In this sense, the low-latitude disturbance is helpful when we discuss the current systems macroscopically. However, it is another question whether the low-latitude magnetic disturbance is truly ascribable to the ionospheric leakage current from the high-latitude auroral electrojet or not. At present, there is no unambiguous interpretation for the low-latitude disturbance, since although some portion would be due to ionospheric return currents, other portions are ascribable to the magnetic effects of the magnetotail current, the enhanced ring current, and field-aligned auroral currents. Indeed, Iijima and Potemra (in preparation, 1976) have shown that the auroral field-aligned current system as measured by the TRIAD satellite is enhanced and moves equatorward during geomagnetic conditions defined by the magnetitude of the AL index (Allen et al., 1975) exceeding 100 γ . We find it extremely suggestive that they find the greatest enhancement and distortion of the current occurring between 1700 and 2300 MLT. These were the ranges of MLT in which the agreement between high intensity particle bursts and ΔH were closest, as seen in Figure 4.

5. CONCLUSIONS

The observation of the tailward high intensity energetic proton bursts on open field lines (which we suggest map from the tail to the westernmost observable intensification of the electrojet), provides further insight into the preferential occurrence of these large proton events exclusively in the dusk sector of the plasma sheet at $\sim 35 R_e$. We feel that this association of high intensity particle events and auroral magnetic disturbances

(both occurring in the premidnight sector in MLT), is established independently of the details of mapping open field lines outward from the auroral zone into the dusk magnetotail. If the acceleration mechanism is indeed the merging of magnetic field lines along one or several magnetic neutral lines (Hones et al., 1973), we have already reported that the pattern of tailward and subsequent sunward bursts is consistent with the location of such neutral lines initially earthward of $35 R_e$ and subsequently tailward of the orbit of IMP-7 (Keath et al., 1976). There is no reason why this pattern for large bursts should be typical of smaller bursts or bursts nearer the midnight meridian, such as the event observed by IMP-6 and IMP-7 only $2 R_e$ into the premidnight sector of the magnetotail (Sarris et al., 1976b).

The observations reported here may carry an additional implication. The acceleration mechanism (which we have now established to be non-thermal at 50 keV in these high intensity proton bursts and hence not necessarily coupled to the motion of the hot plasma), is most efficient on open field lines towards the dusk edge of the plasmashet. Fukushima and Kamide (1973) have suggested that during the expansion phase of substorms the westward auroral electrojet is driven from the neutral sheet tail current (shorted into the ionosphere by Birkeland currents). Field-aligned currents have been observed by the TRIAD satellite (Iijima and Potemra, 1976) with intensities $\leq 1 \mu\text{amp}/\text{m}^2$ between 2100 and 2300 MLT and correlated with electrojet activity. It therefore seems plausible that the electric fields driving the particle acceleration in the magnetotail and those driving the auroral substorm current system in the premidnight sector may be communicated along open magnetic field lines extending into the magnetotail.

ACKNOWLEDGEMENTS

We thank our colleagues and friends, S. M. Krimigis and E. T. Sarris for providing unpublished data from the Charged Particle Measurements Experiment on IMP-7, and R. E. Gold and T. A. Potemra for most helpful discussions. This work was supported by NASA under Task I of Navy Contract N00017-72-C-4401.

REFERENCES

- Allen, J. H., C. C. Abston and L. D. Morris, Auroral electrojet magnetic activity indices AE(11) for 1973, Report UAG-47, World Data Center A for Solar-Terrestrial Physics, NOAA/EDS (Boulder), 1975.
- Fairfield, D. H. and G. D. Mead, Magnetospheric mapping with a quantitative geomagnetic field model, J. Geophys. Res., 80, 535, 1975.
- Fukushima, N. and Y. Kamide, Partial ring current models for worldwide geomagnetic disturbances, Rev. Geophys. Space Phys., 11, 795, 1973.
- Hones, E. W., Jr., J. R. Asbridge, S. J. Bame and S. Singer, Substorm variations of the magnetotail plasmashet from $X_{SM} = -6 R_e$ to $X_{SM} = 60 R_e$, J. Geophys. Res., 78, 109, 1973.
- Hones, E. W., Jr., S. J. Bame and J. R. Asbridge, Proton flow measurements in the magnetotail plasmashet made with IMP-6, J. Geophys. Res., 81, 227, 1976.
- Iijima, T. and T. A. Potemra, The amplitude distribution of field-aligned currents at northern high latitudes observed by TRIAD, J. Geophys. Res., 81, in press, 1976.
- Keath, E. P., E. C. Roelof, C. O. Bostrom and D. J. Williams, Fluxes of ≥ 50 keV protons and ≥ 30 keV electrons at $\sim 35 R_e$. 2. Morphology and flow patterns in the magnetotail, J. Geophys. Res., 81, in press, 1976.
- McPherron, R. L., C. T. Russell and M. P. Aubrey, Satellite studies of magnetospheric substorms on August 15, 1968. 9. Phenomenological model for substorms, J. Geophys. Res., 78, 3131, 1973.
- Mead, G. D. and D. H. Fairfield, A quantitative magnetospheric model derived from spacecraft magnetometer data, J. Geophys. Res., 80, 523, 1975.
- Pytte, T., R. L. McPherron, E. W. Hones, Jr. and H. I. West, Jr., Multiple satellite studies of magnetospheric substorms: Radial dynamics of the plasmashet, J. Geophys. Res., 81, in press, 1976.
- Roelof, E. C., E. P. Keath, C. O. Bostrom and D. J. Williams, Fluxes of ≥ 50 keV protons and ≥ 30 keV electrons at $\sim 35 R_e$. 1. Velocity anisotropy and plasma flow in the magnetotail, J. Geophys. Res., 81, in press, 1976.

Sarris, E. T., S. M. Krimigis and T. P. Armstrong, Observations of magnetospheric bursts of high energy protons and electrons at $\sim 35 R_e$ with IMP-7, J. Geophys. Res., 81, in press, 1976a.

Sarris, E. T., S. M. Krimigis, T. Iijima, C.O. Bostrom and T. P. Armstrong, Location of the source of magnetospheric particle bursts by multispacecraft observations, J. Geophys. Res., 81, in press, 1976b.

TABLE 1

HIGH INTENSITY PROTON BURSTS ASSOCIATED WITH WESTWARD AURORAL ELECTROJET EXPANSION

1973 EVENT	DATE	START (UT)	PEAK FLUX $10^6 \text{ (cm}^2 \text{ s sr)}^{-1}$	X_{SM}	Y_{SM}	Z_{SM}	K P	AURORAL OBSERV.	MLT	ΔH (V)
1	Mar 26	1834	2.2	-27.2	21.9	-4.8	5+	DIX	0040	400
2	Mar 27	0113	6.4	-30.5	18.4	-3.1	4-	GWR	2010	400
3	Mar 28	0109	1.7	-38.0	3.2	-3.9	4+	NAR	2330	400
4	Apr 21	0938	4.2	-34.1	17.2	-2.3	4+	BAR	2140	500
5	Apr 21	1651	7.2	-35.1	14.0	-1.1	5-	DIX	2330	600
6	Apr 21	2341	6.4	-36.6	8.9	-4.7	4+	NAR	2210	400
7	Apr 22	0317	5.0	-37.1	6.8	-3.9	5	GWR	2210	500
8	Apr 22	0813	3.0	-37.6	4.5	3.4	6	BAR	2010	1200
9	May 4	2201	2.2	-31.7	18.5	7.8	3	LEI	2200	400
10	Sep 20	1034	7.0	-31.1	15.0	1.0	4-	COL	2210	400
11	Oct 3	0514	5.0	-31.3	17.5	0.4	8-	BAR	1710	1200
12	Oct 3	0851	11.4	-32.2	14.6	-2.3	6	COL	2140	400
13	Oct 3	1407	7.2	-33.2	11.2	-1.3	6	DIX	2020	800

FIGURE CAPTIONS

- FIGURE 1a** Proton anisotropy contours showing the tailward flow of protons in Event 11 near the neutral sheet at $Y_{SM} = 17.5 R_e$ (see Table 1). The EPE 50-200 keV (upper panel) and CPME 290-500 keV (lower panel) proton fluxes are plotted as a function of arrival direction and time, with the shading density being approximately proportional to the logarithm of the proton flux as shown in the key to the left of each figure. Arrival directions of 0° , 90° , 180° and 270° correspond respectively to protons moving antisunward, toward the dawn sheath, sunward and toward the dusk sheath. Multiple tailward bursts of intensity $> 3 \times 10^6 (\text{cm}^2 \text{s sr})^{-1}$ 0524-0527 UT preceded by a flux "dropout" at 0519 UT.
- FIGURE 1b** The continuation of Figure 1a showing the second phase of Event 11 during which the sunward flow of protons was observed.
- FIGURE 2a** Proton anisotropy contours for Event 1 inside the dusk magnetopause at $Y_{SM} = 21.9 R_e$ (see Table 1). The format is the same as in Figure 1. A single high intensity burst of tailward flowing protons was observed at 1829 UT and was preceded by a bi-directional burst at 1829 UT. Subsequent to 1829 UT the proton flow was sunward.
- FIGURE 2b** The continuation of Figure 2a showing the remainder of Event 1.
- FIGURE 3** Proton and electron time intensity profiles and the proton anisotropy contour for Event 2 (see Table 1). The presentation of the proton anisotropy contours (a) is the same as that in Figure 1. The proton fluxes shown in (b) are the average of the three sunward and antisunward (i.e., 1, 2, 3, 8, 9 and 10) sectors while the electron fluxes (c) are the average of sectors 1 and 8, as shown in the inset in (b). Periods of sunward (S) or tailward (T) flow are indicated in (b) and (c). Except for the 5-second intervals shown by the arrows, the electron flux was essentially isotropic (to within 10%). For the protons however, either sunward or tailward flow persisted throughout much of the event.

FIGURE 4 Burst association with geomagnetic activity for the 13 events listed in Table 1. Shown for each event is the H-component of the auroral station earliest in magnetic local time (MLT) which detected the apparent intensification of the westward electrojet. The MLT of the observatory at the onset of the tailward burst is shown at the lower left of each panel. The bars at the top and bottom mark the periods in which high intensity proton bursts were observed. Periods in which the flow was tailward are shaded, while the periods of sunward flows are outside the shaded areas. The position of the spacecraft for each of the events is given in the inset at the lower left. The contours for MLT (hours circled) and 70° latitude at $X = -10 R_e$ were taken from a model by Mead and Fairfield (1975) as described in the text, and the indicated MLT at the spacecraft Y-Z coordinates is given in parentheses in the lower right of each magnetometer trace panel. The 7 events in the lower panels (3, 6-8 and 11-13) all occur at MLT within 2 hours of the MLT contours in the inset; these events all show a cleaner association of tailward bursts with the intensification phase than the 6 other events in the upper panels (for which the corresponding MLT difference always exceeds 2 hours).

FIGURE 5 Auroral zone magnetograms for Event 11. The representation using bars and shading of the periods of tailward and sunward bursts is the same as that used in Figure 4. The AU and AL indices are taken from Allen et al. (1975).

FIGURE 6 H and D-components of the geomagnetic fields at low latitude stations for Events 11 and 12. The stations are arranged from top to bottom in decreasing MLT starting with the station nearest magnetic local midnight. Burst events are indicated as in Figure 5.

FIGURE 7 H and D-components of the geomagnetic fields at low latitude stations for Event 13. See Figure 6.

FIGURE 8 H and D-components of the geomagnetic fields at low latitude stations for Event 4. See Figure 6.

FIGURE 9 H and D-components of the geomagnetic fields at low latitude stations for Events 6 and 7. See Figure 6.

IMP-7 Anisotropy Contour

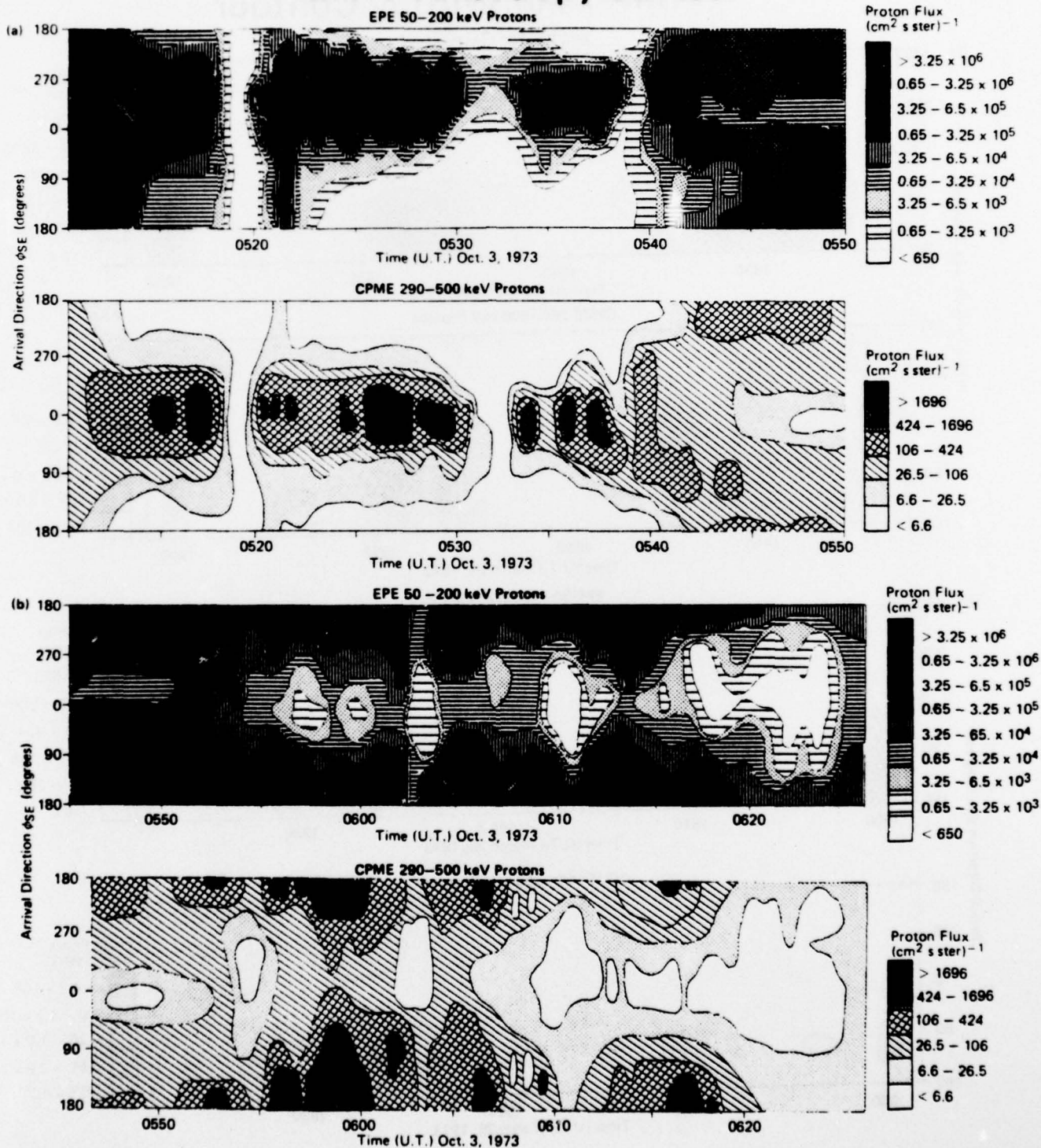


FIGURE 1a & 1b

IMP-7 Anisotropy Contour

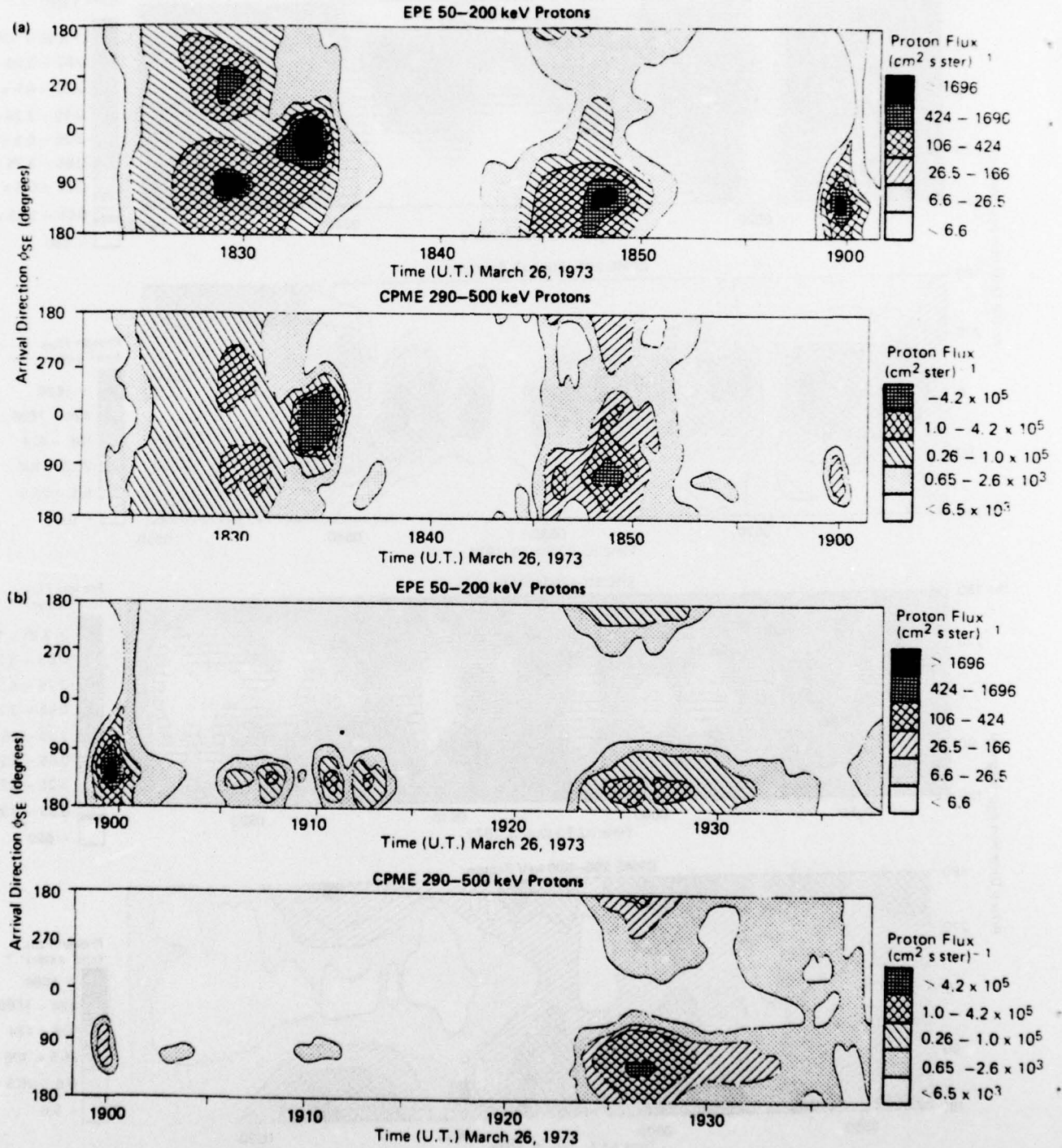


FIGURE 2a & 2b

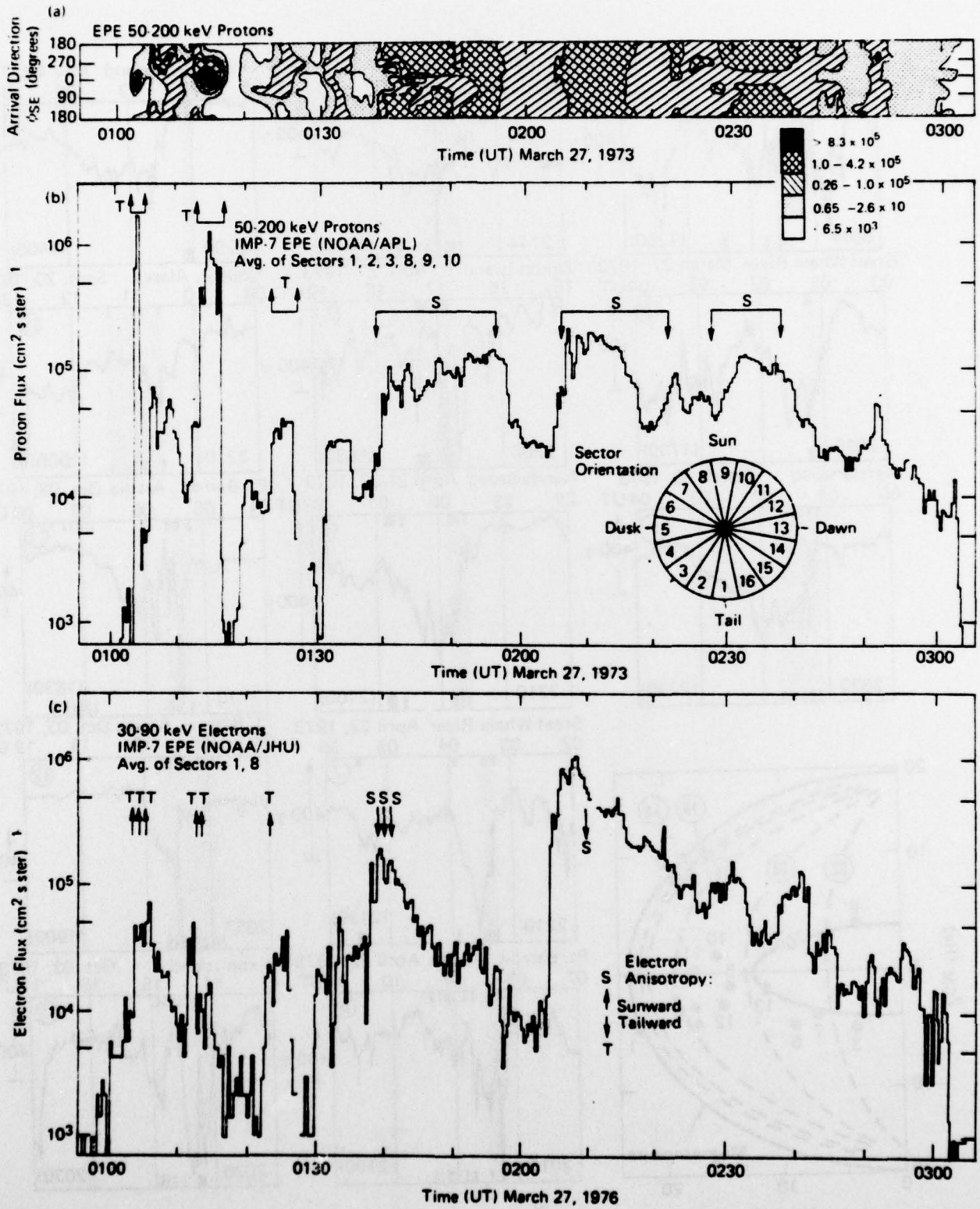


FIGURE 3

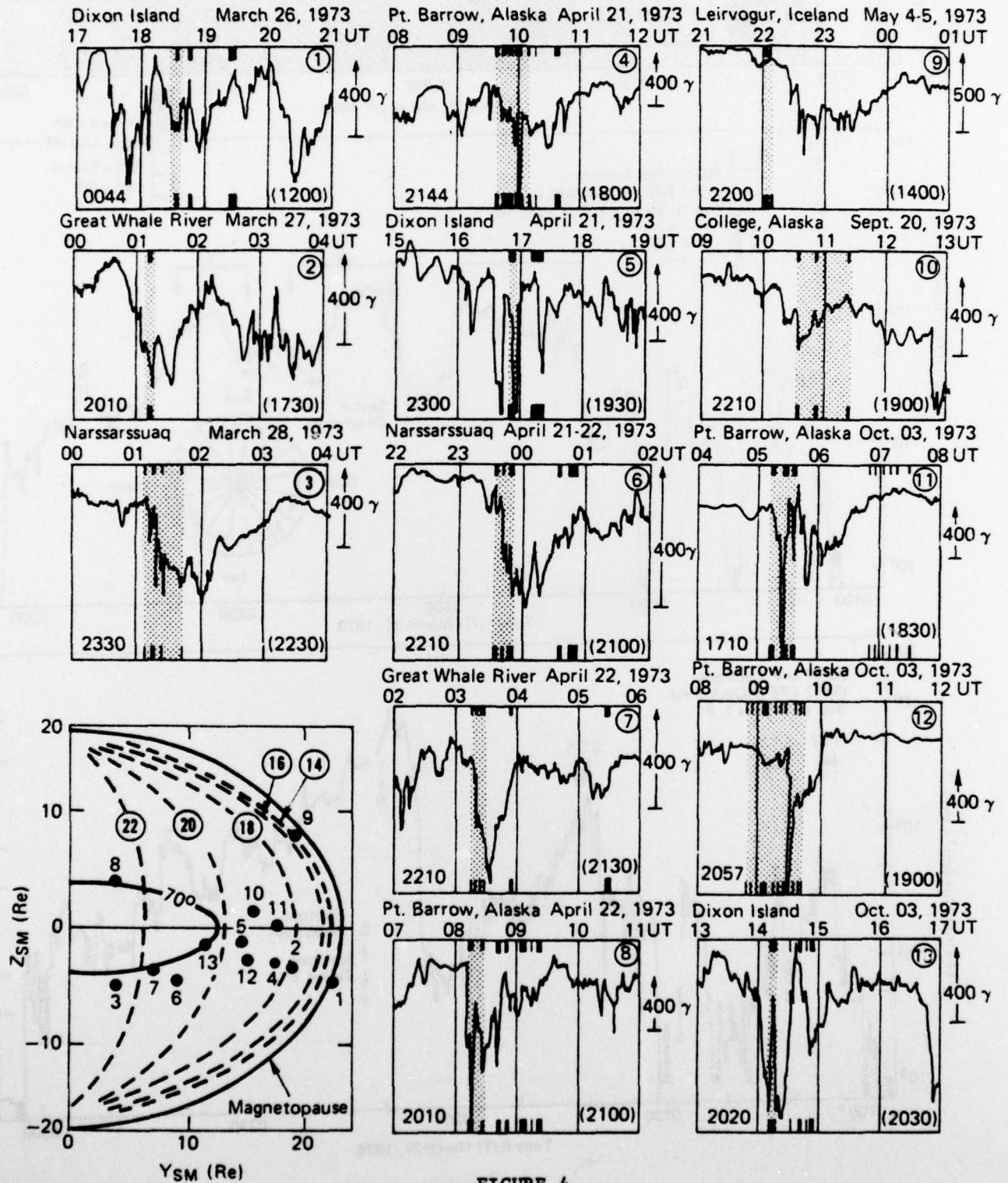


FIGURE 4

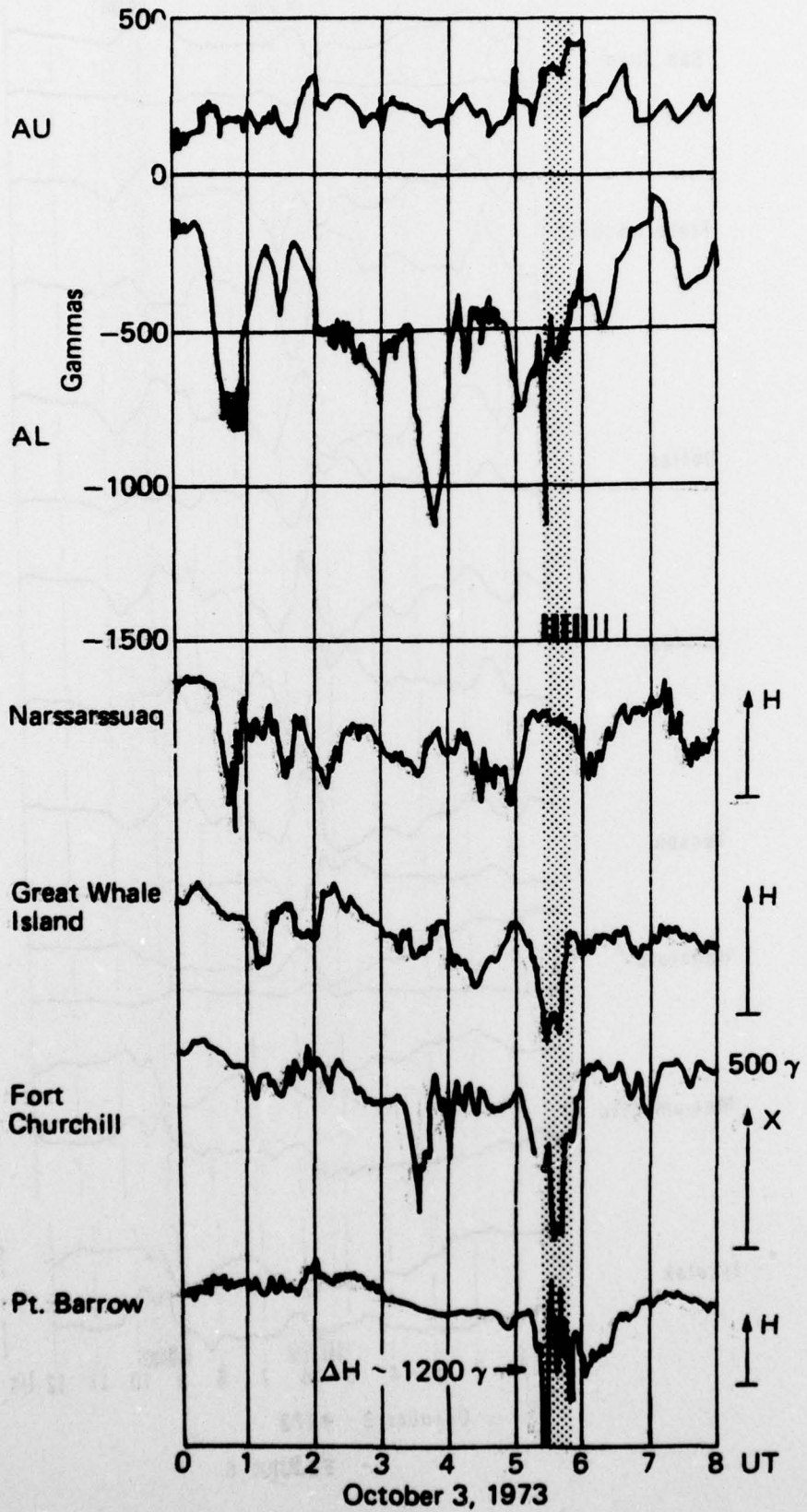


FIGURE 5

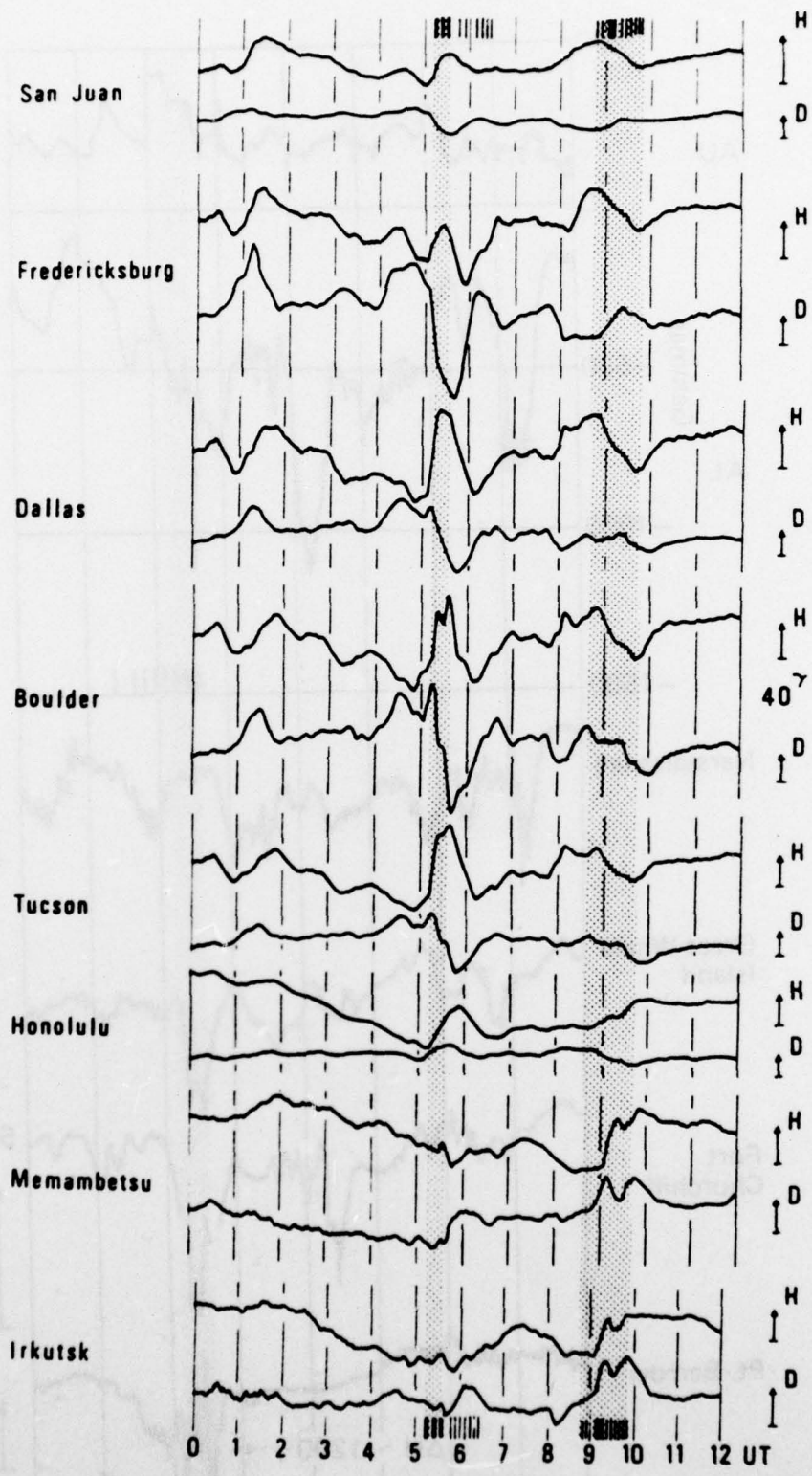
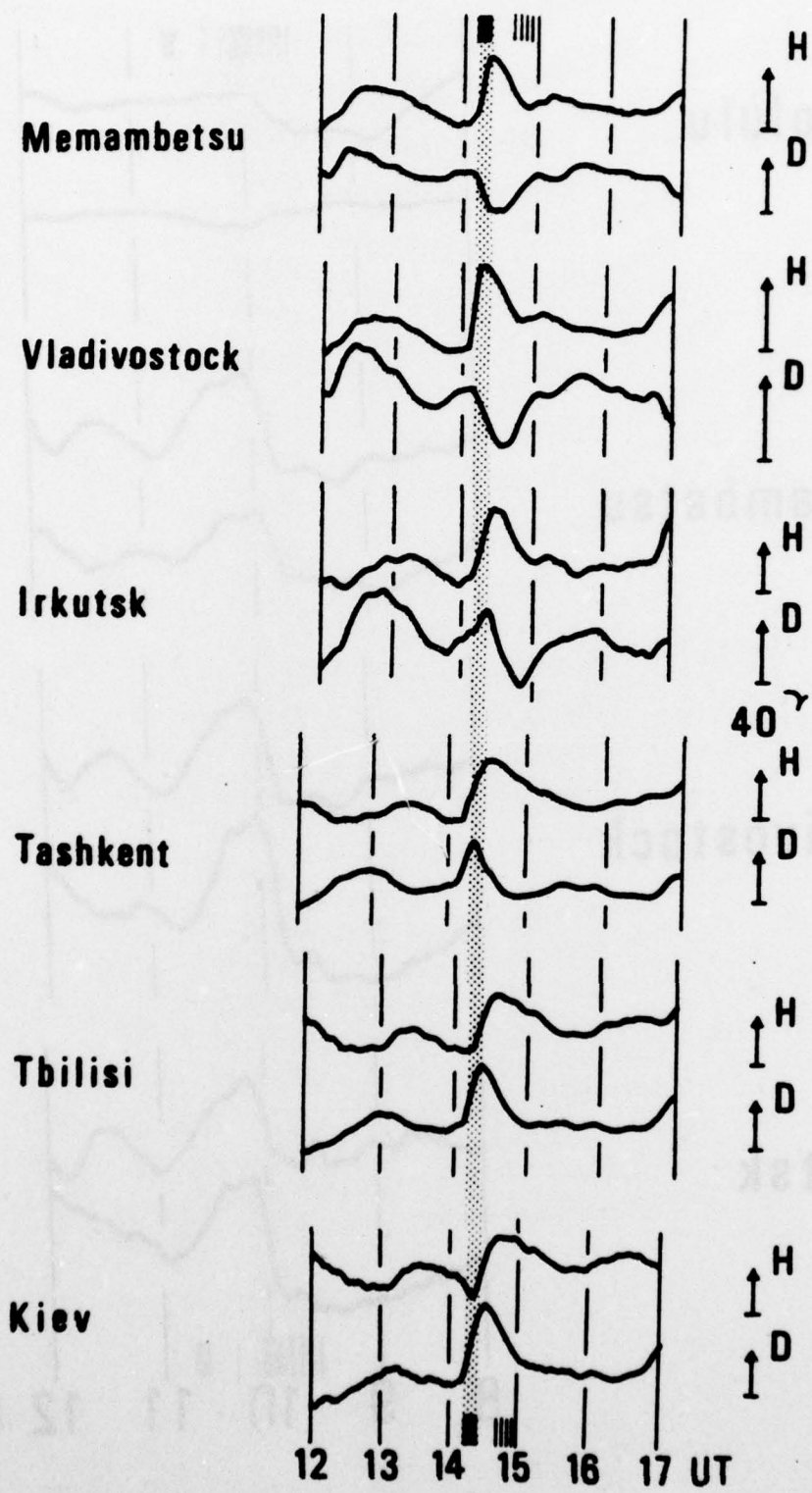
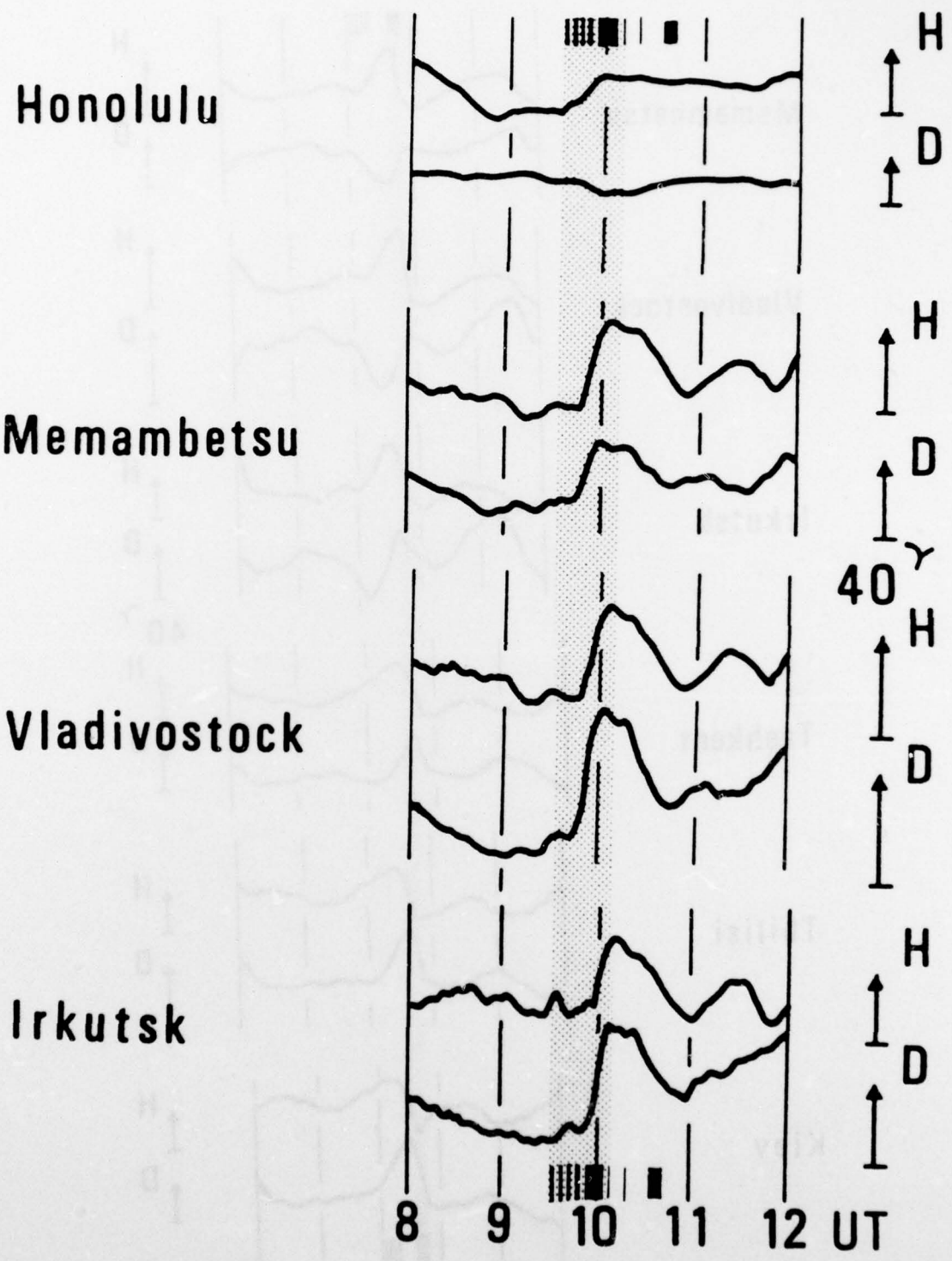


FIGURE 6



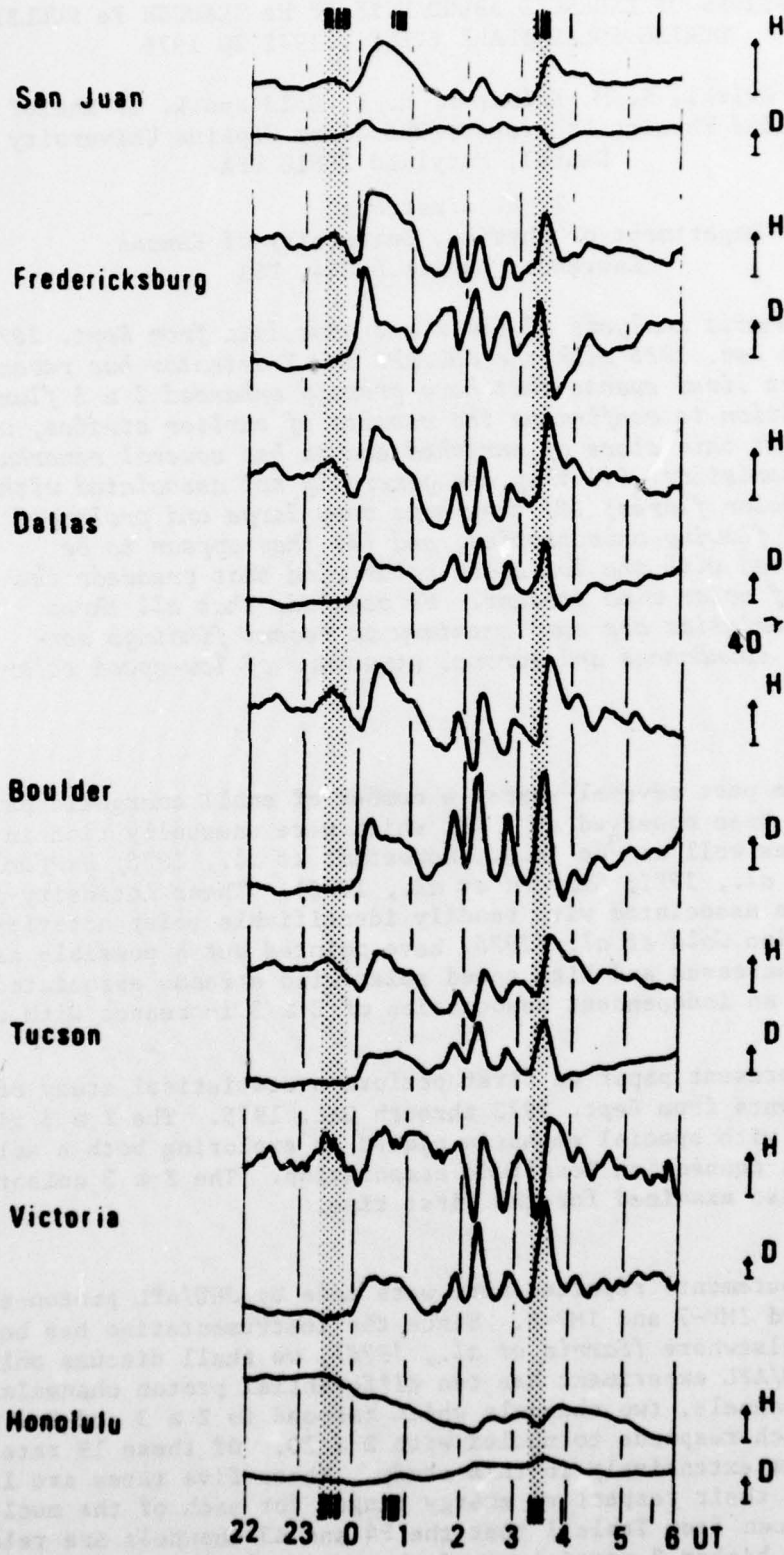
October 3, 1973

FIGURE 7



April 21, 1973

FIGURE 8



April 21-22, 1973

FIGURE 9

OBSERVATIONS OF ENHANCED ABUNDANCES OF He THROUGH Fe NUCLEI
DURING SOLAR FLARE EVENTS, 1972 TO 1976

R. D. Zwickl, S. M. Krimigis, R. E. Gold and E. C. Roelof
Applied Physics Laboratory/The Johns Hopkins University
Laurel, Maryland 20810 USA

T. P. Armstrong
Department of Physics, University of Kansas
Lawrence, Kansas 66044 USA

A systematic analysis of the $Z \geq 3$ rate data from Sept. 1972 through Dec. 1975 with the JHU/APL IMP-7 detector has revealed 10 short lived events that have greatly enhanced $Z \geq 3$ fluxes. In addition to confirming the results of earlier studies, we find that this class of enriched events has several remarkable characteristics: (1) they are generally not associated with major solar flares; (2) they have very large and prolonged outward flowing anisotropies; and (3) they appear to be associated with the low speed solar wind that precedes the onset of solar wind streams. We conclude that all three characteristics are complementary to recent findings concerning abundances and coronal structure of low-speed solar wind.

INTRODUCTION

Over the past several years, a number of small energetic particle enhancements have been observed at 1 AU, which were unusually rich in medium and heavy nuclei as well as ^3He (e.g., Hovestadt et al., 1975; Hurford et al., 1975a,b; Price et al., 1971; Garrard et al., 1973). These intensity increases did not seem to be associated with readily identifiable solar activity such as flares. In addition Gold et al. (1975) have pointed out a possible association between He-rich increases and high speed solar wind streams associated with a coronal hole, and an independent association of $Z \geq 3$ increases with recurrent He-rich events.

In the present paper we first perform a statistical study of all identifiable $Z \geq 3$ events from Sept. 1972 through Dec. 1975. The $Z \geq 3$ rich events are then examined with special emphasis placed on exploring both a solar wind and a heliographic connection longitude association. The $Z \geq 3$ anisotropy for these events is also examined for the first time.

INSTRUMENTATION

The measurements reported here were made by JHU/APL proton-electron telescopes on-board IMP-7 and IMP-8. Since the instrumentation has been presented in detail elsewhere (Sarris et al., 1976), we shall discuss only the rate channels. The JHU/APL experiment has ten differential proton channels, six differential alpha channels, two channels which respond to $Z \geq 3$ and $Z \geq 6$ and a single channel which responds to nuclei with $Z \geq 20$. Of these 19 rate channels we use five of them extensively in this study. These five rates are listed in Table I along with their respective energy ranges for each of the nuclei studied here. It can be seen from Table I that the P4 and A3 channels are relatively insensitive to the higher Z particles and thus they allow us to accurately determine the proton and alpha particle contribution of solar particle events in the 1.8 to 4.5 MeV/nuc energy range. The relative contribution of higher charge Z nuclei in a solar particle event can be determined from the Z1, Z2, and Z3 rate channels.

TABLE I
PASSBAND DATA IMP-7

Passband Name	Energy Range (MeV/nuc)					
	Protons	Alphas	Carbon	Nitrogen	Oxygen	Iron
P4	1.85-4.50	1.74-2.15	3.00-3.10	3.15-3.40	3.40-3.55	3.80 -4.00
A3	—	1.74-4.30	3.00-3.80	3.15-3.80	3.40-4.00	3.80 -4.30
Z1	—	—	0.89-1.85	0.77-1.59	0.68-1.38	0.225-0.450
Z2	—	—	1.85-2.85	1.59-3.15	1.38-3.40	0.45 -3.80
Z3	—	—	—	—	—	3.20 -7.00

OBSERVATIONS

In order to identify $Z \geq 3$ rich events we have carried out a systematic statistical analysis of *all* energetic particle events that exhibited a maximum flux in excess of $0.001 \text{ cm}^2 \text{sr sec/MeV}$ in the Z1 channel (See Table I). This criterion enabled us to catalog 92 such events from Sept. 1972 to Jan. 1976.

To identify systematically those events that have enhanced $Z \geq 3$ abundances, we have recorded the flux at the time to maximum (t_{max}) during each of the 92 events for four of the five channels listed in Table I. Scatter plots of various combinations of these channels are shown in Figure 1. The open and closed circles represent temporal and spatial events, respectively (Gold *et al.*, 1977). Events to which we were unable to assign a temporal or spatial structure were called unknown and are denoted by a star. Events that have been reported as ^3He rich are represented by a square (Hurford *et al.*, 1975a,b; Hovestadt *et al.*, 1975). In Figure 1c we have arbitrarily drawn a dashed line labelled Z3-rich. Events that fall above this line are called Fe rich and are shown as triangles. Those events in Figure 1b that are Z1 rich but not Z3-rich are called CNO rich and are labelled by a diamond. Figure 1 now shows a natural band at the upper edge of each scatter plot that is formed by the ^3He , Fe, and CNO rich events.

We can conclude from Figure 1 that: (1) all ^3He -rich events are Fe-rich (panel C); (2) all Fe-rich events produce large enhancements in all $Z > 1$ species when compared to protons; (3) in the Fe-rich events, the $Z \geq 3$ species are enhanced when compared to He; (4) there is less variability among the $Z \geq 2$ species when compared to the medium and heavy nuclei than when compared to protons; (5) all the $Z \geq 3$ -rich events are relatively small events; and (6) the spatial events are generally small events that are richer in alphas than in $Z \geq 3$. We note that experimental conclusions 1-5 confirm those given previously by Hurford *et al.*, 1975b.

We now examine in more detail the ten $Z \geq 3$ -rich events shown in Figure 1. These events are listed in Table II along with several of their associated characteristics. We feel it is quite significant that although the 1975 data were scanned using the same criteria as 1972-1974, no $Z \geq 3$ rich events were found in that year, indicating an abrupt change in their production and/or propagation. We see from the first and second columns of Table II that these events usually last less than two days and that only one event is clearly associated with a solar flare (importance 2N). Note that this event is not rich in ^3He . A second event is possibly associated with a 1B flare. Although there is no clean flare association we did find that many of the other events occurred when a series of small (-N) flares are seen in western plage regions (W25-W70). The spectral index γ for protons, alphas and $Z \geq 3$ in Table II indicates that

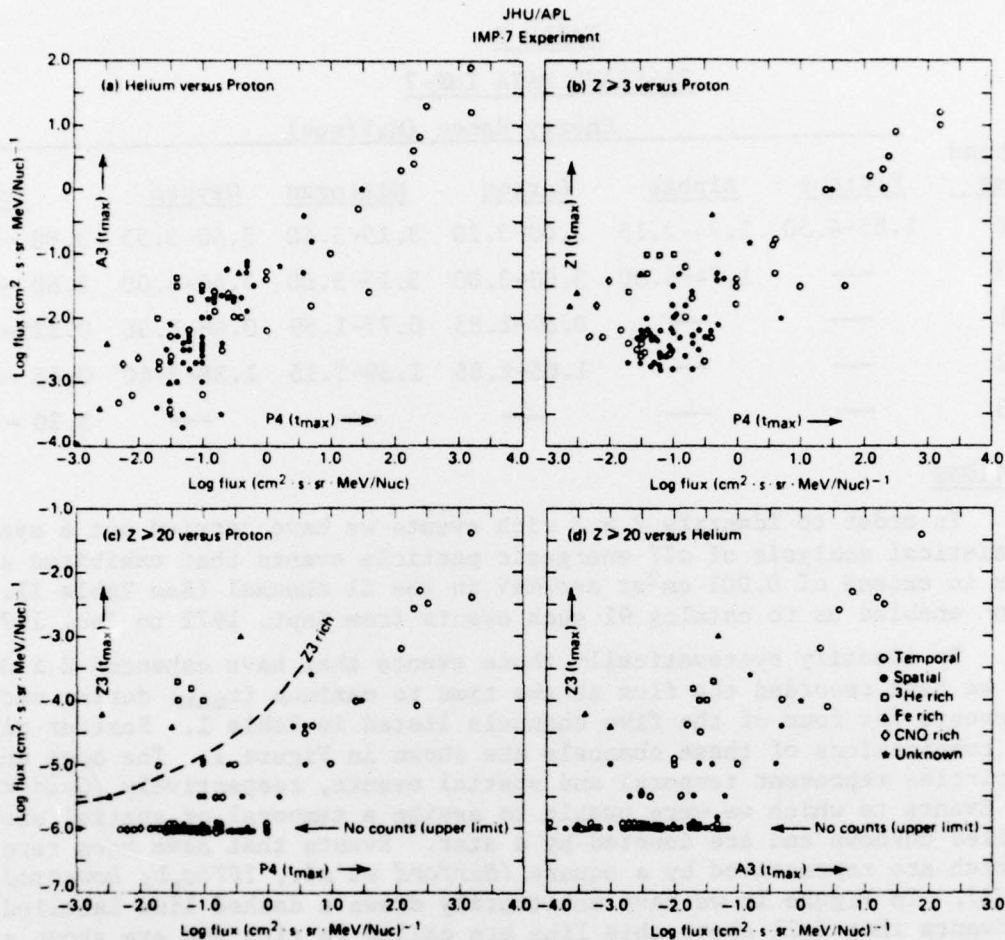


Figure 1 Scatter plots for 92 events from Sept. 1972 to December 1975. The $Z \geq 3$ rich events form a band near the top portion of each plot.

$\gamma(P)$ is harder for these events than for spatial events (see Gold *et al.*, 1977) and that $\gamma(Z)$ is generally harder than $\gamma(P)$. However, part of this effect might be due to counting low energy Fe particles in the Z2 channel (see Table I). The P/α and α/M ratios which range from 4 to 34 and from 0.3 to 7 respectively, are both a factor of 10 to 100 below those of the large flare-associated events. This implies that, while many of these events are rich in ³He, they are also rich in $Z \geq 3$ - a conclusion also reached by Hurford *et al.* (1975b).

A definite solar wind association is evident in Table II. We find that the solar wind velocity is very low during 8 of the events and that these events either occurred towards the end of a decay that was followed by a rise (2 events) or during the early portion of a rise (6 events). The two remaining events are related to small temporal solar wind enhancements that occur during larger solar wind streams. Also shown for each event is the range of connection longitudes of the large-scale interplanetary magnetic field, estimated in the approximation of "frozen-in" fields in non-accelerating solar wind plasma (Nolte and Roelof, 1973). The last column in Table II contains the enrichment identification which was taken from Figure 1 for the Fe and CNO designations and from Hurford *et al.* (1975a,b) and Hovestadt *et al.* (1975) for the ³He designation.

The flux anisotropy in the ecliptic plane of the $Z \geq 3$ particles were also examined for each of the Z -rich events listed in Table II. For each event

TABLE II
Z ≥ 3 RICH EVENTS FROM SEPTEMBER 1972 - JANUARY 1976

Event Duration	Flare Assoc.	Particle Data ¹					Solar Wind ² (km/s)	Connection Longitude (°)	Enrichment ³
		$\gamma(P)$	$\gamma(A)$	$\gamma(Z)$	P/α	α/M			
72 302:00 - 304:00	?	2.4	2.0	1.4	25	3.0	360 - 410 S(i)	~ 40 → 15	Fe
73 46:00 - 47:18	?	2.7	3.2	2.0	5	7.1	325 - 380 D,S	30 → 10	Fe, ³ He
73 96:12 - 99:00	?	2.8	1.5	2.2	15	0.6	(?) - 425 D(i)	90 → 70	CNO
73 141:06 - 142:12	?	2.2	2.3	2.2	11	0.8	500 - 750 T	190 → 180	CNO
73 179:12 - 181:15	?	3.0	4.5	1.5	4	1.9	475 - 750 S,T	45 → 30	Fe, ³ He
73 248:15 - 250:12	?	2.5	3.6	2.9	4	6.2	375 - (?) ?(i)	250 → 230	Fe, ³ He
74 51:12 - 52:09	?	2.9	3.5	1.6	6	2.2	350 - 415 S	200 → 100	Fe, ³ He
74 127:08 - 130:15	1E,W38 ?	2.4	3.6	1.5	8	1.7	450 - 750 T	230 → 210	Fe, ³ He
74 133:15 - 136:12	2N,W66	3.6	3.6	1.2	25	0.8	350 - 410 S	180 → 140	Fe
74 335:12 - 336:12	?	3.1	—	1.6	34	0.3	320 - 350 S	60 → 40	Fe

¹ Particle data are derived from ~ 6 hour average at t_{max} . $\gamma(P)$, $\gamma(A)$, $\gamma(Z)$ refer to spectral index for 1.85-7.8 MeV protons, 1.74-11.5 MeV/nuc alpha, and 0.77-3.2 MeV/nuc Z ≥ 3, respectively. P/α is the proton to alpha ratio at 1.74 to 4.3 MeV, and α/M is the alpha to Z ≥ 3 ratio at 1.6 to 4.3 MeV.

² S = Solar wind stream onset and early portion of rise.
D = Solar wind stream decay with nearly constant high coronal connection latitude
T = Temporal solar wind stream superimposed on a large stream
i = Incomplete solar wind data

³ Fe and CNO rich designations are derived from scatter plots in Figure 2. ³He designations are taken from Hurford et al. (1975a,b) and Hovestadt et al. (1975).

we summed the Z1 sector rate data for several hours just after the onset of the event. The results for four of these events observed on IMP-7 along with the hours summed and the spacecraft location in solar ecliptic coordinates are shown in Figure 2. In each event the IMP-7 spacecraft was located well outside the magnetosphere. It is very clear from Figure 2 that each distribution shows an *outwardly directed, highly anisotropic* component. Upon examination of the interplanetary magnetic field data for the day 46 and day 141, 1973 events, we find that in both events the magnetic field swung through ~ 120° in azimuth during the time period summed. The enhanced sectors in Figure 2 fell within these swings. Also, in both cases the magnetic field solar ecliptic colatitude angle was greater than 45° during part of the period. Since our detectors scan the ecliptic plane with a 22½° half-angle, this strongly implies that the anisotropy for these two events are vastly underestimated in Figure 2. Their actual particle distributions would most likely resemble the very strong anisotropy on day 134, 1974. Unfortunately we do not have any magnetic field data for the day 96, 1973 event. Although we have shown anisotropy data for only four of the events, the remaining events that were observed while IMP-7 was located outside of the magnetosphere also show very large anisotropies.

DISCUSSION

We have systematically analyzed the Z ≥ 3 rate data from the JHU/APL detector on-board IMP-7 from Sept. 1972 through Dec. 1975. During this time period we found and examined 10 events that were classified as Z ≥ 3 rich events. Several of these events augment existing ³He and Fe rich events that have been reported in the literature (Hurford et al., 1975a,b; Hovestadt et al., 1975). In addition to being Z ≥ 3 rich, these 10 events appear to have several other common characteristics which carry important implications. (1) Only one of the events could be associated with a major flare and that event was not ³He rich.

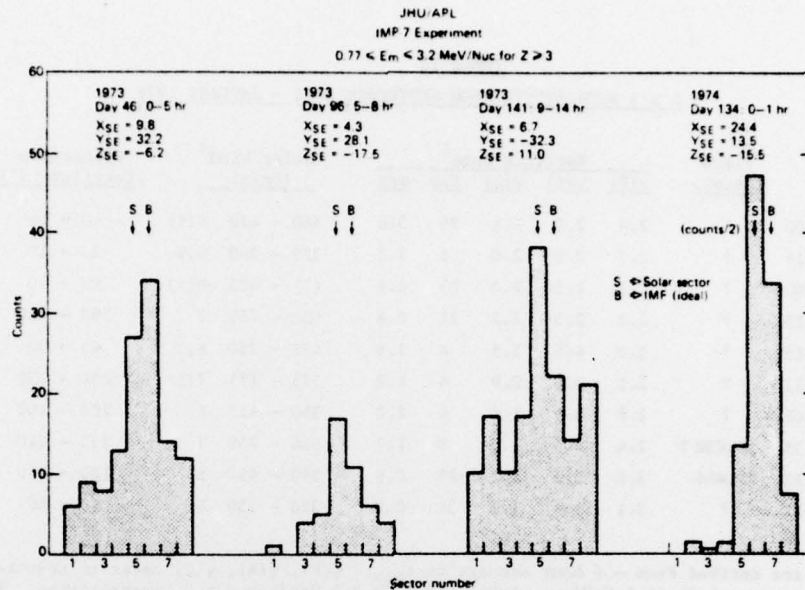


Figure 2 Sectorized data for four $Z \geq 3$ rich events from the Z1 channel (see Table I).

Several events were, however, associated with extended weak activity in the western hemisphere. The lack of association of these events with significant flares (importance ≥ 1) implies that if the present theoretical nuclear reaction models (*Ramaty and Kozlovsky, 1974*) describe the production of ${}^3\text{He}$, they must apply to conditions of either no flares or (at the very best) to a series of very weak flares (importance $\leq -N$) which do seem to accompany some of these events. However, storage of the ${}^3\text{He}$ over many days before release is then clearly required. (2) The $Z \geq 3$ rich events have very large and long-lasting anisotropies. This observation, coupled with the fact that the events typically last ≤ 2 days, implies that the source of these events is temporal, short-lived, and lies inside 1 AU and therefore cannot be ascribed to suggested interplanetary acceleration beyond 1 AU (*McDonald et al., 1976*). (3) There is a very strong association between $Z \geq 3$ rich events and the low speed solar wind just prior to or within the onset of solar wind streams. This association is quite complementary to the recent results of *Bame et al. (1977)* that the solar wind He abundance is most variable in low-speed solar wind and *Bame et al (1975)* that Si and Fe show significant correlated variations in low-speed solar wind. They suggest that the abundance variations could be produced either by coronal transient events or by magnetic reconnection processes near the edges of coronal open-field regions which result in locally strong heavy element fractionation. We suggest in addition that the eastern edge of a coronal source region of high speed solar wind is a likely location for the escape of energetic particles, since the three-dimensional structure of the Alfvén critical surface, at the edge of the coronal stream source (*Nolte et al., 1977*), implies strong interactions between the western edge of the stream and the slow solar wind just to the west of it. Such interactions are minimized at the eastern source edge. The temporal nature of the $Z \geq 3$ rich events implied by the very large particle anisotropies is therefore consistent with the dynamic release of the energetic particles by changes in coronal magnetic structure due to temporal solar wind interactions. Moreover, since *Bame et al. (1975)* point out that " ${}^{16}\text{O}$, Si, and Fe abundances are, within error, the same as those determined for the lower corona and photosphere", the same $Z \geq 3$ rich region in the lower solar atmosphere (e.g., the low-activity

regions found (W20-W70) may serve as a common source for the energetic particles and low speed solar wind, even though the altitudes of the particle acceleration and plasma heating may still differ.

ACKNOWLEDGEMENTS

We are indebted to R. E. Cashion, S. A. Gary, J. W. Kohl and J. H. Crawford of JHU/APL for their diligent efforts in making the IMP-7 experiment a success. The efforts of the GSFC project personnel, especially those of Mr. M. A. Davis and Dr. N. Ness are acknowledged with thanks. We are grateful to A. J. Lazarus and J. D. Sullivan for providing solar wind data from the MIT detector on IMP-7 and 8. This research has been supported by NASA under Task I of Contract N00017-72-C-4401, between The Johns Hopkins University and the Department of the Navy. Two of us (REG and ECR) acknowledge support from Air Force Geophysics Laboratory under Task ZF10 of the same contract.

REFERENCES

- Armstrong, T. P. and S. M. Krimigis, *J. Geophys. Res.*, 76, 230, 1971.
- Bame, S. J., J. R. Asbridge, W. C. Feldman, M. D. Montgomery and P. D. Kearney, *Solar Phys.*, 43, 463, 1975.
- Bame, S. J., J. R. Asbridge, W. C. Feldman and J. T. Gosling, *J. Geophys. Res.*, 82, 1487, 1977.
- Garrard, T. L., E. C. Stone and R. E. Vogt, *High Energy Phenomena on the Sun Symposium Proceedings (NASA SP-342)*, 341, 1973.
- Gold, R. E., S. M. Krimigis, E. C. Roelof, A. S. Krieger and J. T. Nolte, *Proc. 14th International Cosmic Ray Conf. (Munich)*, 5, 1710, 1975.
- Gold, R. E., S. M. Krimigis and E. C. Roelof, *Proc. 15th International Cosmic Ray Conf. (Ploudiv)*, 1977.
- Hovestadt, D., B. Klecker, O. Vollmer, G. Gloeckler and C. Y. Fan, *Proc. 14th International Cosmic Ray Conf. (Munich)*, 5, 1613, 1975.
- Hurford, G. J., E. C. Stone and R. E. Vogt, *Proc. 14th International Cosmic Ray Conf. (Munich)*, 5, 1624, 1975a.
- Hurford, G. J., R. A. Mewaldt, E. C. Stone and R. E. Vogt, *Ap. J.*, 201, L95, 1975b.
- McDonald, F. B., B. J. Teegarden, J. H. Trainor, T. T. von Rosenvinge and W. R. Webber, *Ap. J. Lett.*, 203, L149, 1976.
- Nolte, J. T. and E. C. Roelof, *Solar Phys.*, 33, 241, 1973.
- Nolte, J. T., A. S. Krieger, E. C. Roelof and R. E. Gold, *Solar Phys.*, in press, 1977.
- Price, P. B., I. Hutcheon, R. Cowsik and D. J. Barber, *Phys. Rev. Lett.*, 26, 916, 1971.
- Ramaty, R. and B. Kozlovsky, *Ap. J.*, 193, 729, 1974.
- Sarris, E. T., S. M. Krimigis and T. P. Armstrong, *J. Geophys. Res.*, 81, 2341, 1976.
- Van Allen, J. A., P. Venkatarangan and D. Venkatesan, *J. Geophys. Res.*, 79, 1, 1974.